Role of Polarity and BAR domain proteins in plasma membrane re-modelling in syncytial *Drosophila* embryos

विद्या वाचस्पति की
उपाधि की अपेक्षाओं की आंशिक पूर्ति में प्रस्तुत शोध प्रबंध

A Thesis submitted in partial fulfillment of the requirements
of the degree of Doctor of Philosophy

द्वारा / By

देबास्मिता मित्रा / Debasmita Mitra

पंजीकरण सं. / Registration No.: २०१७२००९ / 20172009

शोध प्रबंध पर्यवेक्षक / Thesis Supervisor: प्रो. ऋचा रिखी / Prof. Richa Rikhy

भारतीय विज्ञान शिक्षा एवं अनुसंधान संस्थान पुणे
INDIAN INSTITUTE OF SCIENCE EDUCATION AND RESEARCH PUNE

2024

Dedicated to Ma, Baba, Souraj

and

the loving memory of Sukanya…

CERTIFICATE

It is certified that the work incorporated in the thesis entitled "**Role of Polarity and BAR domain proteins in plasma membrane re-modelling in syncytial *Drosophila* embryos**" submitted by Ms. Debasmita Mitra, represents original work conducted by her at IISER in Pune under my direction and supervision from August 2019 to July 2024. Any portion of the work provided here has never been a part of a thesis that was previously submitted for the granting of a degree or certificate from another university or institution. I further attest that, to the best of my knowledge, the claims she made above regarding his thesis are true.

Date: 29-07-2024

Prof. Richa Rikhy

(Supervisor)

DECLARATION

Name of Student: **Debasmita Mitra**

Reg. No.: **20172009**

Thesis Supervisor(s): **Prof. Richa Rikhy**

Department: **Biology**

Date of joining program: **01-08-2019**

Date of Pre-Synopsis Seminar: **15-02-2024**

Title of Thesis: **Role of Polarity and BAR domain proteins in plasma membrane re-modelling in syncytial Drosophila embryos**

I declare that this written submission represents my idea in my own words and where others' ideas have been included; I have adequately cited and referenced the original sources. I declare that I have acknowledged collaborative work and discussions wherever such work has been included. I also declare that I have adhered to all principles of academic honesty and integrity and have not misrepresented or fabricated or falsified any idea/data/fact/source in my submission. I understand that violation of the above will be cause for disciplinary action by the Institute and can also evoke penal action from the sources which have thus not been properly cited or from whom proper permission has not been taken when needed.

The work reported in this thesis is the original work done by me under the guidance of

Prof. **Richa Rikhy**

Date: **29-07-2024**

Signature of the student: Debasmita Mitra

ACKNOWLEDGEMENTS

While writing the acknowledgement section of the thesis, I am flooded with emotions. The journey of pursuing this degree has been a passion that was not an easy job. It not only required a lot of perseverance and dedication from my side but it also would not have been possible without the efforts and support of the people who surround me.

Firstly, I would express my gratitude towards my guide, Prof. Richa Rikhy, for considering me potent enough to join her lab and work on this amazing model system and research topic. I am extremely grateful for the amount of freedom she has provided me all along my journey to pursue my project. Whenever I have felt stuck or doubtful, it was through her immense support and valuable advice, that I could make my way through the hindrances. Her suggestions added refinement to not only the exceptional findings that I came across but also to the otherwise superficially insignificant observations. I am extremely grateful for her guidance. I am also extremely grateful towards Dr. Tom Millard and Dr. Georgina Goddard, The University of Manchester, UK, for their tremendous co-operation with reagents for the MIM project. I am also indebted to Dr. Millard for the discussions and valuable suggestions. I would also like to take this opportunity to thank my Research Advisory Committee members Dr. Mayurika Lahiri, Dr. Nagaraj Balasubhramanian and Dr. Jomon Joseph, for providing important suggestions and advice during the annual review meetings.

I am also extremely grateful to the Department of Biology at IISER Pune as a whole. I remember, when I joined as a naive Integrated PhD student, I was vastly unaware of this rather competitive yet extraordinarily exciting academic and research world. It is through the exposure that this one of a kind department provided me as a young researcher, whether it be the opportunities to meet eminent scientists, or attend scientific talks and conferences, the unbounded sharing of scientific ideas and troubleshootings, or the technical support with respect to latest technologies, I have become more aware and empowered with knowledge. To begin with I am extremely grateful towards Dr. Santosh Podder and Mr. Vijay Vitthal for the training and guidance as well as for the maintenance and coordination of the Microscopy facility, without which it would have been impossible for us to accomplish our work. I also wish to thank Snehal, Yashwant, and Ashwini for their assisting with the fly stock maintenance and fly food preparation that keep our flies and crosses running. The staff at IISER-Pune Biology office Mrinalini, Shabnam, Mahesh, Piyush, Kalpesh and Hariprasad, who are

indispensable for our day-to-day work, whether it be placing orders for reagents or repairing instruments. I would like to thank them for their relentless assistance and services.

For the past 7 years, IISER Pune has not been only a place of work but also a second home where I have been surrounded with a second family, the MAD lab members- Harsh, Sanjana, Shashwat Somya, Rahul, Anirban, Aparna, Sakshi and Rhishikesh. The chai-coffee breaks in between work, provided the much-needed breaks for vents and rants, shared from either failed experiments or our daily lives. The hostel-cooking episodes, monsoon treks and trips to conferences with this group of people are a treasure trove of memories that I have proudly collected during my PhD journey and will always hold them closely to my heart. The younger lot comprising Shweta, Sanskruti, Mridusmita, Achyusman, Neelanshi and Atharva also added to the camaraderie with their own dose of cheerfulness. I am indebted to the seniors as well who were a part of the lab when I had joined - Bipasha, Swati, Sameer, Sayali, Dnyanesh and Bhavin. They not only taught me the basics of my work but also gave valuable advice that have stayed with me till today. I also would like to thank Amruta, with whom I had the opportunity to work during her tenure in the lab as a Masters student. I was supposed to mentor her for the project but in turn I got to learn a lot from her. All of these people made life at IISER a lot easier.

I am thankful as well to my funding agencies - IISER Pune and CSIR for the graduate fellowship, IISER Pune-IDEAS fellowship for support, Infosys, EMBO and CSIR travel grant for financial support required for attending international conferences, Wellcome trust DBT India alliance for economic support to lab.

I am indebted for the strong support system that I have outside IISER, that has kept me going through the harsh days. Rashmi has been one of the strongest shoulders to lean on. From discussing random zoology trivias to to new year parties, from beach hopping and treks to hospital visits, she has been by my side, all these past years, as a batch-mate, friend and confidante. Soumi and Sukanya have been the warmest of friends, my go to people for any heartfelt conversation and biggest cheerleaders all along the journey. The journey of a PhD student is filled with shadows of self-doubt, feeling of incompetence and loneliness. The person who has shown me the brighter side by setting all of such negativity aside and therefore has been one of my strongest pillars of support, is my best friend and now husband, Souraj. He has always shared my passion for science, boosted my ambition and shared the responsibilities through the past years that has allowed me to focus better on my work. And at last but not the least, I am most grateful for and indebted to my parents. They have always been the wind beneath my wings. They have always encouraged me to stride forward with utmost confidence

and bravery and whenever I have felt desolate and discouraged, I have always looked up to them for advice and guidance. This PhD degree would be as much their achievement as it would be mine. Without their unconditional sacrifice and love, I would not have dared to embark on this journey let alone finish it successfully.

TABLE OF CONTENTS

LIST OF FIGURES

LIST OF TABLES

LIST OF ABBREVIATIONS

ADP	Adenosine Di-Phosphate
ARP	Actin-Related Protein
ATP	Adenosine Tri-Phosphate
AJ	Adherens Junction
AP	Anterio-Posterior
BAR	Bin/Amphiphysin/Rvs Domain
BDSC	Bloomington Drosophila Stock Center
BSA	Bovine Serum Albumin
CARMIL	Capping Protein Arp2/3 Myosin I Linker
CIP4	Cdc42-Interacting Protein-4
CLIC	Clathrin-Independent Carriers
CMLE	Classic Maximum Likelihood Estimation
CXCR	CXC Motif Chemokine Receptor 4 [(Human)]
DABCO	1,4-Diazabicyclo [2.2.2] Octane,
DMIM	Drosophila Missing-In-Metastasis
DN	Dominant Negative
DOCK	Dedicator Of Cytokinesis
DSHB	Developmental Studies Hybridoma Bank
DV	Dorso-Ventral
ELMO	Engulfment And Cell Motility
ER	Endoplasmic Reticulum
FBP17	Formin-Binding Protein 17
FRT	Flp Recombinase Recognition Target
FWHM	Full Width At Half Maximum
GAP	Gtpase-Activating Proteins
GBF	G-Box-Binding Factor
GEEC	Glycosylphosphatidylinositol-Anchored Protein (GPI-AP) Enriched Compartments
GEF	Guanine Nucleotide Exchange Factors
GFP	Green Fluorescent Protein
GRAF	Gtpase Regulator Associated with Focal Adhesion Kinase
GTP	Guanosine Triphosphate
IRSp53	Insulin Receptor Phosphotyrosine 53 Kda Substrate
LASX	Leica Application Suite X
LSM	Laser Scanning Microscopy
MBS	Myosin Binding Subunit
MTSS	Metastasis Suppressor Protein 1
NPF	Nucleation Promoting Factor
PBS	Phosphate Buffer Saline

PBST	Phosphate Buffered Saline with Tween 20
PFA	Paraformaldehyde
PIP	Phosphatidylinositol Phosphates
PKC	Protein Kinase C
PRD	Proline Rich Domains
RNA	Ribonucleic Acid
ROI	Regions Of Interest
ROK	Rho-Associated Kinase
SD	Standard Deviation
SEM	Scanning Electron Microscope
SJ	Septate Junctions
STED	Stimulated Emission Depletion Microscopy
TCS	True Confocal Scanning
TIFF	Tagged Image File Format
TIRF	Total Internal Reflection Fluorescence Microscopy
TJ	Tight Junctions
UAS	Upstream Activating Sequence
VDRC	Vienna Drosophila Resource Center
WASP	Wiskott-Aldrich Syndrome Protein
WAVE	WASP Family Verprolin-Homologous Protein
WRC	Wave Regulatory Complex

LIST OF KEYWORDS

Cell
Embryos
Membrane
Drosophila
Microvilli
Syncytial
Metaphase
Interphase
MIM
Furrow
Remodelling
Polarity
DE-Cadherin
Endocytosis
Trafficking
Actin
Arp
Bazooka
Peanut
BAR domain
STED
Development
Shape
Hexagon

ABSTRACT

Extensive plasma membrane remodelling is a hallmark of epithelial cells during their division. The syncytial stage of early *Drosophila* embryogenesis is an excellent model for studying mechanisms involved in epithelial-like plasma membrane remodelling. The apical microvilli present in the pseudo- epithelial cells in interphase get reduced in the metaphase stage of each cortical nuclear division cycle. This is also concurrent with the extension of the lateral plasma membrane in between adjacent nuclei. Effective remodelling requires the interaction of adhesion, polarity, cytoskeletal remodelling and membrane trafficking proteins. BAR domain containing proteins link cytoskeletal and plasma membrane dynamics. We find that polarity protein Bazooka and cytoskeletal regulator septin, Peanut are essential for the establishment of hexagon dominance in the polygonal array of cells at metaphase of nuclear cycle 12. Bazooka and Peanut are present on the lateral membrane at the edges and vertices, respectively and regulate efficient endocytosis of the DE-cadherin. I-BAR domain containing protein Missing-in-metastasis in the syncytial embryos of *Drosophila melanogaster* (DMIM) have a role in microvilli remodelling from interphase to metaphase. Microvilli remain long and abundant in both interphase and metaphase of the syncytial division cycle 12 in DMIM depleted embryos. DMIM is present on the apical membrane from interphase to prometaphase during the time period of villi remodelling. There is a loss of furrow extension and the epithelial-like polygonal array is unstable here as well. DMIM allows for the proper recruitment of actin-regulatory proteins and membrane trafficking at the cortex to promote the remodelling of villi and the formation of furrows in the syncytial division cycle. We found that the Rac-GTP pathway regulates the recruitment of DMIM for villi remodelling and a decrease in activated Rac leads to aberrant association of MIM during villi remodelling. Our studies find an essential role for DMIM recruitment at a precise time to affect villi remodelling during embryogenesis in early *Drosophila* embryogenesis.

SYNOPSIS

Name of the student: Debasmita Mitra
Registration number: 20172009
Name of the thesis supervisor: Prof. Richa Rikhy
Date of registration: 1st August 2019
Place: Indian Institute of Scientific Education and Research (IISER), Pune.
Title: Role of Polarity and BAR domain proteins in plasma membrane re-modelling in syncytial *Drosophila* embryos

Introduction

I have reviewed the literature on the cell shape remodelling events that take place during the metazoan development. In different instances of epithelial cell shape remodelling like cell migration, cell intercalation, apical constriction and other gastrulation events, remodelling of the actomyosin network and adhesion junction molecules, is essential to drive the shape changes (Niewiadomska, Godt, and Tepass 1999; Leptin 1999; Wacker et al. 2000; Medina et al. 2004; Unterseher et al. 2004; (McDonald et al. 2008; Nandadasa et al. 2009; Martin, Kaschube, and Wieschaus 2009). Cellular trafficking forms one of the central mechanisms that regulates the cell remodelling events, like remodelling of the actomyosin dependent cellular protrusions and adherens junction molecules at the cell-cell contacts, across different organisms (Hopkins et al. 1994; Ullrich et al. 1996; Satoh et al. 1997; Echard et al. 1998; Kamiguchi et al. 1998; Hill, Clarke, and Barr 2000; Sisson et al. 2000; Kamiguchi and Lemmon 2000; Kamiguchi and Yoshihara 2001; Lecuit and Pilot 2003; Pelissier, Chauvin, and Lecuit 2003; Riggs et al. 2003; Classen et al. 2005; Sokac and Wieschaus 2008; J.-Y. Lee and Harland 2010; Neto et al., 2011; Schiel and Prekeris, 2013; D. M. Lee and Harris 2013; Liu et al. 2015; Su et al. 2013; Yan et al. 2013; Mayor, Parton, and Donaldson 2014; Holly et al 2015; Mavor et al. 2016; Hemalatha and Mayor 2019; Marsal et al. 2021). The Polarity proteins and Bin/amphiphysin/Rvs (BAR) domain containing protein, have been shown to act as the master regulators of the polarized trafficking and activation of actomyosin network at the plasma membrane (Lawrence and Shelton 1975; Gubb and García-Bellido 1982; Winter et al. 2001;

Ridley et al. 2003; H.-R. Wang et al. 2003; Etienne-Manneville et al. 2005; Osmani et al. 2006; Iden and Collard 2008; Leibfried et al. 2008; Guerrier et al. 2009; Fricke et al. 2009; Nishimura, Honda, and Takeichi 2012; Lim and Thiery 2012; Moreno-Bueno, Portillo, and Cano 2008; Edeling et al. 2009; Y.-C. Wang et al. 2012; Röper 2012; Kovacevic et al. 2012; Su et al. 2013; Yan et al. 2013; Saarikangas et al. 2015; Flores-Benitez and Knust 2015; Zobel et al. 2015; Sherlekar and Rikhy 2016; Rodrigues, Shao, and Harris 2016; Weng and Wieschaus 2017; Sidor et al. 2020; Sherlekar et al. 2020; Sharma and Rikhy 2021). *Drosophila* syncytium progresses through dynamic cell shape remodelling events. It also coincides with polarity establishment and there have been a lot of studies that have shown that a host of actin remodelling proteins are important for the development of syncytial nuclear cycles (Foe and Alberts 1983; Miller et al. 1985; Stevenson et al. 2002; Schmidt and Grosshans 2018; Zhang et al. 2018; Jiang and Harris 2019; Dey and Rikhy 2020; Xie, Budhathoki, and Blankenship 2021; Henry et al. 2022; Miao et al. 2023). BAR domains containing proteins have a role in regulation of the early embryonic cell shape changes in *Drosophila* syncytial embryos through regulation of actin cytoskeleton remodelling and regulation of the cellular trafficking (Guerrier et al. 2009; Leibfried et al. 2008; Fricke et al. 2009; Edeling et al. 2009; Kovacevic et al. 2012; Su et al. 2013; Yan et al. 2013; Zobel et al. 2015; Saarikangas et al. 2015; Sherlekar and Rikhy 2016; Rodrigues, Shao, and Harris 2016; Sherlekar et al. 2020; Sharma and Rikhy 2021). Therefore, we hypothesized that the polarity proteins and BAR domain containing proteins could be the master regulators of the cell shape remodelling events like apical microvilli remodelling and establishment of hexagonal dominance in the polygonal array, that help in the progression of the syncytial nuclear cycles during early *Drosophila* embryogenesis.

Results

We characterized the role of Baz, Pnut, and DE-cadherin proteins in the regulation of the polygon array distribution and cell shape index in the syncytial *Drosophila* embryo. This analysis revealed that the polygon distribution develops 2 kinds of defects due to differential perturbation of the molecules: (1) DE-cadherin depletion in embryos perturbs the establishment of hexagon dominance, and also leads to an increased cell shape index; (2) Bazooka and Peanut depletion leads to a delayed establishment of hexagon dominance and an increased cell shape index as well. This was a result of perturbed cellular trafficking, like endocytosis of DE-cadherin, mediated through polarity proteins.

The microvilli in the apical region of the pseudo-epithelial cell of syncytial *Drosophila* blastoderm development are more prominent and remodel from interphase to metaphase. We observed that at interphase the majority of microvilli protrude from the periphery of the cells, which reduce in length and number from interphase to metaphase. This quantification was possible from both confocal and STED images by using 100x objective. However, the FWHM analysis showed that the structures were resolved significantly better in the STED system. Using this protocol to image the microvilli, allowed us to resolve the structures which were approximately 100-110 nm in width. We also observed that, the depletion of polarity as well as BAR domain containing proteins showed a lack of microvilli remodelling in the nuclear cycle 12 of the syncytial embryos.

DMIM, an I-BAR domain containing protein, regulates the structure, number and remodelling of the microvilli-like membrane protrusions in the apical region of the cells, in the syncytial *Drosophila* embryos. DMIM depleted embryos showed a significant increase in the length and number of the microvilli present apically at interphase of nuclear cycle 12 and a subsequent failure in remodelling of the same, from interphase to metaphase. This is associated with the loss of Arp2/3 complex activation and enrichment on the plasma membrane along with a possible dominance of the bundled actin network, observed through increased Diaphanous enrichment on the apical plasma membrane. Here, in case of DMIM dependent endocytosis, we also observe less punctae of FM1-43fx dye at the metaphase stage of syncytial embryos as compared to the interphase stage. Loss of Arp2/3 mediated branched-actin network also showed lowered endocytosis and a similar lack of microvilli remodelling with increased number and length of microvilli at interphase. Expression of dominant-negative Rac1, led to mislocalization of DMIM on the plasma membrane. All of this data together signifies that there is a DMIM dependent branched actin mediated regulation of endocytosis at the plasma membrane in the syncytial cycles that regulates the cell shape change.

Finally, we summarise that cellular trafficking is one of the most important mechanisms responsible for plasma membrane remodelling in *Drosophila* syncytial blastoderm embryo, namely the remodelling of the apical microvilli and polygonal cell shape dominant with hexagons. The endocytosis and recycling of DE-cadherin is especially crucial for the efficient cell shape regulation. In absence of this the furrow is destabilized and short and also there is a lack of apical plasma membrane remodelling., as observed in Bazooka, Peanut and DMIM depleted embryos. Efficient distribution of DE-cadherin appears to be important for the distribution of both Bazooka and Peanut to the furrow. Loss of Bazooka and Peanut leads to perturbed trafficking of DE-cadherin and formation of unstable furrow formation in the

Drosophila syncytial blastoderm embryo. DMIM regulates the activation and enrichment of the activated Arp2/3 complex at the plasma through interaction with Rac1, to promote branched actin network. In absence of DMIM and the Arp2/3 network, an excess of microvillar protrusions is observed at the apical plasma membrane which do not reduce and remodel from interphase to metaphase, as compared to wildtype embryos. The remodelling of the microvilli in DMIM depleted embryos is due to the lack of branched actin mediated endocytosis. Consistent with the previous findings in Bazooka and Peanut depleted embryos, here also we observed lack of hexagon dominant polygonal array formation at metaphase 12 and 13 of syncytial cycles. Thus, an interplay of different molecular regulators, regulate the plasma membrane remodelling through a spatiotemporal regulation of cellular trafficking.

Publications

Debasmita Mitra, Georgina Goddard, Sanjana S., Aparna K., Tom Millard and Richa Rikhy. Missing-in-Metastasis regulates endocytosis and actin dynamics for apical villi remodelling in *Drosophila* embryogenesis. (In preparation)

Bipasha Dey#, Debasmita Mitra#, Tirthasree Das, Aparna Sherlekar, Ramya Balaji, Richa Rikhy, Adhesion and Polarity protein distribution-regulates hexagon dominated plasma membrane organization in *Drosophila* blastoderm embryos, *Genetics*, Volume 225, Issue 4, December 2023, iyad184, https://doi.org/10.1093/genetics/iyad184
# Equal contribution

Debasmita Mitra, Amruta Swaminathan, Gayatri Mundhe, Richa Rikhy, Imaging and quantification of apical microvilli in the syncytial blastoderm of *Drosophila* embryos, STAR Protocols, Volume 3, Issue 4,2022, https://doi.org/10.1016/j.xpro.2022.101736.

Sameer Thukral, Bivash Kaity, Debasmita Mitra, Bipasha Dey, Pampa Dey, Bhavin Uttekar, Mithun K. Mitra, Amitabha Nandi, Richa Rikhy, Pseudo cleavage furrows restrict plasma membrane-associated PH domain in syncytial *Drosophila* embryos, Biophysical Journal, Volume 121, Issue 12, 2022, https://doi.org/10.1016/j.bpj.2022.05.015.

Chapter 1: Introduction

1.1. Role of epithelial cell shape re-modelling during metazoan development

Metazoans during their development, can undergo a host of tissue morphogenesis events that drive the overall development of the embryos. Cells being the functional unit of any tissue, are building blocks of the organism as well. Therefore, we need to understand the cell biological processes associated with the epithelial cell shape remodelling events, and how they, singularly or in combination, facilitate the tissue morphogenesis (Paluch and Heisenberg 2009). These cell biological processes could be events like cell protrusion formation with the aid of acto-myosin network, junctional remodelling due to cadherin recycling and plasma membrane recycling and growth. We would further discuss some of the morphogenetic events where epithelial cell shape remodelling along with the associated cell biological processes are the major driving forces.

Regulation of plasma membrane protrusions are one of the most abundantly occurring processes that leads to changes in epithelial cell shape. Cell migration is one such major morphogenetic event that several tissues undergo across different species during development. Single cell migration events are undergone by primordial germ cells in zebrafish, which occur through bleb-like protrusions (Blaser et al. 2006), whereas leukocytes in mice form thick pseudopodia-like protrusions, at their leading edge. These structures are usually actin-rich. Although significant force generated by myosin mediated contractility at the leading edge also helps the bulging out of the protrusions (Ridley et al. 2003; Charras and Paluch 2008); (Fig. 1.1.). At the trailing end of the migrating cells, myosin is also responsible for generating contractile force essential to squeeze the cytoplasm and the nucleus forward (Blaser et al. 2006)(Fig. 1.1.). However, these forces generated by the actomyosin network are only able to carry forward the cell migration because of the cell substrate adhesion which provides the traction sites (Lauffenburger and Horwitz 1996).

Similar kind of protrusions are observed during collective cell migration events, like in the cells leading the cluster during collective cell migration in the germ layer progenitors in vertebrates, in the lateral line primordial cells in zebrafish and border cells in *Drosophila* (Montell 2008; Friedl and Gilmour 2009) (Fig. 1.2.). The cluster of cells adhere to each other through E-cadherin in *Drosophila* border cell migration and perturbation to these junctions inhibit the cluster formation, protrusions at the leading edge and thereby hinder the migration

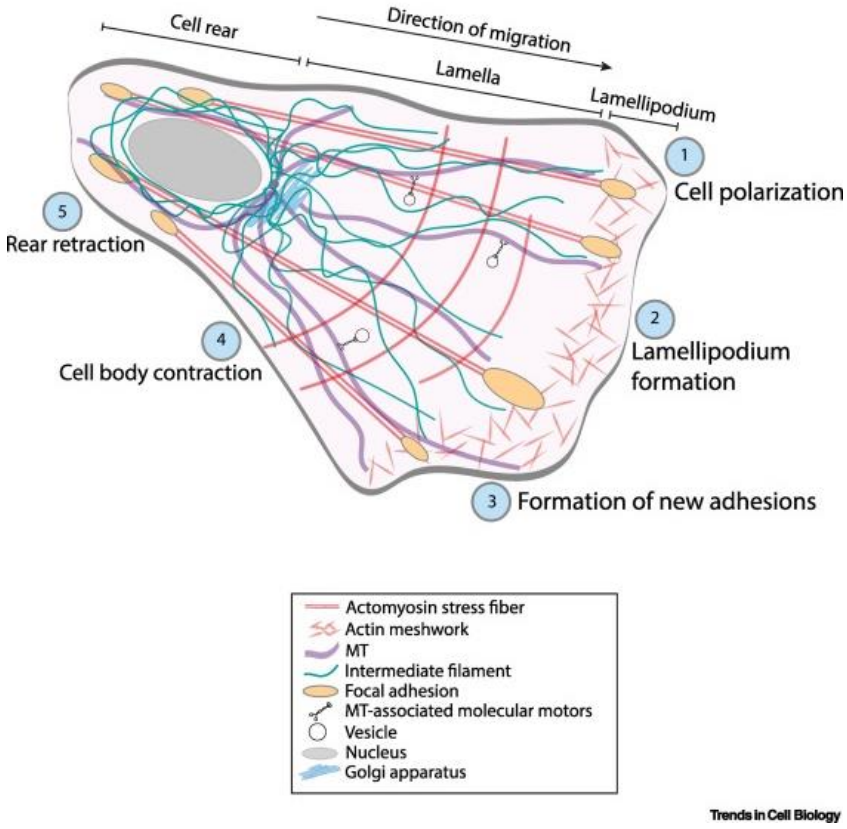

Fig. 1.1: Schematic showing the localisation of the polarised cytoskeletal networks and adhesion junctions during mesenchymal cell migration that leads to cell shape change. (Seetharaman and Etienne-Manneville 2020)

(Niewiadomska, Godt, and Tepass 1999; McDonald et al. 2008) . In the mesoderm progenitors of *Xenopus* and zebrafish undergoing collective cell migration, perturbed cadherin causes polarization, migration, intercalation and separation defects in the migrating cluster of cells (Wacker et al. 2000; Medina et al. 2004; Unterseher et al. 2004; Nandadasa et al. 2009) (Fig. 1.2.). Remodelling of protrusions like filopodia are also observed in the non-migrating cells of metazoan embryos during their early developmental stages, for instance in mouse embryos, the protrusions which appear on the apical region of each of the blastomeres as well as from the junctions between the cells, are enriched with E-Cadherin which helps the cells remain attached to the neighbouring cells through trans interactions. Their remodelling occurs in association

with a process called compaction, where the loosely arranged, rounded cells of the 8-celled embryo become flattened against each other as the cell-cell contact area increases. This gives rise to a more spherical embryo and establishment of a first epithelium like tissue and any form of perturbation to these filopodial structures affects compaction giving rise to non-viable embryos and failed implantation.

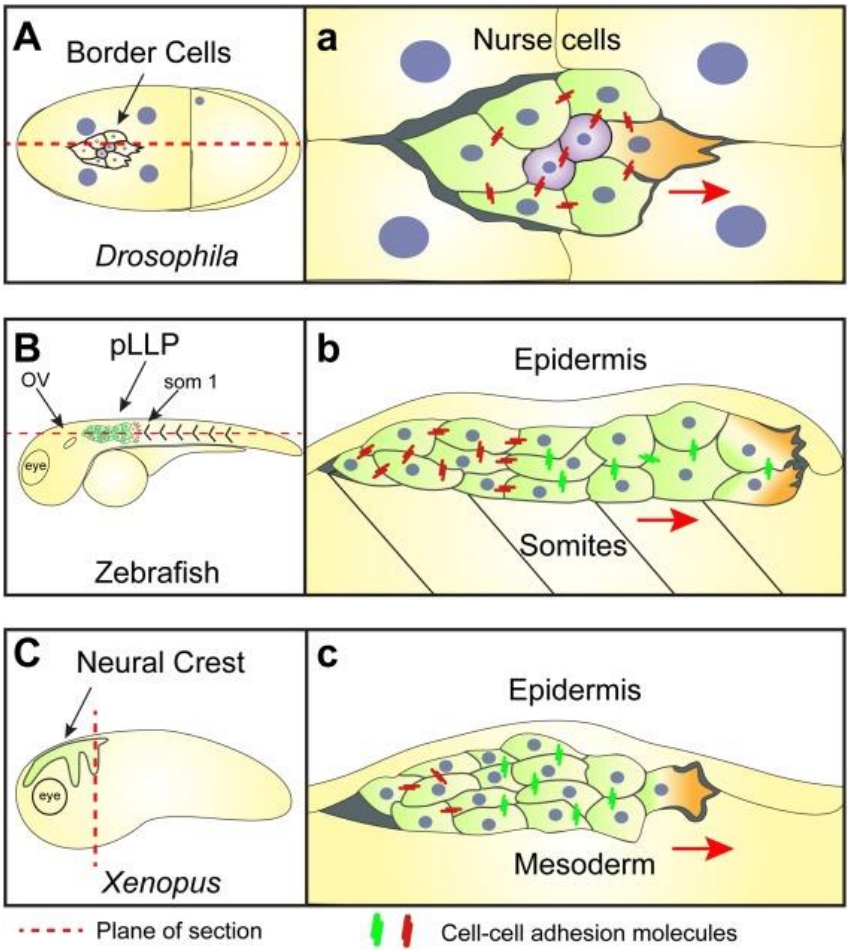

Fig. 1.2: Models representing in vivo models of collective cell migration. (A, a.) Schematics of *Drosophila* border cell migration. (Bib.) Schematics showing collective migration of the posterior lateral line primordia (pLLP) in Zebrafish. C, c. Schematics representing neural crest collective migration in *Xenopus*. (Barriga and Mayor 2019).

Apart from protrusion mediated deformations of plasma membranes in migrating cells, changes in the overall area and volume of the epithelial cells also contribute to tissue morphogenesis in stationary cells. Force generated by the cytoskeletal network drives remodelling of the epithelial cells to regulate Ventral furrow formation during *Drosophila* gastrulation (Fig. 1.3.). Apical constriction occurs in the mesodermal progenitor cells located

at the ventral-most side of the embryos extending all along the anterior-posterior axis of the embryo. These cells constrict in their area apically which is majorly driven by the force generated due to the pulsed contractions of the acto-myosin network, which leads to the formation of wedge-shaped cells and finally leading to excision of the group of cells to form the mesoderm (Leptin 1999; Martin, Kaschube, and Wieschaus 2009) (Fig. 1.3.). Morphogenetic events, like convergent extension, which takes place during gastrulation, leads to narrowing of the embryos along their mediolateral axis and elongation along their apico-basal length. This requires the boundaries of the cells to remodel or reshape to initiate cell rearrangements (Fig. 1.3.). For such remodelling events, cortical actin networks are formed by the activity of myosin II, which consists of foci connected by actin cables. Perturbations to the myosin-II not only affects the contractions but also the cell adhesion (Fig. 1.3.). These cables are polarised along the mediolateral axis and the contractions are also generated along the same direction (Keller 2002; Skoglund et al. 2008; Rolo, Skoglund, and Keller 2009). The importance of junctional remodelling is quite a common

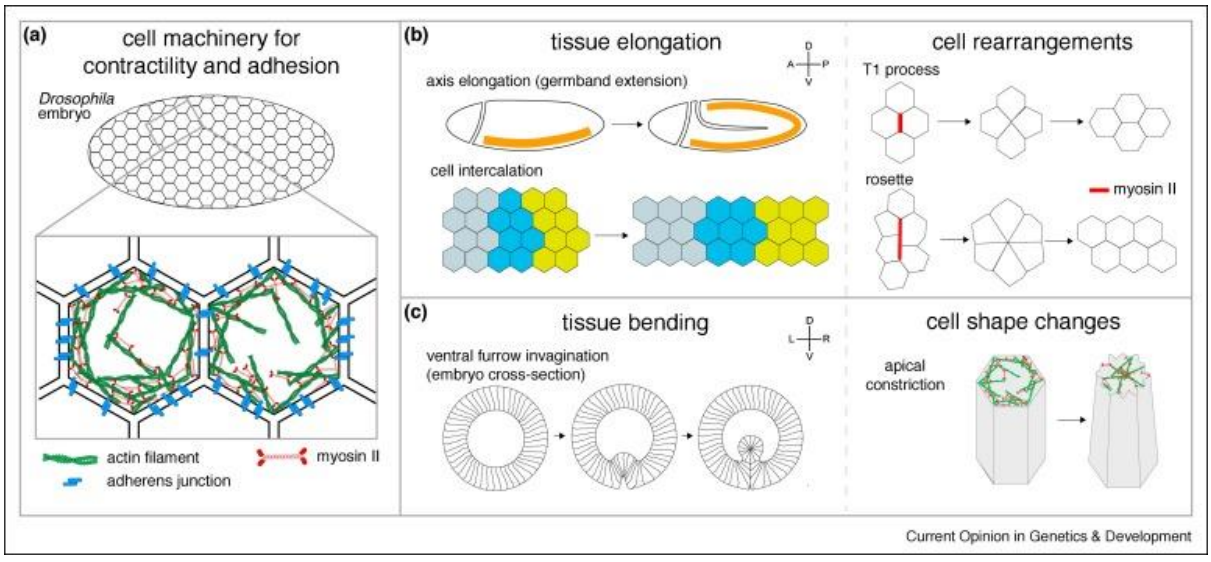

Fig 1.3: Schematics showing the cell rearrangements and cell shape changes regulated by the actomyosin network and adhesion junction remodelling that shape epithelial tissues. (a) The actomyosin and adhesion junctions are organised to regulate the tissue homeostasis in early *Drosophila* embryos. (b) Tissue elongation through cell-rearrangements/ intercalation events require junctional remodelling through the activity of myosin-II. (c) The bending of tissues during ventral furrow formation requires cell shape change in the form of apical

constriction of cells through the remodelling of the cortical actomyosin network (Herrera-Perez and Kasza 2018)

phenomenon observed as the metazoan embryos develop with adhesion having a great role to play in it. During a certain stage of development, across embryos of different species, the cells in the mitotic phase adapt a polygonal cell shape. The cells in the proliferating tissue adapt a network of polygonal cells where hexagonal cells form the majority. The class of polygons in majority also changes from interphase to metaphase (Gibson et al., 2008). During the most part of wing development in early pupal stages of *Drosophila*, the cells are mostly not arranged as a low energy 6-sided packing array. They later get organised into a more regular hexagonal array. This will later ensure an even distribution of the hairs across the wing surface. The attainment of the polygonal cell shape is not stable throughout the developmental timeline of an organism.

Hence, we discussed a host of mechanisms that could possibly lead to the regulation of epithelial cell shape remodelling. However, what could be one the most crucial mechanisms for regulating cell shape changes during the tissue morphogenesis in early development of organisms that is during the embryogenesis? As also mentioned previously, the regulation of morphogenesis through modulating the cytoskeleton and adhesion molecules is crucial during embryogenesis and has also been extensively studied. However, the more recent studies have deciphered the role of plasma membrane remodelling in regulating cellular and tissue morphogenesis. The mechanism of plasma membrane remodelling during morphogenesis is dynamic as the pools of vesicles can be trafficked faster to and from the membrane without much changes in the global organisation of the cell. The role of plasma membrane remodelling in tissue morphogenesis involves cytoskeletal remodelling as well as leads to redistribution of adhesion. Hence more studies dedicated to deciphering this mechanism could in turn elucidate the hierarchy of membrane trafficking with respect to cytoskeleton and adhesion remodelling, across tissue, during development.

1.2. Regulation of cellular trafficking as a mechanism to regulate epithelial cell shape re-modelling during metazoan development

As discussed above, the role of cytoskeletal and adhesion proteins in driving cell shape remodelling events has been extensively studied. However there has been recently quite a few

studies elucidating the role of membrane growth and remodelling in cell morphogenesis during development. A key mechanism for cell shape change could be through change in the cell surface area through addition of plasma membrane (Fig. 1.4.A). This addition could be possible through two processes : one is through the secretory pathway where the plasma membrane is exported as large pools of vesicles from the endoplasmic reticulum through the Golgi to the plasma membrane (Lecuit and Pilot 2003)(Fig. 1.4.A). During *Drosophila* cellularization, membrane invagination is perturbed if the peripheral Golgi protein Lava lamp (Lva), which was also a microtubule/microfilament associated protein, was inhibited. Perturbation of vesicular traffic through the Golgi apparatus perturbed furrow progression while transport across ER-Golgi inhibited rhabdomere formation

A

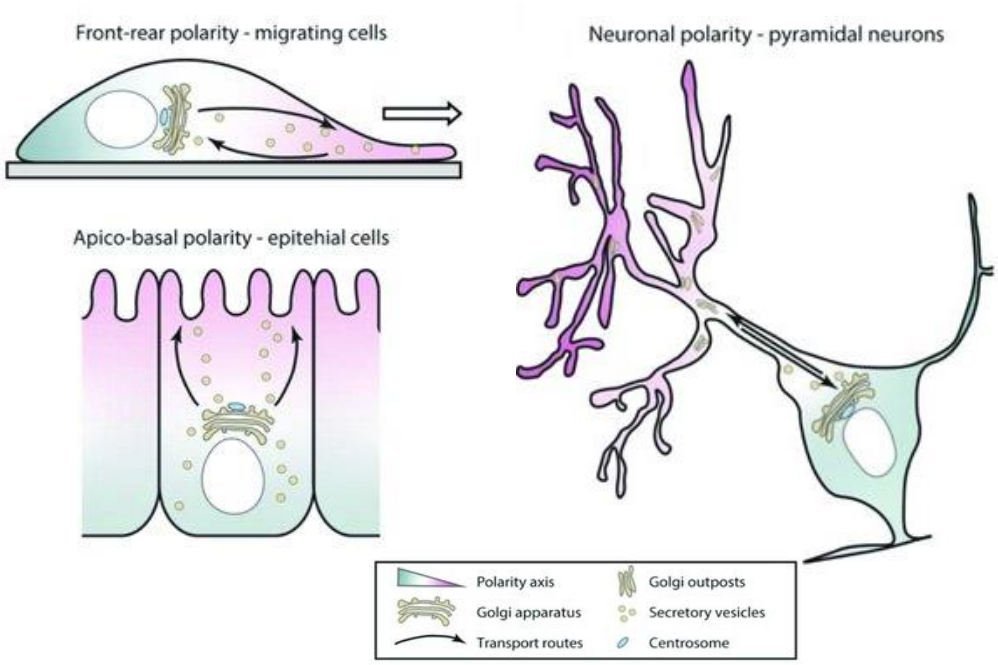

B

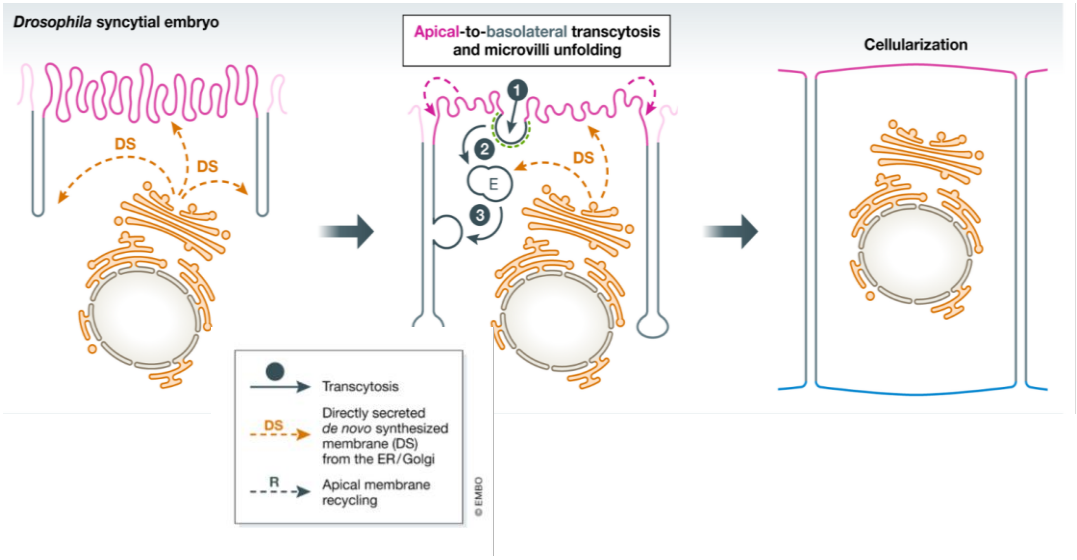

Fig.1.4.: Schematics showing different mechanisms for plasma membrane growth through trafficking. (A) Schematics showing the transport routes of secretory vesicles essential for transport and membrane addition B) Schematics showing the polarised trafficking of the plasma membrane vesicles for localised membrane recycling (Ravichandran, Goud, and Manneville 2020; Serra and Sundaram 2021)

in *Drosophila* photoreceptor cells (Satoh et al. 1997; Echard et al. 1998; Sisson et al. 2000; Hill, Clarke, and Barr 2000;). The other way of plasma membrane remodelling is through the polarised trafficking and recycling of the plasma membrane, which is a more rapid and efficient way of remobilizing the plasma membrane pools across the different regions of the cell. This mechanism is carried out through by balancing between the endocytic machinery, which receives the components from the plasma membrane to maintain a temporary reserve of membrane vesicles and the exocytic machinery which delivers the vesicles to specific regions of the cell in a polarised manner (Lecuit and Pilot 2003) (Fig. 1.4.B). Cellular trafficking is one of the major cellular events that remodel the plasma membrane by transporting a pool of vesicles from one region of the cell to another, and they also carry molecular regulators across the cell viz. polarity regulators, membrane lipids, adhesion proteins and other cytoskeletal regulators. In the migrating chick embryo fibroblasts and nerve growth cones, internalisation of transmembrane proteins through endosome and subsequent recycling of the same to the plasma membrane of the leading lamella and growth cone is essential (Hopkins et al. 1994; Kamiguchi et al. 1998; Kamiguchi and Lemmon 2000; Kamiguchi and Yoshihara 2001). In the *Caenorhabditis elegans* embryo, for the efficient completion of cytokinesis during early cleavages trafficking of recycling endosomes is essential (Ullrich et al. 1996). In the mitotic cells of the syncytial *Drosophila* embryos, the increase in length if the cleavage furrows are mainly carried out by the cumulative efforts of both the membrane trafficking machinery and the cytoskeletal elements of the cell acting simultaneously (Neto et al., 2011; Schiel and Prekeris, 2013, Holly et al 2015). We would be further discussing the various molecular factors that could regulate polarised intracellular trafficking in a spatiotemporal manner.

Intracellular membrane trafficking encompasses various processes that leads to the transport of cargo in membrane bound vesicles across the cell. The cargo is taken up from the surface of the cell and transferred into the cell, bound in membrane vesicles, through endocytosis (Fig. 1.5.). Some of the vesicles are then transcytosed or recycled from endosomes back to being exocytosed, while the rest of the vesicles are either sent to lysosome for through

late endosome for degradation or they are trafficked back to the Golgi and Endoplasmic reticulum through retrograde transport (Huotari and Helenius 2011; Scott, Vacca, and Gruenberg 2014) (Fig. 1.5.). The vesicles at different stages of the trafficking events vary depending on the coat proteins on their surface, the kind of cargo they carry and the route they traverse. The uptake of the vesicles from the plasma membrane through endocytosis is interestingly driven by different mechanisms (Fig. 1.5.). First of all, the coat proteins like Clathrin are concentrated on the endocytic vesicles as they facilitate the uptake of the cargoes. There are other clathrin-independent pathways facilitating the endocytic processes like the CLIC/GEEC pathway, RhoA-dependent pathway, Arf6-dependent pathway and Flotillin-dependent pathway (Mayor, Parton, and Donaldson 2014; Hemalatha and Mayor 2019)(Fig. 1.5.). In some cases, the excision of the endocytic vesicles from the plasma membrane is also facilitated by dynamin which binds to the neck of the vesicles and fuses the two lipid bilayers in a GTP-dependent manner (Fig. 1.5.). The other special group of proteins that further aid the bending of the membrane at the vesicles and either promote or inhibit their scission, which are the BAR domain containing proteins (Bonifacino and Glick 2004; Anitei and Hoflack 2011). Once the vesicles are pinched off from the membrane they traverse across the cells with the help of microtubules and motors like kinesin, dynein, myosin II and myosin V (Hirokawa et al. 2009; Titus 2018). The destination and pathway of the vesicles need to be exact in order to perfectly execute the trafficking events, and this is ensured by the family of Rab small GTPases, which coat the specific transport vesicles and also the membrane at the location. There are several instances of the importance of intracellular trafficking during morphogenesis during development of organisms across various species, which we would be discussing further.

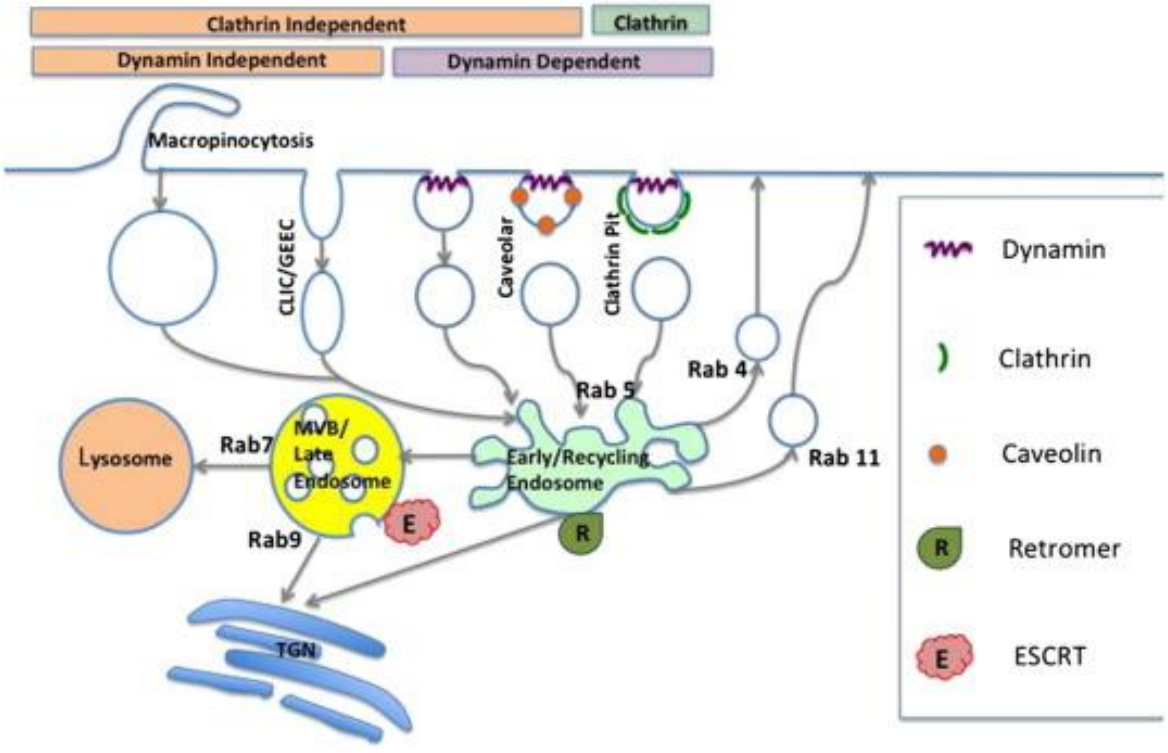

Fig. 1.5.: Summary of the components and pathways involved in polarised cellular trafficking (Juliano and Carver 2015).

The polarised cellular trafficking involves transfer of membrane vesicles across the cell to promote growth or cell shape change in a spatiotemporal manner. The regulation of furrow ingression and complete cytokinesis in *Drosophila* cellularizing embryos is one such morphogenetic event spatiotemporally regulated by the cellular trafficking machinery. The cells at this stage possess an extensive membrane reservoir present apically in the form of microvilli like protrusions, which gets reduced overtime from early to late cellularization. The remodelling of the microvilli requires the function of Rab5 mediated tubular endocytosis from the base of these structures (Fabrowski et al. 2013). Not only does the furrow ingression require efficient remodelling of microvilli but it also requires the furrow tip to possess the right composition of membrane and proteins. In order to regulate this, surplus membrane and protein need to be removed through endocytosis that depends on the Nullo, a zygotic gene product, N- and F-BAR Domain containing proteins Amphiphysin and Cip4/Toca1, respectively; the ADP Ribosylation Factor (ARF) GTPase regulators, Steppke/Cytohesin and Stepping Stone; Dynamin; the F-actin cytoskeleton and also its nucleating factor Arp2/3 Complex (Sokac and Wieschaus 2008; D. M. Lee and Harris 2013; Su et al. 2013; Yan et al. 2013; J. Liu et al. 2015). The endocytic plasma membrane vesicles mobilised through Rab11 endosomes ensures lateral membrane growth at cellularization (Pelissier, Chauvin, and Lecuit 2003). These Rab11 mediated recycling endosomes is also regulated by the ADP ribosylation factor effector Nuclear fallout (nuf) and is crucial for the trafficking (Riggs et al. 2003) and recruitment of RhoGEF to the pseudo cleavage furrows of the cells to promote furrow integrity through actin polymerization (Cao et al. 2008). The growth of the furrows both during *Drosophila* syncytium and cellularization also requires the exocytic machinery mediated by Rab8 to deliver components like membrane and actin regulators, to the furrow. Rab8 mutants show a complete lack of pseudo cleavage furrow formation in syncytial *Drosophila* embryos (Mavor et al. 2016).

Gastrulation in vertebrates is yet another important morphogenetic event that involves the bending of epithelial sheets and the constriction of the apical surface of epithelial cells is brought about by cytoskeletal dynamics as well as membrane trafficking causing tissues to bend and invaginate. During Xenopus Laevis gastrulation, the bottle cells undergo constriction apically. The plasma membrane is internalised as observed through biotinylated membranes getting accumulated in internalised punctaes, that are also positive for Early embryonic antigen

1 (EEA1) and Rab5, early endosome marker. Mutants for dynamin, inhibited the apical constriction and also *rab5*^{DN} embryos showed lack of the internalised vesicles, inefficient apical constriction and failure of the bottle cells to undergo morphogenetic changes during gastrulation (J.-Y. Lee and Harland 2010). During the process of neural tube closure, efficient recycling through Rab11 ensured proper localisation of planar cell polarity proteins, which in turn in a positive regulatory loop, further directs the apical accumulation of Rab11. This organisation of Rab11 regulates activated myosin II localisation that is essential for the apical constriction during neural tube closure (Ossipova et al. 2014). In zebrafish gastrulation the mesodermal and endodermal cells have to migrate to form proper tissue layers. Slb/Wnt11 controls the endocytosis of E-cadherin mediated through Rab5 activity. Lack of *slb/wnt11* showed lowered cytosolic vesicles of E-Cadherin. This caused abnormal migration of the cells and aggregation of the mesendodermal cells. The defect in internalisation of E-Cadherin in *slb/wnt11* mutants, was restored on expressing wildtype Slb/Wnt11 and Rab5c in a constitutively active manner (Ulrich et al. 2005). Rab5ab mediated endocytosis is essential for removal of the external yolk cell syncytial layer (E-YSL) membrane which regulates zebrafish epiboly and is essential for mechanical equilibrium during gastrulation (Marsal et al. 2021).

Cell intercalation is an important morphological event during *Drosophila* embryogenesis, where cellular trafficking has a vital role to play. Following formation of a single epithelial sheet, there is a dramatic reorganisation of cells as they become narrow along the dorso-ventral (DV) axis and elongate along the anterior-posterior (AP) axis, with the whole event being aided by apical and junctional molecules. It was observed that there is a significant role of the cytoskeleton in this process. Scar mediated Arp2/3 activation promotes the endocytic events that facilitate the cell intercalation event. Diaphanous on the other hand allows myosin II to cluster the E-Cadherin through its contractile function that in turn triggers the clathrin and dynamin dependent endocytosis of the same. This cumulatively ensures that the cell boundaries along the DV axis gets shortened by reducing the cell-cell adhesion through endocytic uptake (Levayer, Pelissier-Monier, and Lecuit 2011). As discussed, earlier Rab-GTPases form an integral part of the membrane trafficking and associated cytoskeletal dynamics. In case of the cell intercalation, Rab35 is arranged in a planar polarised manner across the cells and together with Rab5 promotes formation of transient infoldings of plasma membrane. The activity of myosin II is further required for the scission of these vesicles for the final uptake of the plasma membrane. Therefore, in this instance we see that the cytoskeletal dynamics together with the activity of the Rab-GTPases regulate the uptake of E-cadherin from the DV junctions and reduce their length for the intercalation of cells to occur (Jewett et al.

2017). During the wing development in early pupae of *Drosophila*, cells get packed into an energy-minimised, hexagonal array. Throughout this process the percent of hexagonal cells increase from 40% to 8o%. This process is dependent on dynamin dependent uptake and Rab11 dependent recycling of DE-cadherin. This is followed by exocyst/sec5-dependent vesicle trafficking of DE-cadherin to the junctions to facilitate the repacking through remodelling of junctions. This ensures that there is a remodelling of the cellular junctions to pack the array of cells into a more ordered network (Classen et al. 2005).

Thus, we see that cellular trafficking is quite a common phenomenon that is essential for regulation of the cell shape changes at different stages of embryogenesis across different species of metazoans. However, in order to efficiently regulate the morphogenesis, the cellular trafficking needs to be guided in a polarised and spatiotemporal manner and it would be interesting to investigate the crucial regulators involved in the same in the context of embryogenesis.

1.3. Polarity proteins and BAR domain containing proteins as regulators of epithelial cell shape re-modelling during metazoan development

As discussed previously cell shape changes form an integral part of embryogenesis. And there are several molecular regulators that keep the cell shape regulation under control. In the previous sections 1.1. and 1.2. we discussed that for efficient tissue morphogenesis during development, epithelial cell shape remodelling needs to be regulated by modulating the cytoskeletal and adhesion molecules along with plasma membrane dynamics in a polarised and spatiotemporal manner. While the polarisation of the cells and the tissue can be determined by the polarity determining proteins, BAR domain containing proteins belong to a class of proteins who can play a host of roles-right from sensing and bending the plasma membrane to interacting with the actin cytoskeleton and also facilitating E-Cadherin trafficking. Hence it would be really interesting to analyse the role of polarity and BAR domain containing proteins in regulating the cell shape changes during development of an organism.

1.3.1. Role of polarity proteins in epithelial cell shape re-modelling during metazoan development

Establishment and regulation of polarity are major events during the development of epithelial cells, which makes the cells optimised for performing varied functions (St Johnston

and Sanson 2011; Lemke and Nelson 2021). For instance, development of apico-basal polarity allows the epithelial cells to form a barrier between the interior lumen and external environment (Fig. 1.6.). Asymmetric distribution of polarity protein complexes on the plasma membranes allows mature epithelial cells to have a polarised arrangement in a tissue and also the arrangement of junctions in the tissues (Fig. 1.6.). It not only allows the cells to be divided into apical, lateral and basal domains (Fig. 1.6.) but also for maintenance of cell shape, tissue integrity and remodelling (Bilder, Li, and Perrimon 2000; Hayashi and Carthew 2004; Laprise and Tepass 2011; Letizia et al. 2013;). The existing polarity also needs to be reorganised, as and when the cells change their shape in order to undergo morphogenesis. Apico-basal polarity of the epithelial cells indirectly regulate the cell shape

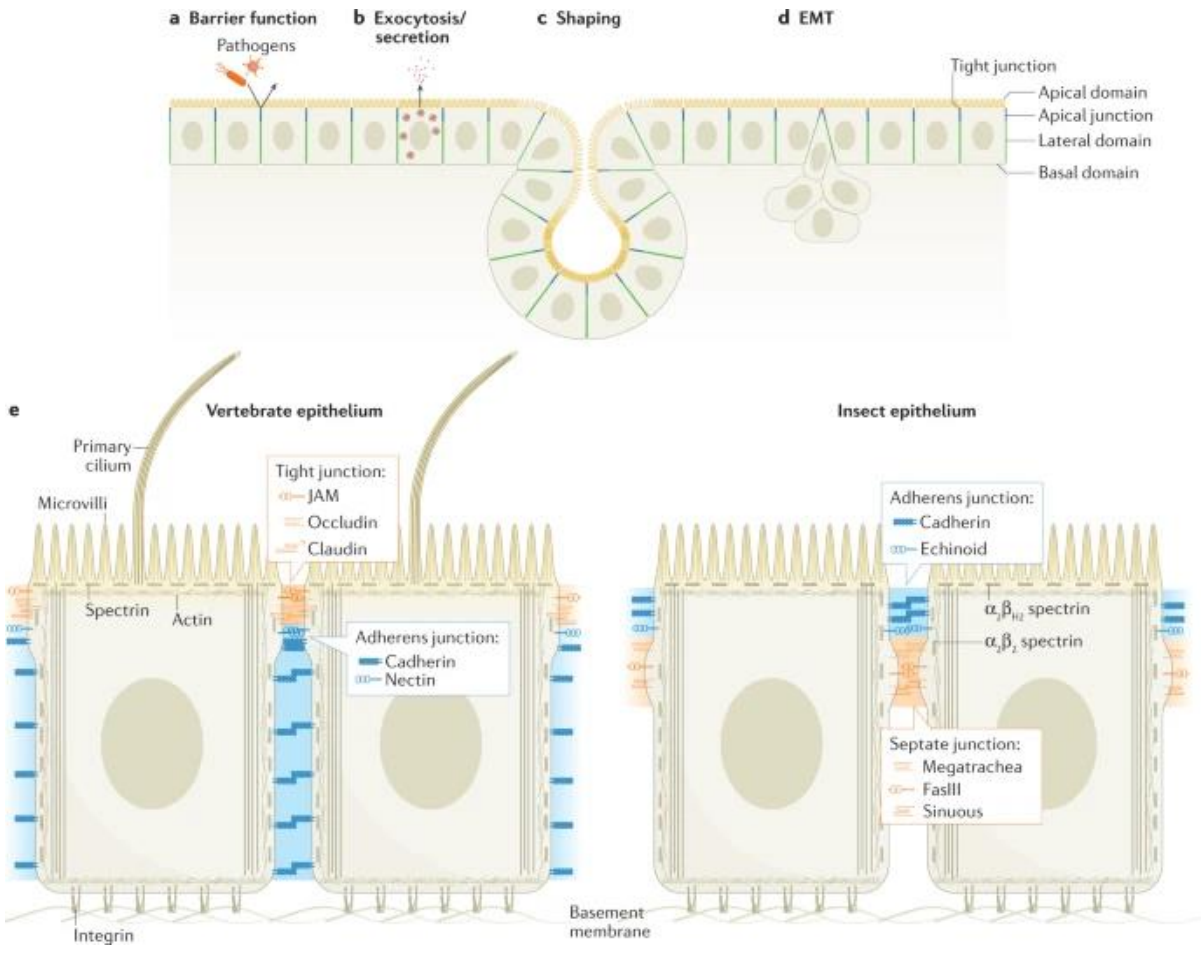

Fig. 1.6.: Schematic showing the arrangement of epithelial cells in a tissue. (a-d) Schematic showing the significance of the polarised arrangement of epithelial cells in the tissue. (e) Schematic showing the apico-basal polarity in epithelial cells of Vertebrates and

invertebrates. Cell polarity is substantially defined by the positioning of the cell–cell junctions which are the adherens junction (AJ) and either the septate junction (SJ) (in invertebrates) or the tight junction (TJ) (in vertebrates) (Buckley and St Johnston 2022).

change by remodelling the junctional and cytoskeletal components of the cell (Buckley and St Johnston 2022). In order to modulate the cell shape changes through regulation of polarity, the localisation of a common set of molecules is required. They are as follows: Par, Crumbs and Scribble complexes, primarily identified in *Drosophila melanogaster* and *Caenorhabditis elegans* (reviewed in (Assémat et al. 2008)), which has been widely studied as the critical polarity determining proteins regulating the development of diverse cell shapes and function in nearly all animals (Wodarz 2002; St Johnston and Ahringer 2010; Nance and Zallen 2011; Thompson 2013). In addition to apico-basal polarity, epithelial cells also show planar-cell polarity along the orthogonal axis in the plane of the epithelium (Fig. 1.7.). Certain types of morphological changes during the development of an organism, require patterning of tissues. For instance, retina patterning, cuticle development, patterning of epidermal appendages like hair follicle or organisation of cilia in ear (Lawrence and Shelton 1975; Gubb and García-Bellido 1982). All these processes require the development of planar-cell-polarity, which primarily is achieved through antagonism between proximal protein complexes - vang-like protein (Vangl) and Prickle (pk) and distal protein complexes -Frizzled (Fz), Dishevelled (Dsh), and Diego (Dgo). Flamingo (Fmi, vertebrate Celsr), associates with both complexes (Fig. 1.7.). Such a distribution is essential for ensuring proper orientation of the patterning's, remodelling of adhesion junctions and polarised actomyosin contractility (Winter et al. 2001; Nishimura, Honda, and Takeichi 2012) that would drive the cell-cell arrangements.

As discussed in section 1.1., one example is during the cell migration, when the cells adopt back-front polarity by responding to the external chemotactic signals (Fig. 1.7.). In order to ensure a polarised forward movement, the migrating cells need to form dynamic lamellipodia and filopodia like structures at the leading edge while at the rear edge establish actomyosin contractility (Ridley et al. 2003)(Fig. 1.7.). Cell migration is an important morphogenetic event during developmental processes like primordial germ cells in zebrafish, mesoderm progenitors of *Xenopus* and border cell migration during oogenesis in *Drosophila*, to name a few. The transition in polarity initiates the epithelial cell-shape remodelling through mechanisms like epithelial-to-mesenchymal transition (Lim and Thiery 2012), where

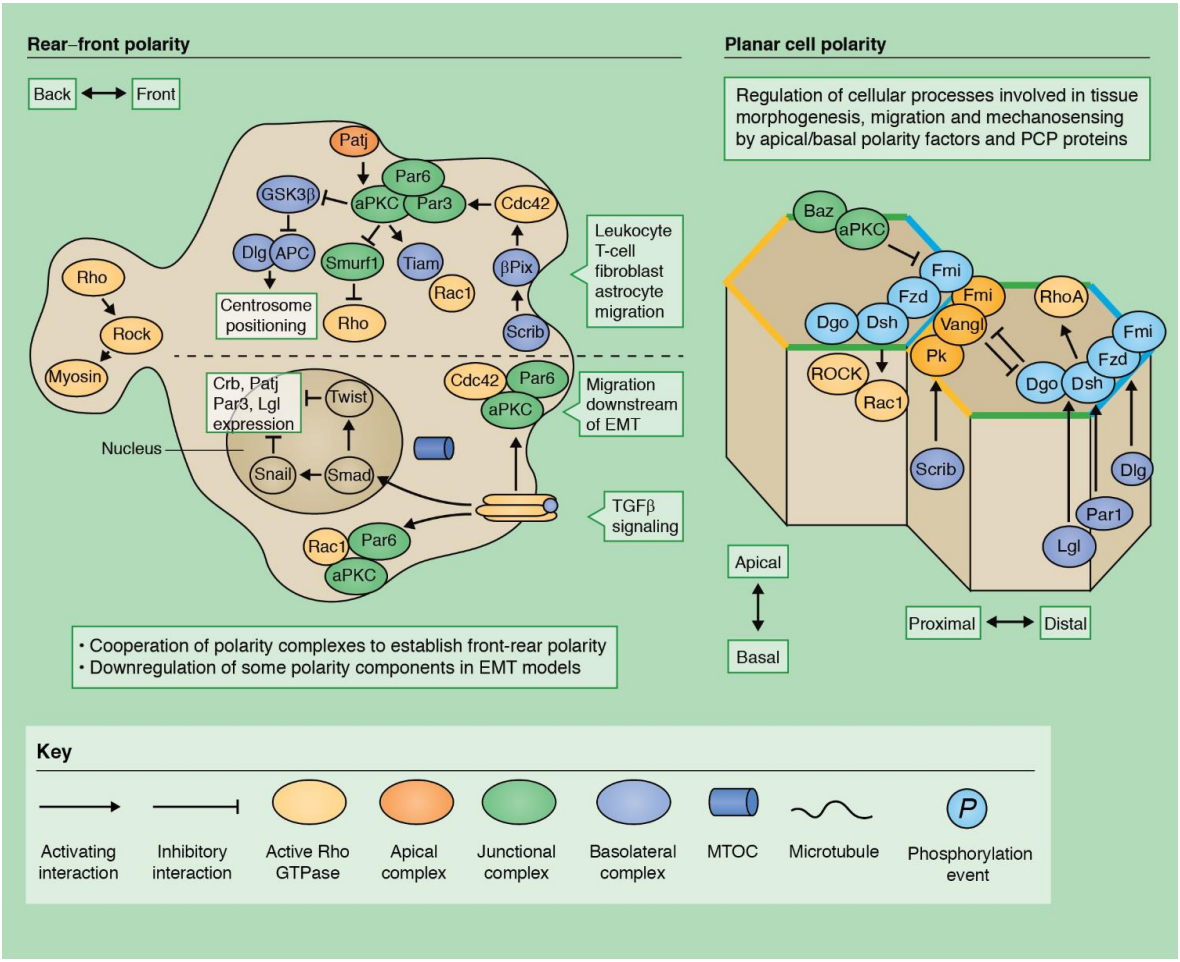

Fig. 1.7.: Schematic showing the arrangement of rear-front polarity in migrating cells and arrangement of planar cell polarity in a tissue (Campanale, Sun, and Montell 2017).

polarity proteins like Crumbs and Lgl, are downregulated to impart a migratory status to the cells (Moreno-Bueno, Portillo, and Cano 2008). Polarity proteins also modulate the cell shape to regulate the directional migration of the cells by remodelling the microtubule arrangement (Etienne-Manneville et al. 2005; Osmani et al. 2006). Whereas, for the formation of protrusions, like, filopodia and lamellipodia, activation of aPKC-Par complex through removal of its inhibitors (H.-R. Wang et al. 2003) or activation of GTPases Cdc42 and Rac1 at the leading edge, and RhoA at the rear to induce contractions (Iden and Collard 2008)(Fig. 1.7.). Polarity proteins also modulate the cell-cell junctions which is essential for the cell migration event. A representation of the polarity establishment in a migrating cell is shown in figure.

Apical constriction is a prominent cell shape change event that drives the tissue morphogenesis in various instances like gastrulation in various organisms and neural tube

formation in vertebrates. For instance, in the salivary gland placode the anisotropic distribution of Crumbs negatively regulates the distribution of Rho-Kinase (ROK) specifically leading to the formation of actomyosin cable on the outer edge of the placode enabling budding of tubes (Röper 2012; Sidor et al. 2020). During dorsal closure also, in *Drosophila* embryos, Crumbs negatively regulates the actomyosin in the amnioserosa to regulate the supracellular actomyosin cable (Flores-Benitez and Knust 2015). However, interaction of Yurt and Crumbs at the apical membrane of the epithelial cells in *Drosophila* embryo and follicular epithelium, activates the non-muscle myosin II to enable apical constriction. While aPKC phosphorylates Yurt and inhibits the Crumbs mediated activation of non-muscle myosin II and apical constriction, while Pak-1 kinase dephosphorylates Yurt to activate non-muscle myosin II mediated apical constriction (Biehler et al. 2021). During gastrulation in *Drosophila,* the folding of the dorsal epithelium is regulated by the re-localization of Bazooka/Par-3 to the basal epithelium. This relocalization is triggered by the downregulation of Par-1 and leads to remodelling of the adhesion junctions as well that facilitates the epithelial cell shape change (Y.-C. Wang et al. 2012). During the mesoderm invagination in *Drosophila*, Bazooka is repositioned to the apical domain of the epithelial cells due to the activity of non-muscle myosin II from and is associated with the disassembly of the adherens junctions (Weng and Wieschaus 2017).

1.3.2. Role of BAR domain Proteins in epithelial cell shape re-modelling during metazoan development

Epithelial cell-shape remodelling requires the modulation of the actomyosin network as well as the localisation of cadherin at cell-cell junctions. However as discussed in section 1.1. apart from the actomyosin and cadherin, remodelling of the plasma membrane is also crucial for the epithelial cell shape remodelling. Plasma membrane remodelling includes forming invaginations like the endocytic vesicles and protrusions like lamellipodia and filopodia that are induced by different classes of the Bin/amphiphysin/Rvs (BAR) domain containing proteins (Fig. 1.8.). The major mechanism for plasma membrane remodelling is through membrane trafficking which involves the internalisation and excision of membrane vesicles from one region of the cell through endocytosis and deposition of the membrane vesicles to another region through exocytosis, depending on where the cell growth is required. These processes require bending of the plasma membrane, controlled spatiotemporally, in a dynamic manner. A special class of proteins which possess BAR domain are widely known as

BAR domain containing proteins and are one of the largest groups of membrane-curving proteins. Dimerized BAR domains form a curved bundle of helices; the shape is reminiscent of a crescent moon (Fig. 1.8.), where either the concave or convex surface can comprise of positively charged residues (Simunovic et al. 2015), through which they associate with the membrane determining the direction in which it gets curved. (Peter et al. 2004).

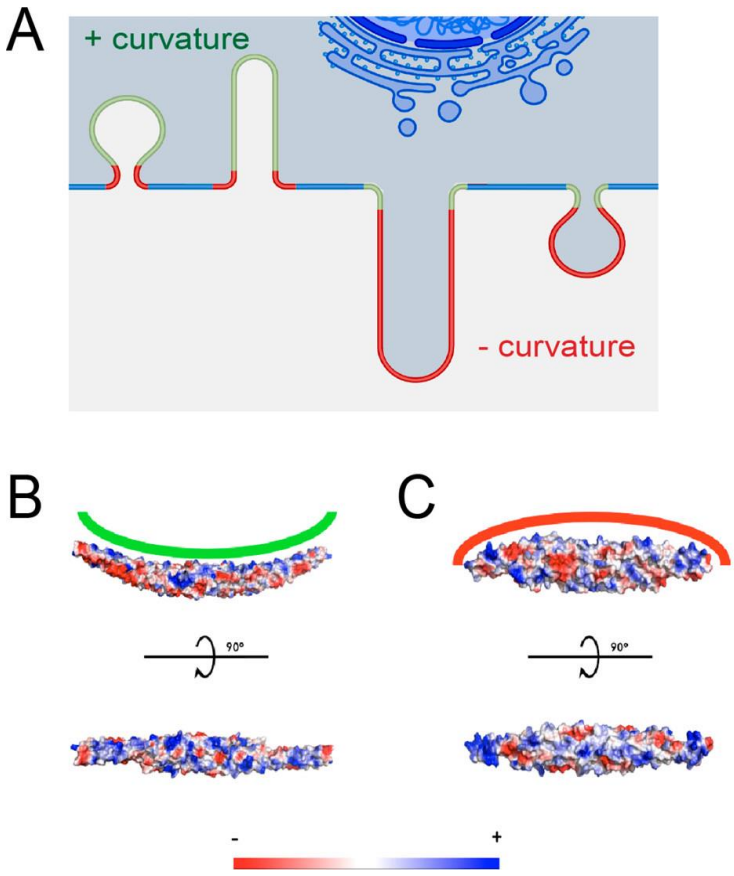

Fig 1.8.: Schematic showing the curvature of the plasma membrane that favours the binding of the respective BAR domain protein. The positive (green) and negative (red) curvature of the cell membrane are marked. There is a probability of both the positive and negative curvature inducing BAR domain proteins to bind to the different regions of both these different structures-membrane invaginations and protrusions. (B) Electrostatic surface potential of the positive curvature inducing FBP17 FBAR domain (PDB ID: 2EFL). (C) Electrostatic surface potential of the negative curvature inducing IRSp53 I-BAR domain (PDB ID: 1Y2O). (Jones, Liu, and Cui 2020)

Members of the different classes BAR domain family are further classified on the basis of the characteristics of their BAR domain. The F-BAR (extended Fes-CIP4 homology

(EFC)/FCH-BAR) domain subfamily of proteins sense and induce positive curvature as they are banana-shaped with positive charge on their concave side, (bend membranes toward the protein binding leaflet), whereas I-BAR (IRSp53-MIM homology domain I-BAR/inverse-BAR) domain proteins, can generate negative membrane curvature as they are more cigar or inverse banana shaped with positive charges on their convex surface (bend membrane away from the protein binding leaflet) (Safari and Suetsugu 2012). Amphiphysin and endophilin, are two of the most notable members of the family which were found to be enriched at the nerve terminals in the mammalian (Lichte et al. 1992; Giachino et al. 1997).

a

Serial no.	FlyBase ID	Gene name (*D. melanogaster*)	Mamalian ortholog (DIOPT)
1	FBgn0264560	Gartenzwerg (garz)	GBF1
2	FBgn0032447	PICK1 (Protein interacting with C kinase 1)	PICK1
3	FBgn0032005	Sortin Nexin 6 (SNX6)	SNX6, SNX32, SNX5
4	FBgn0052082	CG32082	BAIAP2/IRSp53 , BAIAP2L1, BAIAP2L2
5	FBgn0037702	CG8176	FCHO2, FCHO1,
6	FBgn0000723	FER ortholog	FER, FES
7	FBgn0031534	Sortin Nexin 1 (SNX1)	SNX2, SNX1, SNX33, SNX18, SNX30
8	FBgn0038659	Endophilin A (Endo A)	SH3GL3, SH3GL2, SH3GL1
9	FBgn0027356	Amphiphysin (Amph)	BIN1, AMPH
10	FBgn0030685	GRAF ortholog	ARHGAP26
11	FBgn0039056	Centaurin beta 1A	ACAP2, ACAP3, ACAP1
12	FBgn0037884	Arfaptin	ARFIP2, ARFIP1
13	FBgn0038747	Rho GTPase activating protein at 92B	ARHGAP17,ARHGAP44
14	FBgn0037050	ICA69	ICA1L, ICA1
15	FBgn0053094	Syndapin	PASCIN1, PASCIN2
16	FBgn0035533	CIP4 (Cdc42-interacting protein 4)	CIP4
17	FBgn0263456	Nervous wreck (Nwk)	FCHSD1, FCHSD2
18	FBgn0053558	Missing-in-metastasis (MIM)	MTSS1L, MTSS1

b

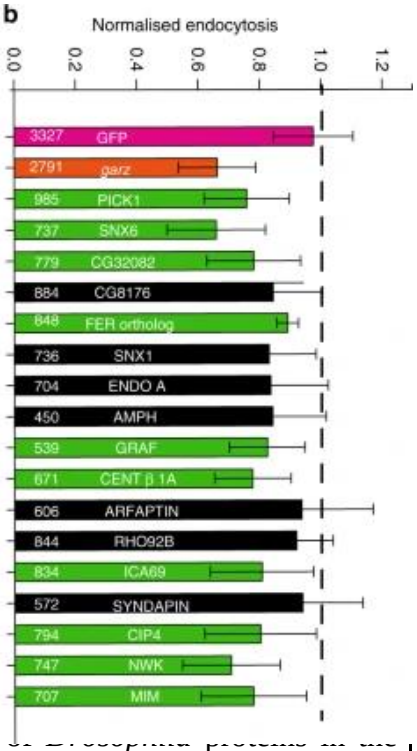

PFAM database that were downregulated. (b) Histogram showing normalised fluid-phase uptake in S2R+ cells where the proteins were downregulated, dsRNA against GBF1(garz) being the positive control, and against GFP the negative control. (Sathe et al. 2018)

Over the years, the role of these BAR domain proteins in membrane-remodelling through endocytosis has become very prominent (Leibfried et al. 2008; Leibfried et al. 2008; Fricke et al. 2009). A recent screening of the BAR domain proteins in *Drosophila* S2R+ cells showed their importance in regulating endocytosis (Fig. 1.9.). It is a process through which cells internalise nutrients, signalling proteins, and other cargo. BAR domain proteins not only modulate the cytoskeleton and also can regulate cadherin trafficking and interact with other

membrane effectors, but they are also direct modulators of membrane shape. A crucial role of these proteins has been observed even in the early development of the organisms, specifically mostly in studies, carried out in *Drosophila melanogaster*. The table below has a list of studies showing the role of BAR domains in regulating the plasma membrane remodelling during development across different species.

Table 1.1.: Role of BAR domain containing proteins in regulating cell shape changes during development

BAR domain protein	Tissue	Function	Reference
srGAP2	Primary neuronal culture of mice	Induces neurite outgrowth and branching	(Guerrier et al. 2009)
MIM/MTSS1	Cultured rat primary neurons	Initiates spine protrusions by coupling phosphoinositide signalling, direct membrane bending, and actin assembly to ensure proper synaptogenesis	(Saarikangas et al. 2015)
Syndapin/ PACSIN	Zebrafish	Influences cellular locomotion to facilitate the columnar organization of the notochord during early development.	(Edeling et al. 2009)
Nostrin	Zebrafish	Regulates filopodia number and length and tip cell morphology, leading to normal intersegmental vessel trajectory	(Kovacevic et al. 2012)

Cdc42-interacting protein 4 (Cip4)	*Drosophila melanogaster*	Cdc42 effector that interacts with Dynamin and the Arp2/3 activator WASP regulating E-cadherin Endocytosis	(Leibfried et al. 2008)
Cdc42-interacting protein 4 (Cip4)	*Drosophila melanogaster*	Cdc42 acts upstream of Cip4 and recruits not only WASP but also Scar/WAVE via Abi to control Dynamin-dependent cell polarization in the wing	(Fricke et al. 2009)
Cdc42-interacting protein 4 (Cip4)	*Drosophila melanogaster*	Cip4 inhibits mainly actin nucleation by Dia which stabilize cortical compartmentalization by antagonizing membrane turnover induced by WASP/WAVE-Arp2/3	(Yan et al. 2013)
Amphiphysin	*Drosophila melanogaster*	Regulation of endocytic tubules that form at cleavage furrow tips (CFT-tubules) and cleavage furrow ingression.	(Su et al. 2013)
Cdc42-interacting protein 4 (Cip4) and Nostrin	*Drosophila melanogaster*	Cip4 initially promotes membrane invagination and early-actin-based endosomal motility, and Nostrin makes contacts with microtubules through the kinesin Khc-73 for trafficking of recycling endosomes to regulate turnover of E-cadherin at the membrane	(Zobel et al. 2015)

Asap	*Drosophila melanogaster*	Recycle Arf1 to the Golgi for cleavage furrow biosynthesis	(Rodrigues, Shao, and Harris 2016)
Syndapin/ PACSIN	*Drosophila melanogaster*	Promotes pseudo cleavage furrow formation and apical cap remodelling through actomyosin organization	(Sherlekar and Rikhy 2016; Sherlekar et al. 2020)
GRAF1	*Drosophila melanogaster*	Restricts Rho-GTP levels in a spatiotemporal manner for inhibiting actomyosin contractility during cellularization	(Sharma and Rikhy 2021)

The activity of such a huge number of BAR domain proteins, being recruited in a very spatiotemporal manner in the developing tissues begs the question of what mechanisms regulate their precise recruitment.

1.4. Early *Drosophila* embryogenesis as a model system to study different epithelial cell shape re-modelling events.

Drosophila syncytial embryos is an extraordinary model to study cell shape remodelling which takes place during the dynamic nuclear division cycles. The fertilised embryos undergo 9 rounds of nuclear cycle divisions at the depth of the embryo following which the nuclei migrate to the surface of the embryos and undergo 4 more rounds of cortical nuclear division cycles which are incomplete, that is without the cytokinesis (Foe and Alberts 1983; Miller et al. 1985). At the interphase of each of these cortical nuclear cycles, an actin cap is formed on top of each nucleus which consists of actin filaments present as microvilli like protrusions mostly emerging from the periphery of the caps. These microvilli remodel and reduce in number as the cell progresses from interphase to metaphase, which is coincident with

the formation of lateral furrow and further increase in its length (Sherlekar et al. 2020). The increase in furrow length is also associated with the establishment of a hexagon-dominated polygonal array of cells (Dey and Rikhy 2020). We have segregated the cell shape changes that take place in the syncytial *Drosophila* blastoderm into three distinct morphogenetic events, which are: **Apical cap expansion and actin microvilli remodelling, Furrow formation and extension and Polygonal distribution formation.** We would further discuss in detail how the different molecular regulators are responsible for these epithelial cell shape remodelling events in detail.

1.4.1. Apical cap expansion and actin microvilli remodelling:

Towards the beginning of nuclear cycle 10, the nuclei reach the earlier flat cortex of the single-celled embryo in order to form dome shaped compartments, just above each of them. Taking cues from the centrosome (Cao et al. 2010), a cap made of polymerised actin forms on top of each nucleus at the beginning of each cycle, which expands in area from interphase to metaphase (Fig. 1.9) with an actomyosin border accumulating at the border of the cap. These caps expand or grow in an Arp 2/3 dependent manner and a reduction in levels of myosin activity by perturbing Rho-Kinase has shown predominantly expanded caps (Stevenson et al. 2002; Zhang et al. 2018). The Arp 2/3 structures push against the Dia mediated bundles to facilitate the growth of apical caps under the regulation of Par-1 kinase (Jiang and Harris 2019). A host of Arp2/3 activation factors like Scar, Dpod1, Cortactin, Coronin and CARMIL regulate the expansion of the cap area (Xie, Budhathoki, and Blankenship 2021). These regulators are in turn tightly regulated by Sponge which is a Guanine Nucleotide Exchange Factor and is known to activate the Arp 2/3 complex through the Rac1 mediated pathway (Zhang et al. 2018; Henry et al. 2022).

The caps collide at contact sites during metaphase, with the borders pushing against the expansion all the way to cause the cortical bulging. The borders form the pseudo-cleavage furrow on collision with the neighbouring syncytial cells. At nuclear cycle 10, when the nuclei reach the cortex, an apical cap is formed, consisting of polymerised actin filaments. They are arranged as microvilli arising from the periphery of the caps (Turner and Mahowald 1976; Warn, Magrath, and Webb 1984) which are dependent on the composition of the actin cytoskeleton at the apical caps regulated by Abelson kinase and Enabled (Grevengoed et al. 2003). As these apical caps expand from interphase to metaphase in each nuclear cycle, the microvilli undergo extensive remodelling (Fig. 1.10.). possibly due to restructuring of actin

reservoir through endocytosis, regulated by the BAR domain protein Syndapin and in order to facilitate the growth of pseudo cleavage furrows (Sherlekar et al. 2020).

1.4.2. Furrow formation and extension:

In the syncytial blastoderm stages of the embryo, the pseudo epithelial cells remain attached to the neighbouring cells solely through their lateral membrane due to absence of basal membrane. The lateral membrane or furrow increases in length over time from the interphase to metaphase in a single nuclear cycle (Fig. 1.10.) with the furrow retracting back during anaphase, only for them to start dividing again. The apical caps as mentioned in the previous section also show the presence of Anillin, Syndapin, the septin Peanut and the formin Diaphanous whose absence show a reduction in the furrow length (Fares, Peifer, and Pringle 1995; Foe, Field, and Odell 2000; Silverman-Gavrila, Hales, and Wilde 2008; Sherlekar and Rikhy 2016) . Rho-GEF is known to affect the positioning of furrows while their formation is mostly dependent on the proper apical cap formation and expansion, regulated majorly by the other myosin activity regulators like Rho-Kinase and MBS, which is a phosphatase (Afshar, Stuart, and Wasserman 2000; Padash Barmchi, Rogers, and Häcker 2005; Zhang et al. 2018). The regulators of the Apical cap expansion like the Arp2/3 complex proteins and its activators Scar, Dpod1, Cortactin, Coronin and CARMIL also regulate the progression of furrow growth (Stevenson et al. 2002; Zallen et al. 2002; Xie, Budhathoki, and Blankenship 2021; Henry et al. 2022). Along with the cytoskeletal network, the trafficking machinery of the cell is also an important regulator of the furrow ingression at this point of early *Drosophila* embryogenesis. A Rab39-lp98A-Rab35 mediated endocytic recycling pathway is essential for the progression of furrow ingression in the syncytial *Drosophila* embryos (Miao et al. 2023). A Rab8 mediated exocytic machinery is also essential for the transfer of the cargo through membrane vesicles to the furrow and an absence of this pathway perturbs the furrow ingression at this stage as well (Mavor et al. 2016).

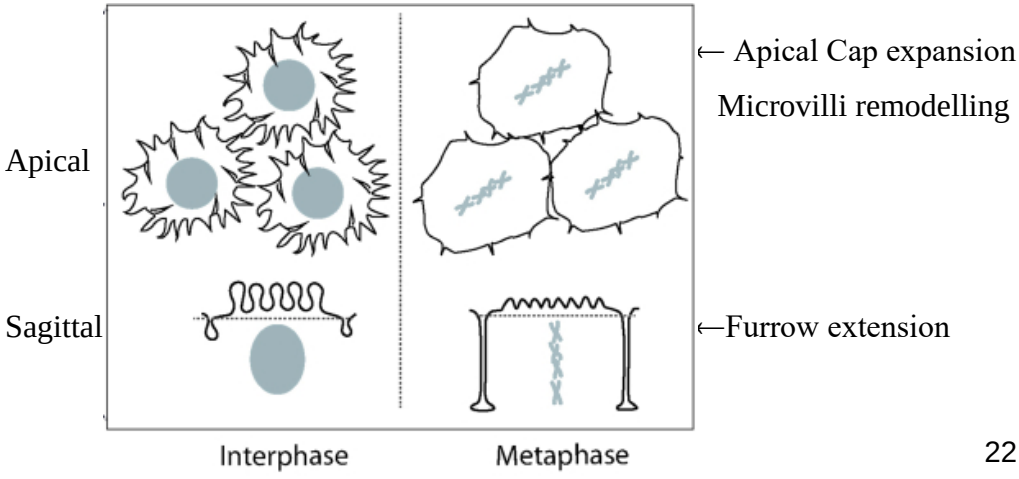

Fig. 1.10.: Schematic of the pseudo epithelial cells in syncytial *Drosophila* embryos at nuclear cycle 12, which shows the remodelling of apical cap area and microvilli along with furrow length ingression , from interphase to metaphase (Adapted from (Mitra et al. 2022).

1.4.3. Polygonal distribution formation:

Following expansion and collision, as a result of apical flattening and straightening of the edges, epithelial cells adopt a polygonal shape and get packed into a sheet of polygonal array. In syncytial *Drosophila* embryos the polygonal array is first formed in the metaphase of each nuclear cycle. DE-cadherin levels on the lateral cell membrane of the pseudo-epithelial cells determine the achievement of its polygonal shape. myosin, on the other hand, maintains contractility in the cell shape to counter the cell expansion, resulting in the polygon formation (Fig. 1.11.). As the cell cycle, progresses from prophase to metaphase, there is an increased recruitment of DE-cadherin on the lateral membrane which reaches its maxima at metaphase followed by a simultaneous drop in the levels of myosin on the cell membrane which eventually becomes cytosolic. Epithelial cells are hence found to undergo a transition in cell shape from circular caps to a polygonal architecture eventually forming pseudo cleavage furrows as a result of a fine balance between myosin mediated contractility and junctional tension maintained by DE-cadherin (Fig. 1.11.) (Dey and Rikhy 2020).

While a considerable amount of study has been carried out to decipher the network that operates to carry out cell shape remodelling in early embryos, much of it still remains to be figured out. For example, what is the cue that initiates the actin villi remodelling that takes place as the actin cap expansion and collision takes place in early embryos? How is the polygonal architecture stabilised in the early embryo when the epithelial cells are still not differentiated into a mature epithelial cell layer and no basal layer present? It would be interesting to look at the mechanistic basis of the above questions related to cell shape transitions in early *Drosophila* syncytial embryos.

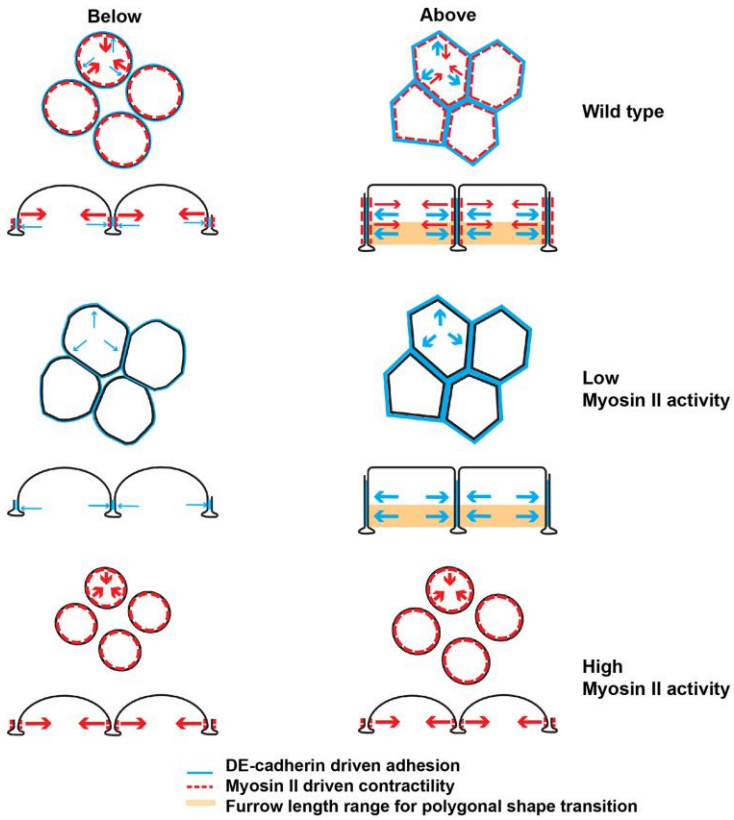

Fig. 1.11.: Schematic showing the summary of the role of DE-cadherin and MyoII in maintaining a balance for formation of polygonal epithelial architecture (Dey and Rikhy 2020).

Table 1.2.: List of proteins that regulate shape remodelling of epithelial-like cells in syncytial *Drosophila* embryos.

Name of the Protein	**Type of protein**	**Phenotype in depletion mutants**	**Reference**
Abelson kinase (abl)	A non-receptor tyrosine kinase that phosphorylates cell adhesion and cytoskeletal proteins	More microvilli and missing furrows	(Grevengoed et al. 2003)
Arp 2/3 (arpc1)	Actin nucleator that promotes branching of actin	Small caps and missing furrows	(Stevenson et al. 2002)

	cytoskeleton filaments		
ArpC4	Actin nucleator that promotes branching of actin cytoskeleton filaments	Small caps and wide but short furrows	(Xie, Budhathoki, and Blankenship 2021; Henry et al. 2022)
Baz	Orthologue to PAR-3 apical polarity protein in vertebrates	Lack of hexagon dominance at metaphase 12 and short furrow	(Dey et al. 2023)
CARMIL	Regulates actin capping protein and also interacts with myosin II.	Small caps	(Xie, Budhathoki, and Blankenship 2021)
Coronin	Recruits Arp2/3 complex to promote actin cytoskeleton nucleation and branching.	Small caps	(Xie, Budhathoki, and Blankenship 2021)
Cortactin	Stabilizes the Arp 2/3 mediated nucleation of actin cytoskeleton	Small caps and no furrow	(Xie, Budhathoki, and Blankenship 2021)
DE-cadherin (Shotgun)	Adhesion junction protein	Round caps and short furrow	(Dey and Rikhy 2020)
Diaphanous (dia)	Formin that bundles the actin cytoskeleton filaments	Small caps and missing furrows	(Afshar et. al 2000) (Xie, Budhathoki, and Blankenship 2021)
Dpod1 (coronin)	A microtubule and actin filament binding protein regulating actin	Small caps	(Xie, Budhathoki, and Blankenship 2021)

	cytoskeleton reorganisation		
Dynamin	GTPase which is an essential component of the vesicles during their formation while vesicular trafficking	Short furrows	(Rikhy, Mavrakis, and Lippincott-Schwartz 2015)
Klp98A	Microtubule based motor	Short furrows	(Miao et al. 2023)
Nuclear fallout (nuf)	An adaptor between the Rab11 and motor proteins in recycling endosome pathway	Gaps in furrows/incomplete furrow	(Sullivan, Fogarty, and Theurkauf 1993)
Par-1	Apical polarity determining protein	Small caps and no furrow	(Jiang and Harris 2019)
Peanut	Septate junction protein in *Drosophila*	Lack of hexagon dominance at metaphase 12 and short furrow	(Dey et al. 2023)
Rab35	Early endosome marker	Short furrows	(Miao et al. 2023)
Rab39	Endosome marker	Short furrows	(Miao et al. 2023)
Rab8	Component of the exocyst complex	Missing furrows	(Mavor et al. 2016)
RhoGEF	Activates Rho1 to regulate acto-myosin constriction	short furrow	(Dey and Rikhy 2020)

Rho-Kinase	Phosphorylates myosin II to regulate acto-myosin constriction	large caps and short/missing furrow	(Zhang et al. 2018)
Scar	A primary regulator of the Arp2/3 complex, which promotes actin polymerization	Small caps and missing furrows	(Xie, Budhathoki, and Blankenship 2021; Zallen et al. 2002)
Scrambled (sced)	Involved in actin filament reorganisation	Lack of furrow formation	(Sullivan, Fogarty, and Theurkauf 1993)
Sponge (spg)	A DOCK family RhoGEF that activates the Arp 2/3 mediated nucleation of actin cytoskeleton	Small caps and wide but short/missing furrows	(Postner, Miller, and Wieschaus 1992; Henry et al. 2022)
Syndapin	F-BAR domain containing protein	More microvilli and short furrow	(Sherlekar and Rikhy 2016; Sherlekar et al. 2020)

1.5. Hypothesis: Plasma membrane remodelling in early *Drosophila* embryogenesis requires extensive cellular trafficking regulated by different classes of proteins like polarity proteins and BAR domain containing proteins

Establishment of polarity in an epithelial cell is important in pertaining functionality and maintaining the cellular architecture of the epithelial sheet. However, there are very few reports about the characterization of the syncytial stage for polarity where the pseudo-epithelial cells in spite of not being fully differentiated, there exists a polarised organisation of various molecules along the lateral cell membrane. The syncytial plasma membrane resembling differentiated cells, shows asymmetrical organisation of Toll, DE-cadherin and Patj, occupying only the lateral domain (Mavrakis et al., 2009). The polarised organisation of epithelial cells

results in the formation of distinct apical and basal domains, also apical microvilli like structures. The establishment of the adherens junctions between the neighbouring pseudo-cells, defines the major polarity landmark, separating the apical domain in mature epithelial cells from the lateral domain, well regulated by polarity determining proteins.

The assembly and mobility of the DE-cadherin on the cell membrane has been shown to be dependent on the presence of bazooka (Harris and Peifer 2004, McGill et al 2009). Polarity proteins can regulate a series of cell shape changes during embryogenesis (Harris and Peifer, 2004). Along with polarity determining proteins, membrane trafficking pathways can also regulate epithelial cell shape. During early *Drosophila* embryo development, membrane trafficking pathways play an important role in regulation of actin turnover on the epithelial cell membrane. When certain drugs are added to perturb exocytosis in the embryos undergoing cellularization, the villi-like projections on the actin caps are reduced much faster as compared to the control (Figard et al. 2016). Exocytic trafficking of the components from the cell's interior to the cell membrane requires the function of Rab8 and Rab11 for the formation of the syncytial furrows. The BAR domain containing proteins are also known to regulate the endocytic trafficking and cytoskeletal network simultaneously. The plasma membrane remodelling events in the syncytial *Drosophila* embryos are dynamic and complex. These processes need to be regulated through the interaction of a host of factors and at a very specific time point. BAR Domain proteins like Cip4, Syndapin, Amphiphysin and Asap1 (Table 1.1.) have already been shown to regulate cell shape remodelling in early *Drosophila* embryogenesis through regulation of endocytosis. Interestingly the BAR domain proteins modulate the actin cytoskeleton in order to facilitate cellular trafficking. This could also affect the relocalisation of the adhesion proteins as cargoes, and therefore regulation of the epithelial cell shape.

It becomes interesting to note how the different classes of proteins interact mechanistically, for regulation of epithelial cell shape in a very specific spatiotemporal manner due to the function of the varied regulatory proteins. Thus, the hypothesis of the thesis is that plasma membrane remodelling in early *Drosophila* embryogenesis requires extensive cellular trafficking regulated by different classes of proteins like polarity proteins and BAR domain containing proteins

1.6. Broad aims and objectives

The significance of the cell shape remodelling during tissue morphogenesis during the development of an organism. The cell shape changes involve remodelling of plasma membrane

protrusions and junctional remodelling. This leads to formation of epithelial cells and its maturation, into a polarised organisation ultimately, to form a specialised tissue. In order to understand how the mature epithelial cells transition their shape as they mature and adapt into a 3-dimensional tissue, we characterise the major cell shape remodelling events during the syncytial cycles of the early Drosophila embryogenesis. We therefore analyse the role of the molecular regulators that regulate these remodelling events and the mechanism of the regulation. For such analysis the following aims and objectives are designed-

- Characterization of establishment of hexagon dominance and cell shape index in the polygon distribution of cells in early *Drosophila* embryo
- Role of polarity proteins in regulating establishment of hexagon dominance and cell shape index in the polygon distribution of cells in early *Drosophila* embryo
- Microvilli re-modelling event - a major cell shape re-modelling event in early *Drosophila* embryo
- Role of Missing-in-metastasis in regulating apical microvilli remodelling in syncytial *Drosophila* embryo

Chapter 2: Materials and methods

2.1. Fly genetics

All fly stocks are maintained at 25°C in the standard corn meal agar medium. The RNAi crosses are maintained at 28°C or 25°C. RNAi stocks are either from the Transgenic RNAi Resource project (TRiP), Vienna *Drosophila* RNAi centre (VDRC) or Bloomington *Drosophila* Stock Centre (BDSC). The RNAi and the UASp or UASt transgenic lines were driven by crossing them to the respective GAl4 lines (Table 2.1.). *shg*^{i} was driven by being crossed to a single chromosomal copy of *nanos*-Gal4 and was maintained at 18°C. This was done in order to lower the severity of phenotypes that were observed when the cross was set up at a higher temperature and obtained fertilized eggs to perform experiments. The Germline clones of *pnut*^{XP} were made by crossing *ovo*^{D} FRTG13 males to *hsflp; GlaBlc* females to finally obtain hsflp; *ovo*^{D} FRTG13/*GlaBlc* males. These males were then crossed to *pnut*^{XP} FRTG13/*Cyo* females. Larvae, pupae and adults emerging from this cross were heat-shocked at 37.5 °C. hsflp;*ovo*^{D} FRTG13/*pnut*^{XP} FRTG13 adults were then put in a cage to collect embryos depleted of *pnut*. In Table 2.1. are lists of the fly stocks to be used for the project.

Table 2.1.: List of the fly strains used for the experiments.

Genotype	**Description**
CantonS	Wild-type (obtained from L.S. Shashidhara)
tGPH::*matatub*-Gal4 67; *matatub*-Gal4 15	PH domain of Grp1 tagged with GFP-marks PIP3 in the membrane , along with maternal gal4
UASp-Bazooka RNAi	Down regulation of Bazooka val20 (BL-35002)
UASp-Peanut RNAi	Down regulation of Peanut (BL-65157)
Peanut XP FRT G13	Mutant Peanut with FRT sites (obtained from Manos Mavrakis)
Shotgun RNAi	Down regulation of E-cadherin (BL-38207)
Sqh-sqh mCherry, *matatub*-Gal4 67; *ubi*-DE-cad-GFP, *matatub*-Gal4 15/TM3Sb	Myosin regulatory chain tagged to mCherry and DE-cadherin tagged to GFP (obtained from Adam martin lab)

OvoD FRTG13	Dominant female sterile mutant that blocks oogenesis
nanos-Gal4	VP16 fusion protein loaded into eggs, expressed under the control of the nanos promoter
matatub-Gal4 67	VP16 fusion protein loaded into eggs, expressed under the control of the αTub67C promoter
If/Cyo; MKRS/TM3, Ser	Double balancer 2nd and 3rd chromosome for making stocks with balancers
Sp/cyo; MKRS/TM6B, tb	Double balancer 2nd and 3rd chromosome for making stocks with balancers
UASp-mCherry-MIM M3/Cyo	UASp line with MIM M3 isoform tagged with mCherry (obtained from Tom Millard)
UASp-mCherry-MIM M3/TM6B	UASp line with MIM M3 isoform tagged with mCherry (obtained from Tom Millard)
UASp-mCherry-MIM5kb	UASp line with MIM 5kb isoform tagged with mCherry (obtained from Tom Millard)
w [1118]; Df(2R)BSC261/CyO	MIM deficiency line (BL-23161)
w [1118]; Dp (2;3) GV-CH321-43A06, PBac{y[+mDint2] w[+mC] =GV-CH321-43A06} VK00031/TM3, Sb [1]	MIM duplication line (BL-89927)
dmim	MIM deletion mutant (exon 3-10) (Quinones, Jin, and Oro 2010)
UASp-Mim RNAi	UASp line with dsrna against Missing-in-Metastasis (BL-43223)
UASp-Arp3 RNAi	UASp line with shRNA against Arp3 (BL-32921)
UASt-Rac1.N17 (*rac1*^{DN})	UASt line with dominant negative version of Rac1 where a mutant in wildtype Rac1 was generated at N17 position (BL-6292)
UASp-GFP-MIM M3 ΔI-BAR	UASp line with MIM M3 tagged with GFP having the I-BAR domain deleted (obtained from Tom Millard)

UASp-GFP-MIM ΔCentral+WH2	UASp line with MIM tagged with GFP having the central scaffold and WH2 domain deleted (obtained from Tom Millard)
UASp-GFP-MIM M3 ΔWH2	UASp line with MIM M3 tagged with GFP having the WH2 domain deleted (obtained from Tom Millard)
UASp-Dia RNAi	UASp line with dsrna against Diaphanous (BL-33424)
UASp-Dia-EGFP	UASp line with Diaphanous expressing EGFP (BL-56751)

Gal4-UAS system

The Gal4-UAS system was used to drive the expression of fluorescently tagged transgenes and RNAi lines. It is based on the findings by Hitoshi Kakidani and Mark Ptashne (Kakidani and Ptashne 1988) and Nicholas Webster and Pierre Chambon (Webster et al. 1988) that Gal4, on binding to the UAS sequences, can activate gene expression. This method is predominantly derived from the yeast and was introduced into flies by Andrean Brand and Norbert Perrimon in 1993 (Brand and Perrimon 1993). The system has two parts: the Gal4 gene, that encodes the yeast transcription activator protein Gal4, and the UAS (Upstream Activation Sequence), an enhancer to which GAL4 specifically binds leading to activation of gene transcription. Many Gal4 driver lines are available that drive expression in specific tissues and at specific developmental times. To study the syncytial stages, nanos Gal4 and maternal-Gal4 driver lines were mainly used which drive expression during oogenesis and allow maternal dumping of proteins in the egg for the initial stages of embryogenesis.

2.2. Reagents

- **List of Chemicals used**

Table 2.2: List of chemicals used for making the reagents for experiments.

Chemicals	Company	Catalogue no.
Agar	local purchase	non-molecular biology grade
Yeast	local purchase	non-molecular biology grade
Malt	local purchase	non-molecular biology grade
Cornflour	local purchase	non-molecular biology grade
Sucrose	local purchase	non-molecular biology grade
Propionic acid	local purchase	non-molecular biology grade
Orthophosphoric acid	local purchase	non-molecular biology grade
5% methyl-para-hydroxybenzoate	Loba Chemie	Catalogue number: 04660
Ethanol	Jiangsu	Catalogue number: 1170
NaCl	Qualigens	Catalogue number: Q15918
KCl	Qualigens	Catalogue number: Q13305
Na_2HPO_4	HiMedia	Catalogue number: MB024
K_2HPO_4	HiMedia	Catalogue number: MB044
Triton X-100	Sigma	Catalogue number: T8787
Sodium Azide	Sigma	Catalogue number: S2002-25G
Paraformaldehyde	HiMedia	Catalogue number: GRM3660
BSA	HiMedia	Catalogue number: MB083
Mowiol	Sigma-Aldrich	Product number: 81381
DABCO	Sigma-Aldrich	Catalogue number: 290734
HCl	Fisher Scientific	Catalogue number: 29505
NaOH pellets	Qualigens	Catalogue number: Q15895
4% Sodium Hypochlorite (bleach)	Sigma	Catalogue number: 1056142500

Glycerol	HiMedia, India	Catalogue number: MB060
n-Heptane	Merck	Catalogue number: 1.04365.2521

- **Protocol for making Fly Media (1 L)**

Table 2.3.: List of the components and their quantities required for making fly media

Reagents	Amount for 3% / 1 L	Amount for 6% / 1 L
Agar	10 g	10 g
Yeast	15 g	24 g
Malt	30 g	60 g
Cornflour	75 g	75 g
Sugar	80 g	80 g
Deionized water	900 mL	900 mL
Propionic acid	5 mL	5 mL
Orthophosphoric acid	1 mL	1 mL
Ethanol	5 mL	5 mL
5% Methyl-para-hydroxybenzoate	0.7 g in ethanol	1.7 g in ethanol

The required amounts of agar, yeast, malt, cornflour and sugar were added and deionized water was added to that by stirring. The mixture was autoclaved at 121°C and 15 psi for 15–20 min. Propionic acid and orthophosphoric acid were mixed in a 15 mL conical tube and kept aside. Ethanol and methyl p-hydroxybenzoate were mixed in a 15 mL conical tube (to make a 5% solution) and kept aside. The autoclaved media was mixed continuously for a few

minutes, and the propionic acid and orthophosphoric acid mixture was added to the autoclaved media. Following this the ethanol and methyl p-hydroxybenzoate mixture was added. The solution was mixed well and poured into vials/bottles. The mouths of the vials and bottles were covered with a thin clean cotton cloth and allowed to be dried overnight. Next day the mouths of the vials/bottles were covered with tight cotton plugs and stored at 4°C until further use.

- **Protocol for making 10× PBS (Phosphate Buffer Saline), pH 7.4 (1 L)**

Table 2.4.: List of the components and their quantities required for making 10x PBS.

Reagent	Final concentration	Amount
NaCl	1.37 M	80 g
KCl	27 mM	2 g
Na_2HPO_4	100 mM	14.4 g
KH_2PO_4	18 mM	2.4 g
Deionized water	N/A	Make up to 1 L
NaOH	N/A	As needed for pH adjustment to 7.4
HCl	N/A	As needed for pH adjustment to 7.4

All the components were mixed and the solution was autoclaved. It was stored at room temperature and can be used for up to 3–4 months.

- **Protocol for making 0.3% PBST (Phosphate-buffered saline containing 0.3% [v/v] Triton X-100) (200 mL)**

Table 2.5.: List of the components and their quantities required for making 0.3% PBST.

Reagent	Final concentration	Amount
10× PBS	1×	20 mL

Triton X-100	0.3% [v/v]	600 µL
Deionized water	N/A	Make up to 200 mL

A magnetic bead was added to the solution and placed on a magnetic stirrer to ensure that the Triton X-100 dissolves completely. The solution is then stored at room temperature and can be used for up to 3–4 weeks.

- **Protocol for making PFA (50 mL)**

Table 2.6.: List of the components and their quantities required for making Paraformaldehyde solution.

Reagent	Final concentration	Amount
Paraformaldehyde	4% [w/v]	2 g
	8% [w/v]	4 g
1× PBS	1×	to 50 mL

The required amount of Paraformaldehyde powder was weighed and dissolved in 1× PBS in a glass beaker. The volume was made up to 50 mL. The glass beaker was covered from the sides and on top with aluminium foil. A magnetic bead was added to the solution and placed on a hot plate magnetic stirrer. The hot plate was set to 60°C and the stirrer was set at 100 rpm till the PFA powder dissolved completely. The solution was allowed to cool to room temperature and stored at −20°C in 1 mL aliquots.

- **Protocol for making 2% PBTA (PBS containing 0.3% [v/v] Triton X-100, 2% [w/v] bovine serum albumin (BSA), and 0.02% sodium azide) (10 mL)**

Table 2.7.: List of the components and their quantities required for making 2% PBTA.

Reagent	Final concentration	Amount

0.3% PBST	0.3%	10 mL
Bovine serum albumin (BSA) powder	2% [w/v]	0.2 g
10 mg/mL Sodium Azide solution	1.2 [w/v]	200 µL

The required amount of Bovine Serum Albumin (BSA) powder was weighed and dissolved in 0.3% PBST solution with sodium azide in a 15 mL conical tube. The tube was placed on a rocker at 4°C to ensure that the BSA dissolves completely. The solution was stored at 4°C and can be used for up to 1 week.

- **Mowiol-DABCO (20 mL)**

Table 2.8.: List of the components and their quantities required for making Mowiol-DABCO.

Reagent	Final concentration	Amount
Mowiol	2.5% [w/v]	2.4 g
Glycerol	30% [w/v]	6 g
Tris-HCl (pH 8.5)	N/A	12 mL
DABCO	2.5% [w/v]	0.5 g
Deionized water	N/A	6 mL

The required amounts of Mowiol powder and glycerol were mixed. This mixture was dissolved in 6 mL of deionized water and mixed with 12 mL of 0.2 M Tris-Cl (pH 8.5) in a 50 mL conical tube. The tube was kept in a water bath set to 50°C for several hours. The solution was centrifuged at 5,000 g for 15 mins and the supernatant was transferred to a fresh 50 mL conical tube. DABCO was added to the supernatant to achieve a final concentration of 2.5% [w/v] of DABCO. The resultant solution was stored at −30°C in 1 mL aliquots and can be used for up to 5–6 months.

2.3. Embryo Immunostaining

The flies are put in a cage for embryo collection. 2.5-3hr old embryos are collected in plates containing 3% sugar, 2.5% agar and a little amount of yeast paste. Embryos are dechorionated by incubating in 100% bleach for 1 min and then fixed using 1:1 heptane and 4% paraformaldehyde (PFA) in 1x Phosphate Buffer Saline (PBS) for 20 mins. This is followed by hand de-vitelinization of the fixed embryos in PBS or de-vitelinization by vigorous shaking in a 1:1 mixture of Heptane and chilled methanol. De-vitelinized embryos are washed three times in 1x PBST (1x PBS and 0.3% Triton X-100). As a blocking agent 2% Bovine serum albumin (BSA) is added for 1 hr. Embryos are then incubated overnight in the primary antibody of required dilution and washed again with 1x PBST. Secondary antibodies are then added and incubated for 45 mins followed by washing, addition of Hoechst for DNA staining and mounting on slides. The Antibodies that are used for the experiments are listed in Table 2.

Table 2.9.: List of antibodies used and the concentrations used.

	Antibody	Company	Catalogue no.	Lab
Primary antibodies	anti-Arp3 raised in Rabbit (1:500)			William Theurkauf
	anti-Diaphanous raised in Rabbit (1:1000)			Brooke M. McCartney
	anti-DCAD2 raised in Rat (1:5)	DSHB	AB_528120	
	anti-Rab5 raised in Guinea pig (1:500)			Akira Nakamura
	anti-Cortactin raised in Mouse (1:100)	BD Biosciences	610049	
	anti-Dynamin raised in Mouse (1:200)	BD Biosciences	610263	
	anti-Rab11 raised in Rabbit (1:500)			Akira Nakamura

	anti-Scar raised in Mouse (1:100)	DSHB	AB_2618386	
	anti-Sqh raised in Rabbit (1:1000)			Adam C. Martin lab
	anti-Rac1 raised in Mouse (1:100)	DSHB	AB_1553767	
	anti- Phospho Histone3 raised in rabbit (1:600)	Invitrogen	MA5-15220	
	anti-DMIM (raised in Rabbit)	Booster Bio		
Secondary antibodies	Alexa Fluor 488, 568, 633 and 647 raised in Mouse/ Rabbit/ Guinea pig/Rat (1:1000)	Molecular Probes		
	Hoechst 3342 (1:1000)	Molecular Probes	H-3569	
Dyes	Phalloidin 488,568,647 (1:100)	Molecular Probes		
	FM 1-43fx	Thermofisher scientific	F35355	

2.4. Dye uptake assay

Embryos were collected after 1.5 hrs in the sucrose-agar plate. The embryos were washed with deionized water and passed through the sieve. The embryos were dechorionated with 100 % bleach for 4 minutes and then permeabilized for 5 minutes using 1:10 Limonene detergent (Citrasolv) and 1x PBS. This is followed by a wash with 1x PBS. The embryos are then incubated with FM 1-43 FX dye (fixable analog of FM™ 1-43 membrane stain, Thermofisher Scientific, Catalogue number: F35355) diluted in 1x PBS for 15 minutes and then fixed using 1:1 heptane and 4% paraformaldehyde (PFA) in 1x Phosphate Buffer Saline

(PBS) for 25 mins. The embryos are then hand de-vitellinized followed by addition of Hoechst 33258 (1:1000) for DNA staining and mounted on slides with Slow fade Gold antifade (Molecular Probes). FM 1-43 FX dye absorbs in the range of 490-510 nm and initially emits at around 626-636 nm and in the 565-590 nm range upon membrane integration.

2.5. Confocal microscopy for imaging fixed samples

Microscopy

Fixed samples were imaged using Laser Scanning Microscopes using a Plan Apochromat 40x/1.3 Oil Iris M27 Objective on LSM 710, Plan Apochromat 40x/1.4 Oil Iris M27 Objective on LSM 780 (Carl Zeiss™) and Plan Apochromat 40x/1.3 CS2 Oil on inverted Leica TCS SP8.

2.6. Confocal microscopy for imaging live samples

Sample preparation for Live imaging

Embryos are collected after 1 hr of incubation and dechorionated with 100% bleach. Embryos are then washed, dried on a tissue and carefully mounted on coverslip Laptek chambers and immersed in 1x PBS.

Microscopy

Live samples were imaged using Laser Scanning Microscopes using a Plan Apochromat 40x/1.3 Oil Iris M27 Objective on LSM 710, Plan Apochromat 40x/1.4 Oil Iris M27 Objective on LSM 780 (Carl Zeiss™) and Plan Apochromat 40x/1.3 CS2 Oil on inverted Leica TCS SP8.

2.7. Super-resolution imaging on Stimulated emission depletion microscopy (STED) (Mitra et al. 2022)

Embryos were collected for 1.5-2hr at 25 degree C and were labelled with Phospho-Histone PH3 (1:600, Invitrogen) which is used to label the nucleus and identify different

syncytial nuclear cycles. This was coupled with anti-mouse Alexa Fluor® 320 488 (1:1000, Life technologies™). F-actin was labelled with Alexa Fluor® 321 568 Phalloidin (1:100, Life technologies™). The samples were embedded in Mowiol supplemented with 2.5% DABCO to reduce fading of the fluorescence. The embryos were then imaged within 1-2 days with an inverted TCS SP8 3x microscope (Leica 326 Microsystems, Mannheim Germany) with a 100X/1.4NA oil immersion (refractive index 327 1.518) objective (Leica HC PL APO CS2-STED WHITE) operated by the Leica LAS X 328 software (version 3.5.3). Fluorophores were excited with 488 nm (for nuclear Lamin) and 561 nm (for Phalloidin) derived from 80 MHz pulsed White Light Laser (Leica 330 Microsystems, Mannheim Germany) at 70% intensity and depletion was performed with a 775 nm pulsed laser (Leica Microsystems, Mannheim Germany) with a maximum power of 820-860 mW. All images were acquired in 2D STED mode. The fluorophore emission was collected with Hybrid Detectors (HyD, Leica Microsystems, Mannheim Germany) and a typical spectral window of 495- 336 550 nm for nuclear Lamin imaging and 570-640 nm for phalloidin was used.

Table 2.10.: Laser settings for confocal microscopy.

Fluorophore	**Labels**	**Excitation wavelength**	**Excitation laser intensity**	**Detector**	**Spectral window for detection**	**Gain**	**Line averaging**
Hoechst 33258	Dividing nuclei	405 nm	70% (90 MHz pulsed white light laser)	Photomultiplier tube (PMT)	443–466 nm	800–1,000	2
Phospho-Histone H3	Dividing nuclei	488 nm	70% (90 MHz pulsed white light laser)	Hybrid detector (HyD)	506–539 nm	100–200	2
Alexa 568 Phalloidin	Microvilli (F-actin)	561 nm	70% (90 MHz pulsed white light laser)	Hybrid detector (HyD)	585–623 nm	100–150	2

Table 2.11: Laser settings for STED super resolution microscopy.

Fluorophore	**Labels**	**Excitation wavelength**	**Excitation laser intensity**	**Detector**	**Time gate**	**Spectral window for detection**	**Gain**	**Line averaging**
Alexa 488 Phalloidin	Microvilli (F-actin)	488 nm	70% (90 MHz pulsed white light laser)	Hybrid detector (HyD)	0.3–6 ns	507–542 nm	100–120	2
Phospho-Histone H3	Dividing nuclei	561 nm	70% (90 MHz pulsed white light laser)	Hybrid detector (HyD)	0.3–6 ns	584–633 nm	50–60	2

2.8. Image processing, quantification and analysis

2.8.1. Deconvolution of STED images using Huygens professional

Huygens Professional version 17.04 (Scientific Volume Imaging, Netherlands) was used to deconvolve the STED images using the STED module on. The average background was estimated using the In/near object module by controlling the radius parameter. The Classical Maximum Likelihood Estimation (CMLE) algorithm was used and the maximum iterations was set at 27. The Signal to Noise Ratio was set at 7.5 and the quality threshold was set at 0.05. The deconvolved images were saved as high-quality TIFF images.

2.8.2. Quantification of Apical microvilli length and number from fixed embryos

A ROI was drawn to form an open-ended line, along the microvillar projections using the “Segmented line” tool in ImageJ. As many as microvilli that could be observed in sharp

focus emerging from one apical cap, were measured. Microvilli from at least 3-5 caps were measured for each embryo and at least 3 embryos for each genotype. The lengths of each ROI were the length measurements for each microvillus and the number of ROIs per cap were the number of microvilli for each cap.

2.8.3. Quantification of furrow length from live movies

An orthogonal plane of the z-stack that showed the lateral furrows at the interphase and metaphase from the live movies of embryos with their plasma membrane fluorescently tagged, was chosen. A ROI was drawn to form an open-ended line, along the furrows using the "Segmented line" tool in ImageJ. At least 3-5 furrows were measured for each embryo and 3 embryos for each genotype. The lengths of each ROI were the length measurements for each furrow and the approximately 3-5 furrows were measured from each embryo.

2.8.4. Quantification of membrane to cytosolic ratio

A grazing section of the z-stack that showed the sub apical section of the cell was chosen. A ROI was drawn on the cell boundary along its length to measure the mean intensity of the fluorophore on the cell membrane. Another ROI was drawn adjacent to the nuclear region of the cell to measure the intensity of the fluorophore in the cytosol. Both were drawn using the "Segmented line" tool in ImageJ. 5 cells were measured for each embryo and 3-4 embryos for each genotype. The mean intensity of the membrane ROI was divided by mean intensity of the cytosolic ROI, and the ratio was plotted as "membrane to cytosolic ratio".

2.8.5. Quantification of normalised apical intensity

A grazing section of the z-stack that showed the apical section of the cell was chosen. A ROI was drawn to form a closed area, along the boundaries of the apical caps using the "Polygon Selection" tool in ImageJ. This selection measures the intensity of the whole area chosen in the ROI. Another similar ROI was drawn on a plane above the apical cap of the cell to measure the mean intensity of the background noise of the fluorophore. 5 cells were measured for each embryo and 3-4 embryos for each genotype. The mean intensity of the membrane ROI was divided by mean intensity of the ROI for background noise, and the ratio termed as normalised apical intensity" was plotted.

2.8.6. Quantification of Polygon analysis (Dey et al. 2023)

The brightest grazing section was chosen from the base of the cells, with the sharpest boundaries for the metaphase of each nuclear cycle, per embryo and fed into the Packing analyzer software (Benoit Aigouy, Classen et al.,2005, https://idisk-srv1.mpi-cbg.de/~eaton/). The software performs segmentation of the plasma membrane surrounding each cell. The cell area and perimeter are estimated from each cell in the rendered image. Each of the cells are colour coded according to the polygon type depending on the number of neighbours. The output is available as an Excel sheet with the area, perimeter, and polygon type of each cell in the field. For this analysis 3 or more embryos were used per nuclear cycle and all the cells in the field A line of cells at the border of the images was omitted during the analysis to obtain the polygon distribution within the tissue per cycle.

2.8.7. Quantification of cell shape index (Dey et al. 2023)

Based on the cell segmentation data obtained from the packing analyzer and its output in the form of the area (A) and perimeter (P), the average cell shape index was calculated from all the cells excluding one row from the boundary, in the frame, using the formula : $P/\sqrt{A}$ (Bi et al. 2015). The cell shape index was estimated from the segmented images. 3 or more embryos were used for each nuclear cycle and all the cells in the field except a line of cells at the border of the images were analysed to calculate the average cell shape index.

2.8.7. Statistical analysis

The data is represented as the mean ± s.d. for all the quantifications. The n-values are mentioned in their respective figure legends, for all the experiments. The data were plotted in GraphPad Prism 5.0. The means were compared using a two-tailed unpaired Student's t-test .

Chapter 3: Hexagon dominated polygon architecture is achieved with reduction in cell shape index value and regulated by polarity proteins and DE-cadherin
(Done in collaboration with Bipasha Dey)

3.1. Introduction

3.1.1. Polarised organisation in syncytial epithelial cells

During metazoan embryogenesis an onset of epithelial-like-polarity is observed as the epithelial cells get formed. This also coincides with the formation of a polygonal array of cells packed in a tissue. Such coordinated mechanisms enable us to investigate the mechanisms that regulate the arrangement of the packed tissue (Nance 2014). Syncytial *Drosophila* embryos show the asymmetric distribution of various polarity proteins as well as cytoskeletal regulators on the plasma membrane (Schmidt and Grosshans 2018) (Fig. 3.1.). While initially in the pre blastoderm stage, the cortical domains are not polarised, the differentiation of the cortical domains begins as the cortex is divided into 2 domains at the interphase of nuclear cycle 10. The 2 domains are the cap and the intercap regions (Fig. 3.1.). F-actin and actin-associated proteins such as Arp2/3, Scar, Moesin, ELMO, Sponge, and α-spectrin, mark the cap region while myosin II, Toll and Slam localise to the intercap region (Fig. 3.1.). During the syncytial cycles, at metaphase the furrow is increased to its maximum length of each nuclear cycle and the cortical domain is segregated into 3 domains: apical, lateral and basal. The lateral domain is marked by the localisation of Canoe, Peanut (Pnut), Scrambled, DE-cad, Bazooka (Baz), Dlg, and Toll (Fig. 3.1.). The basal domain is mostly formed by the tip of the pseudo cleavage furrow and comprises PatJ, Amphiphysin, Anilin, Diaphanous, and Syndapin (Pesacreta et al. 1989; Thomas and Williams 1999; Foe, Field, and Odell 2000; Stevenson et al. 2002; Zallen et al. 2002; Mavrakis, Rikhy, and Lippincott-Schwartz 2009; Rikhy, Mavrakis, and Lippincott-Schwartz 2015; Sherlekar and Rikhy 2016; Schmidt, Lv, and Großhans 2018; Schmidt and Grosshans 2018; Dey and Rikhy 2020).

A

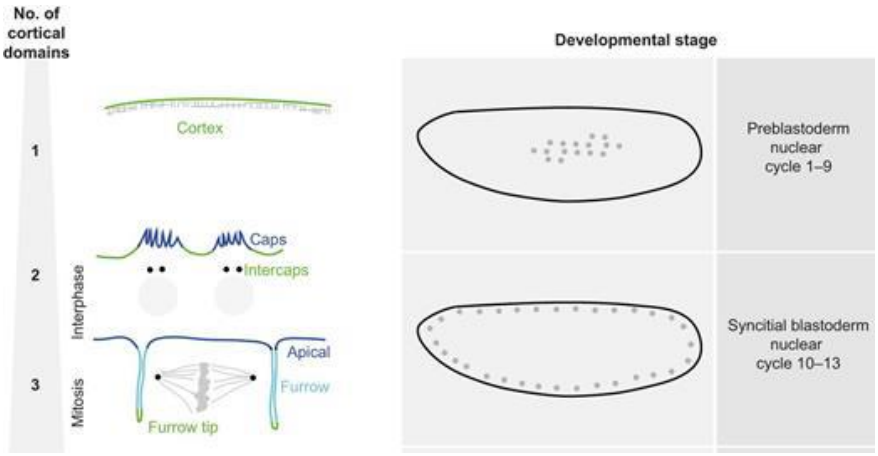

B

Table 1. Marker proteins of cortical domains in early *Drosophila* embryos

Position	Protein	Comment	Vertebrate homolog	References
Pre-blastoderm cortex				
Cortex	F-actin	Cortical filaments		Karr and Alberts (1986)
	Tubulin	Short polymerized forms at cortex		Karr and Alberts (1986)
	Myosin II	Uniform distribution; also called zipper in *Drosophila*	Non-muscle myosin II	Abreu-Blanco et al. (2011)
Syncytial blastoderm – interphase				
Cap	ELMO	Forms a complex with Sponge	Ced-12	Schmidt et al. (2018)
	F-actin			Karr and Alberts (1986)
	Sponge	Forms a complex with ELMO	DOCK3	Schmidt et al. (2018)
	Moesin	Binds to F-actin		Rikhy et al. (2015)
	α-Spectrin			Pesacreta et al. (1989)
	Arp2/3	Enriched at the rims of caps		Stevenson et al. (2002)
Intercap	Slam	Membrane associated		Schmidt et al. (2018)
	Toll	Transmembrane protein	Toll-like proteins	Mavrakis et al. (2009)
	Peanut	Member of the septin family	SEPT7	Fares et al. (1995); Field and Alberts (1995)
	Anillin	Scraps (Scra) in *Drosophila*, septin		Fares et al. (1995); Field and Alberts (1995)
	Myosin II		Non-muscle myosin II	Royou et al. (2004); Warn et al. (1980)
	β-Spectrin		SPTBN1	Thomas and Williams (1999)
	β_{heavy}-Spectrin	Isoform of β-Spectrin		Thomas and Williams (1999)
	E-Cadherin	Enriched in intercap		Mavrakis et al. (2009)

Fig. 3.1.: Cortical organisation of polarity proteins in the syncytial blastoderm *Drosophila* embryos. (A) Schematic showing the dynamics of the cortical domains in pre blastoderm stage and syncytial nuclear cycles of early *Drosophila* embryos.
(B) List of proteins that get localised to the different cortical domains in an asymmetric manner with the initiation of the syncytial nuclear cycles. (adapted from Schmidt and Grosshans 2018)

We have also observed that during the syncytial cycles of *Drosophila* embryogenesis, DE-cadherin, an adhesion junction protein, Bazooka, a Par-3 homolog and a polarity determining protein and Peanut, a septate junction protein., becomes polarized on the cell boundaries. While DE-cadherin and Bazooka become enriched at the edges, Peanut is enriched at the vertices of the polygonal cells. The loss of DE-cadherin leads to a short furrow as well

as Baz and Pnut depletion also leads to a minor decrease in furrow length. Therefore, in the syncytial *Drosophila* blastoderm embryo, molecular and morphological asymmetries in the cortical domain are observed which is concurrent with the onset of a polygonal array of cells at metaphase, during the syncytial cycles (Dey and Rikhy 2020; Dey et al. 2023). However, how the onset and dynamics of the polygonal array is regulated by the asymmetric arrangement and polarised arrangement of the molecules on the plasma membrane remains to be investigated.

3.1.2. Regulation and significance of a hexagon dominated polygonal array

Tissues are a collection of cells which should be packed efficiently. Cell packing refers to the spatial arrangement of cells, in a sheet of epithelial cells. This sheet of epithelial cells typically lines the organs and form a barrier between the compartments. The cells comprising the tissue can undergo shape changes and rearrangements, which leads to stretching, bending or folding of the tissues, essential for the final formation of the organs. The shape and geometry of the cells forming the tissue is of great significance for the homeostasis and stability as well as the functionality of the tissue. A change in cell shape leads to a heterogeneity in their size or area as well. This causes the cells to rearrange and possibly a perturbed cell packing within the epithelium. In cases of cancer, cells that become extremely small in shape can get dispersed within the tissue. During metazoan embryogenesis as the epithelial cells are formed, the onset of polygonal organization of the cells takes place (Gibson et al. 2006). For instance, during early *Drosophila* embryogenesis the cells are arranged as polygons for the first time (Dey and Rikhy 2020). Even in the wing epithelium of *Drosophila* the tissue is able to reach an energetically favourable state as the cells rearrange the number of neighbours they are surrounded with by getting dispersed between normally sized cells (Classen et al. 2005; Ramanathan, Krajnc, and Gibson 2019).

In order to quantitatively analyze the distribution and arrangement of the cells in the polygonal array, the simplest metric is to count the number of neighbours of each cell, in a two-dimensional projection of the tissue. The shape and packing of the tissues can also be analyzed using the same strategies as used for the packaging of soap bubbles in a foam, described in seminal work by D'Arcy Thompson ("On Growth and Form," n.d.). However, cells grow and remodel their shape actively and move around within the tissues and are not passive objects like soap bubbles (Lecuit and Lenne 2007; Graner and Riveline 2017) . One way to measure the dynamics of the cell shape changes is to measure the cell-shape index, which is calculated

by dividing the perimeter of a cell by the square root of its area. A cell closer to circular or an isotropic shape possesses the smallest shape index for a given area. The value increases for more elongated and anisotropic cell shapes. Thus, cells that have shorter contacts with their neighbours yield a smaller shape index value, which is typically assumed to be a more solid-like or 'jammed' tissue. Here, the cells are too tightly packed and stable to exchange their neighbours frequently. Alternatively, cells that engage with their neighbours through longer intercellular contacts, possess a shape index with higher value and are considered to be more fluid-like or 'unjammed' tissue with cells frequently exchanging neighbours. The shape index value of an isotropic hexagonal shaped cell is observed to be around 3.81 in lung epithelial tissue (Bi et al. 2014). Thus, the cell-shape index proves to be a useful metric to analyse the fluidity of cells packed in a tissue. During germ band extension in *Drosophila*, an increase in cell shape index is observed simultaneously along with the cell movements within the tissue (X. Wang et al. 2020). We utilise both the strategies- to count the number of neighbours of the cells packed in the tissue as well as the cell shape index values to quantify the onset and dynamics of the polygonal array of cells in the *Drosophila* syncytial blastoderm embryos.

3.1.3. Polarity proteins regulate cadherin trafficking and cell-cell junctional remodelling.

Epithelial tissues consist of cells adherent to each other, that the interior and exterior surfaces of various metazoans are lined with. The segregation of the epithelial plasma membrane in apical, lateral and basal domains is crucial for stabilising the adhesion proteins on the lateral membrane, as well as essential for trafficking of cadherin (Buckley and St Johnston 2022) (Fig. 3.2.), either along the apico-basal or planar axis of the tissue, as observed during apical constriction and cell rearrangements, respectively. Par-3/Bazooka is itself arranged in planar polarised manner during *Drosophila* germband extension and interacts with the p120-catenin to facilitate cadherin endocytosis around the cell boundaries for recycling the cadherin molecules to the specific cell–cell contacts (Zallen and Wieschaus 2004; Bulgakova et al. 2013; Bulgakova and Brown 2016). Polarity complexes like the Par6-aPKC cassette also interact with the actin cytoskeleton to regulate cadherin endocytosis.

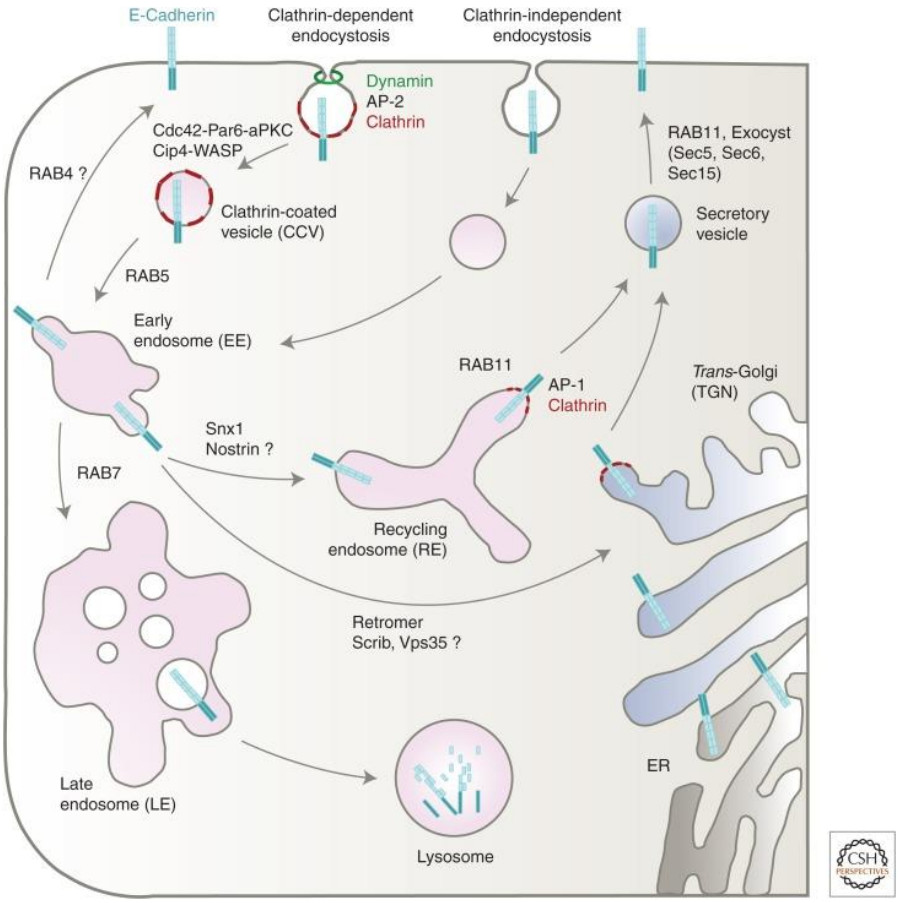

Fig. 3.2.: Schematic showing the polarised trafficking of E-cadherin (Brüser and Bogdan 2017).

Absence of Par6-aPKC leads to cadherin getting stuck in extended endocytic vesicles which are not efficiently internalised, in *Drosophila* notum (Georgiou et al. 2008). A perturbed cadherin trafficking was also observed due to lack of Cdc42, an activator of Par6-aPKC cassette, and it's cytoskeletal effectors like Cip4, WASP, Arp2/3 complex and dynamin (Leibfried et al. 2008) (Fig. 3.2.). Trafficking of DE-cadherin is key to controlling the dynamics of adherens junctions (Fig. 3.2.). The cellular trafficking of DE-cadherin starts with its constant internalisation from the plasma membrane which could be clathrin-mediated as well as clathrin-independent endocytosis, including Rac1 mediated macropinocytosis (Braga et al. 1997; Le, Yap, and Stow 1999; Akhtar and Hotchin 2001; Palacios et al. 2002; Paterson et al. 2003). The cadherin molecules enter early endosomes marked by Rab5 and then get sorted through Rab7, Rab11 and also get exocytosed through the exocyst complex back to the cell surface (Brüser and Bogdan 2017) (Fig. 3.2.). The dynamics of cadherin at the cell-cell-

junctions regulates the plasticity of the tissue making it efficient for remodelling (Fig. 3.3.). This in turn is important for polarised morphogenesis that could extend tissues along a specific axis of the body or organ, as in elongation of the *Drosophila* embryo along the dorsal–ventral (D-V) body axis. Another example of adherens junction remodelling where the junctions need to be removed in case of cell–cell intercalation and shrink anterior-posterior cell-cell contacts while simultaneously delivering cadherin newly forming contacts along the D-V axis (Zallen 2007). Cdc42 effector, Pak1, regulates trafficking of cadherin from apico-lateral to baso-lateral domain in *Drosophila* salivary gland, which is essential for remodelling the organ's size and shape and overall tissue development (Pirraglia, Walters, and Myat 2010). The efficient trafficking of adhesion could regulate polarised arrangement of the mature epithelial cells in a developing tissue. Hence, an understanding of such a mechanism is essential to understand the overall process of cell shape remodelling.

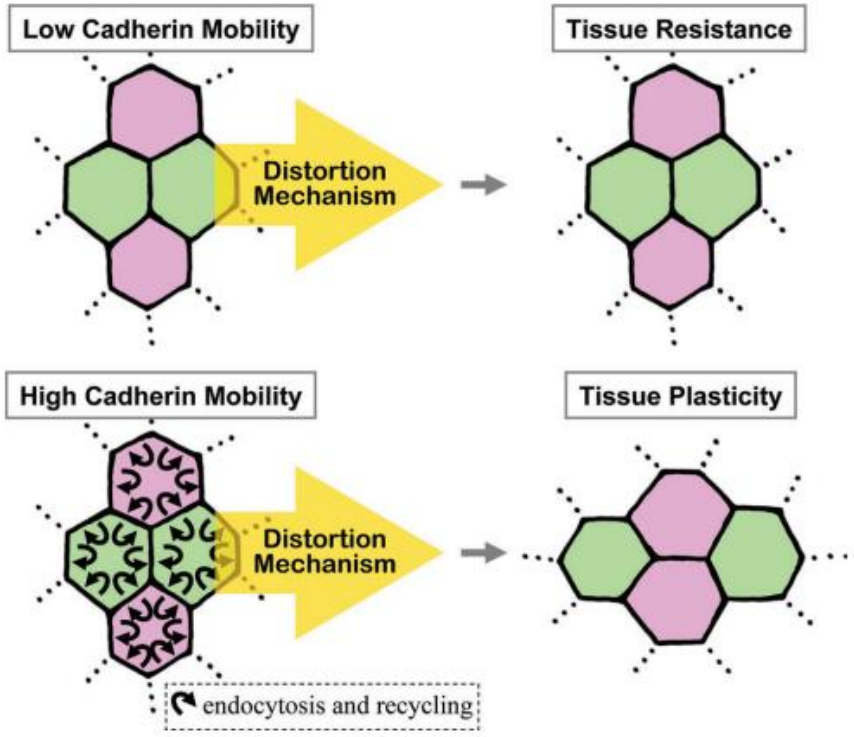

Fig. 3.3.: Schematic showing that trafficking of cadherin along the cell boundaries regulates the maintenance of tissue remodelling. Low cadherin trafficking (top) leads to a tissue resistant to remodelling, whereas high cadherin remodelling (bottom) makes the tissue plastic allowing it to undergo junction remodelling and cell intercalation events. Arrows represent the directionality of cadherin endocytosis and recycling (West and Harris 2016).

Core trafficking mechanisms regulate the cadherin trafficking during cell shape remodelling. Perturbed endocytic machinery regulated by the clathrin, dynamin or Rab5 increases cadherin at the PM while depleting the same from intracellular vesicles, whereas, if the recycling or exocyst mechanism regulated by the Rab11 or the exocyst complex is perturbed, the level of cadherin on the plasma membrane is lowered which also leads to abnormal cadherin accumulation in intracellular vesicles (West and Harris 2016). Lowered turnover of *Drosophila* E-cadherin (DE-cad) in endocytic mutants leads to perturbed distribution of the polygonal classes in the *Drosophila* wing discs, specifically lowered hexagonal classes. Planar cell polarity (PCP) proteins, were found to be the regulators of DE-cadherin turnover along the cellular junctions in *Drosophila* wing discs. Thus, it shows that an interplay of adhesion and PCP proteins was responsible for regulating the frequency of hexagons in wing disc epithelium (Classen et al. 2005; Iyer et al. 2019). Hexagon-dominance in a polygonal array of packed epithelial cells in a tissue, is a property that remains conserved across organisms ranging from the diploblastic *Hydra* to the triploblastic *Xenopus* (Gibson et al. 2006). Theoretical studies suggest that maintenance of such polygonal architecture is attributed to the function of surface tension and that reduced surface tension leads to minimisation of the cell area. Additionally, the cells mechanical properties such as contractility and adhesion along with global tissue level forces also have a possible role in regulating the cellular rearrangements and hence the polygonal packing (Gibson et al. 2006; Farhadifar et al. 2007a; Sugimura and Ishihara 2013). The other branch of studies elucidating on the role of molecular factors, regulating cellular adhesion, in maintaining the polygonal distribution of the cells has however not been fully understood yet. These above examples substantiate that adhesion and polarity proteins are important regulators for maintenance of hexagon dominance in a polygonal distribution of cells.

Here we used the *Drosophila* embryogenesis as a model system to study the onset of a polygonal arrangement of cells. During early *Drosophila* embryogenesis the cells are arranged as polygons for the first time and simultaneously the establishment of polarity proteins is also observed during this period of time (Classen et al. 2005; Dey et al. 2023). Therefore, since the two events of polarity establishment and polygonal arrangement of cells occur simultaneously, we further analysed if the latter was correlated to the polarity establishment. We hence tested the role of adhesion and polarity proteins in regulation of the polygonal arrangement of cells in the embryo. We observed that the cells are packed into a polygonal arrangement at the metaphase of nuclear cycle 11 and the cell shapes become hexagonally dominant at the metaphase of nuclear cycle 12. At this specific time point, DE-Cad and apical polarity protein,

Bazooka, a Par3 homolog gets arranged on the edges whereas the septin, Peanut gets enriched at the vertices. Disrupting DE-Cad leads to perturbed hexagon dominance in the polygonal arrangement of cells whereas the disruption of Bazooka and Peanut leads to a delayed achievement of hexagonal dominance with increase in furrow length from the metaphase of nuclear cycle 12 to nuclear cycle 13.

3.2. Materials and methods

Fly stocks

Refer to Chapter 2: Material and Methods section 2.1.

Embryo Immunostaining

Refer to Chapter 2: Material and Methods section 2.3.

Fixed and Live Imaging

Refer to Chapter 2: Material and Methods section 2.6.

Quantification and statistical analysis

Membrane to cytosolic ratio of dynamin, rab5 and DE-cadherin

Refer to Chapter 2: Material and Methods section 2.8.4.

Polygon analysis

Refer to Chapter 2: Material and Methods section 2.8.6

Quantification of cell shape index

Refer to Chapter 2: Material and Methods section 2.8.7

3.3. Results

3.3.1. Analysis of the cell shape index and polygonal distribution of the plasma membrane architecture and in syncytial *Drosophila* blastoderm embryos

We wanted to assess the establishment of a hexagon-dominated polygonal network during the syncytial nuclear cycles which emerges during the early *Drosophila* embryogenesis. For this we used embryos expressing tGPH which contains the PH domain of GRP fused to GFP that binds the phospholipid PIP3 and labels the plasma membrane uniformly (Britton et al. 2002; Sherlekar and Rikhy 2016; Dey and Rikhy 2020). The experimental setup was mounted such that a grazing section of the cells as shown in the schematic could be observed (Fig. 3.4.A). A z-stack image was captured and one of the stacks that showed an array of the tautest cells with brightest intensity, from the metaphase stage of each nuclear cycle was chosen for analysing the polygon distribution. We used the packing analyzer software to estimate the cell shape index as well as the polygon distribution (Fig. 3.4.A). A theoretical approach to quantify a non-dimensional parameter called the shape index for confluent epithelial monolayers involves estimation of the ratio of the perimeter and area of each cell (see materials and methods) (Park et al. 2015; Bi et al. 2015). A cell shape index value lower than the critical value of 3.81 signifies a jammed state of the tissue that is more solid-like with isotropic cells whereas a value higher than 3.81 leads to non-jammed , fluid-like, anisotropic cells (Bi et al. 2015). An instance where there is a transition of the cells from a jammed to a non-jammed state is during *Drosophila* germ band extension, where during the tissue elongation phase there is an increase in anisotropic cell shapes along with increase in cell shape index and percentage distribution of pentagons in the polygonal distribution of cells (X. Wang et al. 2020).

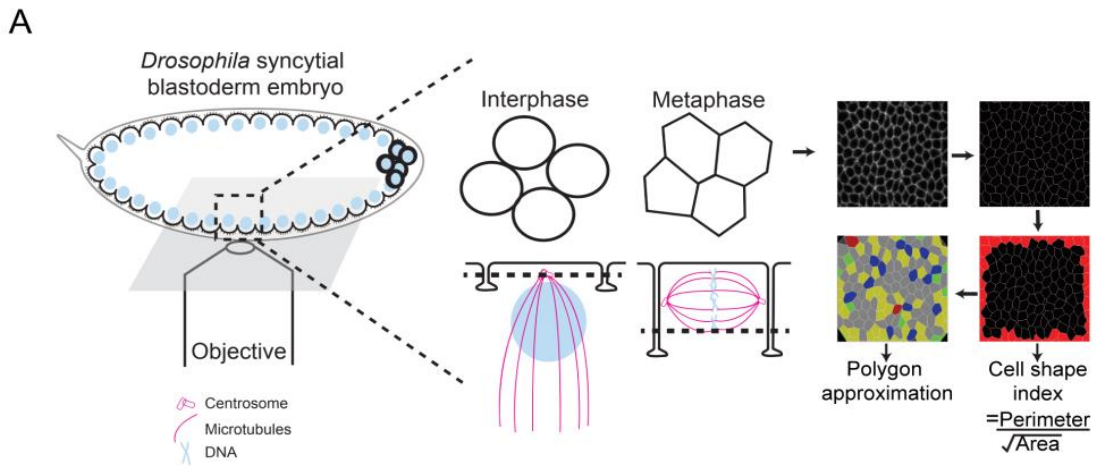

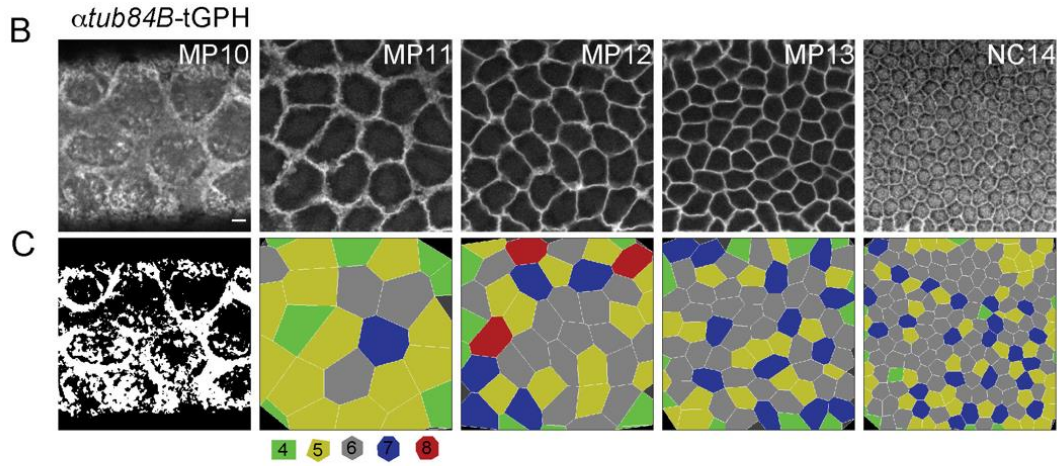
B
αtub84B-tGPH
MP10
MP11
MP12
MP13
NC14
C
4
5
6
7
8

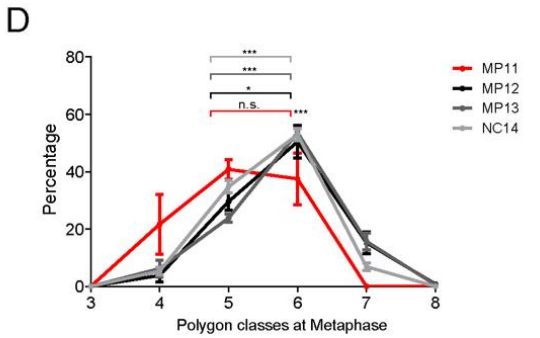
D
Percentage
Polygon classes at Metaphase
MP11
MP12
MP13
NC14
n.s.

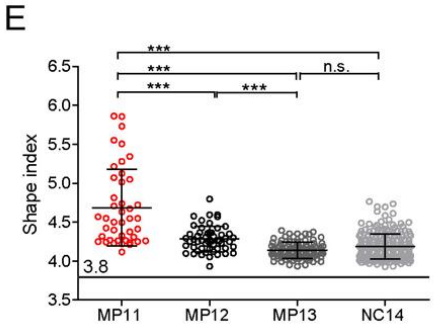
E
Shape index
3.8
MP11
MP12
MP13
NC14
n.s.

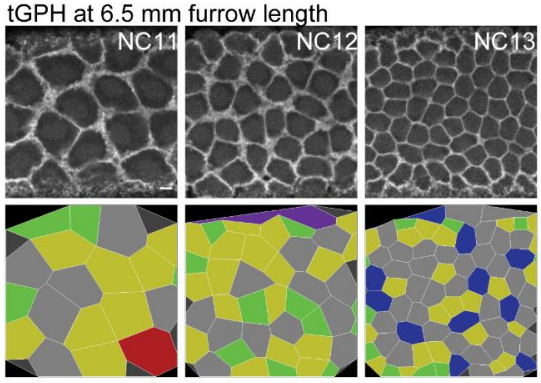
F
tGPH at 6.5 mm furrow length
NC11
NC12
NC13

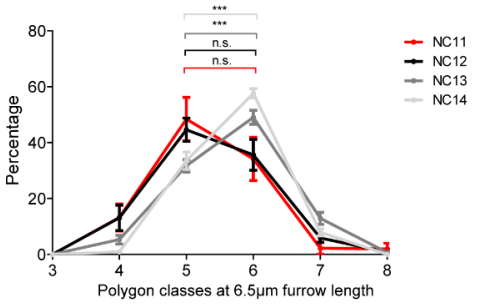
G
Percentage
Polygon classes at 6.5μm furrow length
NC11
NC12
NC13
NC14
n.s.

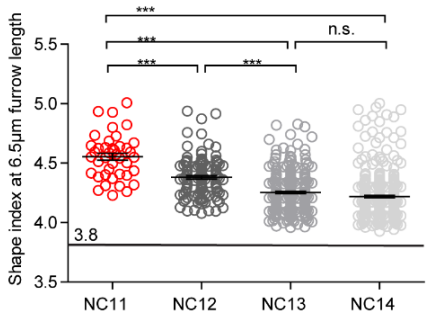
H
Shape index at 6.5μm furrow length
3.8
NC11
NC12
NC13
NC14
n.s.

Fig. 3.4.: Hexagon dominated plasma membrane organisation is established for the first time in nuclear cycle 12

(A)Schematic showing the setup for imaging syncytial *Drosophila* blastoderm embryo being imaged using an inverted confocal microscope. The zoomed inset shows apical and sagittal views of syncytial cells in both interphase and metaphase. The syncytial epithelial cells show polygonal organisation in metaphase. The right-hand side of the schematic shows the methodology for image analysis. The acquired fluorescent images are segmented in the software-packing analyzer for obtaining segmented cell boundaries which are subsequently also used to estimate the average cell shape index. The segmented images are rendered further for estimation of polygon distribution across the metaphase 10-14.

(B) Images showing grazing sections of tGPH expressing embryos from metaphase 10-13 and nuclear cycle14.

(C) Colour-coded polygon rendering of the respective images in (B) using the packing analyzer software.

(D) Quantitative analysis of polygon distribution in metaphase 11-13 and nuclear cycle14 (n= 20-60 cells from nuclear cycle 11-14 per embryo, 4 embryos). Each curve represents a single nuclear cycle Pentagons and hexagons are compared using the unpaired, two-tailed, Student's t test. Data is represented as mean $\pm$ SEM, *p<0.05, **p<0.01, and ***p<0.001.

(E) Graph shows the average cell shape index of all the cells in the field for control embryos (n= 20-60 cells from metaphase 11-13 and nuclear cycle14 per embryo, 4 embryos). Data is represented as mean $\pm$ SEM, *p<0.05, **p<0.01, and ***p<0.001, two-tailed, unpaired Student's t test. Scale bar: 5 μm.

(F) Grazing sections showing tGPH expressing embryos from nuclear cycle 11-13 at furrow length just above the threshold (approximately 6.5μm) and the respective colour-coded polygon rendering using the packing analyzer software

(G) Quantitative analysis of polygon distribution in nuclear cycle 11-14 at approximately 6.5μm (n=4 embryos). Pentagons and hexagons are compared using the unpaired, two-tailed, Student's t test. Data is represented as mean $\pm$ SEM, *p<0.05, **p<0.01, and ***p<0.001.

(H) Graph showing the average shape index of all the cells in the field in control embryos nuclear cycle 11-14 at furrow length of approximately 6.5μm (n=4 embryos). Data is represented as mean $\pm$ SEM, *p<0.05, **p<0.01, and ***p<0.001, two-tailed, unpaired Student's t test. Scale bar: 5 μm.

During *Drosophila* embryogenesis actin caps are formed above each of the nuclei at the cortex of the embryo and their boundaries are far apart in the metaphase stage of nuclear cycle10 with large gaps between them. There is a gradual increase in furrow length, extending between each of the nuclei from interphase to metaphase, through each of the nuclear cycles, that is from nuclear cycle 11 to 13.and reaches a maximum length at the metaphase of nuclear cycle13 (Foe and Alberts 1983; Holly et al. 2015; Xie and Todd Blankenship 2018; Dey and Rikhy 2020). We observed that during these syncytial cycles the plasma membrane gets organised into a polygonal array for the first time in the metaphase of nuclear cycle11 (Fig. 3.4. B-C) and the polygonal distribution of cells at this stage showed almost equal numbers of pentagons and hexagons (Fig. 3.4. D). At the metaphase of the nuclear cycle 12, the polygonal array becomes dominated by hexagons. This hexagonally dominated polygonal network persisted through the metaphase of nuclear cycle 13-14 (Fig. 3.4. D). As mentioned earlier, the attainment of more isotropic cell shape like hexagons in a polygonal distribution is associated with lowering of cell shape index (Park et al. 2015; Bi et al. 2015). We therefore wanted to test if the onset of a hexagon-dominated polygonal distribution is associated with the tissue becoming more jammed. Hence, we estimated the cell shape index for the cells at the following cell cycle stages- metaphase 11, metaphase 12, metaphase 13, and nuclear cycle14. The area and perimeter values for each of the cells were obtained from the segmented images from the movies of tGPH expressing embryos. These were obtained as output from the packing analyzer software and applied to the formula (see materials and methods). The most significant finding was that for all of the nuclear cycles 11,12,13 and 14 at metaphase, when the polygonal organisation is most taut with sharp boundaries, the cell shape indices were greater than the optimal value of 3.81. This suggests that the tissue in the syncytial cycles exists in a soft or unjammed state with more fluid-like properties. However, there is a gradual decrease in the shape index values across the nuclear cycles from 11-14 (Fig. 3.4. E). Previous studies from our lab have shown that the formation of polygonal architecture is based on the progression of the lateral furrow length, specifically achieved at 6.5 μm, known as the threshold length (Dey and Rikhy 2020). We analysed the frequency of the polygonal distribution at a furrow length of approximately 6.5 μm in nuclear cycle11, nuclear cycle12 and nuclear cycle13. We found that at this shorter furrow length in nuclear cycle12, the pentagons were more in number than hexagons, although not statistically significant, whereas in nuclear cycle13 hexagons became dominant at 6.5 μm itself (Fig. 3.4. F-G). Therefore, hexagon dominance was essentially first seen in nuclear cycle12 at increased furrow lengths in metaphase (furrow length 9 μm) and at the short furrow length of 6.5 μm already, in nuclear cycle 13. The cell shape index was also

significantly increased at 6.5 μm furrow length in the nuclear cycle 12 (4.38) and nuclear cycle 13 (4.25) as compared to when the cells are at the longest furrow length in metaphase (Fig. 3.4. H). This shows that the organisation of cells in the syncytial epithelium forms an unjammed network initially which can sustain the dynamic plasma membrane remodelling events during this stage of embryogenesis. The gradual reduction in the cell shape index values along with increase in lateral furrow length progression and increase in cell number with cell cycle progression is observed in the syncytial *Drosophila* embryos. This is consistent with an earlier finding in mammalian epithelial cells where the cell shape index also reduces over time with increase in cell proliferation (Vishwakarma et al. 2020).

3.3.2. Analysis of cell shape index and polygonal distribution of plasma membrane architecture in *Drosophila* E-cadherin, Bazooka and Peanut mutants

We tested the distribution of polygons and the cell shape index values of the cells in the syncytial tissue at metaphase of nuclear cycle 12 and 13, in DE-cadherin, Bazooka and Peanut knockdown embryos. In order to knockdown the DE-cadherin, Bazooka and Peanut we used the RNAi lines (refer to Materials and methods). At first, their loss-of-function effects were investigated on the distribution of the polarity proteins in the syncytial cycles. The role of DE-cadherin was assessed in the recruitment of Bazooka and Peanut by maternally expressing DE-cadherin RNAi (*shg*^{i}). Similar to our previous studies, DE-cadherin depletion showed a decrease in DE-cadherin immunostaining as compared to controls (Dey and Rikhy 2020). DE-cadherin-depleted embryos also showed a significant decrease in the localization of Bazooka and Peanut on the syncytial furrows and an increase in their cytoplasmic distribution. The enrichment of Pnut at vertices as compared to controls was not seen upon DE-cadherin depletion (Dey et al. 2023).

We have imaged embryos expressing tGPH or with Phalloidin staining, both of which mark the boundaries of the cells. For *shg*^{i} expressing embryos, we used the tGPH tag for marking the plasma membrane (Fig. 3.5.A-B)., which showed a lack of hexagon dominance completely both at metaphase 12 and metaphase 13, as compared to control embryos where the hexagon dominance is achieved by the at metaphase 12 itself (Fig. 3.5. C). The cell shape index values in *shg*^{i} expressing embryos were also increased as compared to that of the control embryos, both at metaphase 12 and 13 (Fig. 3.5. D). This finding therefore indicates that disrupting the DE-cadherin levels perturbs the hexagon dominated polygonal distribution and leads to formation of anisotropic cells and a more fluid-like unjammed network of cells. Further

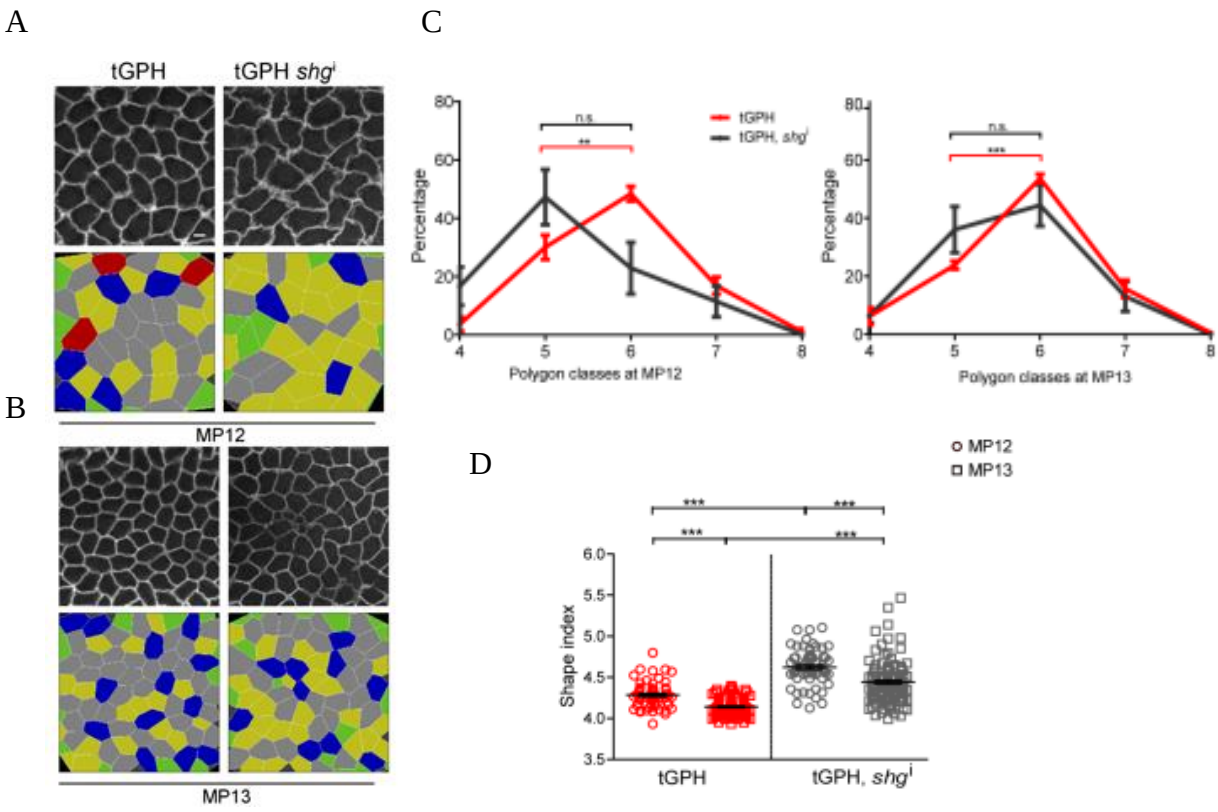

Fig. 3.5.: DE-cadherin depletion shows a loss of hexagon dominance in the polygon distribution of cells.

(A-B) Images showing grazing sections of tGPH/+ and tGPH; *matatub*-Gal4, UAS-*shg*^{i} (*shg*^{i}) embryos in metaphase 12 and 13 along with the respective colour-coded polygon renderings (C). Graph showing polygonal distribution in *shg*^{i} expressing embryos in metaphase 12-13 (n=approximately 120 syncytial cells, 20-30 cells/embryo; 4 embryos). Pentagons and hexagons are compared in each cycle using the unpaired, two tailed, Student's t test. Data is represented as mean ± SEM, *p<0.05, **p<0.01, and ***p<0.001.

(D) Graph showing average shape index of all the cells in the field in control and *shg*^{i} expressing embryos in metaphase 12-13 (n=approx. 120 syncytial cells, 20-30 cells/embryo; 4 embryos). The control tGPH cell shape index is repeated from Fig. 1E. Data is represented as mean ± SEM, *p<0.05, **p<0.01, and ***p<0.001, two-tailed, unpaired Student's t test. The nuclear cycle13 polygon distribution for the control is repeated from Fig. 1D. Scale bar: 5 µm.

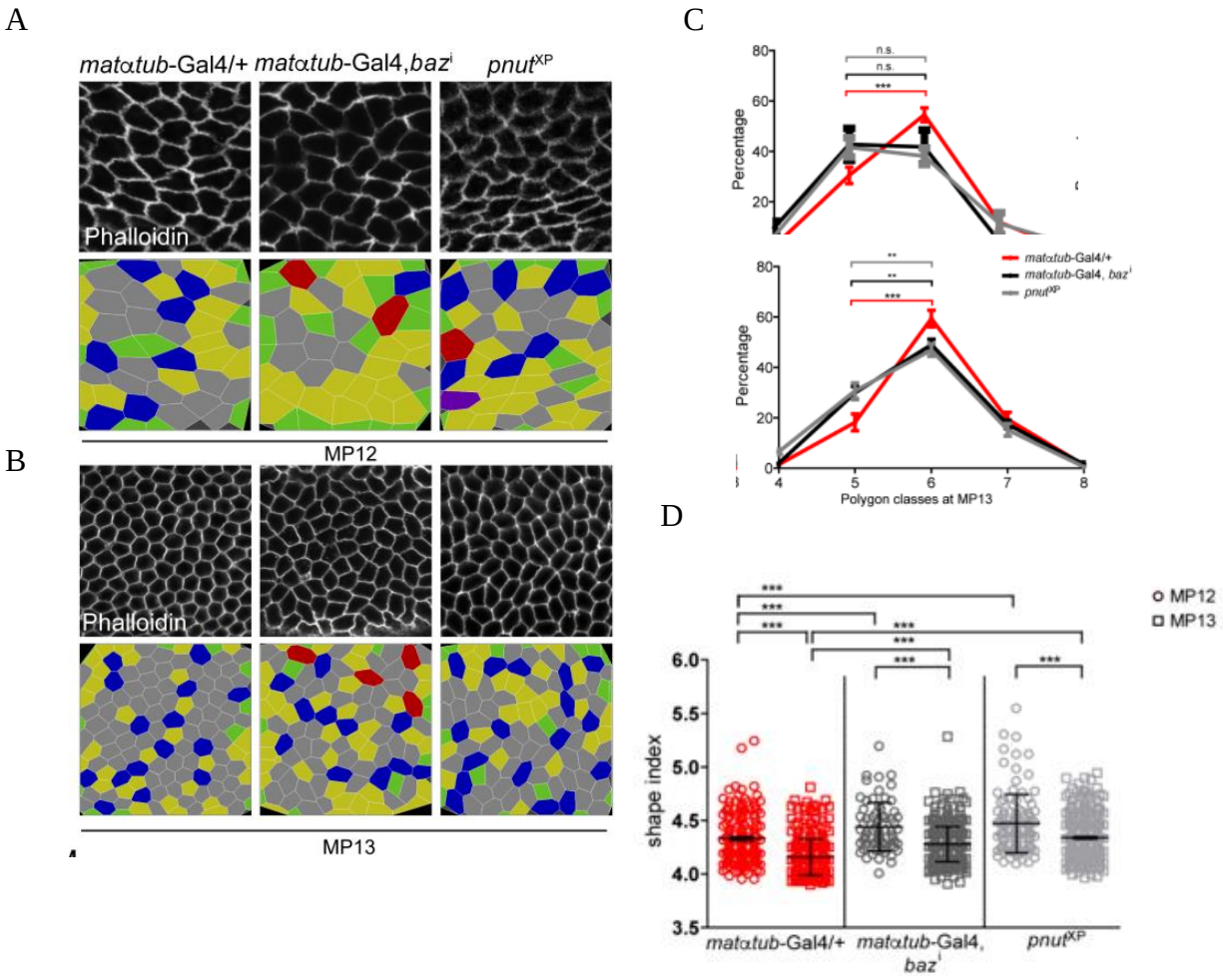

Fig. 3.6.: Bazooka and Peanut depleted embryos show a delay in the onset of hexagon dominance in the polygon distribution of cells.

(A-B) Images showing grazing sections of control (*matatub*-Gal4/+), *matatub*-Gal4, UAS-*baz*^{i} (*baz*^{i}) and *pnut*^{XP} (germ line clone) embryos stained with phalloidin in metaphase 12-13 along with the respective colour-coded polygon renderings.

(C) Graph showing polygonal distribution in *baz*^{i} and *pnut*^{XP} embryos in nuclear cycle 12-13, (n= 60-80 syncytial cells, 20-30 cells/embryo; 4-5 embryos). Pentagons and hexagons are compared in each cycle using the two tailed, unpaired, Student's t test. Data is represented as mean $\pm$ SEM, *p<0.05, **p<0.01, and ***p<0.001.

(D) Graph showing average shape index of all the cells in the field in Control, *baz*^{i} and *pnut*^{XP} embryos in metaphase 12-13 (n=approx. 60-80 syncytial cells, 20-30 cells/embryo; 4-5 embryos). Data is represented as mean $\pm$ SEM, *p<0.05, **p<0.01, and ***p<0.001, two-tailed, unpaired Student's t test. Scale bar: 5 µm.

we disrupted the polarity determining protein, Par3 homolog Bazooka and the septin, Peanut and analysed the polygonal distribution in *baz*^{i} expressing embryos and *pnut*^{XP} germline clone embryos by staining them with fluorescently coupled phalloidin (Fig. 3.6. A-B). Both the mutants showed a loss of hexagon dominance at metaphase 12 as compared to the control embryos. However, the polygonal distribution achieved a hexagonal dominance comparable to the control embryos at metaphase 13 (Fig. 3.6. C). The cell shape index values in *baz*^{i} expressing embryos and *pnut*^{XP} germline clone embryos, were also higher than that of the control embryos (Fig. 3.6. D). Therefore, our data demonstrates that a disrupted polygonal distribution along with a high average cell shape index is observed in shows upon loss of DE-cad, Baz, and Pnut. Therefore, it shows that polarity and adhesion molecules are important determinants of a stable, jammed and isotropic tissue whereas their disruption causes leads to a more unjammed and fluid-like tissue that comprises unstable, anisotropic and unjammed cells.

3.3.3. The delayed hexagon dominance in Bazooka and Peanut mutant embryos was recovered during syncytial cycle 13 with furrow extension

Previous study from our lab has shown that in the syncytial stages of *Drosophila* embryogenesis the cells are circular in shape at the beginning of each nuclear cycle that is at interphase, when the lateral furrows are also shorter as they are just beginning to form. With gradual transition from interphase to metaphase there is a change in the cell shape and area. As the cell area increases the shape also transitions from circular to polygonal. An increase in the furrow length beyond 6.5 µm is essential for the shape transition. Mutants that affect the furrow length progression beyond 6.5 µm show a lack of transition from a circular to polygonal shape (Dey and Rikhy 2020). Therefore, we wanted to analyse the stage at which the rescue of the cell shape is achieved and if it occurs with increase in furrow length. We analysed the polygonal distribution from live movies of embryos expressing tGPH at 6.5 µm in prophase and at metaphase of nuclear cycle 13. For control embryos at 6.5 µm in prophase, the cells were already arranged in a hexagonally dominant polygon distribution and such an organisation was maintained till metaphase 13 (Fig. 3.7. A-B, E). In Bazooka and Peanut depleted embryos there was a lack of hexagon dominance at a furrow length of 6.5 µm in prophase and the hexagon dominance was achieved at the maximum furrow length in metaphase 13 (Fig. 3.7. C-D, E). An analysis of the ratio of pentagons to hexagons increased in Baz and Pnut depleted embryos at 6.5 µm in nuclear cycle 13 and metaphase 13 was carried out. The ratio was significantly

higher in the mutants than controls at 6.5 µm in prophase whereas at metaphase 13, it was not significantly different from controls (Fig. 3.7. F). The average cell shape index value however remained higher than controls in both prophase of nuclear cycle13 and metaphase 13 (Fig. 3.7. G). To summarise, we observed that the establishment of a hexagonally dominant polygon distribution was delayed and it occurred in nuclear cycle 13 and not at nuclear cycle 12 as in controls. In nuclear cycle 13 also the transition was achieved with increase in furrow length. Therefore, it can be speculated that in the bazooka and peanut depleted embryos, with increase in furrow length there could be an increased stability due to possible recruitment of adhesion proteins, which can possibly also be responsible for the establishment of a hexagon dominant polygon distribution finally.

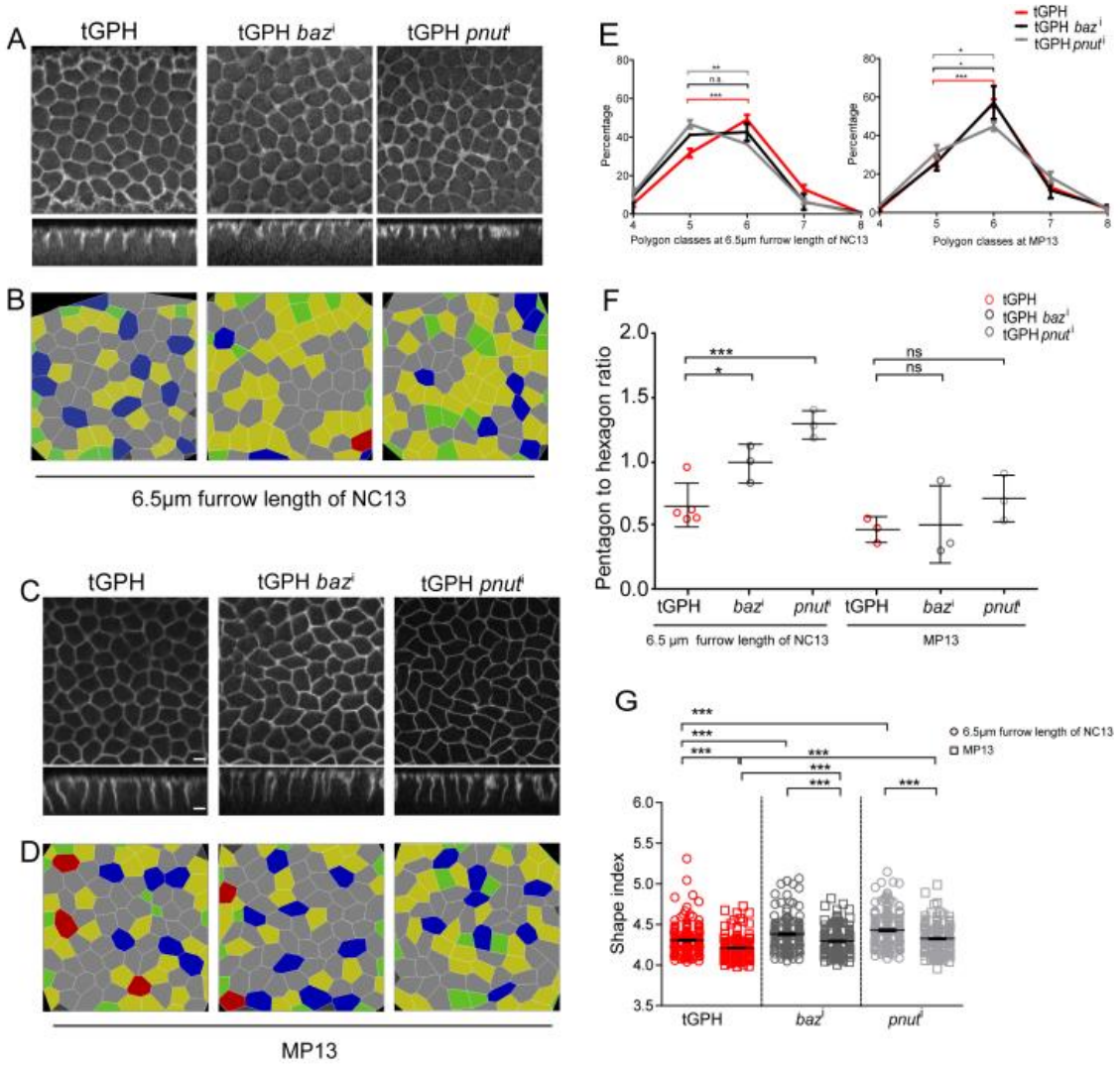

Fig. 3.7.: Appearance of hexagon dominance in Bazooka and Peanut knockdowns occurs in

the metaphase of nuclear cycle13 with increase in furrow length.
(A, C) Images showing grazing sections of *matatub*-Gal4; *baz*^{i} (*baz*^{i}) and *matatub*-Gal4; *pnut*^{i} (*pnut*^{i}) embryos also expressing tGPH at a shorter furrow length of 6.5µm and at metaphase of nuclear cycle13, (B, D) along with the respective colour-coded polygon renderings.
(E) Graph showing the polygon distribution of control, *baz*^{i} and *pnut*^{i} embryos at nuclear cycle13 at a short furrow length of 6.5 µm and at metaphase.
(F) Graph showing the pentagon to hexagon ratio of control, *baz*^{i} and *pnut*^{i} embryos at nuclear cycle13 at a short furrow length of 6.5 µm and at metaphase. Data is represented as mean $\pm$ SEM, *p<0.05, **p<0.01, and ***p<0.001, two-tailed, unpaired Student's t test.
(G) Graph showing average shape index of all the cells in the field in control, *baz*^{i} and *pnut*^{i} embryos at nuclear cycle13 at a short furrow length of 6.5 µm and at metaphase. Data is represented as mean $\pm$ SD, *p<0.05, **p<0.01, and ***p<0.001, two-tailed, unpaired Student's t-test. Scale Bar=5 µm

3.3.4. Analysis of DE-cadherin levels at the plasma membrane in Bazooka and Peanut depleted embryos in the syncytial *Drosophila* embryos

We analysed the levels of DE-cadherin in Baz and Pnut depleted embryos. For this we performed immunostaining of the fixed embryos depleted of Bazooka and Peanut with DE-cadherin antibody together with phalloidin that marked the cortical F-actin localised very close to the plasma membrane and imaged the syncytial *Drosophila* embryos at metaphase 12 and metaphase 13 (Fig. 3.8. A, B). We also imaged the distribution of DE-cadherin distribution in live Baz and Pnut depleted embryos using *ubi*-DE-Cad-GFP in the syncytial *Drosophila* embryo at metaphase 12 and 13 (Fig. 3.8. D, E). The levels of the DE-cadherin distribution on the membrane and cytosol were measured from the sum projections of all the z-sections and their ratios were plotted.

The levels of DE-cadherin analysed using immunostaining with the anti-DE-cadherin antibody were increased on the membrane on the furrow both at metaphase 12 and metaphase 13 (Fig. 3.8. C). Embryos depleted of Baz and Pnut, expressing *ubi*-DE-cad-GFP however did not show a significant change in *ubi*-DE-cad-GFP levels on the membrane as compared to controls in metaphase 12. However, 50% of these embryos showed an increase in *ubi*-DE-cad-GFP intensity on the furrow. The *ubi*-DE-cad-GFP levels on the membrane were significantly increased in metaphase 13 in Baz and Pnut depleted embryos as compared to controls (Fig.

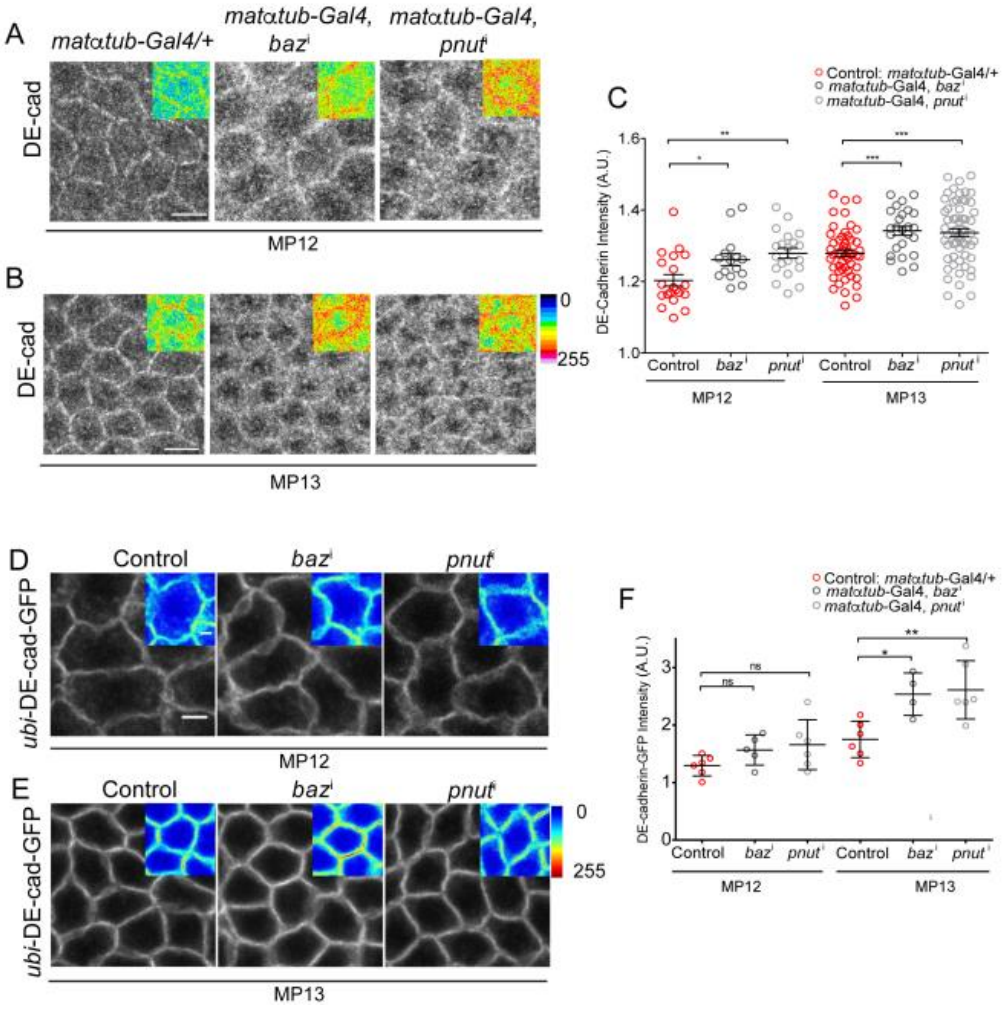

Fig. 3.8.: DE-cadherin accumulation increases on the plasma membrane in Bazooka and Peanut knockdown embryos in Bazooka and Peanut knockdown embryos.

(A-B) Images showing grazing sections of control, *matatub*-Gal4; *baz*^{i} (*baz*^{i}) and *matatub*-Gal4; *pnut*^{i} (*pnut*^{i}) stained with DE-cadherin in metaphase 12-13. Insets show zoomed in images. The 16-colour rainbow scale from the ImageJ is used to show fluorescent intensities. (C) Graph showing quantification of the intensity of DE-cadherin on the membrane using membrane to cytosol ratios in *baz*^{i} (n=15-25, 4-10 cells per embryo from metaphase 12-13, 3-5 embryos) and *pnut*^{i} embryos (n=20-60, 5-10 cells per embryo from metaphase 12-13, 4-5 embryos) For metaphase 12 DE-Cad accumulations are observed at approximately 2-2.4 microns of furrow length in both *baz*^{i} and *pnut*^{i} embryos. For metaphase 13, DE-Cad accumulations are observed at around 2.4-4 microns of furrow length in both *baz*^{i} and *pnut*^{i} embryos. Data is represented as mean $\pm$ SD, *p<0.05, **p<0.01, and ***p<0.001, two-tailed, unpaired Student's t-test. Scale Bar=10 µm

(D-E) Images showing grazing sections of *ubi*-DE-cad-GFP/+, *ubi*-DE-cad-GFP; *matatub*-Gal4, UAS-*baz*^{i} (*baz*^{i}) and *ubi*-DE-cad-GFP; *matatub*-Gal4, UAS-*pnut*^{i} (*pnut*^{i}) embryos in metaphase 12-13. Insets show zoomed in images. The 16-colour rainbow scale from the imageJ is used to show fluorescent intensities.
(F) Graph showing quantification of normalised intensity of DE-cadherin on the membrane using membrane to cytosol ratios in *baz*^{i} and *pnut*^{i} embryos (n=12-15, metaphase 12-13, 5 cells per embryo, 5 embryos). Data is represented as mean $\pm$ SD, *p<0.05, **p<0.01, and ***p<0.001, two-tailed, unpaired Student's t-test. Scale Bar=5 µm

3.8.D). This increased accumulation of DE-cadherin was observed majorly along the sub-apical region of the cells. Summarising this, we observed that both the *ubi*-DE-cadherin levels as well as the endogenous DE-cadherin levels as observed with the antibody staining, were increased on the membrane as compared to the control embryos. This possibly hinted at the fact that the internalisation of DE-cadherin from the plasma membrane of the furrows was perturbed, which leads to the increased accumulation of DE-cadherin.

3.3.5. Analysis of endocytosis in Baz and Pnut depleted embryos at the plasma membrane in the syncytial *Drosophila* embryos

As discussed in the introduction section, several studies have shown that polarity proteins are known to regulate endocytosis at the plasma membrane (Shivas et al. 2010) especially of DE-cadherin, for example during the dynamic tissue remodelling in the *Drosophila* tracheal tissues (Shindo et al. 2008). In notum epithelial cells loss of polarity proteins like Par6-aPKC leads to reduced DE-cadherin trafficking (Georgiou et al. 2008). Dynamin-mediated endocytosis has been shown to be crucial for furrow extension in the syncytial blastoderm embryo and temperature-sensitive mutants of Dynamin, *shibire*, show reduced endocytosis and DE-cadherin accumulation on the plasma membrane (Rikhy, Mavrakis, and Lippincott-Schwartz 2015). Since we observed a possible reduced DE-cadherin internalisation due to perturbed cellular trafficking in Baz and Pnut depleted embryos in metaphase 12 and metaphase 13, we analysed the levels of Dynamin and early endosome protein Rab5 at the plasma membrane in Baz and Pnut depleted embryos. We immunostained Baz and Pnut depleted embryos with Dynamin (Rikhy, Mavrakis, and Lippincott-Schwartz 2015) and Rab5 (Tanaka, Tani, and Nakamura 2021) antibodies together with phalloidin that

marked the cortical F-actin localised very close to the plasma membrane. We measured the levels of Dynamin and rab5 on the plasma membrane and cytosol. The ratios of the membrane to cytosolic intensities were plotted in metaphase 12 and metaphase 13.

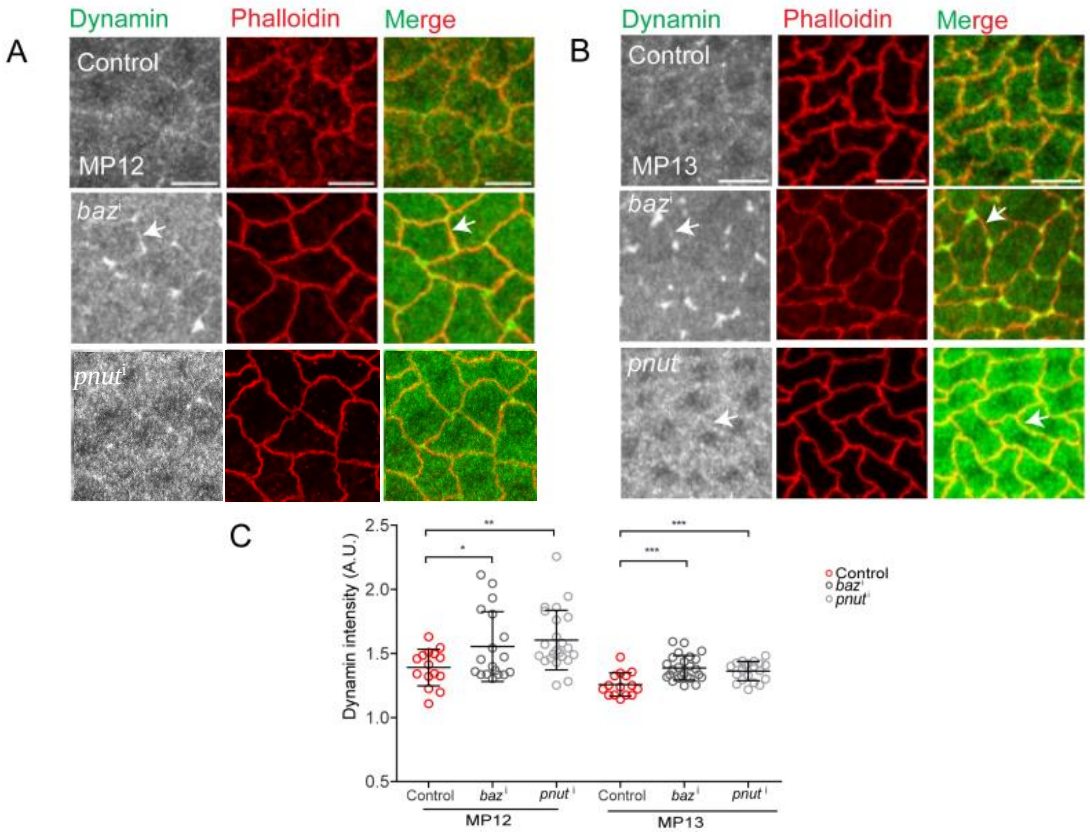

Fig. 3.9.: Dynamin accumulation increases on the plasma membrane in Bazooka and Peanut knockdown embryos.

(A-B) Images showing grazing sections of control (*matatub*-Gal4/+), *matatub*-Gal4, UAS-*baz*^{i} (*baz*^{i}) and *matatub*-Gal4, UAS-*pnut*^{i} (*pnut*^{i}) stained with Dynamin and Phalloidin in metaphase 12 and metaphase 13

(C) Graph showing quantification of fluorescence intensity of Dynamin on the membrane using membrane to cytosol ratios in *baz*^{i} (n= 15-40, 5 cells per embryo from metaphase 12-13, 3-8 embryos) and *pnut*^{i} embryos (n= 30-39, 4-5 cells per embryo metaphase 12-13, 6-8 embryos). For metaphase 12, the image shown for Dynamin accumulations is at approximately 1.8-2.4 microns of furrow length in both *baz*^{i} and *pnut*^{i} embryos. For metaphase 13, the image shown for Dynamin accumulation is at around 2.4-4 microns of furrow length in both *baz*^{i} and *pnut*^{i} embryos. Data is represented as mean $\pm$ SD, *p<0.05, **p<0.01, and ***p<0.001, two-tailed, unpaired Student's t test. Scale Bar=10 µm

Dynamin is usually localised weakly on the plasma membrane at the furrow as marked with phalloidin in control embryos in metaphase 12 and metaphase 13 (Fig. 3.9. A, B). We observed an accumulation of Dynamin with an increase in its intensity on the plasma membrane both at the furrow and in the cytoplasm in the form of distinct punctae's in both Baz and Pnut depleted embryos. We specifically quantified the Dynamin intensity on the plasma membrane at the furrow marked by phalloidin and cytosol and plotted the ratios of the same. We found that there is a significant increase of the dynamin intensity on the plasma membrane at the furrows in metaphase 12 and metaphase 13 in Baz and Pnut depleted embryos (Fig. 3.9. C).

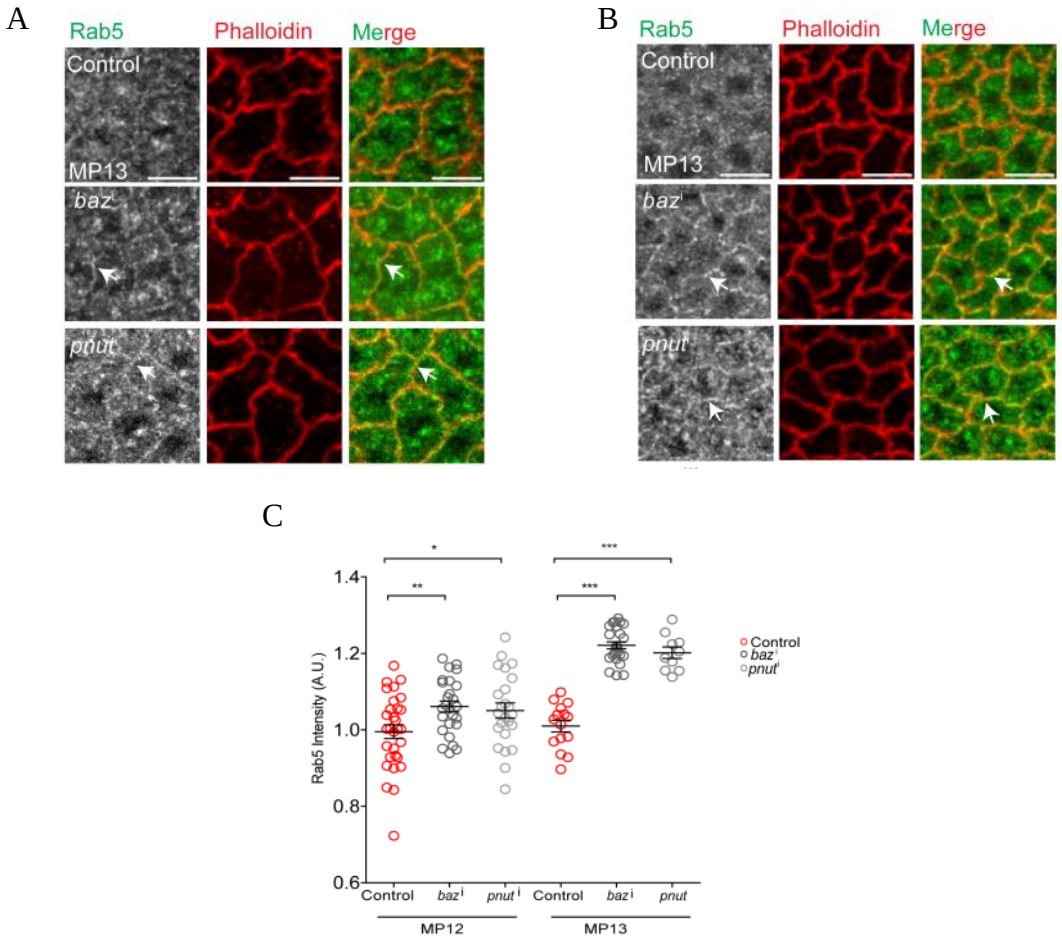

Fig. 3.10.: Rab5 accumulation increases on the plasma membrane in Bazooka and Peanut knockdown embryos.

(A-B) Images showing grazing sections of control (+/+), *baz*^{i} and *pnut*^{i} stained with Rab5 in the metaphase of metaphase 12-13.

(C) Graph showing quantification of intensity of Rab5 on the membrane using membrane to

cytosol ratios in *baz*^{i} (n= 25-26,4-5 cells per embryo from nuclear cycle 12-13, 5 embryos) and *pnut*^{i} embryos (n= 10-25, 5 cells per embryo from metaphase 12-13, 2-5 embryos). For metaphase 12, the image shown for Rab5 accumulation is at approximately 1.8-2.4 microns of furrow length in both *baz*^{i} and *pnut*^{i} embryos. For metaphase 13, the image shown for Rab5 accumulations is at around 2.4-4 microns of furrow length in both *baz*^{i} and *pnut*^{i} embryos. Data is represented as mean $\pm$ SD, *p<0.05, **p<0.01, and ***p<0.001, two-tailed, unpaired Student's t test. Scale Bar=10 μm

Rab5 fluorescence intensity was observed as punctae and localised weakly on the plasma membranes at the furrow which is marked by phalloidin in control embryos in metaphase 12 and metaphase 13 (Fig. 3.10. A, B). We observed that there was an increased accumulation of Rab5 on the plasma membrane at the furrow in Baz and Pnut depleted embryos. We specifically quantified the rab5 intensity on the plasma membrane from a single plane at the furrow marked by phalloidin and cytosol and plotted the ratios of the same. We found that there is a significant increase of the rab5 intensity on the plasma membrane at the furrows in metaphase 12 and metaphase 13 in Baz and Pnut depleted embryos (Fig. 3.10. C). This accumulation of Dynamin and Rab5 at the sub-apical region on the furrow clearly indicates that there is a possible reduction of endocytosis at the plasma membrane, in Baz and Pnut depleted embryos implicates which led to an increased accumulation of DE-cadherin on the plasma membrane a decrease in endocytosis at the furrow PM in and this is likely to be the cause of the accumulation of DE-cadherin both at nuclear cycle12 and nuclear cycle13.

3.4. Discussion and conclusion

In summary, we show that across successive division cycles, the syncytial *Drosophila* blastoderm embryos show an increase in furrow length with the progression of the nuclear cycles. This is also associated with the establishment of a polygonal array of cells from the metaphase of cycle 11 onwards. Pentagons and hexagons were present in equal probability at nuclear cycle 11 when edges were formed for the first time. Hexagons were found to be present at double the number of pentagons at metaphase 12 and 13. There is also a concurrent decrease in cell shape index as the cells become more isotropic and jammed, with increased crowding signifying the formation of a more stable polygonal array. This is associated with reduced surface tension and minimised surface energy, all facilitating the formation of a stable tissue.

In syncytial cycles, the embryos do not have a sealed basal domain and therefore the lateral membrane, i.e. the pseudo cleavage furrow, keeps the cells attached to each other and may be sufficient for the regulation of the stability and distribution of the polygonal array of cells. We have therefore characterised the role of Baz, Pnut, and DE-cadherin proteins in the regulation of polygon array distribution and cell shape index in the syncytial embryo. This analysis reveals that the polygon distribution can possibly have 2 kinds of defects: (1) Depletion of DE-cadherin in embryos lead to loss of hexagon dominance, and an increased cell shape index; (2) Depletion of Baz and Pnut lead to a delay in establishment of hexagon dominance in the polygonal array and an increased cell shape index as well. From previous work in the lab we also know that in De-Cad mutants the furrow length is much shorter than the control while in the Baz and Pnut mutants, the furrow length is only slightly shorter (Dey et al. 2023). Although the cell shape index was found to be more than controls in DE-cad, Baz, and Pnut depleted embryos, there is a gradual decrease from metaphase 12 to 13. This shows that cell proliferation and the associated changes in the plasma membrane remodelling packing of cells in the tissue, a more stable network. Baz and Pnut depleted embryos show delayed hexagon dominance and higher cell shape index which was coincident with increased accumulation in levels of DE-cadherin on the plasma membrane as compared to controls, with a gradual increase in furrow lengths. This increase is possibly brought about by the accumulation of endocytic machinery at the furrow plasma membrane, marked by Rab5 (Fig. 3.11.) as has also been observed in the case of *shibire* mutants, in early *Drosophila* embryos (Rikhy, Mavrakis, and Lippincott-Schwartz 2015). The increased E-cadherin levels on the plasma membrane due to the loss of the polarity proteins could be retention of non-mobile E-cadherin as loss of baz is known to reduce the mobility of E-cadherin which leads to the formation of aberrant cell packing, like rosette-like structures. The endocytosis of the E-cadherin depends on its association with baz and a formation of the mobile complex that can functionally lead to efficient turnover of the cellular junctions crucial for the isotropic cell shape and packing within the tissue (Bulgakova et al. 2013). Therefore, in spite of the excess E-cadherin accumulated on the plasma membrane, it is possible due to the absence of baz, the accumulated E-cadherin is less mobile and leads to defect in the packing of cells and increasing the average cell shape index values of the tissue.

These observations highlight that an interaction of polarity, adhesion, and endocytosis proteins is crucial for achieving a stable developing tissue which can sustain the forces and remodelling that it would have to undergo in later stages of development during early *Drosophila* embryogenesis.

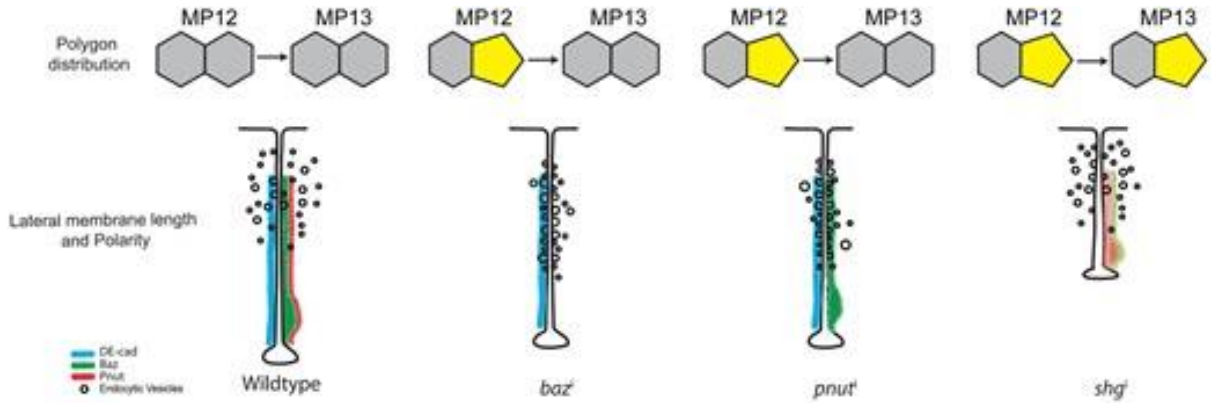

Fig 3.11.: Schematic summarising the concurrent establishment of polarised distribution of DE-cad, Baz and Pnut on the lateral furrow and polygon distribution in the *Drosophila* syncytial blastoderm embryo in Nuclear Cycle 13. Control embryos show hexagon dominance in metaphase 12–13 as the DE-cadherin undergoes efficient endocytosis at the plasma membrane. Loss of Bazooka or Peanut results in a shorter furrow and a delay in the onset of hexagon dominance while loss of DE-cadherin leads to shorter furrow along with a loss of hexagon dominance.

Chapter 4: Microvilli length and number reduce from interphase to metaphase during the syncytial cycles of *Drosophila* embryos
(Done in collaboration with Amruta Swaminathan)

4.1. Introduction

One of the most important traits of change in apical cell surface area drives remodelling of epithelial cell shape, during several morphogenetic events like cell growth and tissue invagination. This is also associated with change in tension in the cells or tissue. The apical surfaces of epithelial cells usually possess structures like the microvilli which are observed across various cell types like polarised epithelia of kidney, liver and lung, to neurosensory cells, Schwann cells, immune cells, and embryos (Revenu et al. 2004). Functionally the microvilli are known to increase surface area for absorption of water in kidney cells, or increase the exposure of digestive enzymes in gut or for adhesion of lymphocytes to the walls of blood vessels (Louvard, Kedinger, and Hauri 1992; Ashworth and Molitoris 1999; Sundd et al. 2011). While in the microvillar protrusions of stereocilia in the inner ear are known to transmit mechanotransduction, there has always been an widely accepted notion that these microvilli like structure act as reservoir of excess plasma membrane which is utilised for fuelling cellular growth in events like cytokinesis, wound healing, morphogenesis, osmotic regulation, cell spreading and phagocytosis (Arnold 1969; Fullilove and Jacobson 1971; Porter, Prescott, and Frye 1973; Ducibella et al. 1977; Betchaku and Trinkaus 1978; Schroeder 1978; Bement, Forscher, and Mooseker 1993; Herant, Heinrich, and Dembo 2005).

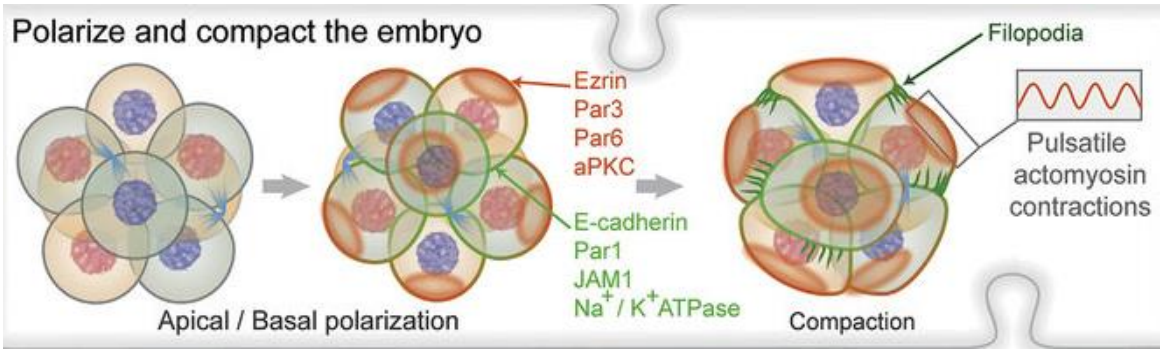

Fig. 4.1.: Early mouse embryo showing the distribution of polarity proteins as well the localisation of the filopodia-like protrusions that appear from the boundary of the cells due to the activity of E-cadherin and actomyosin contractility. (White et al. 2018)

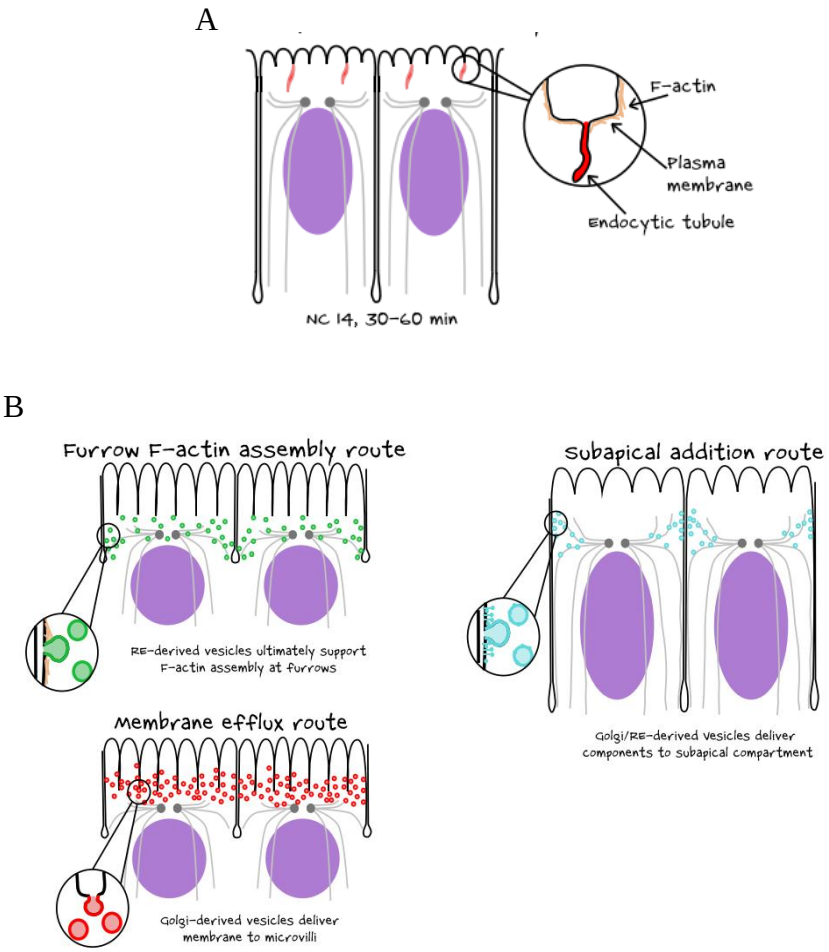

Fig. 4.2.: Schematic showing the remodelling of microvilli like protrusions that are present at the apical surface of the epithelial-like cells during the cellularization stage of *Drosophila* embryos, through cellular trafficking processes. (A) They get internalised through the apical tubular endocytosis and (B) get effluxed or added to the lateral or sub-apical region to support the F-actin assembly there. (Sokac, Biel, and De Renzis 2023)

The shaping of the apical plasma membrane into finger-like protrusions requires the activity of bundled cytoskeletal filaments attached to the plasma membrane. In case of cilia, the filaments are microtubules, whereas in case of microvilli, stereocilia and filopodia the filaments are made of F-actin (Lewis and Bridgman 1992; DeRosier and Tilney 2000). In mouse preimplantation embryos, long cellular protrusions appear at the time of compaction which are enriched with E-cadherin. These filopodia become extended from the cell-cell junctions on the apical membrane of the neighbouring cells in order to maintain tension and increased adhesion, thus facilitating compaction, where the cells transition from a more circular

to a polygonal shape and compact structure. A disruption to the structures of these filopodia through laser ablation, perturbs the compaction process and makes the cells circular. Perturbing the levels of E-cadherin, α-catenin, β-catenin, or Myo10, that usually mark the filopodia, disrupts the filopodia formation and embryo compaction (Fierro-González et al. 2013). In *Drosophila* cellularization embryos, the apical surface of the cells possesses a reservoir of excess plasma membrane present in the form of microvilli initially (Turner and Mahowald 1976). The reservoir is maintained by golgi-dependent delivery of the membrane vesicle through the Rab8 mediate exocytosis. Over time the exocytosis is reduced and the microvilli like structures gets reduced over time to aid in the elongation of the lateral furrow either through dynamin and Rab5 dependent endocytic pathway or through stretching of plasma membrane. A lack of the remodelling of the microvilli affects the furrow ingression (Figard et al. 2013; Fabrowski et al. 2013). The microvilli in these studies were visualised either using confocal microscopy, TIRF or SEM, which didn't provide enough resolution and hence precise quantification of the density and structure of these microvilli was not possible. Therefore, we identified the syncytial blastoderm embryo as a model system to look at the microvilli remodelling dynamics very precisely. The major reason for choosing this specific stage is the presence of bigger cells and longer microvilli with lesser number of cells, making the frame less crowded and allowing for the achievement of better resolution of the microvilli structures.

In the syncytial blastoderm stage of *Drosophila* embryogenesis the nuclei undergo rapid division cycles cortically (Foe and Alberts 1983) and at this stage each nucleus is surrounded partially by the plasma membrane with an actin-rich cap present atop. During interphase of the syncytial division cycles, these actin caps bear filamentous microvilli-like protrusions (Turner and Mahowald 1976; Warn, Bullard, and Magrath 1980; Warn, Magrath, and Webb 1984; Foe and Alberts 1983; Karr and Alberts 1986; Mavrakis, Rikhy, and Lippincott-Schwartz 2009) . These actin caps expand in area from interphase to metaphase of each nuclear division cycle (nuclear cycle) with simultaneous reduction in microvilli lengths and numbers (Sherlekar et al. 2020) and is coordinated with extension of the plasma membrane in the form of lateral furrows in between the nuclei. This growth in the furrow could be possibly aided by the remodelling of the microvilli as has been observed in cellularizing *Drosophila* embryos. The observation and analysis of the status of microvilli at these stages is key to understanding how the changes in plasma membrane remodelling are coordinated with the development of the embryos. We have used confocal and super-resolution STED microscopy to visualise the apical microvilli present on the surface of Canton-S embryos, wild-type strain of *Drosophila melanogaster*. STED microscopy allows to resolve structures closer than the

diffraction limit of light microscopy which is known to be approximately 200-250 nm. The basic principle of this system makes it possible to overcome this diffraction limit by depleting fluorophores at predefined positions where the objects supposed to be imaged are smaller in size than the diffraction limit and are marked by a special doughnut-shaped profile. Therefore , the fluorophores from the complementary region only emit light, separating the objects closer than the diffraction limit (Vicidomini, Bianchini, and Diaspro 2018) .We have also used image processing methods to resolve these structures using deconvolution and finally demonstrated image analyses to elucidate the microvilli remodelling event from interphase to metaphase in nuclear cycle12.

4.2. Materials and methods:

Fly stocks

Refer to Chapter 2: Material and Methods section 2.1.

Embryo immunostaining

Refer to Chapter 2: Materials and methods section 2.3.

Super resolution imaging on STED

Refer to Chapter 2: Materials and methods section 2.7.

Image processing, quantification and analysis

Deconvolution of STED images

Refer to Chapter 2: Materials and methods section 2.8.1.

Quantification of microvilli length and number

Refer to Chapter 2: Materials and methods section 2.8.2.

Identification of the nuclear division cycle number in fixed and stained embryos.

Refer to Chapter 2: Materials and methods section 2.8.8

Quantification of Full-Width at half maximum (FWHM)

Refer to Chapter 2: Materials and methods section 2.8.9

4.3. Results

4.3.1. Standardising the setup for imaging and identification of cell cycle stage in the syncytial blastoderm embryo

Microvilli are present in the apical region of the pseudo-epithelial cells in syncytial *Drosophila* blastoderm embryos. The schematic in Fig. 4.3. A, shows the setup for the imaging of apical microvilli using super-resolution microscopy Stimulated Emission Depletion Microscopy (STED). As shown in the inset image the actin caps show projections appearing mostly from the periphery at interphase, which is mostly a reservoir of the excess plasma membrane and actin. The lateral furrows are shorter as they are just beginning to form. By the time the nuclear cycle progresses to metaphase the microvilli get reduced in number and length. This is concurrent with the increase in lateral furrow length. In order to study these structures, we fixed wild type embryos and stained them with phalloidin to look at the F-actin rich projections present on the apical caps.

A

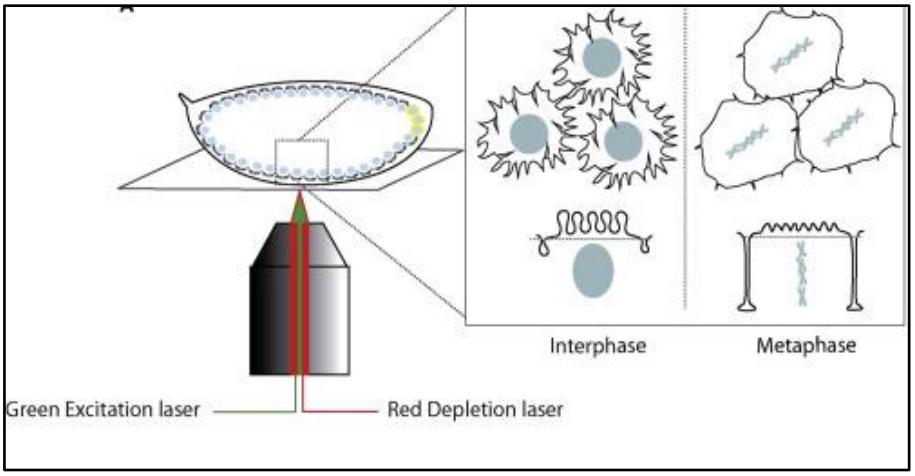

Fig. 4.3: Schematic showing the setup for imaging and identification of the cell cycle stages in the syncytial blastoderm embryo.

(A) Schematic showing syncytial *Drosophila* embryos being imaged using an inverted confocal and STED microscope (left). The schematic of a pseudo-epithelial cell at the syncytial nuclear cycle stage (right, magnified inset), showing an apical view and a sagittal view, with the dashed line indicating the plane of the membrane shown in the top panel.

For imaging the microvillar structure at different stages of the nuclear cycle we need to identify the interphase and other mitotic stages which can be identified by observing the nucleus. While using STED, Hoechst cannot be used to label the nuclei as it interferes with the functioning of the depletion laser. Therefore, we stained the embryos with Phospho-Histone H3, which labels the nuclei only when they are in their dividing/ mitotic stages.

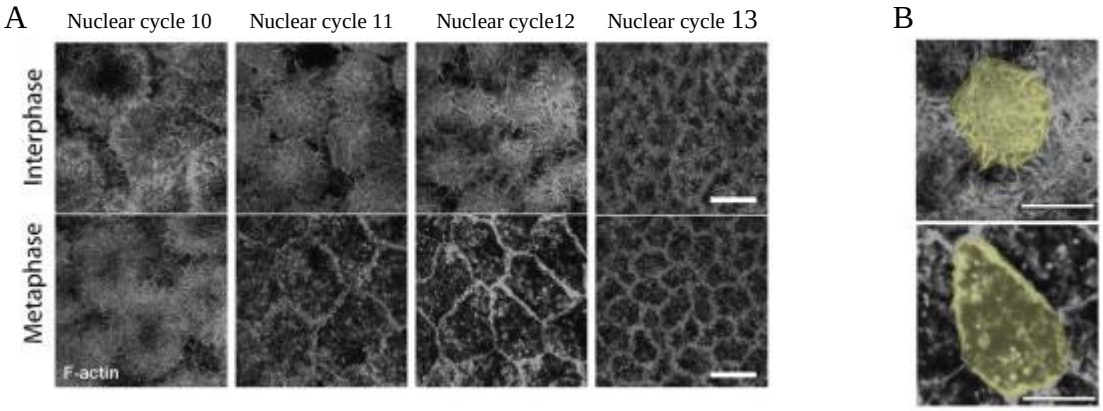

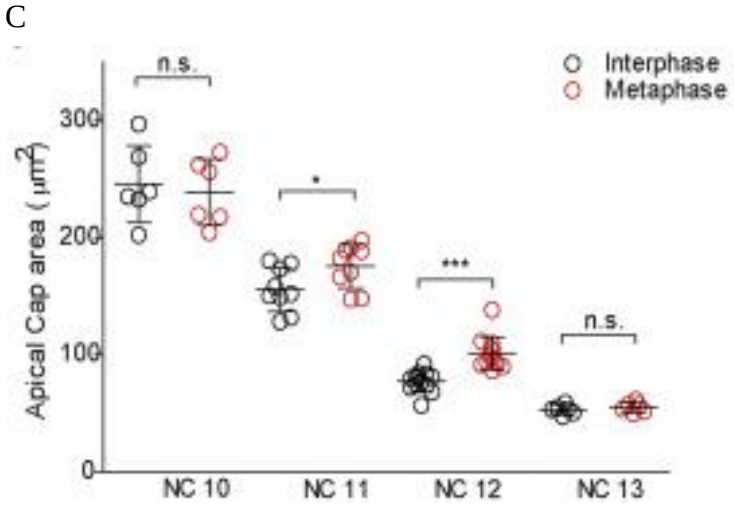

D

Nuclear cycle	10	11	12	13
Cap area range[a]	>240μm^2	120–240μm^2	80–120μm^2	40–80μm^2

a Area ranges identified are approximate.

Fig. 4.4.: Identification of the stages of nuclear cycles for measurement of the apical microvilli in the syncytial *Drosophila* blastoderm.
(A) Grazing sections showing the apical actin caps at interphase and metaphase of nuclear cycles 10–13 imaged using Super-resolution STED in the syncytial *Drosophila* embryo. Scale bar: 5 μm.
(B) ROI drawn using Polygon tool for imageJ/ Fiji (yellow) along the boundaries of the apical cap to measure its area. Scale bar: 5 μm.
(C) Graph showing the quantification of apical cap areas at interphase and metaphase in nuclear division cycles 10–13 in the syncytial *Drosophila* embryo. nuclear cycle 10, n = 6,3 caps from 2 embryos each, nuclear cycle 11, n = 9,3 caps from 3 embryos each; nuclear cycle 12, n = 12,3 caps from 4 embryos each, nuclear cycle 13, n = 6,3 caps from 2 embryos each. Data are represented as mean ± SD, ∗p<0.05, ∗∗p<0.01, and ∗∗∗p<0.001, two-tailed, unpaired Student's *t* test.
(D) Estimation of the range of apical area in order to identify the different nuclear cycles. Cells in syncytial nuclear cycle 10 have apical caps are larger than 240 μm2; in nuclear 11 the apical area is in the range of 120–240 μm2; in nuclear cycle 12 the apical area ranges from 80–120 μm2 and in nuclear cycle 13 the apical area lies in the range of 40–80 μm2.

The embryos stained with Phospho-histone H3 and Alexa Fluor 488 Phalloidin to mark the cortical actin were imaged using STED. Several studies show that the apical actin cap as well as the microvilli remodel majorly between the interphase and metaphase of every nuclear cycle. Therefore, it is pertinent that we can estimate the exact stage of the nuclear cycle while imaging with STED, in order to observe the microvilli remodelling. A single plane from the apical section of the pseudo-epithelial cells was imaged using the STED system. For the settings used for imaging refer to the materials and methods. The embryos were imaged at interphase and metaphase of each of the nuclear cycles from 10 to 13 (Fig.4.4. A). The

polygonal tool from Fiji was used to draw an ROI around the apical caps to measure the area of the cells as shown in Fig.4.4. B. The apical cap areas were plotted for interphase and metaphase of each nuclear cycle (Fig.4.4.C). We observed that the apical cap area changes were most significant at nuclear cycle12 between the interphase and metaphase. Summarised in Fig.4.4. D is the range of apical cell area for each of the nuclear cycles measured from interphase to metaphase which can be used as a guideline for imaging and quantifying the microvillar structures at specific stages of the nuclear cycle.

4.3.2. Analysis and quantification of microvilli like structures using both Confocal and STED

We wanted to verify quantitatively if there was difference in the resolution of the microvilli between the confocal and STED images. For this we drew an ROI in the form of a straight line across the microvilli as shown in the Fig. 4.5. And used the plot profile option in imageJ to obtain the distribution of the intensity across the ROI as shown in the graphs (Fig. 4.5.B and C). We used the MATLAB code as mentioned in material and methods in order to obtain the Full-width half max (FWHM) values from the distribution. We plotted the curves and obtained the FWHM values, from Confocal and STED images of microvilli at interphase and metaphase of nuclear cycle12. The values obtained from STED images of the microvilli both at interphase and metaphase were both smaller than that of the Confocal images. This signifies that the microvilli were definitely better resolved using STED images as compared to confocal images at 100X magnification.

A

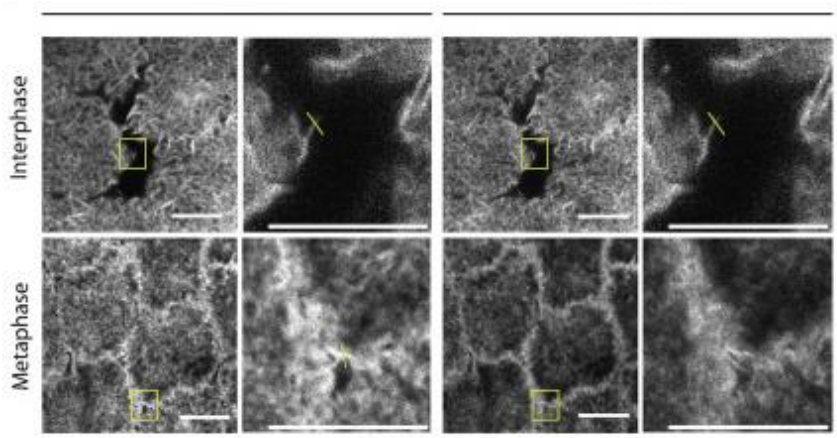

B

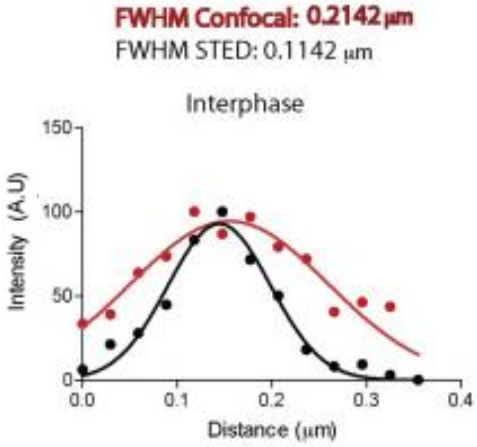

C

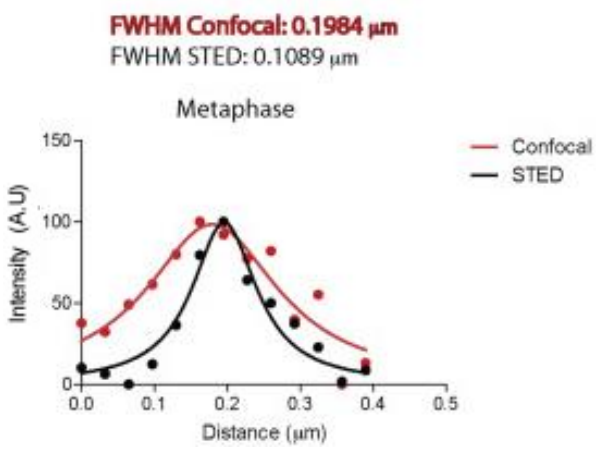

Fig. 4.5.: Comparison of confocal and STED images of apical microvilli.
(A) Grazing sections of confocal and STED images of the apical actin caps of syncytial nuclear cycle 12 at interphase and metaphase Scale bar: 5 µm. A section is zoomed in to show the apical microvilli and an ROI is drawn across a single microvillus and used to plot its intensity profile. Scale bar: 5 µm.
(B) Intensity profile of one microvillus at interphase obtained from confocal (red) and STED (black) imaging.
(C) Intensity profile of a microvillus at metaphase obtained from confocal (red) and STED (black) imaging.

We wanted to verify quantitatively if there was difference in the resolution of the microvilli post deconvolution of the STED images. For this we drew an ROI in the form of a straight line across the microvilli (Fig. 4.6. A) and used the plot profile option in imageJ to obtain the distribution of the intensity across the ROI as shown in the graphs (Fig. 4.6. B and C). We used the MATLAB code as mentioned in material and methods in order to obtain the Full-width half max (FWHM) values from the distribution. We plotted the curves and obtained the FWHM values, from STED and STED with deconvolution images of microvilli at interphase and metaphase of nuclear cycle12. The values obtained from STED with deconvolution images of the microvilli both at interphase and metaphase were both smaller than that of the STED images. This signifies that the microvilli were definitely better resolved using STED with deconvolution images as compared to STED images at 100X magnification.

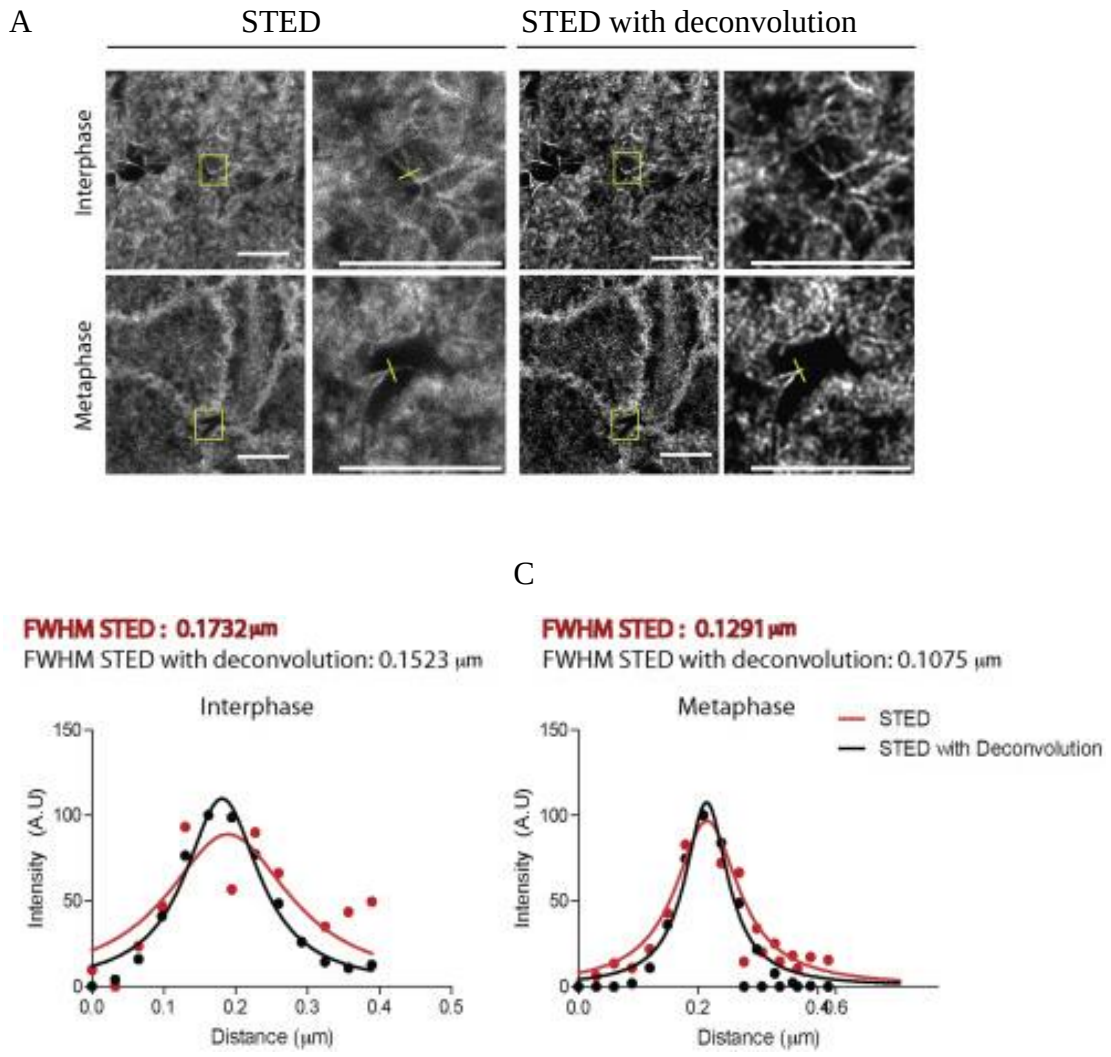

Fig. 4.6.: Comparison of STED and STED with deconvolution images of apical microvilli.
(A) Grazing sections of STED and STED with deconvolution images of the apical actin caps of syncytial nuclear cycle 12 at interphase and metaphase Scale bar: 5 µm. A section is zoomed in to show the apical microvilli and an ROI is drawn across a single microvillus and used to plot its intensity profile. Scale bar: 5 µm.
(B) Intensity profile of a microvillus at interphase obtained from STED imaging (red) and the STED image with deconvolution (black).
(C) Intensity profile of a microvillus at metaphase obtained from STED imaging (red) and the STED image with deconvolution (black).

We wanted to quantify the length and number of the microvilli at interphase and at metaphase in order to understand the microvilli remodelling across the nuclear cycle 12 from interphase to metaphase. To measure the microvilli length, we drew an ROI using the segmented line

along the microvilli (Fig.4.7. A). The measurement of length was noted down. The lengths of all the microvilli that could be observed in the single plane of focus were plotted for both interphase and metaphase. The number of such microvilli observed across the stages were also noted and plotted for both the stages. This was done for both STED and STED with deconvolution images. We observed a significant decrease in the length and number of the microvilli from interphase to metaphase in both STED and STED with deconvolution images (Fig.4.7. B-E).

A STED with Deconvolution

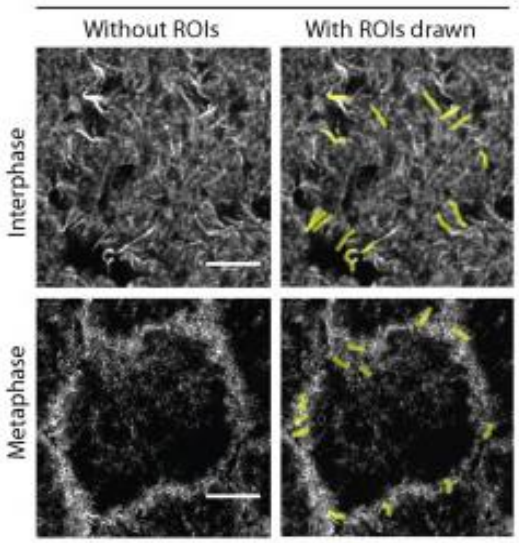

B STED with Deconvolution

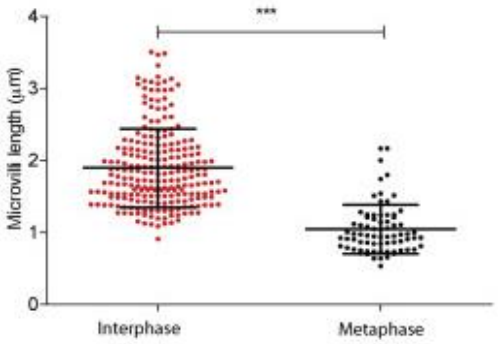

C STED with Deconvolution

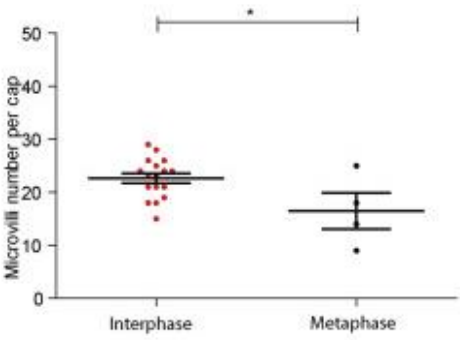

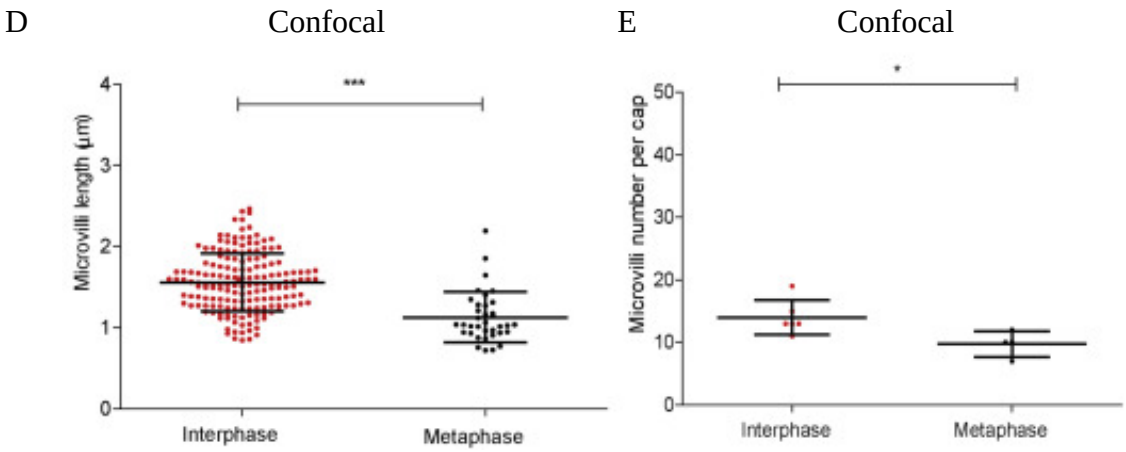

Fig. 4.7.: Quantification of microvilli lengths and numbers from deconvolved STED and confocal images.

(A) Grazing sections of Confocal and STED with deconvolution images of the apical actin caps of syncytial nuclear cycle 12 at interphase and metaphase Scale bar: 5 µm. ROIs are drawn across a single microvillus and used to plot the graphs. Scale bar: 5 µm.

(B, C) The lengths of microvilli (B) and numbers of microvilli per cap (C) are measured and plotted for interphase and metaphase in the deconvolved STED images. n= 2–4 cells each from 3 embryos. Data are represented as mean ± SD, ∗p<0.05, ∗∗p<0.01, and ∗∗∗p<0.001, two-tailed, unpaired Student's *t* test. Scale bar: 5 µm.

(D, E) Quantification of microvilli lengths and numbers using confocal images of apical actin caps in nuclear cycle 12 of the syncytial *Drosophila* embryo. The lengths of microvilli (D) and numbers of microvilli per cap (E) are measured and plotted for interphase and metaphase. n= 2–3 cells each from 3 embryos. Data are represented as mean ± SD, ∗p<0.05, ∗∗p<0.01, and ∗∗∗p<0.001, two-tailed, unpaired Student's *t* test. Note that the numbers of villi and their lengths are reduced in the confocal images in interphase as compared to deconvolved STED images with a significance of p<0.001 possibly due to the reduced resolution.

4.3.3. Loss of polarity protein, Bazooka, septin, Peanut and I-BAR protein Missing-in-Metastasis (MIM) in *Drosophila* syncytial embryos showed lack of microvilli remodelling

We checked the status of microvilli remodelling in Bazooka, Peanut and DMIM mutant embryos from interphase to metaphase of nuclear cycle12. We visualised microvilli by

labelling the cortical actin to fluorescently coupled Alexa fluor phalloidin 488 in fixed embryos. We used super-resolution STED microscopy to look at the microvilli. As previously observed, in (Sherlekar et al. 2020; Mitra et al. 2022), we found that in control embryos, the microvilli were enriched at the edges of the actin cap on the pseudo epithelial in interphase and were reduced in appearance in metaphase. In Bazooka, Peanut and DMIM depleted embryos (see materials and methods for the depletion methods), we observed a lack of microvilli remodelling. Loss of DMIM showed a more extensive lack of microvilli remodelling (Fig.4.8. A-B).

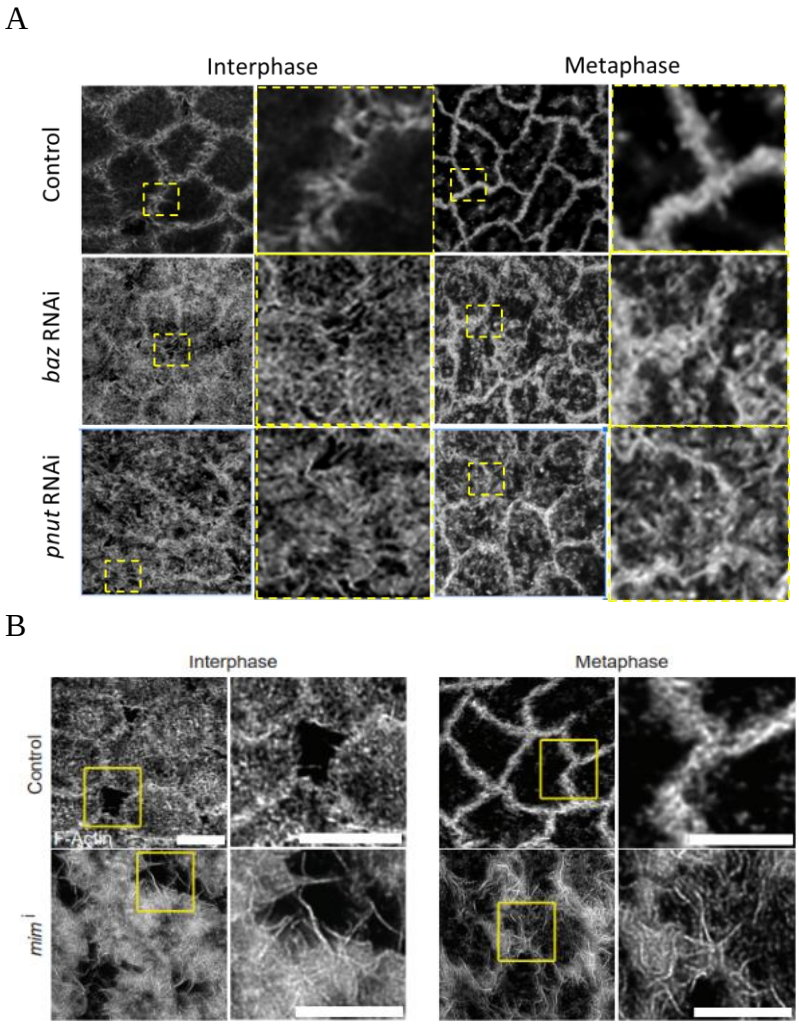

Fig. 4.8.: STED images showing the F-actin mediated microvillar protrusions at interphase and metaphase of nuclear cycle 12 for control, *baz* RNAi and *pnut* RNAi (A) and Control and *mim* RNAi (B). The region in the yellow box is further zoomed in to show the microvilli. Scale bar: 5 microns.

4.4. Discussion and conclusion

Standardising the protocol helped us to analyse the change in the microvilli width, length and number across different stages of development from nuclear cycle 10 to nuclear cycle 12. The microvilli at these stages of syncytial *Drosophila* blastoderm development are more prominent and less crowded as the cells are bigger and also show significant increase in area from interphase to metaphase. We also observed that at interphase the majority of microvilli protrude from the periphery of the cells, which reduce in length and number from interphase to metaphase. This quantification was possible from both confocal and STED images when imaged using 100x objective, although the FWHM analysis clearly showed that the structures were resolved better in the STED system as compared to the confocal images. Using this protocol to image the microvilli, allowed us to resolve the structures which were approximately 100-110 nm in width. The structures were resolved well enough such that quantification of their length and number was possible at the syncytial nuclear cycle 12, and we observed that remodelling of the microvilli takes place from interphase to metaphase of each nuclear cycle, which possibly fuels the growth of lateral furrow length. We therefore screened for the molecular regulators that could possibly regulate the microvilli remodelling. As discussed in the introduction chapter, 1.3. that polarity determining proteins and BAR domain proteins, could be the master regulators of the cell shape change through regulation of cellular trafficking, we chose to perturb Bazooka, Peanut and MIM and analyzed the structure, number and status of microvilli remodelling. We observed that the microvilli remodelling was perturbed in these mutant embryos, but it was perturbed extensively in the embryos depleted of Missing-in-Metastasis. As discussed in the introduction to this chapter, in cellularization embryos, the microvilli remodelling is regulated through tubular endocytosis and we have also observed in our lab that *shibire* mutants, where dynamin dependent endocytosis is perturbed, the microvilli remodelling in syncytial embryos is perturbed (unpublished results). Therefore, it is a possibility that in all of these mutants cellular trafficking is perturbed. We chose to analyze MIM further with respect to the mechanistic regulation of microvilli remodelling in syncytial *Drosophila* embryos.

Chapter 5: Missing-in-metastasis is a major protein regulating microvilli remodelling and cellular trafficking during the syncytial cycles of *Drosophila* embryos

5.1. Introduction

Drosophila syncytial embryos is an exceptional model to study cell shape remodelling during dynamic nuclear division cycles. As discussed previously in 1.4., in the syncytial cycles of the *Drosophila* embryogenesis, an actin cap is formed on top of each nucleus at interphase. This actin cap consists primarily of actin filaments and an excess of membrane reservoir present as microvilli-like protrusions made of bundled actin. These microvilli appear from the periphery of the caps and reduce in number and length as the cell progresses to metaphase, which is coincident with the formation and increase in length of the furrows. A special family of proteins that could regulate the cytoskeletal network to regulate cell shape remodelling are the BAR domain family of proteins. The BAR domain containing family of proteins might have a role in regulating the microvilli remodelling during the syncytial nuclear cycles through regulating endocytosis and interacting with the actin cytoskeleton and its nucleators. Here we characterise the role of an I-BAR domain containing protein Missing-in-Metastasis in syncytial *Drosophila* embryos (DMIM), in regulating the microvilli remodelling.

MIM was identified for the first time as a gene product that is possibly involved in invasion and metastasis in bladder cancer cells, through interaction with the actin cytoskeleton (Y.-G. Lee et al. 2002). It is a multidomain protein that contains an I-BAR domain at the N terminus, a central scaffold region containing a Proline Rich domain (PRD) and WH2 domain at the C terminus. The l-BAR domain enables its interaction with the phospholipids on the plasma membrane and acts as a scaffold for Rac1. PIP2 is known to promote the recruitment of MIM and subsequent assembly of the Arp2/3-mediated branched actin network (Saarikangas et al. 2015).

The different developmental roles of MIM were studied in mouse, *Drosophila* and *Xenopus.* The role of MIM in murine development was dispensable (Mattila et al. 2003). However, in another study mice depleted of MIM showed development of progressive kidney disease. MIM was found to localise to the adherens junctions at the cell boundaries through its I-BAR domain and recruit the actin filaments to the contacts thus regulating the maintenance of the integrity of kidney epithelial cells (Saarikangas et al. 2015). Depletion of MIM in mouse perturbs dynamics of actin cytoskeleton and endocytosis in mouse embryonic fibroblasts. Although there was no difference observed in filopodia number in fibroblasts depleted of MIM,

altered levels of Rac1 was observed (D. Yu et al. 2012). Loss of MIM during embryogenesis of *Xenopus laevis* resulted in defective anterior neural tube closure due to restructuring of actin cytoskeleton and apical constriction and interestingly here, Daam1, a formin was also found to be an interactor of MIM (W. Liu et al. 2011).

MIM-B isoform in mouse induces lamellipodia-like actin protrusions which requires the Rac activity. The IRSp53/MIM domain of MIM-B but not the WASP homology 2 motif binds and activates Rac. Therefore MIM-B is more of a scaffold protein that interacts with Rac and associated actin binding proteins to induce lamellipodia lie structures (Bompard et al. 2005). The PRD in the central scaffold region enables binding to the SH3 domain of other actin network regulator proteins like Cortactin. The WH2 domain allows the protein to regulate the actin cytoskeleton via an interaction with actin monomers (Mattila et al. 2003). Together, this hints at the fact that MIM might be a crucial activator and regulator of the Arp2/3 network and facilitate the formation of the branched actin network. MIM might regulate the cell shape regulators by regulating the branched actin network through promoting the Arp2/3 complex. This could be done by activating the Nucleation Promoting Factors (NPFs) like Scar/WAVE (Scar/WASP family verprolin-homologous protein). Together they are responsible for generating flat protrusion-like structures, called lamellipodia during neural crest cell migration, macrophage migration in *Drosophila* or neurons migrating along radial glia (Stramer et al. 2010; Moore et al. 2013; Cooper 2013; Krause and Gautreau 2014). While Scar/WAVE complex recruits the Arp2/3 network to the leading edge of the lamellipodia, WASP (N-WASP) and WASH NPFs recruit and activate the Arp2/3 complex at the clathrin-coated pits and the surface of endosomes (Mund et al. 2018);(Jin et al. 2022); (Krause and Gautreau 2014) to aid with endocytosis of cargoes like Delta to facilitate notch activation as observed in *Drosophila* (Trylinski and Schweisguth 2019). Force generated through the actin assembly is harnessed for mediating vesicle formation and scission during endocytic events (Qualmann, Kessels, and Kelly 2000). A special family of proteins that could activate this cytoskeletal network to regulate cell shape remodelling are the BAR domain family of proteins. Syndapin, a F-BAR domain containing protein is crucial for regulating the apical microvilli remodelling in syncytial *Drosophila* embryos and in its absence these protrusions are retained in the cells till metaphase (Sherlekar et al. 2020). It has also previously been shown that Syndapin is required for efficient endocytosis (Sherlekar and Rikhy 2016). BAR domain proteins under the regulation of small GTPases are known to activates Arp2/3 through WASP, like the *Drosophila* Cdc42-interacting protein 4 (Cip4), which is an effector of Cdc42, and also interacts with Dynamin facilitating E-cadherin endocytosis (Leibfried et al. 2008).

MIM or its homologue in vertebrates MTSS1 (Metastasis suppressor 1) along with IRSp53, a member of the same I-BAR domain family is known to regulate endocytosis by modulating the branched actin network and in some instances through the clathrin and dynamin-independent pathway (Fig. 5.1). MIM/ MTSS1 regulates the trafficking and internalisation of various cargoes (nanoparticles and receptors) through interacting with the actin cytoskeleton and Rab GTPases (Dan Yu et al. 2011; P. Zhao et al. 2016; Li et al. 2017; Sathe et al. 2018; P. Zhao et al. 2019; Y. Wang et al. 2023) (Table 5.1.) . These findings are interesting due to fact that the members of I-BAR domain family of proteins have always been known to induce protrusions or negative curvature membranes (H. Zhao, Pykäläinen, and Lappalainen 2011) and due to this nature also inhibit endocytosis (Quinones, Jin, and Oro 2010). However, it seems that the function of this intriguing gene product is contextual. It not only performs varying functions in a tissue specific manner but also depending on the density cells in a tissue (Dawson et al. 2012). Also as discussed in the introduction chapter 1.3.2. the two different structures, whether a protrusion or an invagination both show the presence of positively and negatively bent membrane curvature (Jones, Liu, and Cui 2020). During the formation of the endocytic pits or invaginations, the neck of the pits are the regions of negative architecture and there is a possibility that the I-BAR domain containing proteins and even MIM bind to that region.

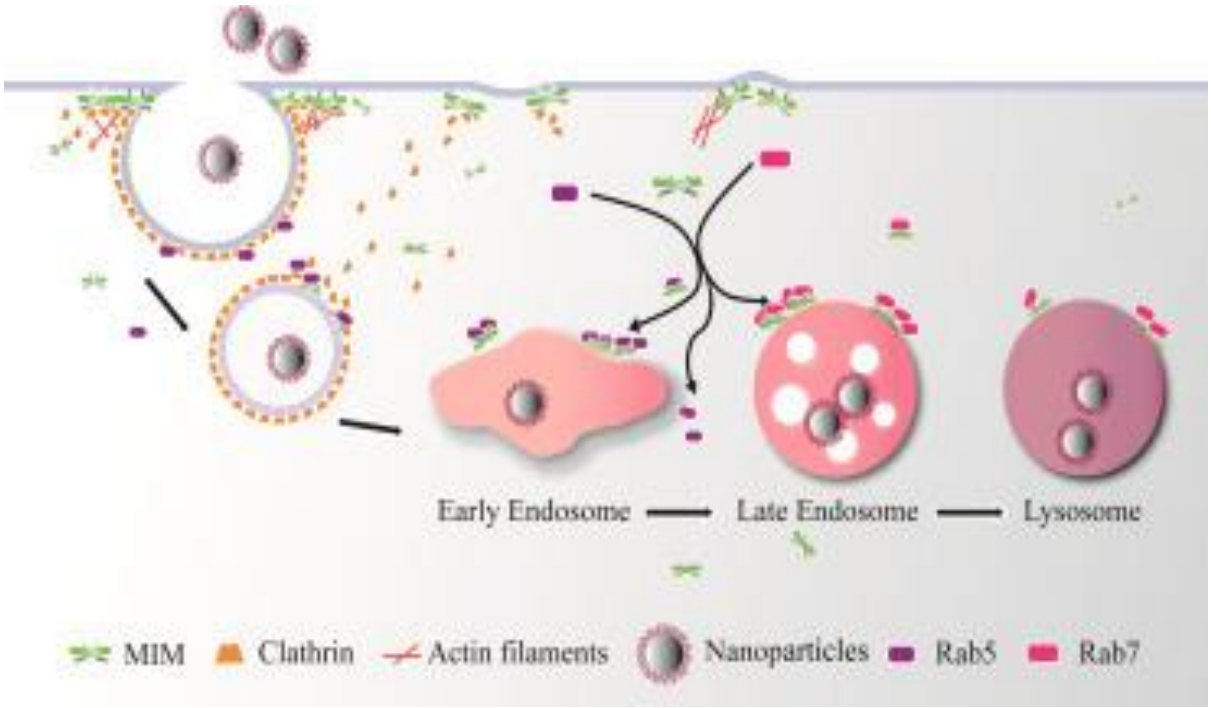

Fig. 5.1: Missing-in-metastasis promotes endocytosis of magnetic nanoparticles through clathrin light chain and Rab7 mediated pathway (P. Zhao et al. 2016).

Table 5.1: Literature showing the role of MIM/MTSS1 in regulating cellular trafficking

MIM / MTSS1 Promotes endocytosis	MIM / MTSS1 inhibits endocytosis	MIM / MTSS1 promotes/inhibits endocytosis
Murine Missing in Metastasis (MIM) mediates cell polarity and regulates the motility response to growth factors (Dan Yu et al. 2011)	I-BAR protein antagonism of endocytosis mediates directional sensing during guided cell migration (Quinones, Jin, and Oro 2010)	Mtss1 regulates epidermal growth factor signalling in head and neck squamous carcinoma cells (Dawson et al. 2012)
Small GTPases and BAR domain proteins regulate branched actin polymerisation for clathrin and dynamin-independent endocytosis (Sathe et al. 2018)		
Downregulation of MIM protein inhibits the cellular endocytosis process of magnetic nanoparticles in macrophages (P. Zhao et al. 2016)		
Missing-in-metastasis protein downregulates CXCR4 by promoting ubiquitylation and interaction with small Rab GTPases(Li et al. 2017)		
Differential interactions of missing in metastasis and insulin receptor tyrosine kinase substrate with RAB proteins in the endocytosis of CXCR4. (Li et al. 2019)		
Missing-in-metastasis protein promotes		

internalisation of magnetic nanoparticles via association with clathrin light chain and Rab7 (P. Zhao et al. 2019)		
MTSS1 curtails lung adenocarcinoma immune evasion by promoting AIP4-mediated PD-L1 monoubiquitination and lysosomal degradation (Y. Wang et al. 2023)		

In our findings, we observe that MIM localised to the plasma membrane promoting endocytosis and recruitment of actin-regulatory proteins Arp3, Cortactin and Scar at the cortex at a very specific time to regulate villi remodelling and furrow formation. We also found that activated Rac1 is essential for efficient localisation of MIM at the cortex region for villi remodelling and also regulating endocytosis. Hence, our studies find an essential role for MIM mediated regulation of villi remodelling in a spatio-temporal manner in early *Drosophila* embryogenesis.

5.2. Materials and methods:

Fly stocks

Refer to Chapter 2: Material and Methods section 2.1.

Embryo Immunostaining

Refer to Chapter 2: Material and Methods section 2.3.

Dye uptake assay

Refer to Chapter 2: Material and Methods section 2.4.

Microscopy

Refer to Chapter 2: Material and Methods section 2.5. and 2.6.

Super resolution imaging on STED

Refer to Chapter 2: Material and Methods section 2.7.

Image processing, quantification and analysis

Refer to Chapter 2: Material and Methods section 2.8.

5.3. Results

5.3.1. Depletion of DMIM leads to perturbed microvilli remodelling in the syncytial division cycles in *Drosophila* embryogenesis

We checked the status of microvilli length and number in *dmim* mutant and also if there was significant remodelling of the microvilli from interphase to metaphase of nuclear cycle12. We visualised microvilli by labelling the cortical actin to fluorescently coupled Alexa fluor phalloidin 488 in fixed embryos. We used super-resolution STED microscopy to look at the microvilli. As previously observed, in (Sherlekar et al. 2020; Mitra et al. 2022), we found that in control embryos, the microvilli were enriched at the edges of the actin cap on the pseudo epithelial in interphase and were significantly reduced in number and length in metaphase (Fig. 5.2.A) of syncytial nuclear cycle 12 . We used two different strategies to generate embryos depleted of DMIM - First strategy was to use shRNA expression against it and second, was a previously generated *dmim* mutant (Quinones, Jin, and Oro 2010). The *dmim* allele resulted from excision of a P transposon and has a deletion of most of the gene. It lacks the conserved I-BAR domain and much of the scaffolding domain and functions as a strong loss-of-function mutant (Quinones, Jin, and Oro 2010) (Fig. 5.2.A). *mim* shRNA (*mim*^{i}) was crossed to maternal Gal4 (see material and methods) to deplete MIM during oogenesis and embryogenesis (Fig. 5.2.A). Embryos from F1 females containing both the Gal4 and shRNA were collected and stained for F-actin. In *dmim* and *mim*^{i} expressing embryos the average microvilli length was

significantly more than the control in both interphase and metaphase (Fig.5.2. B-D, G-H). The mutant embryo also showed a significant increase in average microvilli numbers per cap as compared to controls in interphase and metaphase (Fig.5.2. B, D). There was also a reduced remodelling in the length and number of microvilli in the *dmim* and *mim*^{i} expressing embryos (Fig.5.2. B-D, G-H).

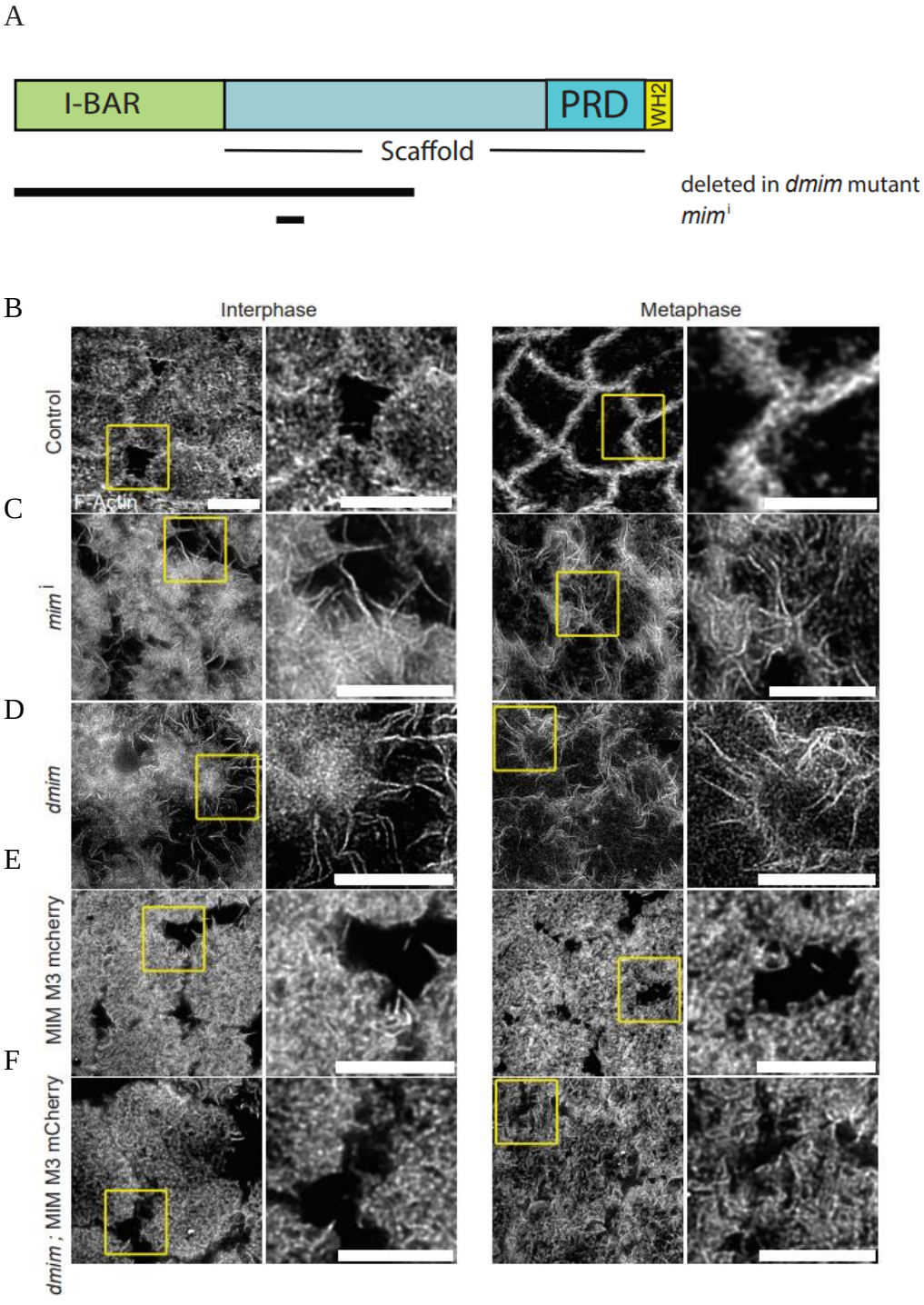

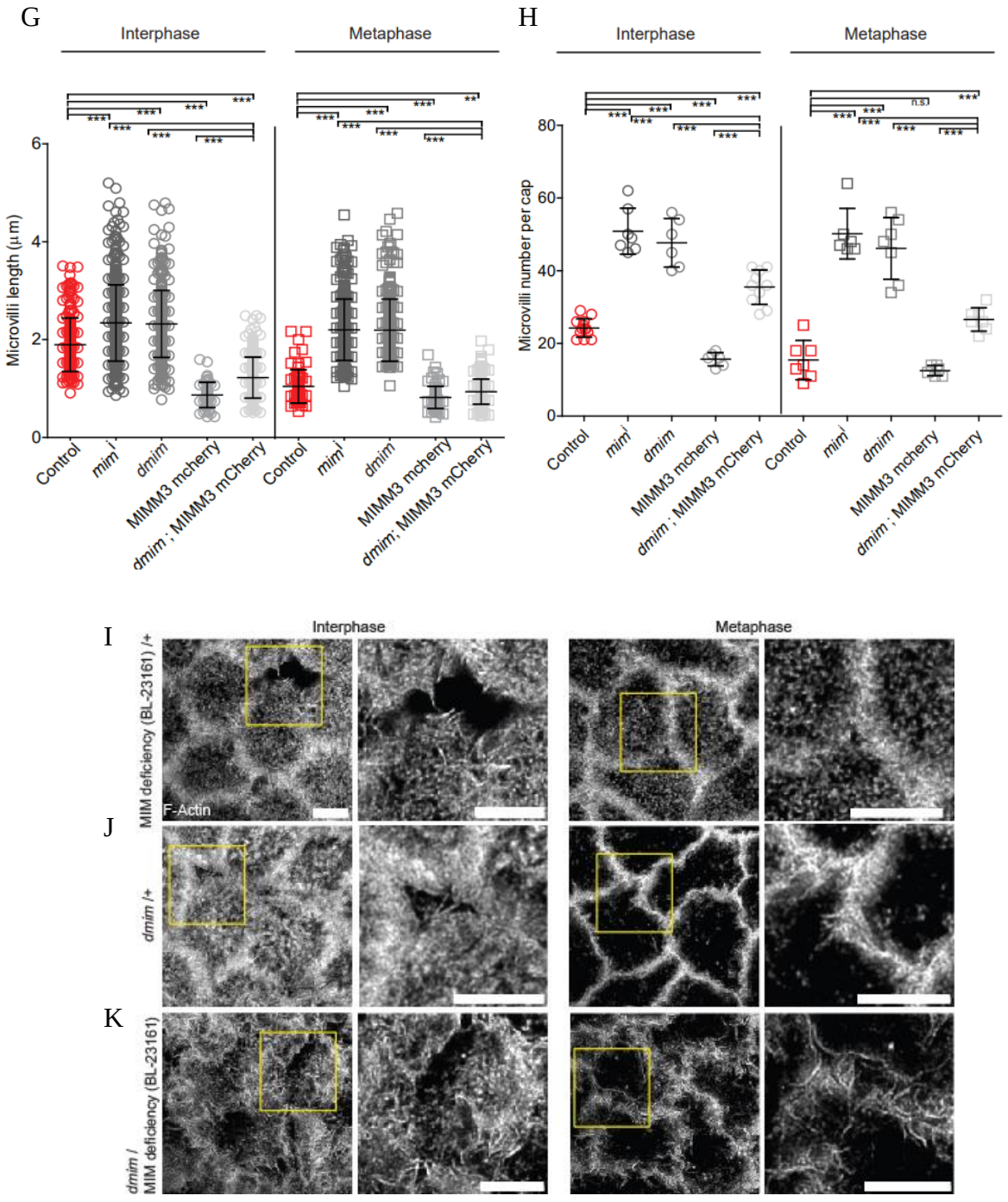

Fig. 5.2.: Depletion of DMIM leads to increased numbers and length and perturbed remodelling of microvilli in the syncytial nuclear cycle 12.

(A) Schematic showing the grazing and sagittal sections of pseudo-epithelial cells of syncytial *Drosophila* blastoderm embryo at interphase and metaphase.

(B-F) STED images showing the F-actin mediated microvillar protrusions at interphase and metaphase of nuclear cycle 12 for control, *mim* RNAi, *dmim*, MIM overexpression (NG4>UASp-mCherry-MIM M3), *dmim*; mCherry-MIM M3 embryos. The region in the yellow box is further zoomed in to show the microvilli.
(G-H) Graphs showing the microvilli length (G) and numbers per apical cap (H) at interphase and metaphase, n=2-3 cells from 3 embryos for each genotype. Data is represented as mean ± SD, $*p<0.05$, $**p<0.01$, and $***p<0.001$, two-tailed, unpaired Student's *t* test. Scale bar: 5 microns
(I-K) STED images showing the F-actin mediated microvillar protrusions at interphase and metaphase of nuclear cycle 12 in *dmim* / + (A), mim deficiency / + (B) and *dmim*; mim deficiency (BL-23161) (C) embryos. The region in the yellow box is further zoomed in to show the microvilli. Scale bar : 5 microns.

The MIM M3 isoform was overexpressed using maternal Gal4 lines during oogenesis and embryogenesis (see material and methods). Embryos were collected from the F1 females containing the UASp-mCherry-MIM M3 and maternal Gal4 together. They were further stained with fluorescently labelled phalloidin (see material and methods) for studying the microvilli remodelling. The average microvilli length and number in interphase and metaphase in MIM overexpression embryos was significantly lower than the control as well as the *dmim* embryos and embryos expressing *mim*^{i} (Fig.5.2.B,E, G-H). The excess microvilli that were observed in the *dmim* embryos both in interphase and metaphase, was rescued by combining it to the mCherry-MIM M3 (Fig. 5.2.B-F, G-H). The average microvilli length and number per cap at interphase in *dmim* ; mCherry-MIM M3 expressing embryos was significantly lower than that of the *dmim* embryos and *mim*^{i} expressing embryos in both interphase and metaphase (Fig. 5.2.B-F, G-H). In order to verify if the allele is indeed a DMIM loss-of-function mutant, we performed the complementation assay where we crossed the *dmim* females to DMIM Deficiency (BL-23161) males and the F1 flies with the genotype *dmim*/Def, were put in the cage and embryos were collected. Further they were stained with fluorescently labelled Alexa fluor 488 phalloidin to stain the cortical actin. As controls the embryos from *dmim*/+ and Def/+ were also processed (Fig. 5.2.I-K). The *dmim*/Def embryos showed a similar defect of increased microvilli length and number both in interphase and metaphase as was seen in DMIM depleted embryos in the combination, whereas the *dmim*/+ and Def/+embryos didn't show such severe microvilli remodelling defects (Fig. 5.2.I-K).

Overall, in the absence of MIM the microvillar protrusions increase in number and length at interphase and fail to remodel and reduce over time till metaphase. The over expression of MIM however limits the length and number of the microvillar protrusion significantly right from the beginning of the nuclear cycle 12 that is at interphase. Thus, the function of MIM is therefore likely to be involved in the limiting of the length and number of the microvillar protrusions as well as facilitate their remodelling to reduce the number per apical cap and length, from interphase to metaphase of nuclear cycle 12.

5.3.2. DMIM is responsible for regulation of apical actin cap and lateral furrow dynamics in the syncytial division cycle 12

As discussed in the introduction section, an apical actin cap is formed at the beginning of each interphase of the syncytial blastoderm cycles on top of each nucleus. This cap is primarily formed of branched and bundled F-actin and this actin as well as excess plasma membrane is stored as microvillar protrusions apically, that appear projecting mostly from its periphery. The plasma membrane remains folded along these microvillar protrusions and any fluorescent tags labelling the plasma membrane also marks the apical protrusions. As these microvilli remodel, the boundaries of the caps not only become taut but they also expand in their area, until they meet with their neighbours and form the lateral furrow. Following this there is a downward contractile force exerted by non-muscle myosin-II that helps in extension of the lateral furrows down towards the centre of the embryo. The furrow reaches its maximum length at metaphase where the area of the cells reaches their highest.

In Fig.5.3. A-C snapshots obtained from live imaging of embryos expressing tGPH are shown. In the tGPH tag the domain of the Steppke protein is fluorescently tagged to a GFP that binds to the PIP3 phospholipids which essentially labels the plasma membrane. This tagged-line was combined with 13.4 Mat-α-tub gal4 and maintained as a stable line. The other rnai and UASp lines were crossed to this tGPH::*matαtub gal4* 67; *matαtub gal4* 15 line to drive the downregulation and overexpression both during oogenesis and early embryogenesis. In tGPH::*matαtub gal4* 67; *matαtub gal4* 15(here onwards referred to as tGPH) /+ embryos the apical area increases from interphase to metaphase in the syncytial nuclear cycle 12 (Fig. 2A). The average area of the apical caps in the tGPH/+ embryos in the nuclear cycle 12 increases till metaphase (Fig.5.3. A-B). Also, at interphase the lateral furrow length gradually increases to its maximum at metaphase. The tGPH also marks the microvillar protrusions which are

present abundantly at interphase and gets reduced with the progression till metaphase along with the cell boundaries becoming tauter (Fig.5.3. A-B). In tGPH / *mim*^{i} expressing embryos, the average apical cell area was found to be significantly larger than the control at interphase and remained larger till metaphase (Fig.5.3. A-B, D). Along with expanded area, the cells were misshapen and possessed of a lot of protrusions present along the periphery of the apical actin caps (Fig.5.3. A-B). While in tGPH / + embryos these protrusions reduced over time, in the tGPH / *mim*^{i} expressing embryos, the remodelling was perturbed and the microvillar protrusions remained equally abundant from interphase to metaphase (Fig.5.3. A-B). In the tGPH / *mim*^{i} expressing embryos, the lateral furrow length remained much smaller with a length of at interphase and reached to a maximum of at metaphase as compared to the controls (Fig.5.3. A-B, E). The embryos expressing tGPH / mCherry-MIM M3 where MIM M3 isoform was overexpressed, showed a smaller apical cap area at interphase than the control embryos (Fig.5.3. A, C, D). The lateral furrow length of tGPH / mCherry-MIM M3 expressing embryos were comparable to the tGPH/+ embryos at interphase whereas the furrow remained only slightly shorter than the tGPH / + expressing embryos at metaphase (Fig.5.3. A, C, E). This showed that the cell boundaries were loose and irregularly shaped, possibly due to either a loss of tension and the cell membrane looked like it failed to remodel which also perturbed the furrow ingression.

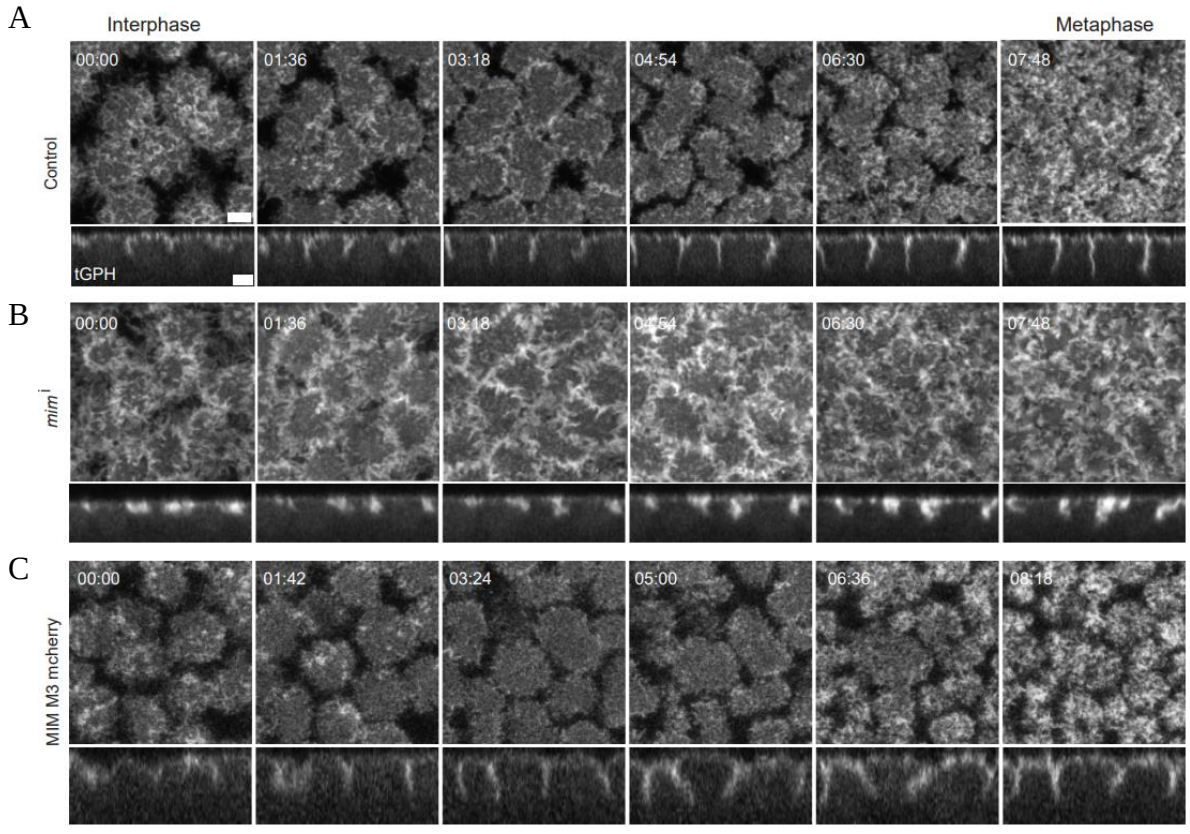

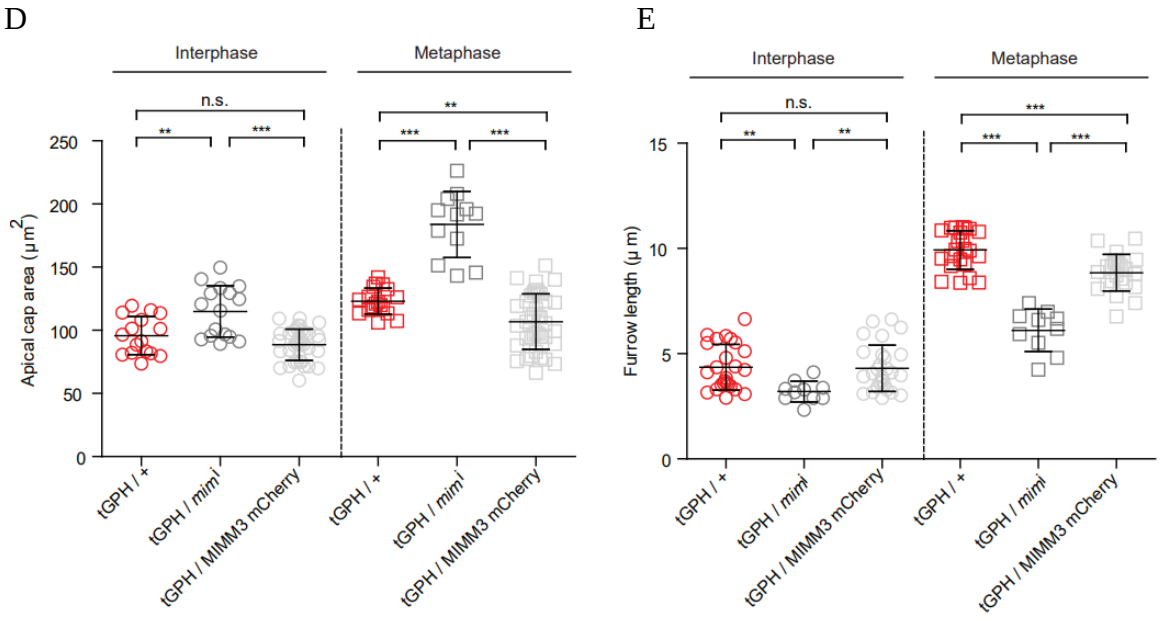

Fig. 5.3.: DMIM depletion leads to expanded cap area and shorter furrow length in syncytial nuclear cycle 12

(A-C) Timelapse images of the grazing and sagittal sections of the syncytial epithelial cells tagged with tGPH labelling the plasma membrane of control (A), *mim* RNAi (B) and mCherry-MIM M3 (C) embryos. (D-E) Graphs showing the quantification of apical cell area (D) and furrow length (E) at interphase and metaphase. n=5 cells from 3 embryos for each genotype. Data is represented as mean ± SD, ∗p<0.05, ∗∗p<0.01, and ∗∗∗p<0.001, two-tailed, unpaired Student's *t* test. Scale bar: 5 microns

5.3.3. DMIM is localised cortically at the cap and at the furrows with the help of its I-BAR domain, in interphase and becomes cytosolic at metaphase with the help of its WH2 domain.

In order to visualise the localization and recruitment of MIM in syncytial blastoderm embryos, we used a MIM M3 isoform tagged with mCherry at the C-terminal in UASp vector (see Materials and methods for more details). We expressed the mCherry-MIM M3 tagged line with maternal Gal4 (see Materials and methods) and with fluorescently labelled plasma membrane tag tGPH (*matαtub gal4* 67; *matαtub gal4* 15). The mCherry-MIM M3 and tGPH fluorescence was visualised together in syncytial blastoderm nuclear cycle 12. The time lapse

images show that mCherry-MIM M3 gets recruited to the cortical region where it localises at the cap on top of the nucleus and also at the lateral furrows in interphase to prophase and just as the nuclear cycle progresses to metaphase it becomes cytosolic. The membrane to cytosolic ratio of the mCherry-MIM M3 and tGPH intensities were quantified from a single optical plane and plotted across the different timepoints from interphase to metaphase (Fig.5.4. A-B).

A

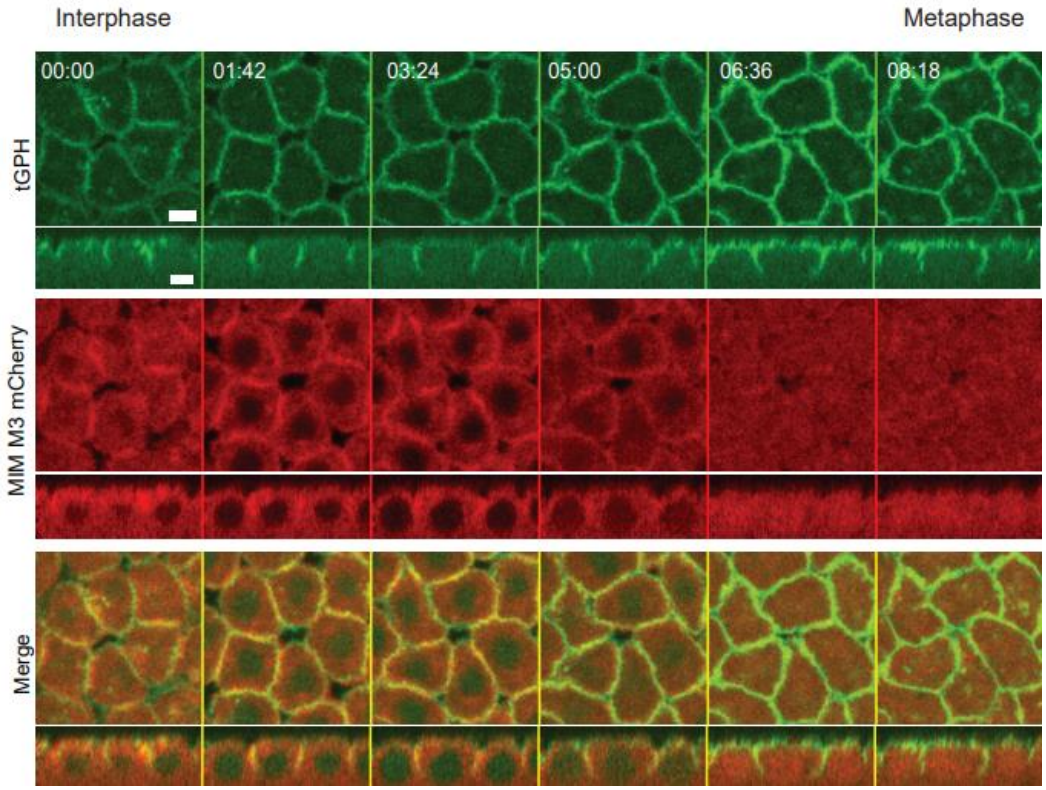

B

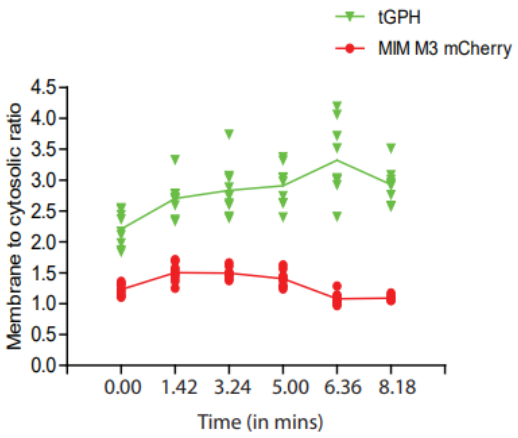

C

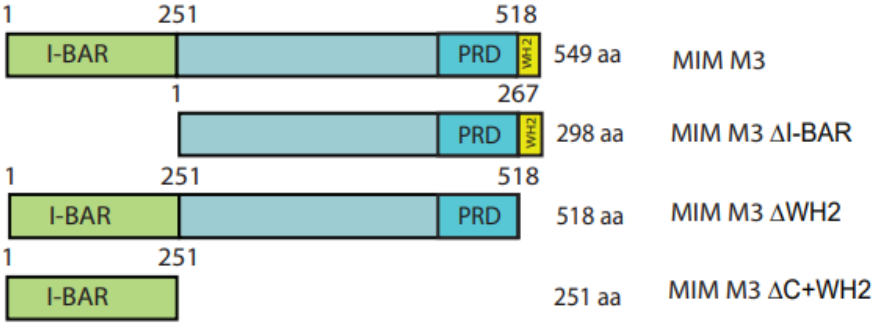
1
251
518
I-BAR
PRD
WH2
549 aa
MIM M3
1
267
PRD
WH2
298 aa
MIM M3 ΔI-BAR
1
251
518
I-BAR
PRD
518 aa
MIM M3 ΔWH2
1
251
I-BAR
251 aa
MIM M3 ΔC+WH2

D

E

F

G

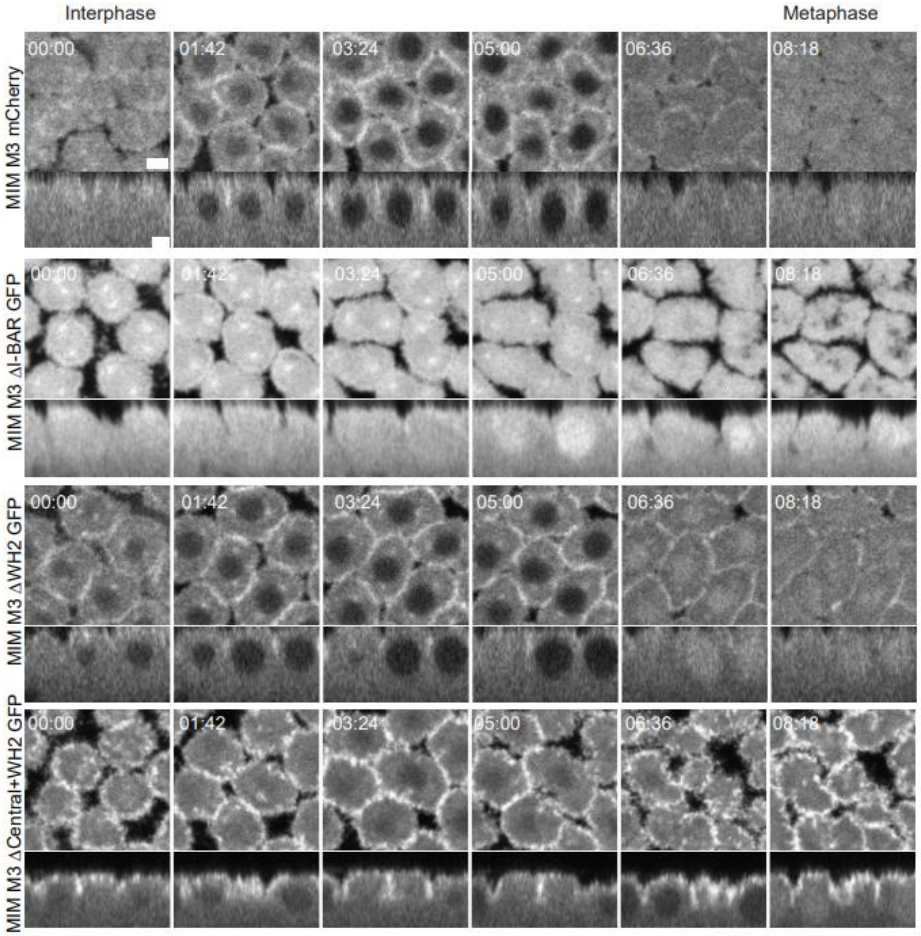
Interphase
Metaphase
MIM M3 mCherry
MIM M3 ΔI-BAR GFP
MIM M3 ΔWH2 GFP
MIM M3 ΔCentral+WH2 GFP
00:00
01:42
03:24
05:00
06:36
08:18

H

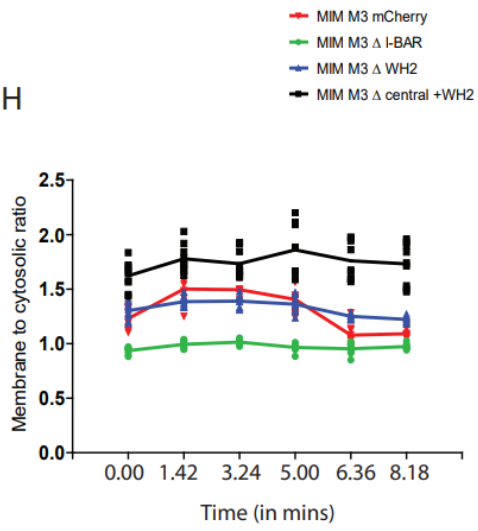
MIM M3 mCherry
MIM M3 Δ I-BAR
MIM M3 Δ WH2
MIM M3 Δ central +WH2
Membrane to cytosolic ratio
2.5
2.0
1.5
1.0
0.5
0.0
0.00
1.42
3.24
5.00
6.36
8.18
Time (in mins)

Fig. 5.4.: DMIM enriches cortically at the cap and furrow between interphase to prophase and becomes cytosolic in the metaphase stage of the syncytial cycle 12 with the help of its I-BAR and WH2 domain respectively. The cortical localisation is dependent on the presence of the I-BAR domain and the cytosolic distribution requires the central scaffold and WH2 domain.

(A) Timelapse images of the grazing and sagittal sections of the syncytial epithelial cells tagged with tGPH labelling the plasma membrane (green) and mCherry-MIM M3 (red) and both merged together. Scale bar: 5 microns.

(B) Quantification of the membrane to cytosolic ratio of mCherry-MIM M3 and tGPH, showing their distribution in the cells across time from interphase to metaphase. n= 3 cells from 3 embryos.

(C) Schematic of the domain deletion lines of MIM in order to show the domains present in each of the transgenic lines.

(D-G) Timelapse images of the grazing and sagittal sections of the syncytial epithelial cells tagged with mCherry-MIM M3 (B) GFP-MIM M3ΔI-BAR (C), GFP-MIM M3 ΔWH2 (D) and GFP-MIM M3ΔCentral+WH2 (E), showing their distribution. Scale bar: 5 microns.

(H) Quantification of the membrane to cytosolic ratio of mCherry-MIM M3 (B) GFP-MIM M3ΔI-BAR (C), GFP-MIM M3 ΔWH2 (D) and GFP-MIM M3ΔCentral+WH2 (E), showing their distribution, in the cells across time from interphase to metaphase. n= 3 cells from 3 embryos.

Further to study how the different domains are responsible for the recruitment of MIM, we used truncated domains of MIM M3 isoform tagged with GFP at the C-terminal in the UASp vector. The domain deletion lines were GFP-MIM M3ΔI-BAR, GFP-MIM M3ΔCentral+WH2 and GFP-MIM M3 ΔWH2 where the I-BAR domain, Central scaffold along with WH2 domain and only WH2 domain were deleted respectively (see Materials and methods for more details). We expressed the GFP tagged domain deletion lines with maternal Gal4 (see Materials and methods), and the fluorescence was visualized in syncytial blastoderm nuclear cycle 12. The time lapse images show that GFP-MIM M3ΔI-BAR does not get enriched at the cortical region and furrows from interphase to metaphase of the nuclear cycle but remains evenly distributed all over the cytosol compared to the mCherry-MIM M3 expression (Fig.5.4. D-E). However, both GFP-MIM M3ΔCentral+WH2 and GFP-MIM M3 ΔWH2 get enriched

at the cortical region and on the furrows from interphase to metaphase and they do not become cytosolic at metaphase as observed in the control embryos (Fig.5.4. F-G). The membrane to cytosolic ratio of the mCherry-MIM M3, GFP-MIM M3ΔI-BAR, GFP-MIM M3ΔCentral+WH2 and GFP-MIM M3 ΔWH2 intensities were quantified from a single optical plane and plotted across the different timepoints from interphase to metaphase (Fig.5.4.H).

This suggests that the I-BAR domain of MIM is essential for the protein to be recruited to the cortical region and the furrows whereas both the central and WH2 domain were required for MIM to become cytosolic at metaphase.

5.3.4. DMIM regulates the localization of key actin regulatory proteins in the syncytial division cycles

We tested the levels of Arp 2/3 complex in nuclear cycle 12 of DMIM depleted syncytial blastoderm embryos. We imaged the Arp3 distribution in fixed embryos of *dmim* mutant and *mim*^{i} expressing embryos using an antibody against Arp3. Immunostaining with Arp3 antibody showed that its levels were reduced significantly in both *dmim* mutant and *mim*^{i} expressing embryos both in interphase and metaphase. We quantified the membrane to cytosolic ratios of Arp3 intensity in both *dmim* mutant and *mim*^{i} expressing embryos and plotted it (Fig.5.5. A). The membrane to cytosolic ratio of Arp3 intensity in the DMIM depleted embryos showed significant reduction as compared to the control (Fig.5.5. B).

Further we tested if the levels of the Nucleation Promoting Factors (NPFs) like Scar/WAVE and stabiliser of Arp 2/3 network, Cortactin, were altered in embryos depleted of MIM. Cortactin levels were estimated in *mim*^{i} expressing embryos by immunostaining for Cortactin using an antibody. The enrichment of Cortactin levels were reduced from the cell cortex in MIM depletion embryos as compared to the control (Fig.5.5.C). We quantified the membrane to cytosolic ratios of cortactin intensity in *mim*^{i} expressing embryos at metaphase and plotted it. The membrane to cytosolic ratio of cortactin intensity in the DMIM depleted embryos showed significant reduction as compared to the control (Fig.5.5. D). Further, Scar/ WAVE levels were estimated in *dmim* embryos by immunostaining for Scar using an antibody. The enrichment of Scar levels was also reduced from the cell cortex in MIM depletion embryos as compared to the control (Fig.5.5. E).

We quantified the membrane to cytosolic ratios of Scar intensity in *dmim* mutant embryos at metaphase and plotted it. The membrane to cytosolic ratio of Arp3 intensity in the DMIM depleted embryos showed significant reduction as compared to the control (Fig.5.5. F).

A

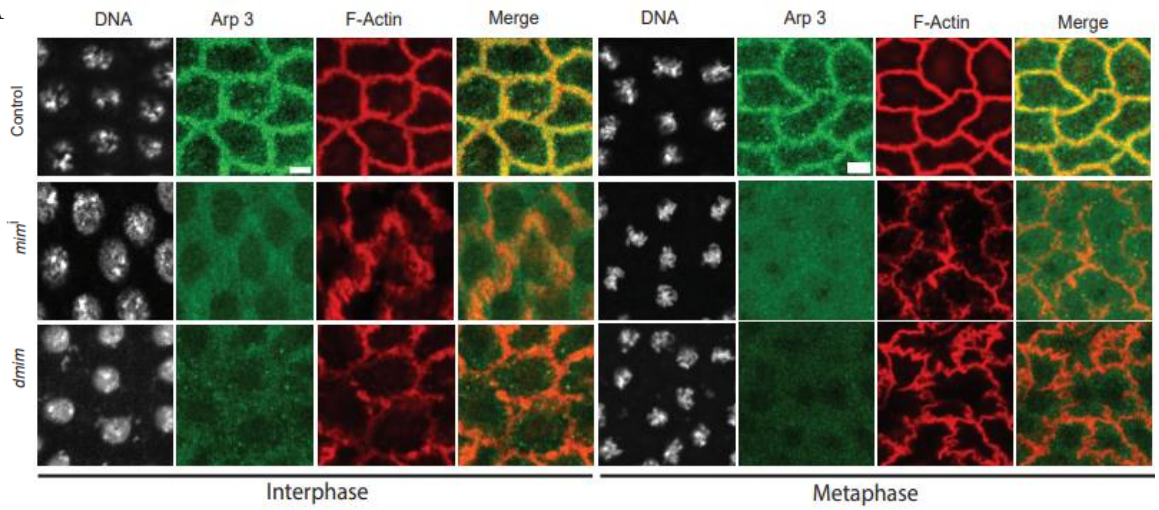
DNA
Arp 3
F-Actin
Merge
DNA
Arp 3
F-Actin
Merge
Control
mim-i
dmim
Interphase
Metaphase

B

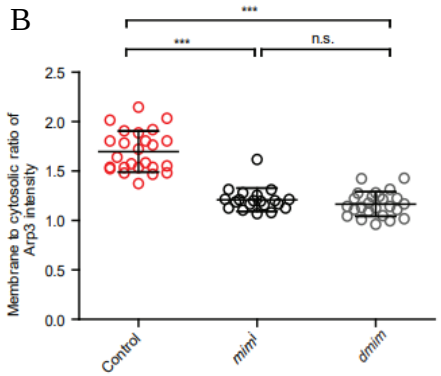
***
***
n.s.
Membrane to cytosolic ratio of Arp3 intensity
2.5
2.0
1.5
1.0
0.5
0.0
Control
mim-i
dmim

C

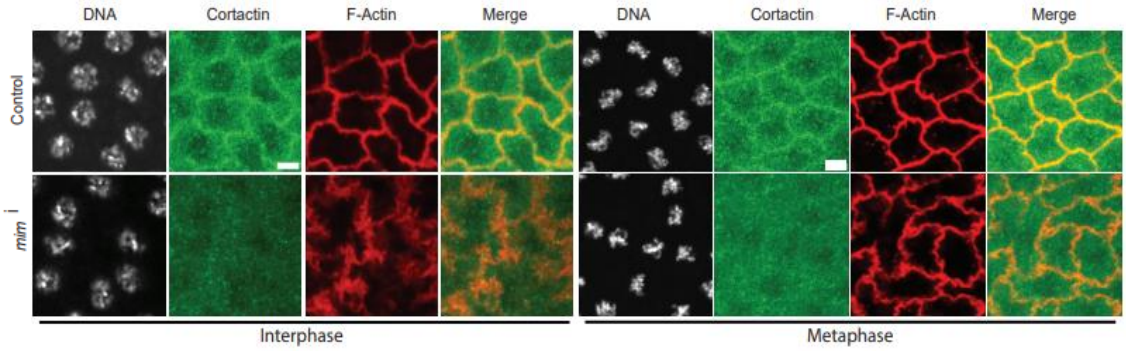
DNA
Cortactin
F-Actin
Merge
DNA
Cortactin
F-Actin
Merge
Control
mim-i
Interphase
Metaphase

D

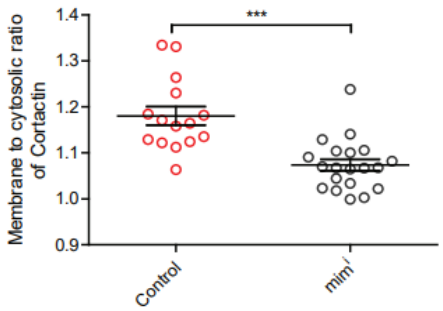
***
Membrane to cytosolic ratio of Cortactin
1.4
1.3
1.2
1.1
1.0
0.9
Control
mim-i

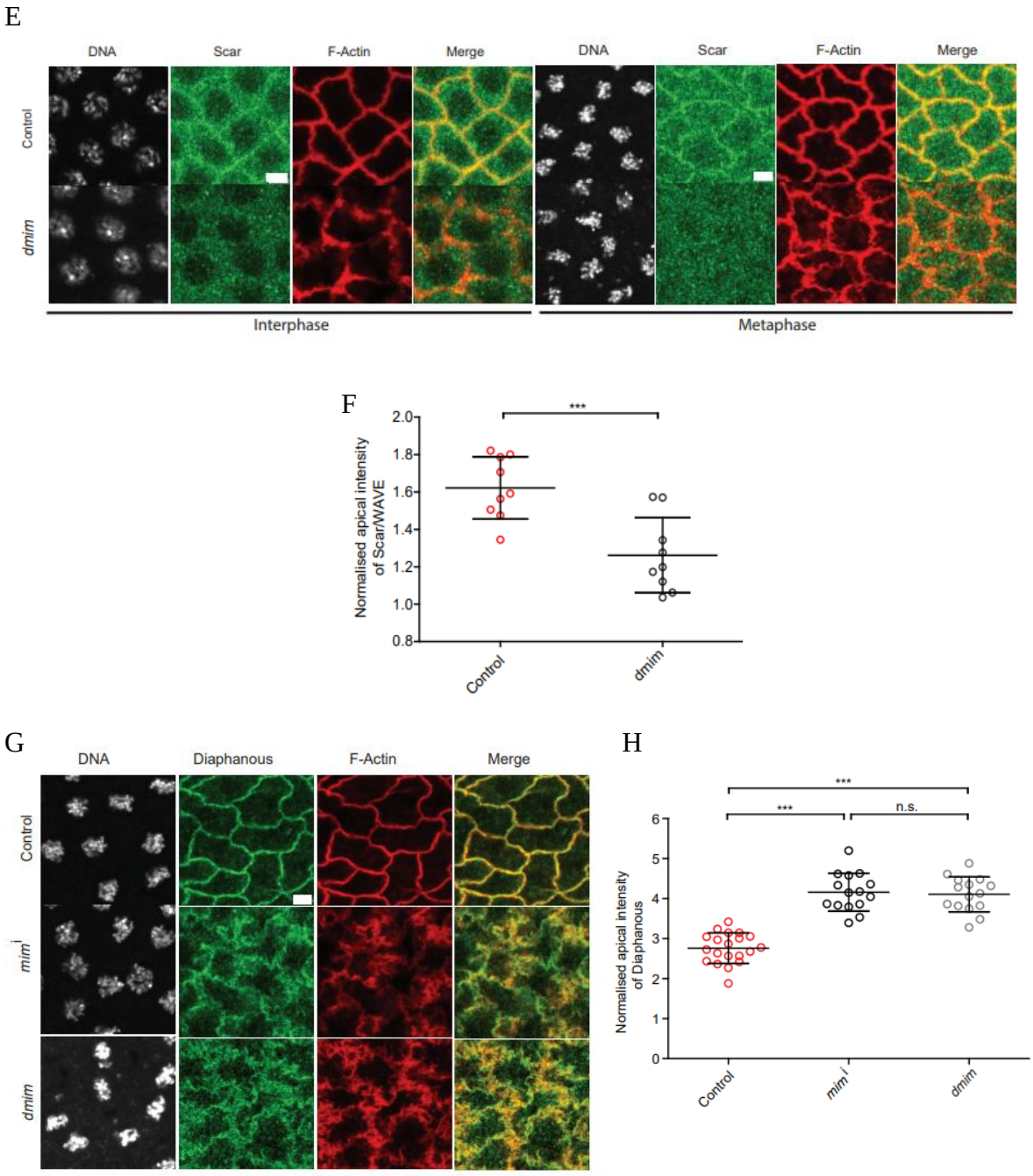

Fig. 5.5.: Depletion of DMIM leads to loss of Arp3, Scar and cortactin from the cell cortex and increase in apical Diaphanous intensity in the syncytial nuclear cycles.

(A) Grazing sections of cells showing nucleus labelled with Hoechst (grey), Arp2/3 network labelled with Arp3 (green) and cortical F-actin labelled with Alexa Fluor 568 (red) in interphase and metaphase in control, *mim*^{i} and *dmim* embryos.

(B) Graph showing the quantification of membrane to cytosolic ratio of Arp3 in control, *mim*^{i} and *dmim* embryos, n=5 cells from 3-4 embryos for each genotype. Data is represented as mean ± SD, ∗p<0.05, ∗∗p<0.01, and ∗∗∗p<0.001, two-tailed, unpaired Student's *t* test.

(C) Grazing sections of cells showing nucleus labelled with Hoechst (grey), Arp2/3 network activator Cortactin (green) and cortical F-actin labelled with Alexa Fluor 568 (red) in interphase and metaphase in control and *mim* RNAi embryos.
(D) Graph showing the quantification of membrane to cytosolic ratio of cortactin in control and *mim*^{i} embryos, n=5 cells from 3-4 embryos for each genotype. Data is represented as mean ± SD, $*p<0.05$, $**p<0.01$, and $***p<0.001$, two-tailed, unpaired Student's *t* test.
(E) Grazing sections of cells showing nucleus labelled with Hoechst (grey), Arp2/3 network activator Scar/WAVE (green) and cortical F-actin labelled with Alexa Fluor 568 (red) in control and *dmim* embryos.
(F) Graph showing the quantification of membrane to cytosolic ratio of Scar/WAVE in control and *dmim* embryos, n=3 cells from 3 embryos for each genotype. Data is represented as mean ± SD, $*p<0.05$, $**p<0.01$, and $***p<0.001$, two-tailed, unpaired Student's *t* test.
(G) Grazing sections of cells showing nucleus labelled with Hoechst (grey), bundled actin network labelled with Diaphanous (green) and cortical F-actin labelled with Alexa Fluor 568 (red) in control, *mim* RNAi and *dmim* embryos.
(H) Graph showing the quantification of normalised apical intensity of Diaphanous in control, *mim* RNAi and *dmim* embryos. n=5 cells from 3-4 embryos for each genotype. Data is represented as mean ± SD, $*p<0.05$, $**p<0.01$, and $***p<0.001$, two-tailed, unpaired Student's *t* test. Scale bar: 5 microns.

Thus, the activation and levels of the Arp 2/3 complex in the cell cortex was disrupted in DMIM depletion embryos. This could be the reason for reduced branched actin network and the presence of excess bundled actin network in the form of the excess microvilli network, as observed in DMIM depleted embryos. We therefore tested the levels of Diaphanous - a formin that regulates the formation of bundled actin structures in the actin caps in nuclear cycle 12 of *Drosophila* syncytial blastoderm (Jiang and Harris 2019) , in the embryos depleted of DMIM. We imaged the Diaphanous distribution in fixed *dmim* mutant and *mim*^{i} expressing embryos using an antibody. Immunostaining with Diaphanous antibody showed that its levels were increased apically all over the cap instead of only being restricted to the furrows in both *dmim* mutant and *mim*^{i} expressing embryos (Fig.5.5. G). We quantified the normalised apical intensity of Diaphanous and plotted it (See materials and methods). The normalised apical intensity of Diaphanous in the MIM depleted embryos showed significant increase as compared to the control (Fig.5.5.H).

In summary we observed that the Arp2/3 network activation was perturbed in DMIM mutant embryos, which could possibly be due to DMIM acting as a scaffold for Rac1 to activate its downstream interacting partners. In absence of DMIM, therefore there is a lack of branched actin network in the syncytial epithelial cells. However, the bundled network of actin is still existing and overtakes the existing architecture to form excess microvilli as compared to the control embryos.

5.3.5. MIM overexpression leads to increased endocytosis along with increased apical Arp2/3 and decreased Diaphanous levels

The MIM M3 isoform was overexpressed in the syncytial blastoderm stage by crossing the UASp-mCherry-MIM M3 to maternal Gal4 lines (see material and methods). Embryos were collected from the F1 females containing both the UASp-mCherry-MIM M3 and maternal Gal4. We further stained the embryos with anti-Arp3 antibody and tested if the levels of the Arp 2/3 complex changed in nuclear cycle 12 of MIM M3 overexpressing embryos. We imaged the Arp3 distribution in fixed embryos and its levels were increased apically all over the cap, in mCherry-MIM M3 expressing embryos, instead of only being restricted to the cortical region in the control embryos (Fig.5.6. A). We quantified the normalised apical intensity of Arp3 (see material and methods for more details) and it was significantly increased as compared to the control (Fig.5.6. B). We also analysed the distribution pattern of the Arp2/3 complex in the cortex of the syncytial epithelial cells. For this we drew an ROI with the help of a "segmented line" tool from imageJ and plotted the intensity profile across the length in the graph, for both phalloidin and Arp3. In the control embryos the peak intensity of Arp3 antibody staining co-localized with the peak intensity of phalloidin marking the cortical actin. However, in the embryos overexpressing mCherry-MIM M3, not only was the normalised intensity of Arp3 higher but also there was no sharp peak co-localizing with the cortical actin. Instead, the distribution of Arp 3 was more widely spread across the cortex, indicating an increase in the branched actin network during mCherry-MIM M3 overexpression (Fig.5.6.C-D).

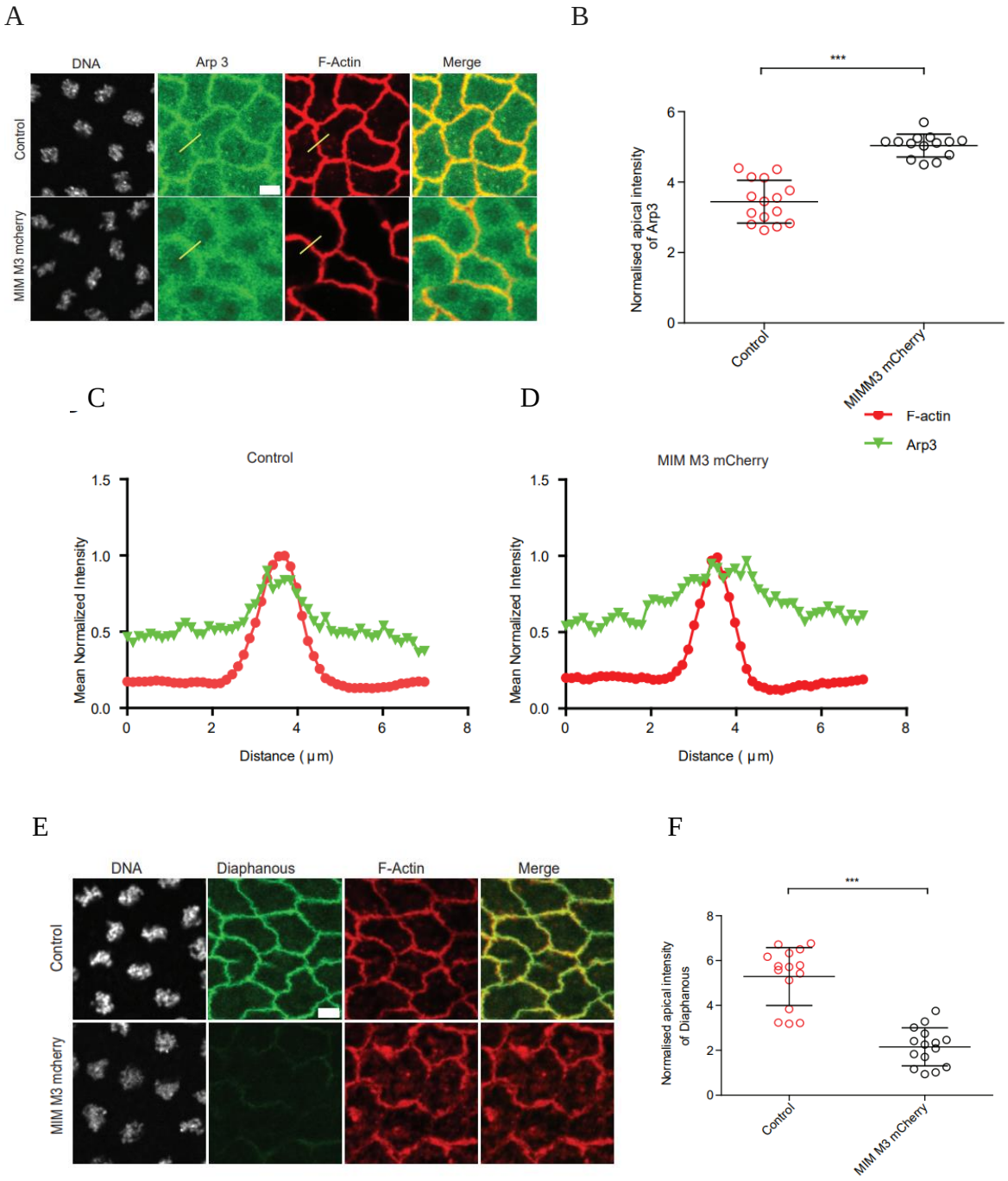

Fig. 5.6.: Overexpressing MIM increases Arp3 intensity and reduces Diaphanous in the syncytial division cycles.

(A) Grazing section of syncytial cells showing nucleus labelled with Hoechst (grey), Arp2/3 network labelled with Arp3 (green), cortical F-actin labelled with Alexa Fluor Phalloidin 647 (red) in control and mCherry-MIM M3 embryos.

(B) Graph showing the quantification of normalised apical intensity of Arp3 in control, and mCherry-MIM M3 embryos. n=5 cells from 3-4 embryos for each genotype. Data is

represented as mean ± SD, ∗p<0.05, ∗∗p<0.01, and ∗∗∗p<0.001, two-tailed, unpaired Student's *t* test.
(C-D) Graphs showing the relative distribution of Arp3 and F-actin along the line drawn across the cell boundary. Data is represented as the mean of 3-line profiles drawn across 3 edges, normalised to the maximum value, from 1 embryo.
(E) Grazing sections of cells showing nucleus labelled with Hoechst (grey), bundled actin network labelled with Diaphanous (green) and cortical F-actin labelled with Alexa Fluor 568 (red) in control and mCherry-MIM M3 embryos.
(F) Graph showing the quantification of normalised apical intensity of Diaphanous in control and mCherry-MIM M3 embryos. Data is represented as mean ± SD, ∗p<0.05, ∗∗p<0.01, and ∗∗∗p<0.001, two-tailed, unpaired Student's *t* test. Scale bar: 5 microns.

We therefore tested the levels of Diaphanous- a formin that regulates the formation of bundled actin structures, in nuclear cycle 12 of *Drosophila* syncytial blastoderm overexpressing mCherry-MIM M3. We imaged the Diaphanous distribution in fixed mCherry-MIM M3 expressing embryos using an antibody against Diaphanous and its levels were reduced from the cortical region (Fig.5.6. E). We quantified the membrane to cytosolic ratio of Diaphanous intensity and plotted it. The membrane to cytosolic ratio of Diaphanous intensity in the MIM depleted embryos showed significant reduction as compared to the control (Fig.5.6. F).

5.3.6. Arp2/3 complex and active Rac1 are crucial for regulating microvilli remodelling

We have already observed that a lack of DMIM led to reduction in the levels of Arp3 and its activators. We further wanted to test if the perturbation of the branched actin network could also lead to the excess of microvilli formation as we see in the mutants of DMIM. This would therefore signify, that absence of a branched actin network by itself can lead to a formation of excess of bundled actin network and hence excess of microvilli formation. We therefore tried to perturb the levels of Arp3 and also express the dominant-negative version of Rac1, which is the major activator of the Arp2/3 complex. The *arp3*^{i} was expressed during oogenesis and in the syncytial blastoderm stage by crossing it to maternal Gal4 lines (see material and methods). Embryos were collected from the F1 females containing both the *arp3*^{i} and maternal Gal4. We further stained the embryos with fluorescently labelled Alexa fluor 488

and used super-resolution STED microscopy to image the microvilli. In embryos expressing *arp3*^{i} the microvilli appeared to be extensively longer than the control both at interphase and at metaphase (Fig.5.7. A). We also stained these embryos with an antibody against Arp3 to test the level of its knockdown and found the cortical levels of Arp3 to be significantly reduced in the mutants as compared to the controls (Fig.5.7. B). We also stained them with an antibody against Diaphanous, to look at the level of the bundled actin network and found that the apical Diaphanous levels in the embryos expressing *arp3*^{i} to be more than that of the control embryos (Fig.5.7.C).

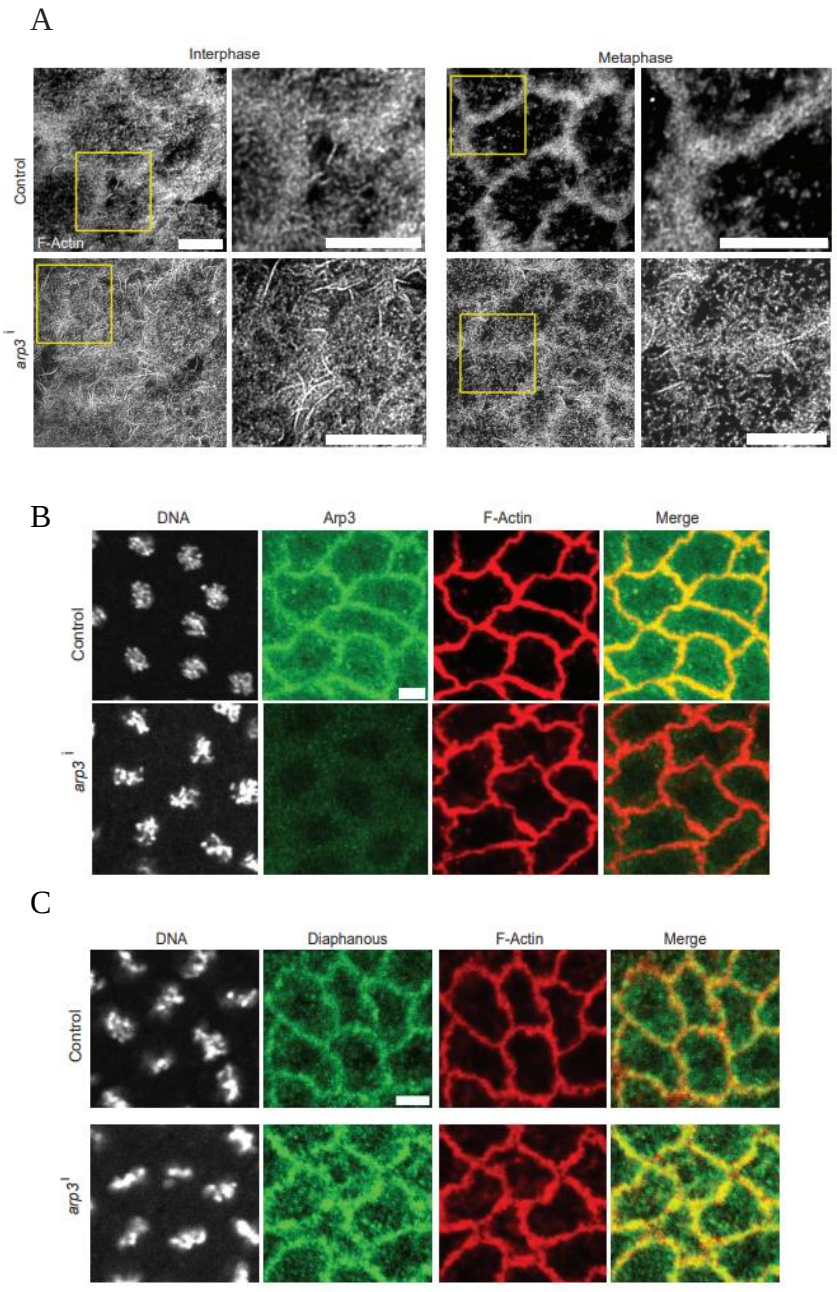

Fig. 5.7.: Arp3 knockdown leads to increased microvilli.
(A) STED images showing the F-actin mediated microvillar protrusions at interphase and metaphase of nuclear cycle 12 for control and *arp3*^{i} embryos. The region in the yellow box is further zoomed in to show the microvilli.
(B) Grazing section of syncytial cells showing nucleus labelled with Hoechst (grey), Arp2/3 network labelled with Arp3 (green), cortical F-actin labelled with Alexa Fluor Phalloidin 568 (red) in control and *arp3*^{i} embryos.
(C) Grazing sections of cells showing nucleus labelled with Hoechst (grey), bundled actin network labelled with Diaphanous (green) and cortical F-actin labelled with Alexa Fluor 568 (red) in control and *arp3*^{i} embryos. Scale bar: 5 microns.

In order to test if the activation of the Arp 2/3 network is crucial for regulation microvilli remodelling, we expressed *rac1*^{DN} in oogenesis and embryogenesis by crossing it to maternal Gal4 lines (see materials and methods). Embryos from F1 females containing Gal4 and *rac1*^{DN} (Dominant negative version of Rac1) were collected and stained for cortical F-actin with fluorescently labelled phalloidin. Phalloidin marked the apical actin cap and the microvilli which were observed using Stimulated Emission Depletion (STED) microscopy. In embryos expressing *rac1*^{DN} the microvilli number and length appeared to be significantly more than the control both at interphase and at metaphase (Fig.5.8. A-C). We also stained for Arp3 in the *rac1*^{DN} expressing embryos and found that the levels of Arp3 in was significantly reduced as compared to controls (Fig.5.8. D).

A

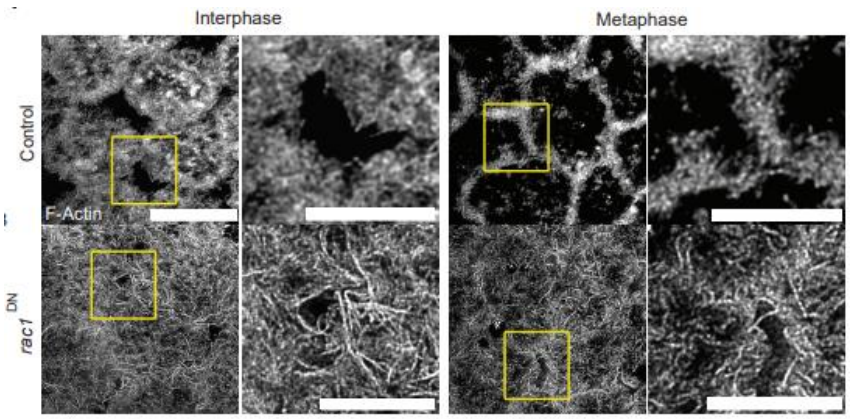

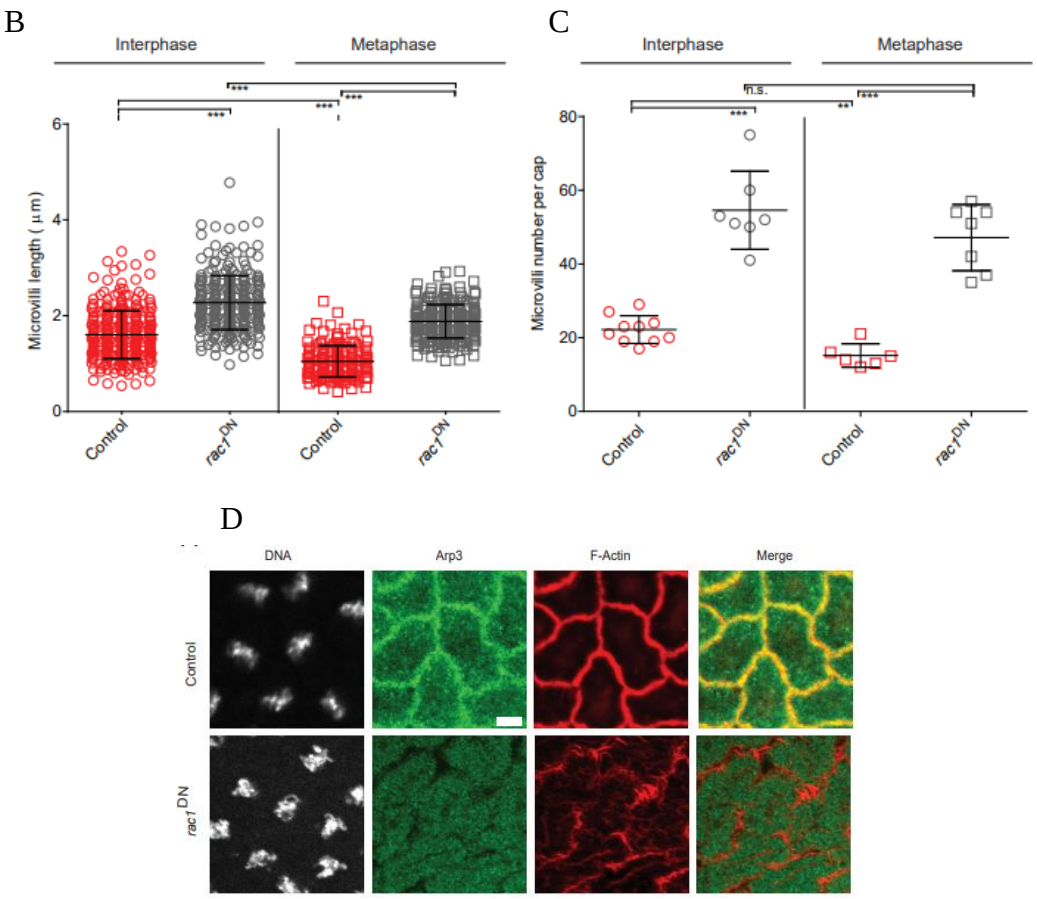

Fig. 5.8.: Active Rac1 is required to limit microvilli formation and regulate its remodelling. (A) STED images showing the F-actin mediated microvillar protrusions at interphase and metaphase of nuclear cycle 12 for control and *rac1*^{DN} embryos. The region in the yellow box is further zoomed in to show the microvilli.

(B-C) Graphs showing the microvilli length (B) and numbers per apical cap (C) at interphase and metaphase, n=3 cells from 3 embryos for each genotype. Data is represented as mean ± SD, ∗p<0.05, ∗∗p<0.01, and ∗∗∗p<0.001, two-tailed, unpaired Student's *t* test.

(D) Grazing section of syncytial cells showing nucleus labelled with Hoechst (grey), Arp2/3 network labelled with Arp3 (green), cortical F-actin labelled with Alexa Fluor Phalloidin 568 (red) in control and *rac1*^{DN} embryos.

Hence, it was clearly observed that perturbation of the Arp 2/3 complex and its activation leads to an increase in microvilli both at interphase and metaphase in the syncytial *Drosophila* embryos in nuclear cycle 12., which phenocopies the defects as observed in the embryo's mutant for DMIM. Hence, DMIM could possibly be a regulator of the Arp 2/3 complex mediated branched network though its interaction with the Rac1.

5.3.7. Activated Rac recruits MIM for affecting villi remodelling in a spatio-temporal manner in the syncytial division cycles

We further tested the epistatic interaction between Rac1 and DMIM, in order to understand if they interact mechanistically. We expressed *rac1*^{DN} and mCherry-MIM M3 together during oogenesis and embryogenesis, by crossing them to maternal gal4 lines. Embryos from F1 females containing Gal4, *rac1*^{DN} (Dominant negative version of Rac1) and mCherry-MIM M3 were collected and stained for cortical F-actin with fluorescently labelled phalloidin Alexa fluor 488. Phalloidin marked the apical actin cap and the microvilli which were observed using Stimulated Emission Depletion (STED) microscopy. In embryos expressing mCherry-MIM M3 and *rac1*^{DN} together with the maternal Gal4, the microvilli appeared to be extensively longer than the control embryos and mCherry-MIM M3 expressing embryos, both in interphase and metaphase (Fig.5.9. A-E). However, the microvilli appeared to be slightly shorter than the *rac1*^{DN} expressing embryos, both in interphase and at metaphase (Fig.5.9. A-E). The average microvilli number in *rac1*^{DN}; mCherry-MIM M3 expressing embryos were also significantly more than the mCherry-MIM M3 expressing embryos in interphase and metaphase and not significantly different from that of *rac1*^{DN} expressing embryos.

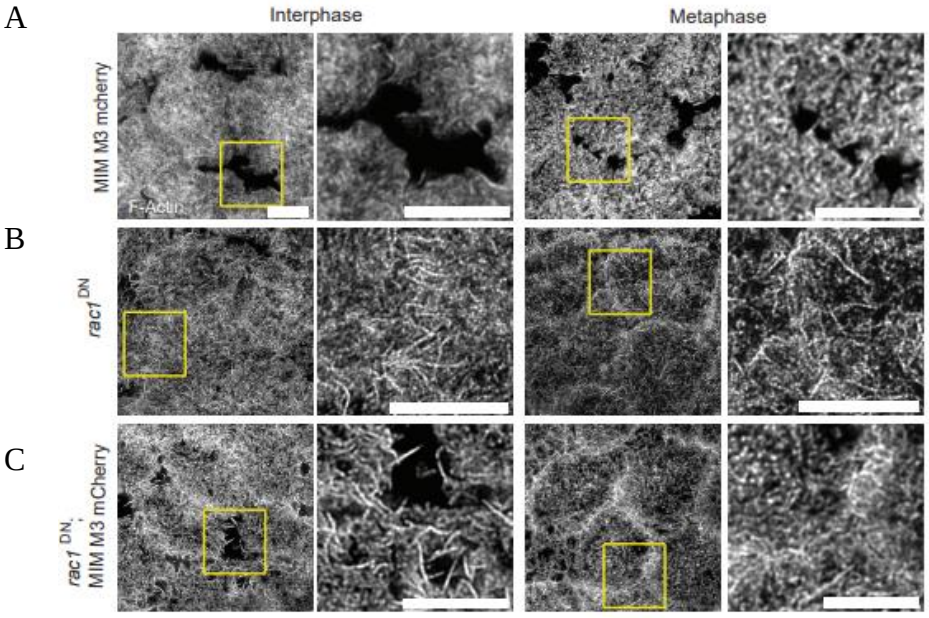

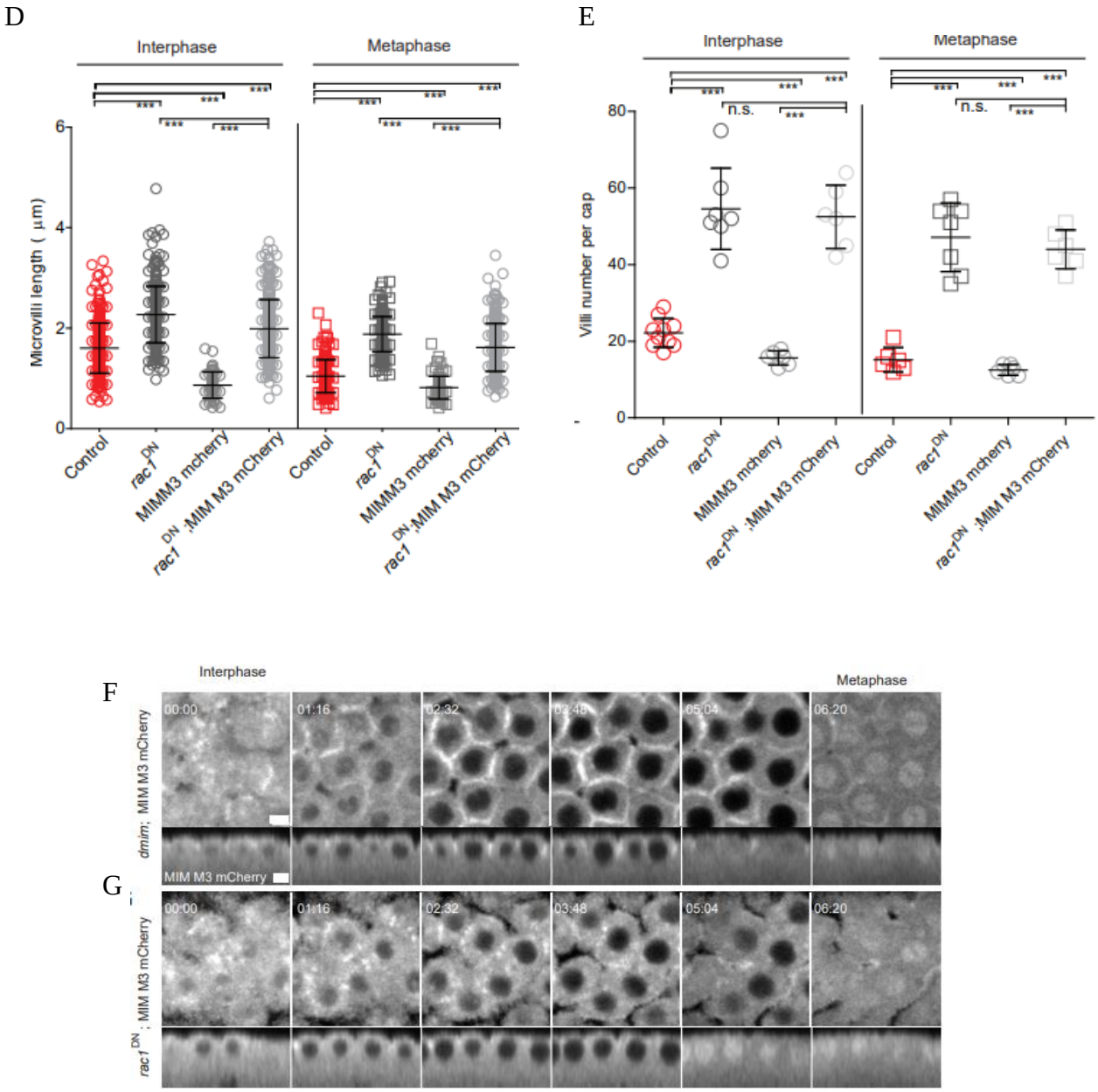

Fig. 5.9.: Active Rac1 regulates MIM recruitment to the plasma membrane during microvilli remodelling.

(A-C) STED images showing the F-actin mediated microvillar protrusions at interphase and metaphase of nuclear cycle 12 in (A) mCherry-MIM M3 embryos, (B) *rac1*^{DN} and (C) *rac1*^{DN} ; mCherry-MIM M3 embryos. The region in the yellow box is further zoomed in to show the microvilli.

(D-E) Graphs showing the microvilli length (D) and numbers per apical cap (E) at interphase and metaphase, n=3 cells from 3 embryos for each genotype. Data is represented as mean ± SD, ∗p<0.05, ∗∗p<0.01, and ∗∗∗p<0.001, two-tailed, unpaired Student's *t* test.

(F-G) Timelapse images of the grazing and sagittal sections of the syncytial epithelial cells showing the localisation of mCherry-MIM M3 in *dmim*: mCherry-MIM M3 and *rac1*^{DN} ; mCherry-MIM M3 embryos from interphase to metaphase of syncytial nuclear cycle 12. Scale bar: 5 microns.

Further we tested the localisation of mCherry-MIM M3 in embryos also expressing *rac1*^{DN}. *rac1*^{DN}; mCherry-MIM M3 expressing embryos showed mislocalization of mCherry-MIM M3 on the membrane as compared to the precise distribution of mCherry-MIM M3 on the plasma membrane in *dmim*; mCherry-MIM M3 (Fig.5.9. F-G). This signifies that active Rac1 might be crucial for proper localisation of MIM M3 on the plasma membrane. Such distribution of DMIM might be vital for ensuring efficient endocytosis and microvilli remodelling and mislocalized DMIM due to the embryos expressing *rac1*^{DN} is possibly leading to perturbed microvilli remodelling.

5.3.8. Diaphanous is necessary for inducing formation of the apical microvilli.

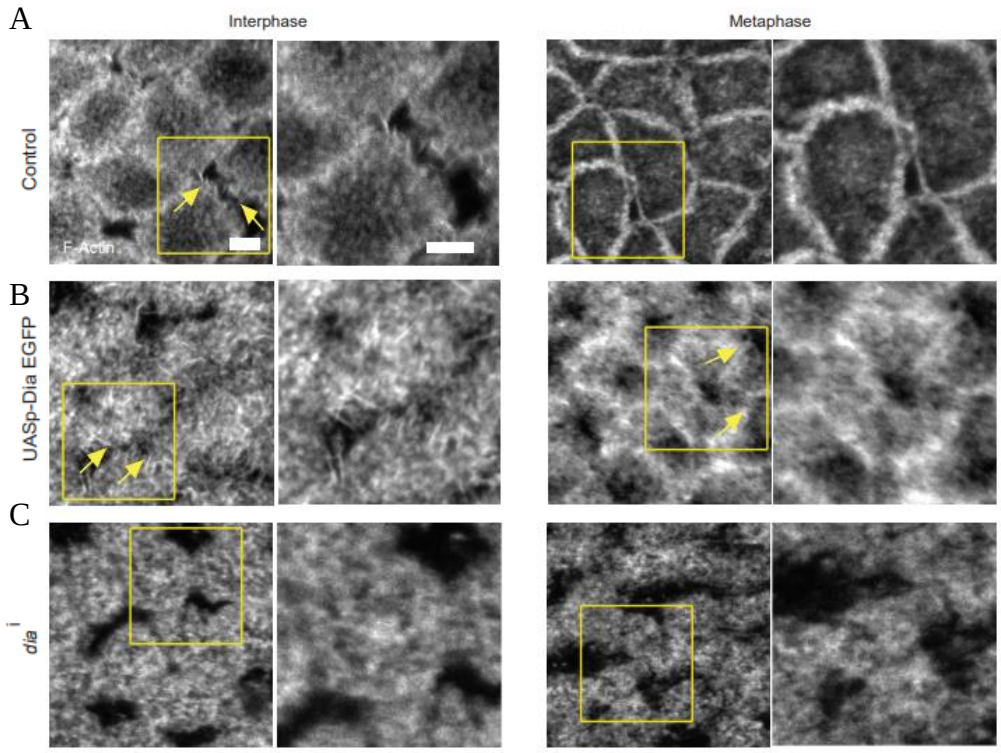

Fig. 5.10.: Diaphanous is necessary for inducing formation of the apical microvilli.

Confocal images showing the F-actin mediated microvillar protrusions at interphase and metaphase of nuclear cycle 12 for control (A), Dia overexpression (B) and *dia* RNAi (C). The region in the yellow box is further zoomed in to show the microvilli. Scale bar: 5 microns.

Since, lack of Arp 2/3 network led to both increase in the Diaphanous enriched bundled actin network and microvilli formation, we wanted to test if the presence of Diaphanous was essential for formation of microvilli. We expressed *dia*^{i} and Dia-EGFP during oogenesis and embryogenesis, by crossing them to maternal gal4 lines. Embryos from F1 females containing maternal Gal4 with *dia*^{i} and Dia-EGFP, were collected and stained for cortical F-actin with fluorescently labelled phalloidin. Phalloidin marked the apical actin cap and the microvillar protrusions which were observed using confocal microscopy. The reason for this being that only one laser for depletion in the STED system was available which was for 592 nm and the Dia-EGFP embryos could not be labelled with phalloidin 488 and imaged using STED, as it could lead to non-specific signal with a lot of background. In embryos from F1 females expressing maternal Gal4 and *dia*^{i} together, the microvilli appeared to be lesser or almost absent as compared to the control embryos both at interphase and metaphase. Whereas embryos expressing Dia-EGFP together showed excess microvilli both at interphase and at metaphase as compared to the control embryos (Fig.5.10. A-C).

5.3.9. DMIM and Rac1 mediated branched actin network have a crucial role in regulating endocytosis

We decided to analyse the endocytic machinery in *dmim* mutant embryos. We performed the dye uptake assay in the syncytial blastoderm embryos using the FM 1-43FX dye, a fixable analog of FM 1-43 membrane stain. The embryos were permeabilized with a detergent Citrasolv, followed by incubation with the dye for 15 minutes and fixation. The membrane probe is taken up into the cell through endosomes during the incubation with the dye. The embryos were further fixed, hand-devitellinized, mounted on a slide and imaged using a confocal microscope (see Materials and methods for more details). The vesicles taken up by the cells of the embryo were positive for the FM 1-43 dye, which absorbs in the range of 490-510 nm and initially emits at around 626-636 nm and in the 565-590 nm range upon membrane integration. In control embryos the cells showed numerous bright vesicle-like structures, positive for the FM 1-43 FX dye, mostly at the centre and a few at the cortex near the lateral

furrows of the cells (as marked with yellow arrows). These vesicles were reduced from the centre of the cells at metaphase but became enriched at the cortex of the cells. This probably could be the result of reduced endocytosis over time, from interphase to metaphase. In *dmim* mutant the fluorescence intensity of the dye in the vesicles was reduced (Fig.5.11. A) while the embryos over-expressing mCherry-MIM M3 showed increased intensity of the FM 1-43 FX dye as compared to the control both in interphase and metaphase (Fig.5.11. B).

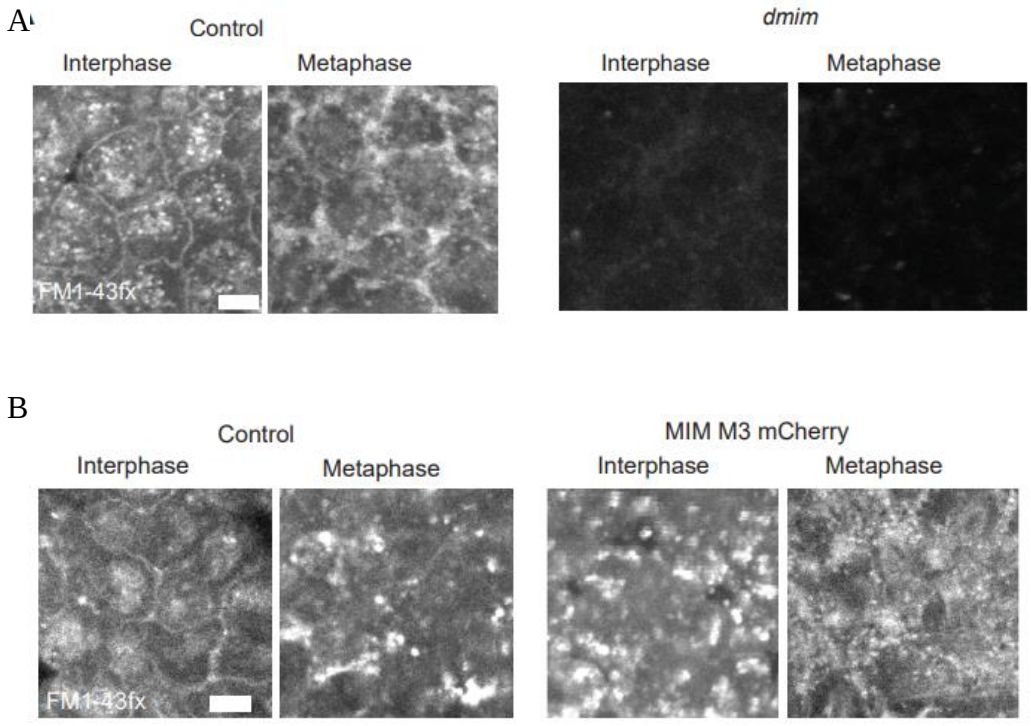

Fig. 5.11.: DMIM depletion leads to a decrease in uptake of FM1-43fx dye during the syncytial division cycles while over-expression of DMIM leads to increased uptake of the dye.
(A) Grazing sections of cells labelled with FM1-43fx dye at interphase and metaphase in control and *dmim* embryos.
(B) Grazing sections of cells labelled with FM1-43fx dye at interphase and metaphase in control and mCherry-MIM M3 embryos.

We checked the levels of Rab5 which marked the early endosomes with an anti-Rab5 antibody. The fluorescence intensity of Rab5 marked vesicles in the cytosol was reduced as compared to the control embryos. We also saw accumulations of Rab5 vesicles on the plasma membrane in *dmim* embryos (Fig. 5.21.A). This has been observed previously in polarity

protein Bazooka and septin Peanut mutants that lead to perturbed endocytosis. Further we checked the levels of Rab11 which marked the recycling endosomes with an anti-Rab11 antibody. In *dmim* embryos the intensity of Rab11 marked compartments was reduced as compared to the control embryos (Fig. 5.12.B). Since, the supply for recycling endosomes requires efficient endocytosis, the reduced intensity of Rab11 signified that there was lowered endocytosis and therefore reduced supply to the recycling endosomes.

A

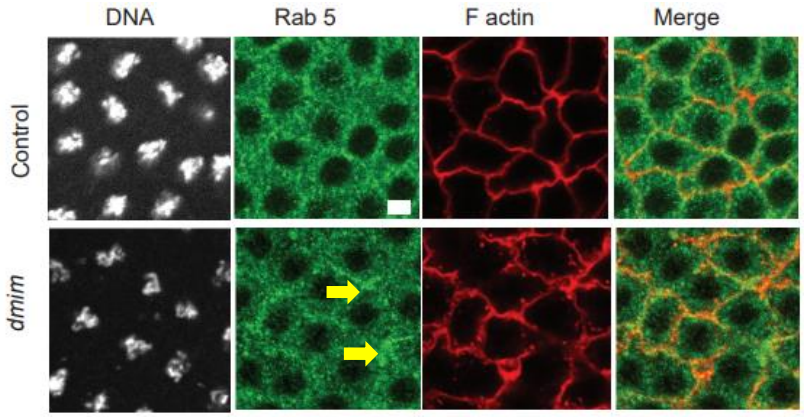

B

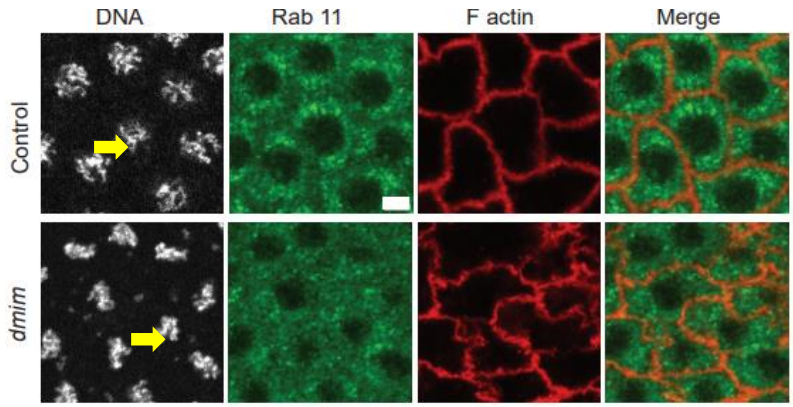

Fig. 5.12.: Rab5 and Rab11 intensity are lowered and their localisation is perturbed in DMIM depleted embryos.

(A) Grazing section of syncytial cells showing nucleus labelled with Hoechst (grey), early endosomes labelled with Rab5 (green), cortical F-actin labelled with Alexa Fluor Phalloidin 568 (red) in control and *dmim* embryos. In *dmim* embryos the Rab5 levels are lowered in the cytosol but accumulate on the plasma membrane (marked with yellow arrows).

(B) Grazing section showing cell's nucleus labelled with Hoechst (grey), recycling endosomes labelled with Rab11 (green), cortical F-actin labelled with Alexa Fluor Phalloidin

647 (red) in control and *dmim* embryos. In *dmim* embryos the intensity of Rab11 punctaes are lowered in the cytosol (marked with yellow arrows).

The levels of DE-cadherin at the plasma membrane can vary depending on the rates of endocytosis in *Drosophila* epithelial cells, as it is an important cargo that is dynamically trafficked during tissue remodelling events. Dynamin-mediated endocytosis in temperature-sensitive mutants of Dynamin, *shibire*, shows decreased endocytosis, perturbed furrow extension in the syncytial blastoderm embryo and accumulation of DE-cadherin at the furrow (Rikhy, Mavrakis, and Lippincott-Schwartz 2015).We have observed that reduced Rab5 mediated endocytosis in mutants of polarity proteins Par 3 homolog Bazooka and Septin Peanut, leads to accumulation of DE-cadherin at the furrow. We tested if DE-cadherin levels changed in DMIM depleted embryos. We hence imaged DE-cadherin distribution in live *mim*^{i} expressing embryos and fixed *dmim* embryos. DE-cadherin levels were estimated in *dmim* embryos by immunostaining for DE-cadherin using an antibody and expressing *ubi*-DE-cad-GFP in *mim*^{i} embryos. Immunostaining with a DE-cadherin antibody showed that DE-cadherin levels increased in the cell cortex, specifically on the plasma membrane in nuclear cycle 12 in *dmim* embryos as compared to controls (Fig. 5.13.A-B). *mim*^{i} embryos expressing DE-cad-GFP showed increased accumulation of DE-cad-GFP fluorescence on the plasma membrane, but a reduced number of DE-cad-GFP positive vesicles in the cytoplasm of the cells as compared to controls, from interphase to metaphase of nuclear cycle 12 (Fig. 5.13.C-D). To summarize, we observe that endocytosis was perturbed in embryos depleted of DMIM and this led to higher levels of DE-cadherin as compared to controls on the furrow in nuclear cycle 12.

A

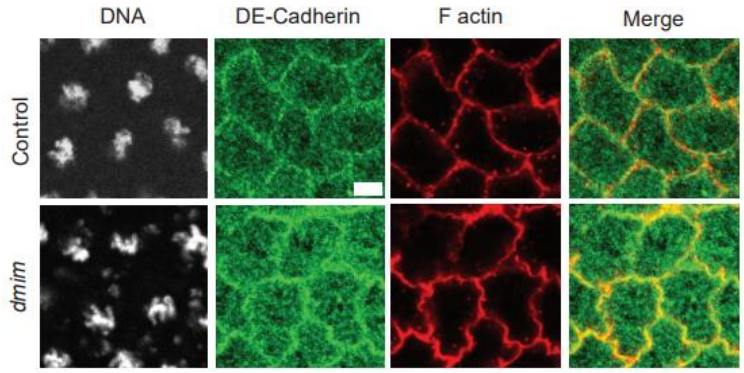

B

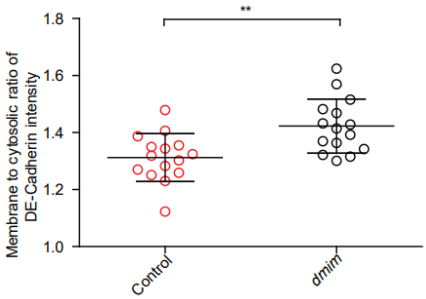

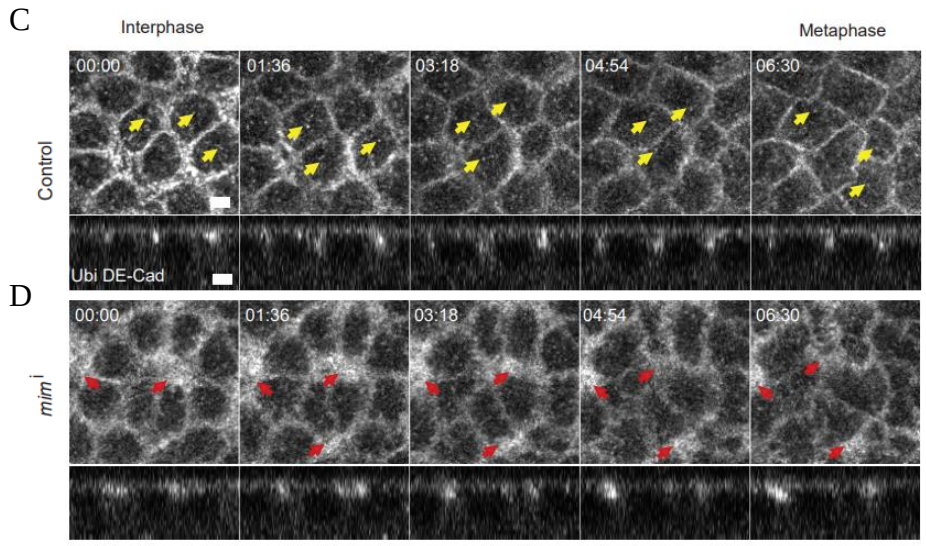

Fig. 5.13.: Endocytosis of DE-cadherin is downregulated in DMIM depleted embryos.
(A) Grazing section showing cells labelled nucleus labelled with Hoechst (grey), adhesion molecule DE-cadherin (green), cortical F-actin labelled with Alexa Fluor Phalloidin 568 (red) in control and *dmim* embryos.
(B) Graph showing quantification of the membrane to cytosolic ratio of DE-cadherin. n=5 cells from 3-4 embryos for each genotype. Data is represented as mean ± SD, ∗p<0.05, ∗∗p<0.01, and ∗∗∗p<0.001, two-tailed, unpaired Student's *t* test.
(C-D) Timelapse images of the grazing and sagittal sections of the syncytial epithelial cells tagged with Ubi DE-cadherin-GFP in control (F) and *mim* RNAi (G) embryos. Scale bar: 5 microns

We tested the levels of endocytic machinery in *rac1*^{DN} expressing embryos. We performed the dye uptake assay in the syncytial blastoderm embryos using the FM 1-43FX dye, a fixable analog of FM 1-43 membrane stain. In *rac1*^{DN} expressing embryos the fluorescence intensity of the dye in the vesicles were reduced along with their numbers as compared to the control embryos (Fig.5.14. A). As discussed previously, levels of DE-cadherin at the plasma membrane can vary depending on the rates of endocytosis and therefore we decided to check the levels of DE-cadherin in *rac1*^{DN} embryos by immunostaining for DE-cadherin using an antibody. Immunostaining with a DE-cadherin antibody showed that DE-cadherin levels increased on the furrow in nuclear cycle 12 in *rac1*^{DN} expressing embryos as compared to controls (Fig.5.14. B-C).

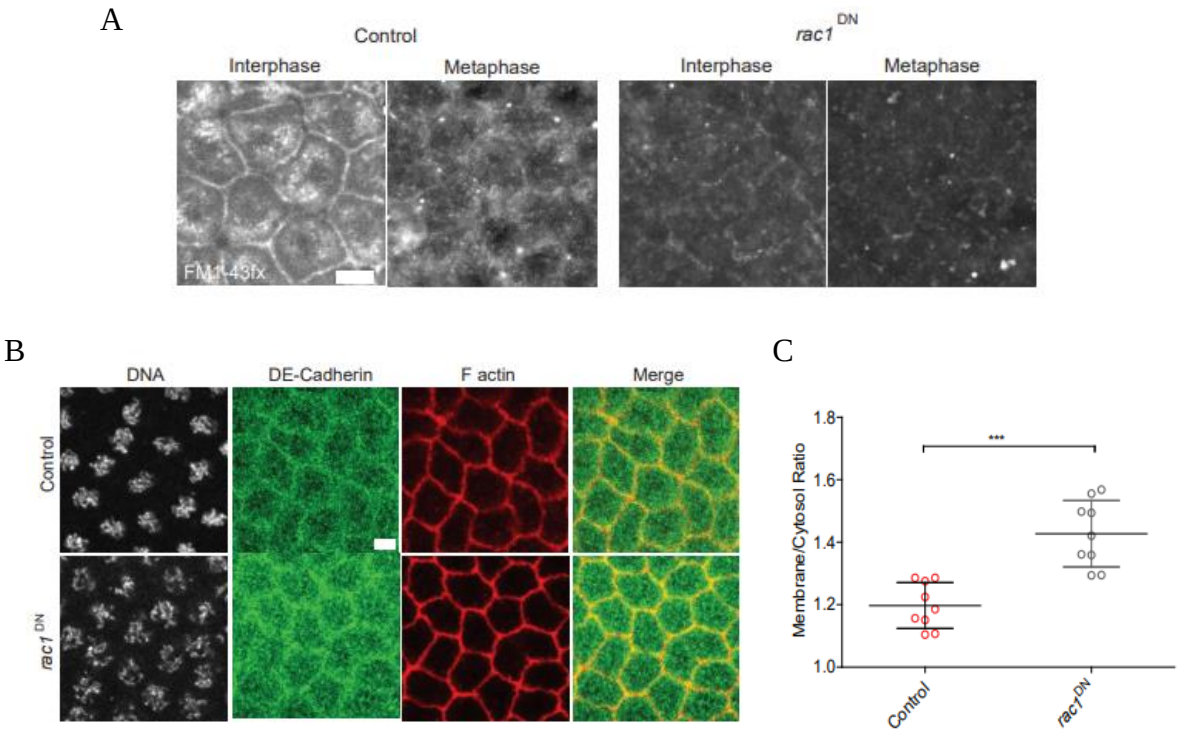

Fig. 5.14.: Endocytosis is downregulated in *rac1*^{DN} embryos.

(A) Grazing sections of cells labelled with FM1-43fx dye at interphase and metaphase in control and *rac1*^{DN} embryos.

(B) Grazing section of syncytial cells showing nucleus labelled with Hoechst (grey), adhesion molecule DE-cadherin (green), cortical F-actin labelled with Alexa Fluor Phalloidin 568 (red) in control and *rac1*^{DN} embryos.

(C) Graph showing the quantification of the membrane to cytosolic ratio of DE-cadherin levels. n=5 cells from 3-4 embryos for each genotype. Data is represented as mean ± SD, ∗p<0.05, ∗∗p<0.01, and ∗∗∗p<0.001, two-tailed, unpaired Student's *t* test. Scale Bar: 5 microns

The small GTPase molecule Rac1 in its active form is a promoter of the Wave Regulatory Complex (WRC), and together with DMIM, active Rac1 and WRC, the Arp 2/3 network gets activated and enriched on the plasma membrane. To understand if there is a hierarchy between the rac1- dependent Arp 2/3 network mediated actin polymerization and DMIM, we tested the endocytosis and the localization of DMIM in Arp and rac1 mutant embryos. We have expressed the MIM M3 mCherry together with the *arp3* ^{i} (Fig. 3) and *rac1*^{DN} (Fig. 5.9., in thesis). Simultaneously, we have also immunostained the *arp3* ^{i} and *rac1*^{DN} expressing

embryos with the antibody against DMIM (Fig. 4). We have observed that MIM, both the tagged line as well as the antibody marking the endogenous DMIM gets mislocalised and its enrichment on the plasma membrane is lost. We had earlier observed that in embryos mutant for MIM, there is a loss of Arp 3 from the plasma membrane (Fig. 5.5., in thesis). However, endocytosis was reduced in both *arp3* ^{i} (Fig. 2) and *rac1*^{DN} (Fig. 5.14., in thesis) embryos, similar to embryos mutant for MIM.

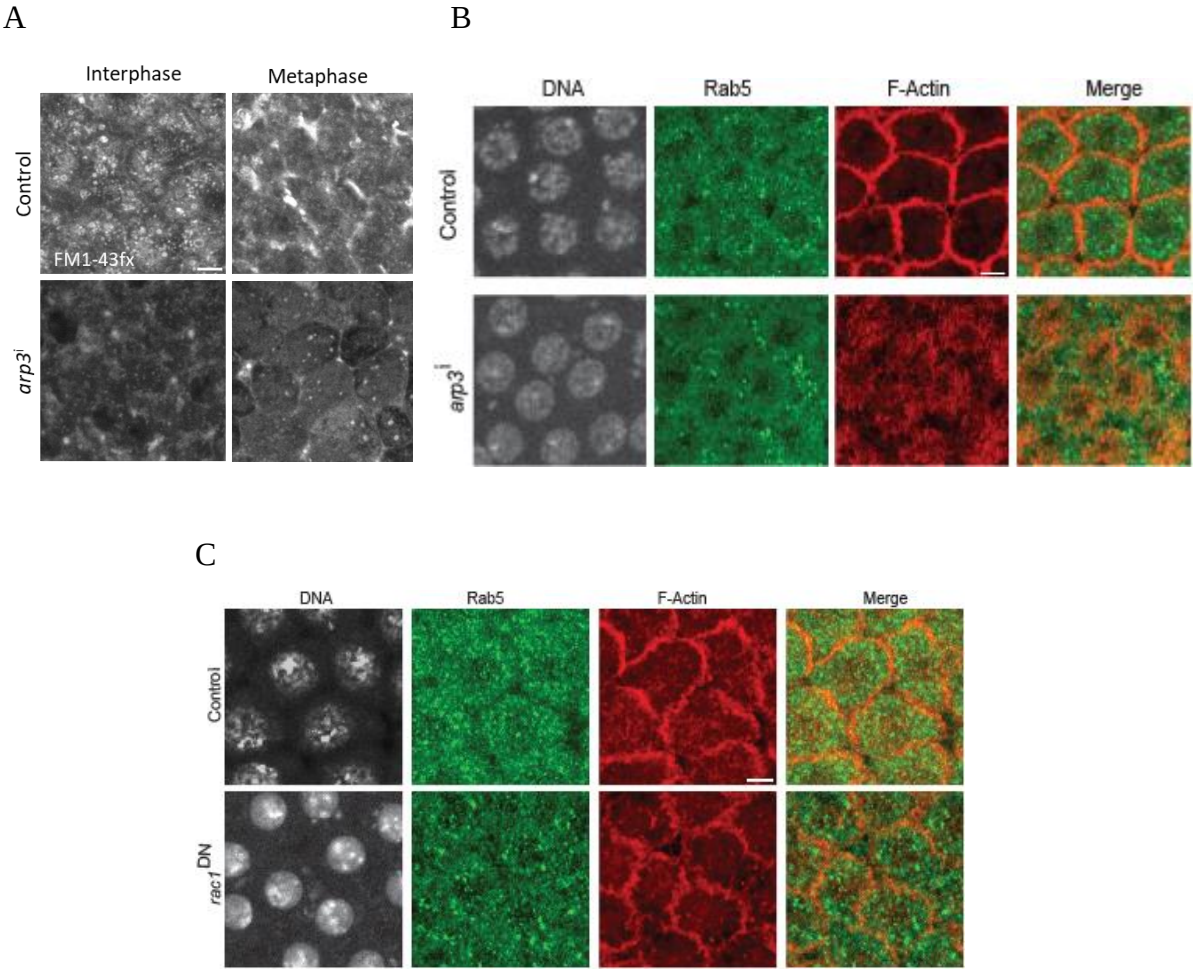

Fig. 5.15.: Endocytosis is downregulated in *rac1*^{DN} and *arp3*^{i} embryos. (A) Grazing sections of cells labelled with FM1-43fx dye at interphase and metaphase in control and *arp3* ^{i} embryos. (B-C) Grazing section of syncytial cells showing nucleus labelled with Hoechst (grey), Rab5 (green) and F-actin (red) in control, *arp3*^{i} and *rac1*^{DN} embryos. Scale Bar: 5 microns

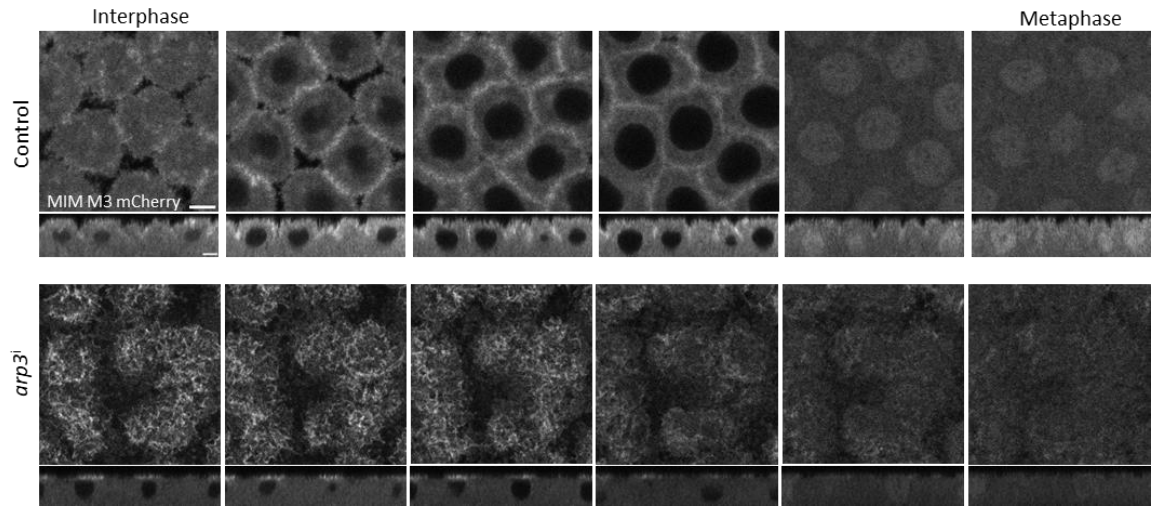

Fig. 5.16.: MIM M3 mCherry is mislocalised in *arp3*^{i} embryos. Timelapse images of the grazing and sagittal sections of the syncytial epithelial cells tagged with MIM M3 mCherry in +; MIM M3 mCherry and *arp3* ^{i}; MIM M3 mCherry embryos. Scale bar: 5 microns

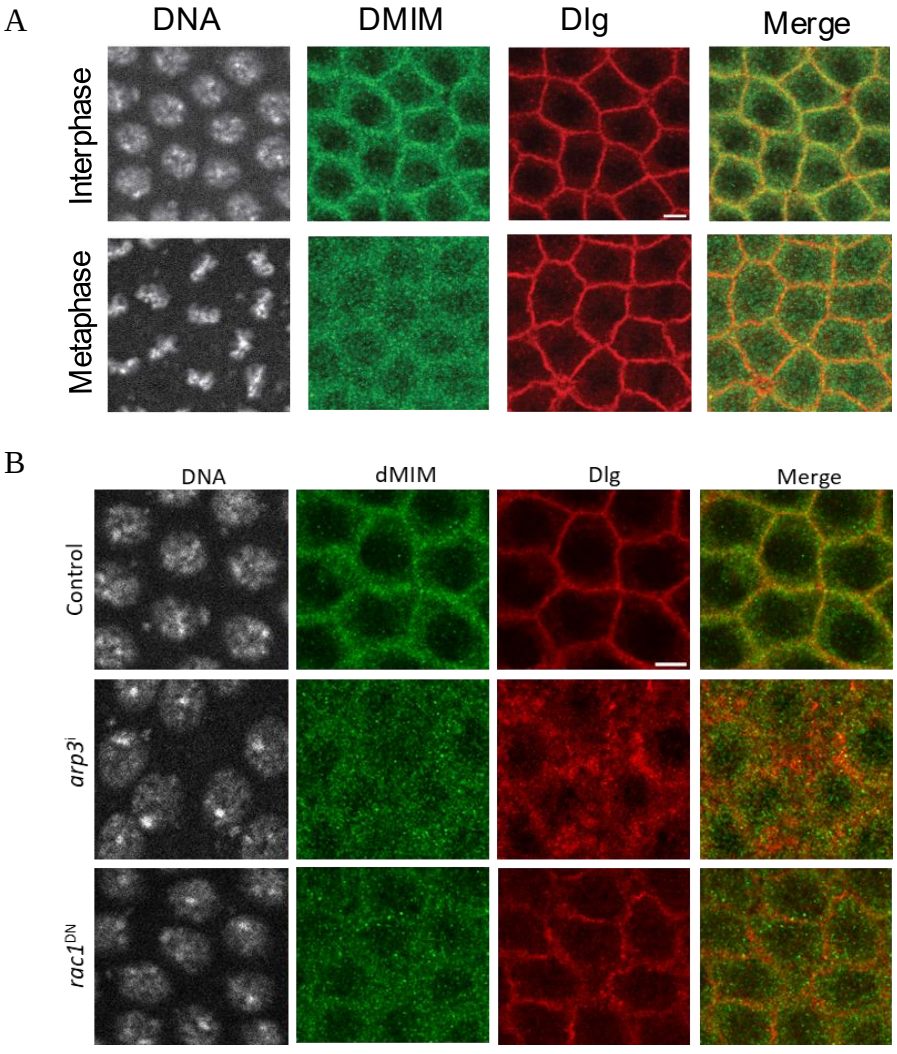

Fig. 5.17.: DMIM localises to furrows at interphase in control embryos and is mislocalised in *arp3*^{i} and r*ac1*^{DN} embryos. Grazing section of syncytial cells showing nucleus labelled with Hoechst (grey), DMIM (raised in Rabbit, 1:500, green) and Dlg (red) in control, *arp3*^{i} and *rac1*^{DN} embryos. Scale Bar: 5 microns

This signifies that rac1 dependent activation of WRC might be crucial for the localisation and activity of DMIM and vice versa. Together they form a combined unit crucial for activation of the branched actin network and that regulates endocytosis and apical microvilli remodelling.

5.3.10. Loss of DMIM leads to lack of hexagon dominance in the polygonal array

Since, a defect in endocytosis and trafficking was observed and specifically the recycling of DE-cadherin was observed, we tested the distribution of polygons and the cell shape index values of the cells in the syncytial tissue at metaphase of nuclear cycle 12 and 13, in DMIM-depleted embryos. In order to knockdown DMIM, we used the RNAi lines (refer to Materials and methods).

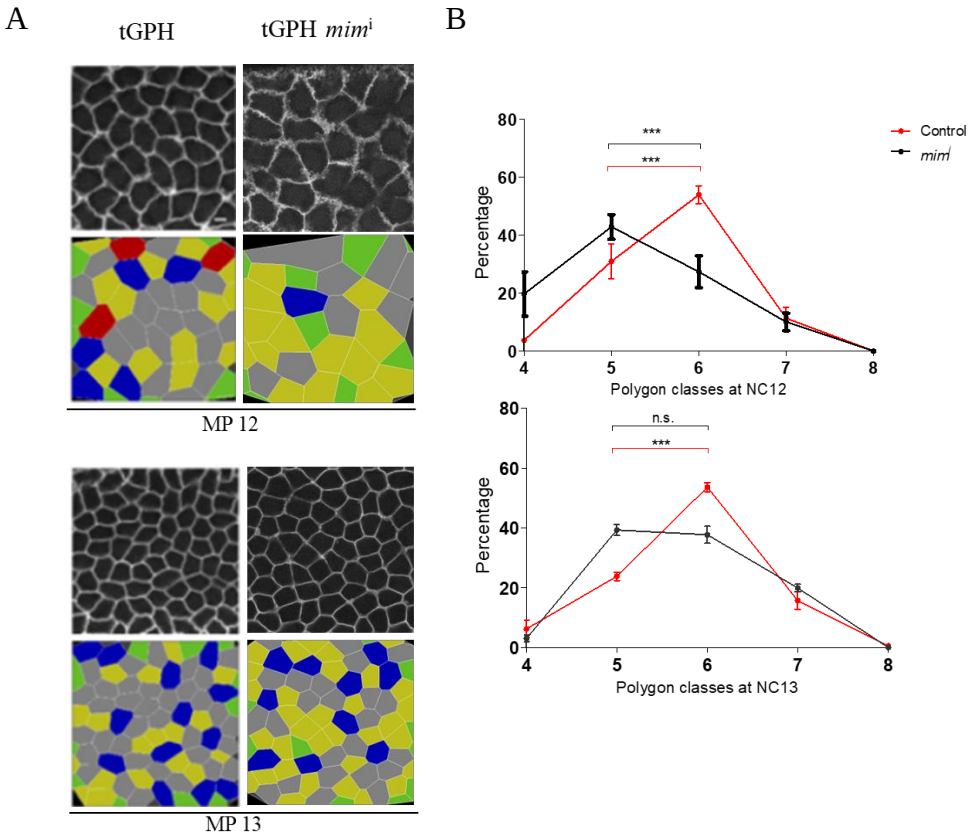

C

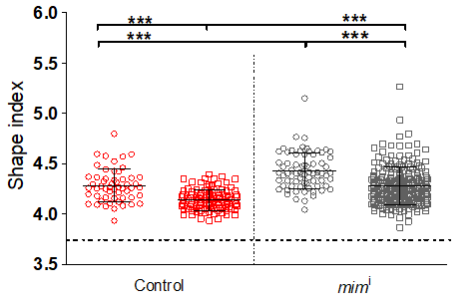

Fig 5.18.: DMIM depleted embryos show a loss of hexagon dominance in the polygon distribution of cells.

(A-B) Images showing grazing sections of control and *mim*^{i} in metaphase 12-13, tagged with tGPH, along with the respective colour-coded polygon renderings.

(C) Graph showing polygonal distribution in control and *mim*^{i} embryos in nuclear cycle 12-13, (n= 60-80 syncytial cells, 20-30 cells/embryo; 4-5 embryos). Pentagons and hexagons are compared in each cycle using the two tailed, unpaired, Student's t test. Data is represented as mean $\pm$ SEM, *p<0.05, **p<0.01, and ***p<0.001.

(D) Graph showing average shape index of all the cells in the field in control and *mim*^{i} embryos in metaphase 12-13 (n=approx. 60-80 syncytial cells, 20-30 cells/embryo; 4-5 embryos). Data is represented as mean $\pm$ SEM, *p<0.05, **p<0.01, and ***p<0.001, two-tailed, unpaired Student's t test. Scale bar: 5 µm.

For *mim*^{i} expressing embryos, we used the tGPH tag for marking the plasma membrane (Fig.5.15. A)., which showed a lack of hexagon dominance completely both at metaphase 12 and metaphase 13, as compared to control embryos where the hexagon dominance is achieved by the at metaphase 12 itself (Fig.5.15. A-B). The cell shape index values in *mim*^{i} expressing embryos were also increased as compared to that of the control embryos, both at metaphase 12 and 13 (Fig 5.15.C). This finding therefore indicates that disrupting the DMIM levels perturbs the hexagon dominated polygonal distribution and leads to formation of anisotropic cells and a more fluid-like unjammed network of cells.

5.4. Discussion and conclusion

We found DMIM, an I-BAR domain containing protein, to be crucial for maintenance of the microvilli-like membrane protrusions in the apical region of the cells, in the syncytial *Drosophila* embryos. In absence of DMIM there is a significant increase in the length and number of the microvilli present apically. This is associated with the loss of Arp2/3 complex activation and enrichment on the plasma membrane. A lack of the Arp2/3 mediated branched actin network can possibly lead to a dominance of the bundled actin network as observed in this case also, where we see an increase in the apical levels of the formin Diaphanous, which also are enriched in the excess microvilli structures formed. The cell boundary also appears to be loose and mis-shapen as the microvilli are increased apically and remain stuck at the apical region. A transition of the actin network is essential for such remodelling where the Arp2/3 network mediated actin structures are known to push the Diaphanous enriched bundles to the furrows and an absence of which perturbs the furrow formation also. A lack of transition of the network from apical to the lateral region through Arp2/3 driven remodelling also leads to a similar defect leading to an increase in the number of the Diaphanous bundles (Jiang and Harris 2019). Here, in our case also we observe the shorter furrows or the lack of it in some occasions. Another reason for lack of furrow progression could be lack of cellular trafficking (Fig.5.16.).

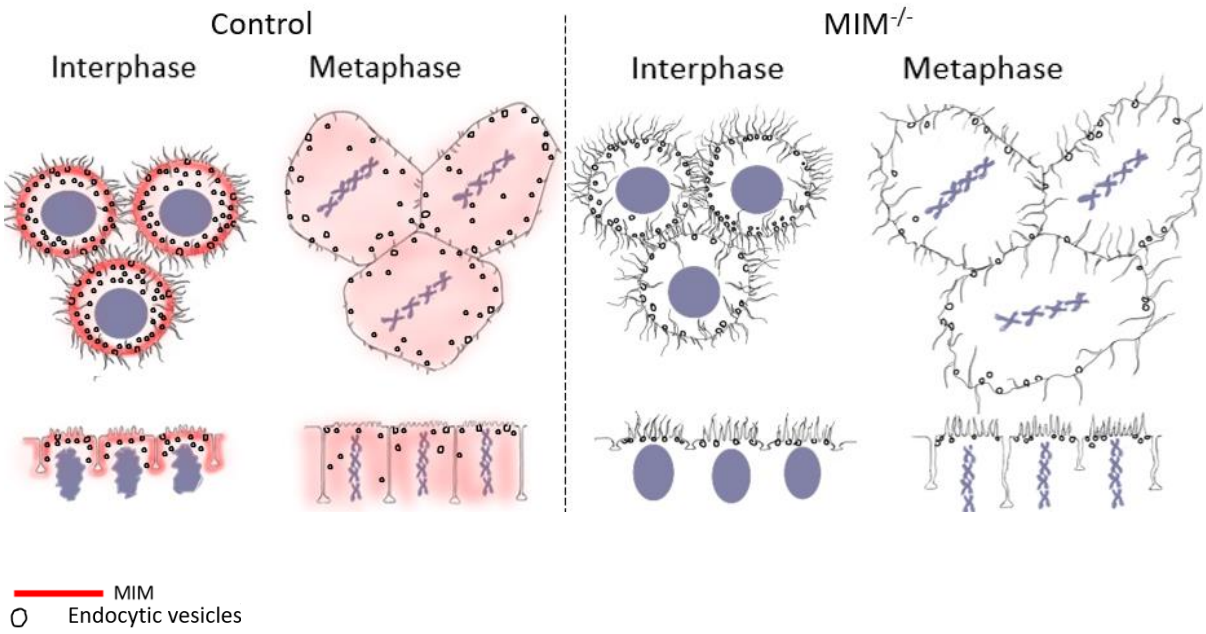

Fig. 5.19.: Schematic showing the defects in cell shape remodelling and microvilli structures in absence of DMIM as compared to control in syncytial cycles of *Drosophila* embryos.

For the process of endocytosis, positive curvatures like endocytic pits need to be formed on the plasma membrane. Although MIM is a negative curvature-inducing molecule and therefore could inhibit endocytosis (Quinones, Jin, and Oro 2010), as discussed in the introduction, even the structures of endocytic pits consist of certain patches of negative curvatures like the neck regions, where the I-BAR domain containing proteins can possibly bind. There are also studies that show the role of MIM in being a positive regulator of endocytosis (Dan Yu et al. 2011; Li et al. 2017, 2019; P. Zhao et al. 2016, 2019; Sathe et al. 2018). Certain BAR domain containing proteins are known to be positive regulators of endocytosis through interaction with the actin cytoskeleton during the metazoan development (Leibfried et al. 2008; Sherlekar and Rikhy 2016; Sathe et al. 2018; P. Zhao et al. 2019). We observed a lack of endocytosis in DMIM-depleted embryos. DMIM localises on the plasma membrane only till prometaphase, possibly till the time-point, remodelling of microvilli occurs through tubular endocytosis as is observed in the cellularization stage also (Fabrowski et al. 2013). We have also observed from findings in our lab that, Rab5 levels also decrease from interphase to metaphase (unpublished data) and a similar trend is observed with the localisation of dynamin and clathrin on the plasma membrane during the syncytial cycles (Rikhy, Mavrakis, and Lippincott-Schwartz 2015). Here, in case of MIM dependent endocytosis, we also observe less punctae of FM1-43fx dye at the metaphase stage of syncytial embryos as compared to the interphase stage and also a lower intensity of Rab5 and Rab11 vesicles in the cytosol. We also observed a lack of junctional remodelling possibly due to inhibited recycling of DE-cadherin and hence loss of hexagon dominance in the polygonal array of cells at metaphase. All of this data together signifies that there is a dynamic regulation of endocytosis at the plasma membrane in the syncytial cycles. We also see that in the embryos where the Arp2/3 network is inactivated by making the Rac1 dominant negative, endocytosis is reduced along with increased prevalence of microvilli and reduced remodelling of the same. We analysed if the recruitment of DMIM on the plasma membrane is dependent on the activity of Rac1, as it is known that MIM acts as a scaffold protein for Rac1 required for further interaction with its effectors (Bompard et al. 2005). The recruitment of DMIM on the plasma membrane was perturbed in the embryos where Rac1 was present in dominant negative form. The microvilli also became increased apically and failed to remodel in the embryos having a combination of dominant negative version of Rac1 and mCherry-MIM M3, as opposed to the embryos only overexpressing mCherry-MIM M3 where the microvilli were much smaller in length and fewer

in number. This suggested that the function of DMIM in activating the Arp2/3 network was mediated through the activity of Rac1.

The apical microvilli formed in the interphase of the syncytial nuclear cycles emerge from the periphery of the actin caps and are bundled actin structures that are primarily enriched with the formin Diaphanous. The Arp 2/3 complex form punctae-like structures at the centre of the actin caps and mostly at the base of the microvilli. The Diaphanous enriched apical microvilli reduce over time and gets relocated to the furrows as the peripheral actin bundles are pushed by the Arp 2/3 complex mediated structures to the periphery and further bundling leads to furrow stabilisation. A failure of branching activity due to loss of Arp 2/3 complex also leads to increased formation of apical microvilli, as the Diaphanous mediated bundles fail to remodel. At this specific transition, DMIM acts as a crucial scaffold protein that interacts with the small GTPase Rac1 and allows for its interaction with the subsequent effectors like the WAVE Regulatory Complex (WRC) and Cortactin. The WRC and WASP are already known to preferentially bind to the negative curvature that is the neck of the endocytic pit (Pipathsouk et al. 2021; Brunetti et al. 2022). Endocytosis at the base of the microvilli-like protrusions remodel is required for the remodelling of the apical microvilli, as observed during the cellularisation stage of development (Fabrowski et al. 2013) . Thus, the activation of the Arp 2/3 mediated branched actin network, through the combined activity of DMIM and WRC, generates enough force leading to excision of endocytic vesicles at the base of the microvilli like structures on the plasma membrane leading to the remodelling of the protrusions from interphase to metaphase in the syncytial nuclear cycles.

Hence, this study not only revealed the function of DMIM in regulating the branched actin network and its activation which facilitates the remodelling of the cortex through physical pushing of the bundled actin to the periphery as well as regulating the endocytosis for the remodelling of microvilli length and number across the syncytial nuclear cycles.

Chapter 6: Thesis Summary and Future perspectives

In this thesis, the epithelial cell shape changes occurring during the development of a syncytial *Drosophila* embryo require dynamic plasma membrane remodelling and are regulated by a host of molecular factors. These molecular regulators belong to different classes of proteins, namely, the polarity determining proteins, adhesion junction proteins, actin cytoskeleton and its nucleators and BAR domain containing proteins. These molecules either singly or in combination regulate cellular trafficking, the common mechanism core to the regulation of morphogenetic changes during the early *Drosophila* embryogenesis. This common mechanism is regulated spatiotemporally to facilitate the dynamic plasma membrane remodelling events and hence also the progression of the embryo development. Here we have elucidated two mechanisms of regulating the different steps of cell shape changes in the syncytial *Drosophila* embryogenesis- Firstly, polarity proteins mediated endocytosis of adhesion junction proteins and secondly, BAR domain protein Missing-in-metastasis and branched actin mediated apical endocytosis.

6.1. Polarity protein mediated cellular trafficking have a major role in regulating the hexagon dominated polygonal array

In this study, it was observed that the formation of hexagon dominated plasma membrane organisation, which is a common trait of a stabilised epithelial array of cells in the tissue. In the syncytial *Drosophila* embryos, a combination of adhesion and polarity proteins regulates the establishment of hexagon dependent polygonal array in the syncytial *Drosophila* blastoderm embryo during the metaphase stage of nuclear cycle 12, which is a relatively stable array of epithelial-like cells. We have also observed previously in the lab that the edges of the cells in nuclear cycle12 are enriched with Baz and vertices show accumulation of Pnut. The presence of Bazooka on the pseudo cleavage furrow membrane is important for the distribution of Peanut while the presence of DE-cadherin is important for both Bazooka and Peanut recruitment on the plasma membrane. DE-cadherin loss led to loss of hexagon dominance and shorter furrow length. However, there could be other cadherin-like adhesion molecules that possibly have a role to play as well during this stage of development like Echinoid (Wei et al. 2005) as the defects in DE-cadherin depleted embryos do not show absence of furrows but just furrows shorter in length.

DE-cadherin levels on the membrane also determine the furrow stabilisation (Dey et al. 2023). A stability in the furrows brings about the establishment of hexagon dominated polygonal arrangement in the tissue (Dey and Rikhy 2020). DE-cadherin levels on the plasma membrane increase from interphase to metaphase (Dey and Rikhy 2020) and the polygonal arrangement of the cells becomes more isotropic as the cell shape index also decreases from the earlier to the later syncytial cycles. In the Bazooka and Peanut mutants, we observe the hexagon dominance to be lost at metaphase of nuclear cycle 12 and more cells with pentagons are seen, that is cells with lesser number of cell edges and also a higher value of cell shape index is observed. A decreased number of edges in a polygonal array favours cell neighbour exchanges which gives rise to a soft and unstable network (Farhadifar et al. 2007b). In the Bazooka and Peanut depleted embryos, a similar transition to a soft network occurs possibly due to a decreased stabilisation of the furrow. It is interesting that it occurs even when DE-cadherin is present along the furrow length. An increase in DE-cadherin on the furrow in metaphase 13 in embryos depleted for Bazooka and Peanut, is possibly allowing for the conversion back to a hexagon-dominated polygonal array through stabilising and forming the additional junction. This also shows that Bazooka and Peanut depleted embryos can show hexagon dominance of the polygonal array at higher levels of DE-cadherin than controls. Since DE-cadherin depletion shows loss of hexagon dominance, this compensatory increase in DE-cadherin is likely to be responsible for the rescue of hexagon dominance in metaphase 13 in Bazooka- and Peanut-depleted embryos.

The interaction between Bazooka and DE-cadherin has long been known to initiate the polarity program in different tissues. While Bazooka actively initiates adherens junction polarity during *Drosophila* cellularization and gastrulation (Müller and Wieschaus 1996; Harris and Peifer 2004; Pilot et al. 2006), in follicle epithelial cells it is dispensable (Shahab et al. 2015). During mesoderm invagination, apical relocation of Bazooka occurs after the movement of DE-cadherin and thus, the asymmetry in DE-cadherin distribution is independent of Bazooka (Weng and Wieschaus 2017). Similarly in mammalian cells Bazooka recruitment to the contact points precedes E-cadherin (Coopman and Djiane 2016). This suggests that the interaction between Bazooka and DE-cadherin depends on the tissue type or developmental stage. Here in our study, DE-cadherin appears to be important for the distribution of both Bazooka and Peanut to the furrow. As a conclusion, it appears that DE-cadherin assumes the most significant role in furrow formation and stabilisation song with recruitment of the polarity proteins in the *Drosophila* syncytial blastoderm embryo.

6.2. The formation and remodelling of cellular protrusions is majorly regulated by the BAR domain containing protein Missing-in metastasis

Missing-In-Metastasis, an I-BAR domain containing protein, is required for maintenance of the microvilli-like membrane protrusions in the apical region of the cells, in the syncytial *Drosophila* embryos. In absence of DMIM there is a significant increase in the length and number of the microvilli present apically. This is associated with the loss of Arp2/3 complex activation and enrichment on the plasma membrane. This is coincident with Diaphanous getting enriched apically. DMIM probably acts as a scaffold protein. It localises closely with the Arp2/3 complex and Diaphanous. DMIM could possibly negatively regulate Diaphanous similar to Cip4 (Yan et al. 2013) as its loss shows an increase in apical Diaphanous levels. In embryos overexpressing DMIM, Diaphanous levels are reduced significantly while Arp3 levels increase. This insists that Diaphanous might have an antagonistic interaction with mim or it might be because of the antagonism between the small GTPases, Rho and Rac, which has been observed to occur across several studies (Salloum, Jaafar, and El-Sibai 2020).

As observed, microvilli in the *mim* mutants are not only bigger to start with, they also fail to remodel as observed in control and reduce over time from interphase to metaphase. In absence of DMIM we observe lowered endocytosis. This is consistent with the findings in cellularization where lowered tubular endocytosis from the base of the microvilli like structures, led to shorter furrows and lack of villi remodelling (Fabrowski et al. 2013). DMIM possibly induces the branched actin and associated nucleation factors to generate force facilitating the excision of the vesicles. The lack of endocytosis also leads to DE-cadherin remaining stuck on the membrane, similar to what was observed in the Bazooka and Peanut depleted embryos. An associated expanded cap area and loose cell membrane is also observed in the DMIM mutants which could be a result of loss of tension as DE-cadherin might be non-functional and stuck in the excess protrusions. This is also consistent with the loss of furrow progression and a loss of hexagon dominance of the polygonal array of cells, as a lack of DE-cadherin leads to shorter furrow and perturbed polygonal distribution of cells, as observed previously in our lab (Dey et al. 2023).

Interestingly, MIM localises on the plasma membrane only till prometaphase, possibly till the time-point endocytosis takes place. We have also observed from findings in our lab that, Rab5 levels also decrease from interphase to metaphase (unpublished data) and a similar trend is observed with the localisation of dynamin and clathrin on the plasma membrane during the syncytial cycles (Rikhy, Mavrakis, and Lippincott-Schwartz 2015). Here, in case of MIM

dependent endocytosis, we also observe less punctae of FM1-43fx dye at the metaphase stage of syncytial embryos as compared to the interphase stage. All of this data together signifies that there is a dynamic regulation of endocytosis at the plasma membrane in the syncytial cycles. Since the localization of MIM also follows the other endocytic regulators and markers closely, it might be a crucial regulator of endocytosis mediated cellular remodelling. This study therefore gives us an idea regarding how the different kinds of plasma membrane deformations require the activity of different kinds of actin nucleator and BAR domain containing proteins are the perfect candidates that can function as an intermediary to regulate these structures in a spatiotemporal manner.

6.3. Future Perspectives

The above studies clearly shed light on the two interconnected yet spatiotemporally distinct mechanisms of cell shape re-modelling events during *Drosophila* embryogenesis. In both the cases we find that cellular trafficking is a core regulatory mechanism driving the cell shape remodelling events. The cellular tension is a crucial factor that also gets remodelled along with the shape in these stages of syncytial *Drosophila* embryos. Although we get some hints of the cell being anisotropic with expanded cell area, a future analysis of change in tension in the various genetic backgrounds will tell us how the cellular tension and endocytosis are related. This along with mathematical modelling, will reveal the mechanisms that drive shape morphogenesis in *Drosophila* syncytial blastoderm embryos. A further analysis of how non muscle myosin-II, a crucial regulator of contractility and tension in these stages, could possibly regulate cellular trafficking, specifically endocytosis, will also elaborate more on the interrelation between tension and endocytosis. An interaction between MIM and lipids on the plasma membrane has also been observed where MIM binds to PI(4,5)P2 rich plasma membrane and induces bending (Mattila et al. 2007). In the Drosophila cellularization stage the balance of the phosphoinositides that is the ratio of PI(4,5)P2/PI(3,4,5)P3 is responsible for regulation of epithelial cell shape (Reversi et al. 2014). However, in the syncytial *Drosophila* embryos, a clear analysis regarding the interaction between the lipids on the plasma membrane and the specific interaction with BAR domain containing proteins, is yet to be assessed. We observed in the DMIM depleted embryos there was an increase in the levels of PI(3,4,5)P3 on the plasma membrane. An analysis of the pathways through which BAR domain proteins and the lipids on the plasma membrane interact could be an interesting future perspective to be pursued.

APPENDIX

A1. Analysis of apical cap area and non-muscle myosin II distribution in *Drosophila* embryos depleted of Bazooka and Peanut

A1.1. Analysis of cap area dynamics in *Drosophila* embryos depleted of Bazooka and Peanut.

We performed live imaging of control, *baz*^{i} and *pnut*^{i} embryos also expressing tGPH. The average area of the apical caps in the tGPH/+ embryos increases from interphase to metaphase. In tGPH /*baz*^{i} and tGPH /*pnut*^{i} expressing embryos, the average apical cell area was found to be significantly larger at the beginning of the nuclear cycle 12 that is at interphase than the control but remained slightly greater in area as compared to the control by the time the embryos reach metaphase.

A

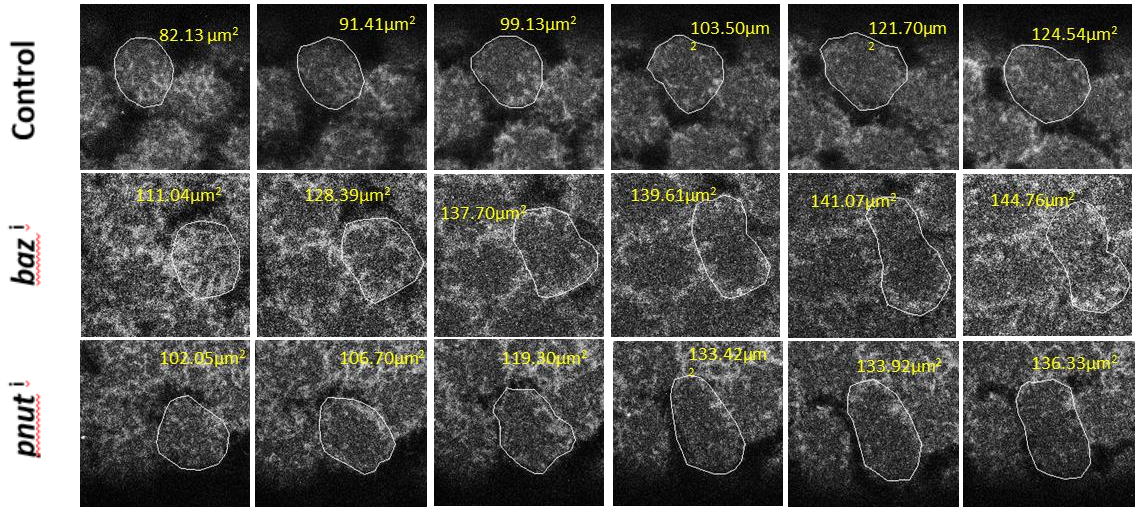

B

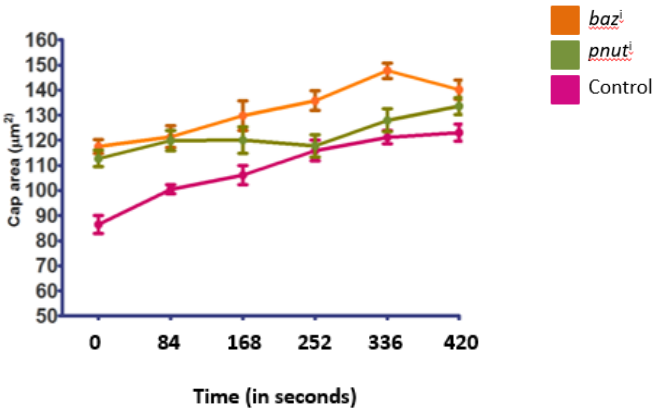

Fig. A1.1: Bazooka and peanut depletion leads to expanded cap area in syncytial nuclear cycle 12

(A) Timelapse images of the grazing and sagittal sections of the syncytial epithelial cells tagged with tGPH labelling the plasma membrane of control, *baz*^{i} and *pnut*^{i} embryos.

(B) Graphs showing the quantification of continuous apical cell area changes n=3 cells from 3 embryos for each genotype.

A1.1. Analysis of myosin II levels in *Drosophila* embryos depleted of Bazooka and Peanut.

We tested the levels of non-muscle myosin II in nuclear cycle 12 of Bazooka and Peanut depleted syncytial blastoderm embryos. We imaged the levels of myosin II distribution in live embryos of Bazooka and Peanut depleted embryos using the regulatory light chain of non-muscle myosin tagged to mCherry (Sqh-mCherry) (Fig.A1.2. A). We quantified the membrane to cytosolic ratios of Sqh-mCherry intensity in control, *baz*^{i} and *pnut*^{i} embryos at interphase and plotted it (Fig.A1.2. B). The membrane to cytosolic ratio of Sqh-mCherry intensity in the *baz*^{i} and *pnut*^{i} embryos did not show any significant change as compared to the control (Fig.A1.2. B).

A

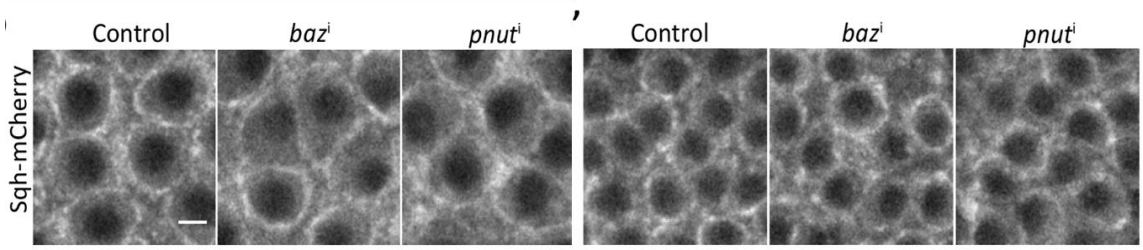

B

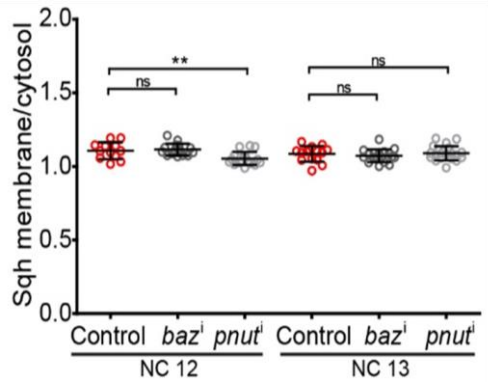

Fig. A1.2.: Analysis of myosin II in control, Bazooka and Peanut depleted embryos.

(A) Grazing sections of cells showing *sqh-sqh* mCherry in interphase at nuclear cycle 12 and 13 in control, *baz*^{i} and *pnut*^{i} embryos.
(B) Graph showing the quantification of membrane to cytosolic ratio of *sqh-sqh* mCherry in control, *baz*^{i} and *pnut*^{i} embryos., n=5 cells from 3-4 embryos for each genotype. Data is represented as mean ± SD, ∗p<0.05, ∗∗p<0.01, and ∗∗∗p<0.001, two-tailed, unpaired Student's *t* test.

A2. Analysis of non-muscle myosin II distribution in *Drosophila* embryos depleted of Missing-In-Metastasis (MIM)

We tested the levels of non-muscle myosin II in nuclear cycle 12 of DMIM depleted syncytial blastoderm embryos. We imaged the levels of myosin II distribution in fixed *dmim* embryos using antibody against the regulatory light chain of non-muscle myosin which is encoded by spaghetti-squash (Fig.A2.). We did not observe any significant change in the intensity of myosin II in *dmim* embryos compared to the control (Fig.A1.2. B).

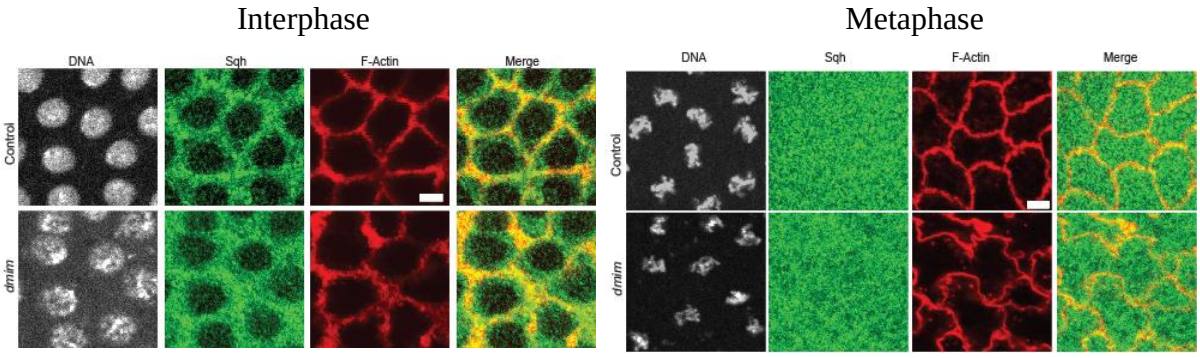

Fig. A2.: Analysis of myosin II in control and DMIM depleted embryos. Grazing sections of cells showing nucleus labelled with Hoechst (grey), myosin II labelled with Sqh (green) and cortical F-actin labelled with Alexa Fluor 568 (red) in interphase and metaphase in control and *dmim* embryos. Scale bar: 5 microns

REFERENCES

Afshar, K., B. Stuart, and S. A. Wasserman. 2000. "Functional Analysis of the *Drosophila* Diaphanous FH Protein in Early Embryonic Development." *Development* 127 (9): 1887–97.

Akhtar, N., and N. A. Hotchin. 2001. "RAC1 Regulates Adherens Junctions through Endocytosis of E-Cadherin." *Molecular Biology of the Cell* 12 (4): 847–62.

Anitei, Mihaela, and Bernard Hoflack. 2011. "Bridging Membrane and Cytoskeleton Dynamics in the Secretory and Endocytic Pathways." *Nature Cell Biology* 14 (1): 11–19.

Arnold, J. M. 1969. "Cleavage Furrow Formation in a Telolecithal Egg (Loligo Pealii). I. Filaments in Early Furrow Formation." *The Journal of Cell Biology* 41 (3): 894–904.

Ashworth, S. L., and B. A. Molitoris. 1999. "Pathophysiology and Functional Significance of Apical Membrane Disruption during Ischemia." *Current Opinion in Nephrology and Hypertension* 8 (4): 449–58.

Assémat, Emeline, Elsa Bazellières, Emilie Pallesi-Pocachard, André Le Bivic, and Dominique Massey-Harroche. 2008. "Polarity Complex Proteins." *Biochimica et Biophysica Acta* 1778 (3): 614–30.

Barriga, Elias H., and Roberto Mayor. 2019. "Adjustable Viscoelasticity Allows for Efficient Collective Cell Migration." *Seminars in Cell & Developmental Biology* 93 (September): 55–68.

Bement, W. M., P. Forscher, and M. S. Mooseker. 1993. "A Novel Cytoskeletal Structure Involved in Purse String Wound Closure and Cell Polarity Maintenance." *The Journal of Cell Biology* 121 (3): 565–78.

Betchaku, T., and J. P. Trinkaus. 1978. "Contact Relations, Surface Activity, and Cortical Microfilaments of Marginal Cells of the Enveloping Layer and of the Yolk Syncytial and Yolk Cytoplasmic Layers of Fundulus before and during Epiboly." *The Journal of Experimental Zoology* 206 (3): 381–426.

Bi, Dapeng, J. H. Lopez, J. M. Schwarz, and M. Lisa Manning. 2014. "A Density-Independent Glass Transition in Biological Tissues."

https://doi.org/10.48550/ARXIV.1409.0593.

———. 2015. “A Density-Independent Rigidity Transition in Biological Tissues.” *Nature Physics* 11 (12): 1074–79.

Biehler, Cornelia, Katheryn E. Rothenberg, Alexandra Jette, Helori-Mael Gaude, Rodrigo Fernandez-Gonzalez, and Patrick Laprise. 2021. “Pak1 and PP2A Antagonize aPKC Function to Support Cortical Tension Induced by the Crumbs-Yurt Complex.” *eLife* 10 (July). https://doi.org/10.7554/eLife.67999.

Bilder, D., M. Li, and N. Perrimon. 2000. “Cooperative Regulation of Cell Polarity and Growth by *Drosophila* Tumor Suppressors.” *Science* 289 (5476): 113–16.

Blaser, Heiko, Michal Reichman-Fried, Irinka Castanon, Karin Dumstrei, Florence L. Marlow, Koichi Kawakami, Lilianna Solnica-Krezel, Carl-Philipp Heisenberg, and Erez Raz. 2006. “Migration of Zebrafish Primordial Germ Cells: A Role for Myosin Contraction and Cytoplasmic Flow.” *Developmental Cell* 11 (5): 613–27.

Bompard, Guillaume, Stewart J. Sharp, Gilles Freiss, and Laura M. Machesky. 2005. “Involvement of Rac in Actin Cytoskeleton Rearrangements Induced by MIM-B.” *Journal of Cell Science* 118 (Pt 22): 5393–5403.

Bonifacino, Juan S., and Benjamin S. Glick. 2004. “The Mechanisms of Vesicle Budding and Fusion.” *Cell* 116 (2): 153–66.

Braga, V. M., L. M. Machesky, A. Hall, and N. A. Hotchin. 1997. “The Small GTPases Rho and Rac Are Required for the Establishment of Cadherin-Dependent Cell-Cell Contacts.” *The Journal of Cell Biology* 137 (6): 1421–31.

Brand, A. H., and N. Perrimon. 1993. “Targeted Gene Expression as a Means of Altering Cell Fates and Generating Dominant Phenotypes.” *Development* 118 (2): 401–15.

Britton, Jessica S., Wendy K. Lockwood, Ling Li, Stephen M. Cohen, and Bruce A. Edgar. 2002. “*Drosophila*’s insulin/PI3-Kinase Pathway Coordinates Cellular Metabolism with Nutritional Conditions.” *Developmental Cell* 2 (2): 239–49.

Brüser, Lena, and Sven Bogdan. 2017. “Adherens Junctions on the Move-Membrane Trafficking of E-Cadherin.” *Cold Spring Harbor Perspectives in Biology* 9 (3). https://doi.org/10.1101/cshperspect.a029140.

Buckley, Clare E., and Daniel St Johnston. 2022. “Apical-Basal Polarity and the Control of Epithelial Form and Function.” *Nature Reviews. Molecular Cell Biology* 23 (8): 559–77.

Bulgakova, Natalia A., and Nicholas H. Brown. 2016. “*Drosophila* p120-Catenin Is Crucial for Endocytosis of the Dynamic E-Cadherin-Bazooka Complex.” *Journal of Cell Science* 129 (3): 477–82.

Bulgakova, Natalia A., Ilya Grigoriev, Alpha S. Yap, Anna Akhmanova, and Nicholas H. Brown. 2013. “Dynamic Microtubules Produce an Asymmetric E-Cadherin-Bazooka Complex to Maintain Segment Boundaries.” *The Journal of Cell Biology* 201 (6): 887–901.

Campanale, Joseph P., Thomas Y. Sun, and Denise J. Montell. 2017. “Development and Dynamics of Cell Polarity at a Glance.” *Journal of Cell Science* 130 (7): 1201–7.

Cao, Jian, Roger Albertson, Blake Riggs, Christine M. Field, and William Sullivan. 2008. “Nuf, a Rab11 Effector, Maintains Cytokinetic Furrow Integrity by Promoting Local Actin Polymerization.” *The Journal of Cell Biology* 182 (2): 301–13.

Cao, Jian, Justin Crest, Barbara Fasulo, and William Sullivan. 2010. “Cortical Actin Dynamics Facilitate Early-Stage Centrosome Separation.” *Current Biology: CB* 20 (8): 770–76.

Charras, Guillaume, and Ewa Paluch. 2008. “Blebs Lead the Way: How to Migrate without Lamellipodia.” *Nature Reviews. Molecular Cell Biology* 9 (9): 730–36.

Classen, Anne-Kathrin, Kurt I. Anderson, Eric Marois, and Suzanne Eaton. 2005. “Hexagonal Packing of *Drosophila* Wing Epithelial Cells by the Planar Cell Polarity Pathway.” *Developmental Cell* 9 (6): 805–17.

Cooper, Jonathan A. 2013. “Cell Biology in Neuroscience: Mechanisms of Cell Migration in the Nervous System.” *The Journal of Cell Biology* 202 (5): 725–34.

Coopman, Peter, and Alexandre Djiane. 2016. “Adherens Junction and E-Cadherin Complex Regulation by Epithelial Polarity.” *Cellular and Molecular Life Sciences: CMLS* 73 (18): 3535–53.

Dawson, J. C., P. Timpson, G. Kalna, and L. M. Machesky. 2012. “Mtss1 Regulates Epidermal Growth Factor Signaling in Head and Neck Squamous Carcinoma Cells.” *Oncogene* 31 (14): 1781–93.

DeRosier, D. J., and L. G. Tilney. 2000. “F-Actin Bundles Are Derivatives of Microvilli: What Does This Tell Us about How Bundles Might Form?” *The Journal of Cell Biology* 148 (1): 1–6.

Dey, Bipasha, Debasmita Mitra, Tirthasree Das, Aparna Sherlekar, Ramya Balaji, and Richa Rikhy. 2023. “Adhesion and Polarity Protein Distribution-Regulates Hexagon Dominated Plasma Membrane Organization in *Drosophila* Blastoderm Embryos.” *Genetics* 225 (4). https://doi.org/10.1093/genetics/iyad184.

Dey, Bipasha, and Richa Rikhy. 2020. “DE-Cadherin and Myosin II Balance Regulates Furrow Length for Onset of Polygon Shape in Syncytial *Drosophila* Embryos.” *Journal*

of Cell Science, April. https://doi.org/10.1242/jcs.240168.

Ducibella, T., T. Ukena, M. Karnovsky, and E. Anderson. 1977. "Changes in Cell Surface and Cortical Cytoplasmic Organization during Early Embryogenesis in the Preimplantation Mouse Embryo." *The Journal of Cell Biology* 74 (1): 153–67.

Echard, A., F. Jollivet, O. Martinez, J. J. Lacapère, A. Rousselet, I. Janoueix-Lerosey, and B. Goud. 1998. "Interaction of a Golgi-Associated Kinesin-like Protein with Rab6." *Science* 279 (5350): 580–85.

Edeling, Melissa A., Subramaniam Sanker, Takaki Shima, P. K. Umasankar, Stefan Höning, Hye Y. Kim, Lance A. Davidson, et al. 2009. "Structural Requirements for PACSIN/Syndapin Operation during Zebrafish Embryonic Notochord Development." *PloS One* 4 (12): e8150.

Etienne-Manneville, Sandrine, Jean-Baptiste Manneville, Sarah Nicholls, Michael A. Ferenczi, and Alan Hall. 2005. "Cdc42 and Par6-PKCzeta Regulate the Spatially Localized Association of Dlg1 and APC to Control Cell Polarization." *The Journal of Cell Biology* 170 (6): 895–901.

Fabrowski, Piotr, Aleksandar S. Necakov, Simone Mumbauer, Eva Loeser, Alessandra Reversi, Sebastian Streichan, John A. G. Briggs, and Stefano De Renzis. 2013. "Tubular Endocytosis Drives Remodelling of the Apical Surface during Epithelial Morphogenesis in *Drosophila*." *Nature Communications* 4: 2244.

Fares, H., M. Peifer, and J. R. Pringle. 1995. "Localization and Possible Functions of *Drosophila* Septins." *Molecular Biology of the Cell* 6 (12): 1843–59.

Farhadifar, Reza, Jens-Christian Röper, Benoit Aigouy, Suzanne Eaton, and Frank Jülicher. 2007a. "The Influence of Cell Mechanics, Cell-Cell Interactions, and Proliferation on Epithelial Packing." *Current Biology*. https://doi.org/10.1016/j.cub.2007.11.049.

———. 2007b. "The Influence of Cell Mechanics, Cell-Cell Interactions, and Proliferation on Epithelial Packing." *Current Biology: CB* 17 (24): 2095–2104.

Fierro-González, Juan Carlos, Melanie D. White, Juan Carlos Silva, and Nicolas Plachta. 2013. "Cadherin-Dependent Filopodia Control Preimplantation Embryo Compaction." *Nature Cell Biology* 15 (12): 1424–33.

Figard, Lauren, Mengyu Wang, Liuliu Zheng, Ido Golding, and Anna Marie Sokac. 2016. "Membrane Supply and Demand Regulates F-Actin in a Cell Surface Reservoir." *Developmental Cell* 37 (3): 267–78.

Figard, Lauren, Heng Xu, Hernan G. Garcia, Ido Golding, and Anna Marie Sokac. 2013. "The Plasma Membrane Flattens out to Fuel Cell-Surface Growth during *Drosophila*

Cellularization." *Developmental Cell* 27 (6): 648–55.

Flores-Benitez, David, and Elisabeth Knust. 2015. "Crumbs Is an Essential Regulator of Cytoskeletal Dynamics and Cell-Cell Adhesion during Dorsal Closure in *Drosophila*." *eLife* 4 (November). https://doi.org/10.7554/eLife.07398.

Foe, V. E., and B. M. Alberts. 1983. "Studies of Nuclear and Cytoplasmic Behaviour during the Five Mitotic Cycles That Precede Gastrulation in *Drosophila* Embryogenesis." *Journal of Cell Science* 61 (May): 31–70.

Foe, V. E., C. M. Field, and G. M. Odell. 2000. "Microtubules and Mitotic Cycle Phase Modulate Spatiotemporal Distributions of F-Actin and Myosin II in *Drosophila* Syncytial Blastoderm Embryos." *Development* 127 (9): 1767–87.

Fricke, Robert, Christina Gohl, Elavarasi Dharmalingam, Astrid Grevelhörster, Baharak Zahedi, Nicholas Harden, Michael Kessels, Britta Qualmann, and Sven Bogdan. 2009. "*Drosophila* Cip4/Toca-1 Integrates Membrane Trafficking and Actin Dynamics through WASP and SCAR/WAVE." *Current Biology: CB* 19 (17): 1429–37.

Friedl, Peter, and Darren Gilmour. 2009. "Collective Cell Migration in Morphogenesis, Regeneration and Cancer." *Nature Reviews. Molecular Cell Biology* 10 (7): 445–57.

Fullilove, S. L., and A. G. Jacobson. 1971. "Nuclear Elongation and Cytokinesis in *Drosophila* Montana." *Developmental Biology* 26 (4): 560–77.

Georgiou, Marios, Eliana Marinari, Jemima Burden, and Buzz Baum. 2008. "Cdc42, Par6, and aPKC Regulate Arp2/3-Mediated Endocytosis to Control Local Adherens Junction Stability." *Current Biology: CB* 18 (21): 1631–38.

Gibson, Matthew C., Ankit B. Patel, Radhika Nagpal, and Norbert Perrimon. 2006. "The Emergence of Geometric Order in Proliferating Metazoan Epithelia." *Nature*. https://doi.org/10.1038/nature05014.

Graner, François, and Daniel Riveline. 2017. "'The Forms of Tissues, or Cell-Aggregates': D'Arcy Thompson's Influence and Its Limits." *Development* 144 (23): 4226–37.

Grevengoed, Elizabeth E., Donald T. Fox, Julie Gates, and Mark Peifer. 2003. "Balancing Different Types of Actin Polymerization at Distinct Sites: Roles for Abelson Kinase and Enabled." *The Journal of Cell Biology* 163 (6): 1267–79.

Gubb, D., and A. García-Bellido. 1982. "A Genetic Analysis of the Determination of Cuticular Polarity during Development in *Drosophila Melanogaster*." *Journal of Embryology and Experimental Morphology* 68 (April): 37–57.

Guerrier, Sabrice, Jaeda Coutinho-Budd, Takayuki Sassa, Aurélie Gresset, Nicole Vincent Jordan, Keng Chen, Wei-Lin Jin, Adam Frost, and Franck Polleux. 2009. "The F-BAR

Domain of srGAP2 Induces Membrane Protrusions Required for Neuronal Migration and Morphogenesis." *Cell* 138 (5): 990–1004.

Harris, Tony J. C., and Mark Peifer. 2004. "Adherens Junction-Dependent and -Independent Steps in the Establishment of Epithelial Cell Polarity in *Drosophila*." *The Journal of Cell Biology* 167 (1): 135–47.

Hayashi, Takashi, and Richard W. Carthew. 2004. "Surface Mechanics Mediate Pattern Formation in the Developing Retina." *Nature*. https://doi.org/10.1038/nature02952.

Hemalatha, Anupama, and Satyajit Mayor. 2019. "Recent Advances in Clathrin-Independent Endocytosis." *F1000Research* 8 (January). https://doi.org/10.12688/f1000research.16549.1.

Henry, Shannon M., Yi Xie, Katherine R. Rollins, and J. Todd Blankenship. 2022. "Sponge/DOCK-Dependent Regulation of F-Actin Networks Directing Cortical Cap Behaviors and Syncytial Furrow Ingression." *Developmental Biology* 491 (November): 82–93.

Herant, Marc, Volkmar Heinrich, and Micah Dembo. 2005. "Mechanics of Neutrophil Phagocytosis: Behavior of the Cortical Tension." *Journal of Cell Science* 118 (Pt 9): 1789–97.

Herrera-Perez, R. Marisol, and Karen E. Kasza. 2018. "Biophysical Control of the Cell Rearrangements and Cell Shape Changes That Build Epithelial Tissues." *Current Opinion in Genetics & Development* 51 (August): 88–95.

Hill, E., M. Clarke, and F. A. Barr. 2000. "The Rab6-Binding Kinesin, Rab6-KIFL, Is Required for Cytokinesis." *The EMBO Journal* 19 (21): 5711–19.

Hirokawa, Nobutaka, Yasuko Noda, Yosuke Tanaka, and Shinsuke Niwa. 2009. "Kinesin Superfamily Motor Proteins and Intracellular Transport." *Nature Reviews. Molecular Cell Biology* 10 (10): 682–96.

Holly, Ryan M., Lauren M. Mavor, Zhongyuan Zuo, and J. Todd Blankenship. 2015. "A Rapid, Membrane-Dependent Pathway Directs Furrow Formation through RalA in the Early *Drosophila* Embryo." *Development* 142 (13): 2316–28.

Hopkins, C. R., A. Gibson, M. Shipman, D. K. Strickland, and I. S. Trowbridge. 1994. "In Migrating Fibroblasts, Recycling Receptors Are Concentrated in Narrow Tubules in the Pericentriolar Area, and Then Routed to the Plasma Membrane of the Leading Lamella." *The Journal of Cell Biology* 125 (6): 1265–74.

Huotari, Jatta, and Ari Helenius. 2011. "Endosome Maturation." *The EMBO Journal* 30 (17): 3481–3500.

Iden, Sandra, and John G. Collard. 2008. “Crosstalk between Small GTPases and Polarity Proteins in Cell Polarization.” *Nature Reviews. Molecular Cell Biology* 9 (11): 846–59.

Iyer, K. Venkatesan, Romina Piscitello-Gómez, Joris Paijmans, Frank Jülicher, and Suzanne Eaton. 2019. “Epithelial Viscoelasticity Is Regulated by Mechanosensitive E-Cadherin Turnover.” *Current Biology: CB* 29 (4): 578–91.e5.

Jewett, Cayla E., Timothy E. Vanderleest, Hui Miao, Yi Xie, Roopa Madhu, Dinah Loerke, and J. Todd Blankenship. 2017. “Planar Polarized Rab35 Functions as an Oscillatory Ratchet during Cell Intercalation in the *Drosophila* Epithelium.” *Nature Communications* 8 (1): 476.

Jiang, Tao, and Tony J. C. Harris. 2019. “Par-1 Controls the Composition and Growth of Cortical Actin Caps during Embryo Cleavage.” *The Journal of Cell Biology* 218 (12): 4195–4214.

Jin, Meiyan, Cyna Shirazinejad, Bowen Wang, Amy Yan, Johannes Schöneberg, Srigokul Upadhyayula, Ke Xu, and David G. Drubin. 2022. “Branched Actin Networks Are Organized for Asymmetric Force Production during Clathrin-Mediated Endocytosis in Mammalian Cells.” *Nature Communications* 13 (1): 3578.

Jones, Taylor, 4th, Aofei Liu, and Bianxiao Cui. 2020. “Light-Inducible Generation of Membrane Curvature in Live Cells with Engineered BAR Domain Proteins.” *ACS Synthetic Biology* 9 (4): 893–901.

Juliano, R. L., and K. Carver. 2015. “Cellular Uptake and Intracellular Trafficking of Oligonucleotides.” *Advanced Drug Delivery Reviews* 87 (June): 35–45.

Kakidani, H., and M. Ptashne. 1988. “GAL4 Activates Gene Expression in Mammalian Cells.” *Cell* 52 (2): 161–67.

Kamiguchi, H., and V. Lemmon. 2000. “Recycling of the Cell Adhesion Molecule L1 in Axonal Growth Cones.” *The Journal of Neuroscience: The Official Journal of the Society for Neuroscience* 20 (10): 3676–86.

Kamiguchi, H., K. E. Long, M. Pendergast, A. W. Schaefer, I. Rapoport, T. Kirchhausen, and V. Lemmon. 1998. “The Neural Cell Adhesion Molecule L1 Interacts with the AP-2 Adaptor and Is Endocytosed via the Clathrin-Mediated Pathway.” *The Journal of Neuroscience: The Official Journal of the Society for Neuroscience* 18 (14): 5311–21.

Kamiguchi, H., and F. Yoshihara. 2001. “The Role of Endocytic l1 Trafficking in Polarized Adhesion and Migration of Nerve Growth Cones.” *The Journal of Neuroscience: The Official Journal of the Society for Neuroscience* 21 (23): 9194–9203.

Karr, T. L., and B. M. Alberts. 1986. “Organization of the Cytoskeleton in Early *Drosophila*

Embryos." *The Journal of Cell Biology* 102 (4): 1494–1509.

Keller, Ray. 2002. "Shaping the Vertebrate Body Plan by Polarized Embryonic Cell Movements." *Science* 298 (5600): 1950–54.

Kovacevic, Igor, Jiong Hu, Ann Siehoff-Icking, Nils Opitz, Aliesha Griffin, Andrew C. Perkins, Alan L. Munn, et al. 2012. "The F-BAR Protein NOSTRIN Participates in FGF Signal Transduction and Vascular Development." *The EMBO Journal* 31 (15): 3309–22.

Krause, Matthias, and Alexis Gautreau. 2014. "Steering Cell Migration: Lamellipodium Dynamics and the Regulation of Directional Persistence." *Nature Reviews. Molecular Cell Biology* 15 (9): 577–90.

Laprise, Patrick, and Ulrich Tepass. 2011. "Novel Insights into Epithelial Polarity Proteins in *Drosophila*." *Trends in Cell Biology* 21 (7): 401–8.

Lauffenburger, D. A., and A. F. Horwitz. 1996. "Cell Migration: A Physically Integrated Molecular Process." *Cell* 84 (3): 359–69.

Lawrence, P. A., and P. M. J. Shelton. 1975. "The Determination of Polarity in the Developing Insect Retina." *Development* 33 (2): 471–86.

Lecuit, Thomas, and Pierre-François Lenne. 2007. "Cell Surface Mechanics and the Control of Cell Shape, Tissue Patterns and Morphogenesis." *Nature Reviews. Molecular Cell Biology* 8 (8): 633–44.

Lecuit, Thomas, and Fanny Pilot. 2003. "Developmental Control of Cell Morphogenesis: A Focus on Membrane Growth." *Nature Cell Biology* 5 (2): 103–8.

Lee, Donghoon M., and Tony J. C. Harris. 2013. "An Arf-GEF Regulates Antagonism between Endocytosis and the Cytoskeleton for *Drosophila* Blastoderm Development." *Current Biology: CB* 23 (21): 2110–20.

Lee, Jen-Yi, and Richard M. Harland. 2010. "Endocytosis Is Required for Efficient Apical Constriction during Xenopus Gastrulation." *Current Biology: CB* 20 (3): 253–58.

Lee, Young-Goo, Jill A. Macoska, Susan Korenchuk, and Kenneth J. Pienta. 2002. "MIM, a Potential Metastasis Suppressor Gene in Bladder Cancer." *Neoplasia* 4 (4): 291–94.

Leibfried, Andrea, Robert Fricke, Matthew J. Morgan, Sven Bogdan, and Yohanns Bellaiche. 2008. "*Drosophila* Cip4 and WAS Define a Branch of the Cdc42-Par6-aPKC Pathway Regulating E-Cadherin Endocytosis." *Current Biology: CB* 18 (21): 1639–48.

Lemke, Sandra B., and Celeste M. Nelson. 2021. "Dynamic Changes in Epithelial Cell Packing during Tissue Morphogenesis." *Current Biology: CB* 31 (18): R1098–1110.

Leptin, M. 1999. "Gastrulation in *Drosophila*: The Logic and the Cellular Mechanisms." *The EMBO Journal* 18 (12): 3187–92.

Letizia, Annalisa, Sara Ricardo, Bernard Moussian, Nicolás Martín, and Marta Llimargas. 2013. “A Functional Role of the Extracellular Domain of Crumbs in Cell Architecture and Apicobasal Polarity.” *Journal of Cell Science* 126 (Pt 10): 2157–63.

Le, T. L., A. S. Yap, and J. L. Stow. 1999. “Recycling of E-Cadherin: A Potential Mechanism for Regulating Cadherin Dynamics.” *The Journal of Cell Biology* 146 (1): 219–32.

Levayer, Romain, Anne Pelissier-Monier, and Thomas Lecuit. 2011. “Spatial Regulation of Dia and Myosin-II by RhoGEF2 Controls Initiation of E-Cadherin Endocytosis during Epithelial Morphogenesis.” *Nature Cell Biology* 13 (5): 529–40.

Lewis, A. K., and P. C. Bridgman. 1992. “Nerve Growth Cone Lamellipodia Contain Two Populations of Actin Filaments That Differ in Organization and Polarity.” *The Journal of Cell Biology* 119 (5): 1219–43.

Li, Lushen, Shaneen S. Baxter, Ning Gu, Min Ji, and Xi Zhan. 2017. “Missing-in-Metastasis Protein Downregulates CXCR4 by Promoting Ubiquitylation and Interaction with Small Rab GTPases.” *Journal of Cell Science* 130 (8): 1475–85.

Li, Lushen, Shaneen S. Baxter, Peng Zhao, Ning Gu, and Xi Zhan. 2019. “Differential Interactions of Missing in Metastasis and Insulin Receptor Tyrosine Kinase Substrate with RAB Proteins in the Endocytosis of CXCR4.” *The Journal of Biological Chemistry* 294 (16): 6494–6505.

Lim, Jormay, and Jean Paul Thiery. 2012. “Epithelial-Mesenchymal Transitions: Insights from Development.” *Development* 139 (19): 3471–86.

Liu, Jiangshu, Donghoon M. Lee, Cao Guo Yu, Stephane Angers, and Tony J. C. Harris. 2015. “Stepping Stone: A Cytohesin Adaptor for Membrane Cytoskeleton Restraint in the Syncytial *Drosophila* Embryo.” *Molecular Biology of the Cell* 26 (4): 711–25.

Liu, Wei, Yuko Komiya, Courtney Mezzacappa, Deepak K. Khadka, Loren Runnels, and Raymond Habas. 2011. “MIM Regulates Vertebrate Neural Tube Closure.” *Development* 138 (10): 2035–47.

Louvard, D., M. Kedinger, and H. P. Hauri. 1992. “The Differentiating Intestinal Epithelial Cell: Establishment and Maintenance of Functions through Interactions between Cellular Structures.” *Annual Review of Cell Biology* 8: 157–95.

Marsal, Maria, Amayra Hernández-Vega, Philippe-Alexandre Pouille, and Enrique Martin-Blanco. 2021. “Rab5ab-Mediated Yolk Cell Membrane Endocytosis Is Essential for Zebrafish Epiboly and Mechanical Equilibrium During Gastrulation.” *Frontiers in Cell and Developmental Biology* 9 (October): 697097.

Martin, Adam C., Matthias Kaschube, and Eric F. Wieschaus. 2009. “Pulsed Contractions of an Actin-Myosin Network Drive Apical Constriction.” *Nature* 457 (7228): 495–99.

Mattila, Pieta K., Anette Pykäläinen, Juha Saarikangas, Ville O. Paavilainen, Helena Vihinen, Eija Jokitalo, and Pekka Lappalainen. 2007. “Missing-in-Metastasis and IRSp53 Deform PI(4,5)P2-Rich Membranes by an Inverse BAR Domain-like Mechanism.” *The Journal of Cell Biology* 176 (7): 953–64.

Mattila, Pieta K., Marjo Salminen, Takashi Yamashiro, and Pekka Lappalainen. 2003. “Mouse MIM, a Tissue-Specific Regulator of Cytoskeletal Dynamics, Interacts with ATP-Actin Monomers through Its C-Terminal WH2 Domain.” *The Journal of Biological Chemistry* 278 (10): 8452–59.

Mavor, Lauren M., Hui Miao, Zhongyuan Zuo, Ryan M. Holly, Yi Xie, Dinah Loerke, and J. Todd Blankenship. 2016. “Rab8 Directs Furrow Ingression and Membrane Addition during Epithelial Formation in *Drosophila melanogaster*.” *Development* 143 (5): 892–903.

Mavrakis, Manos, Richa Rikhy, and Jennifer Lippincott-Schwartz. 2009. “Plasma Membrane Polarity and Compartmentalization Are Established before Cellularization in the Fly Embryo.” *Developmental Cell* 16 (1): 93–104.

Mayor, Satyajit, Robert G. Parton, and Julie G. Donaldson. 2014. “Clathrin-Independent Pathways of Endocytosis.” *Cold Spring Harbor Perspectives in Biology* 6 (6). https://doi.org/10.1101/cshperspect.a016758.

McDonald, Jocelyn A., Anna Khodyakova, George Aranjuez, Colleen Dudley, and Denise J. Montell. 2008. “PAR-1 Kinase Regulates Epithelial Detachment and Directional Protrusion of Migrating Border Cells.” *Current Biology: CB* 18 (21): 1659–67.

Medina, Araceli, Rajeeb K. Swain, Klaus-Michael Kuerner, and Herbert Steinbeisser. 2004. “Xenopus Paraxial Protocadherin Has Signaling Functions and Is Involved in Tissue Separation.” *The EMBO Journal* 23 (16): 3249–58.

Miao, Hui, Megan Millage, Katherine R. Rollins, and J. Todd Blankenship. 2023. “A Rab39-Klp98A-Rab35 Endocytic Recycling Pathway Is Essential for Rapid Golgi-Dependent Furrow Ingression.” *Development* 150 (16). https://doi.org/10.1242/dev.201547.

Miller, K. G., T. L. Karr, D. R. Kellogg, I. J. Mohr, M. Walter, and B. M. Alberts. 1985. “Studies on the Cytoplasmic Organization of Early *Drosophila* Embryos.” *Cold Spring Harbor Symposia on Quantitative Biology* 50: 79–90.

Mitra, Debasmita, Amruta Swaminathan, Gayatri Mundhe, and Richa Rikhy. 2022. “Imaging and Quantification of Apical Microvilli in the Syncytial Blastoderm of *Drosophila*

Embryos." *STAR Protocols* 3 (4): 101736.

Montell, Denise J. 2008. "Morphogenetic Cell Movements: Diversity from Modular Mechanical Properties." *Science* 322 (5907): 1502–5.

Moore, Rachel, Eric Theveneau, Sara Pozzi, Paula Alexandre, Joanna Richardson, Anne Merks, Maddy Parsons, Jubin Kashef, Claudia Linker, and Roberto Mayor. 2013. "Par3 Controls Neural Crest Migration by Promoting Microtubule Catastrophe during Contact Inhibition of Locomotion." *Development* 140 (23): 4763–75.

Moreno-Bueno, G., F. Portillo, and A. Cano. 2008. "Transcriptional Regulation of Cell Polarity in EMT and Cancer." *Oncogene* 27 (55): 6958–69.

Müller, H. A., and E. Wieschaus. 1996. "Armadillo, Bazooka, and Stardust Are Critical for Early Stages in Formation of the Zonula Adherens and Maintenance of the Polarized Blastoderm Epithelium in *Drosophila*." *The Journal of Cell Biology* 134 (1): 149–63.

Mund, Markus, Johannes Albertus van der Beek, Joran Deschamps, Serge Dmitrieff, Philipp Hoess, Jooske Louise Monster, Andrea Picco, François Nédélec, Marko Kaksonen, and Jonas Ries. 2018. "Systematic Nanoscale Analysis of Endocytosis Links Efficient Vesicle Formation to Patterned Actin Nucleation." *Cell* 174 (4): 884–96.e17.

Nance, Jeremy. 2014. "Getting to Know Your Neighbor: Cell Polarization in Early Embryos." *The Journal of Cell Biology* 206 (7): 823–32.

Nance, Jeremy, and Jennifer A. Zallen. 2011. "Elaborating Polarity: PAR Proteins and the Cytoskeleton." *Development* 138 (5): 799–809.

Nandadasa, Sumeda, Qinghua Tao, Nikhil R. Menon, Janet Heasman, and Christopher Wylie. 2009. "N- and E-Cadherins in Xenopus Are Specifically Required in the Neural and Non-Neural Ectoderm, Respectively, for F-Actin Assembly and Morphogenetic Movements." *Development* 136 (8): 1327–38.

Niewiadomska, P., D. Godt, and U. Tepass. 1999. "DE-Cadherin Is Required for Intercellular Motility during *Drosophila* Oogenesis." *The Journal of Cell Biology* 144 (3): 533–47.

Nishimura, Tamako, Hisao Honda, and Masatoshi Takeichi. 2012. "Planar Cell Polarity Links Axes of Spatial Dynamics in Neural-Tube Closure." *Cell* 149 (5): 1084–97.

"On Growth and Form." n.d. Accessed July 10, 2024. https://www.gutenberg.org/files/55264/55264-h/55264-h.htm.

Osmani, Naël, Nicolas Vitale, Jean-Paul Borg, and Sandrine Etienne-Manneville. 2006. "Scrib Controls Cdc42 Localization and Activity to Promote Cell Polarization during Astrocyte Migration." *Current Biology: CB* 16 (24): 2395–2405.

Ossipova, Olga, Kyeongmi Kim, Blue B. Lake, Keiji Itoh, Andriani Ioannou, and Sergei Y.

Sokol. 2014. “Role of Rab11 in Planar Cell Polarity and Apical Constriction during Vertebrate Neural Tube Closure.” *Nature Communications* 5 (May): 3734.

Padash Barmchi, Mojgan, Stephen Rogers, and Udo Häcker. 2005. “DRhoGEF2 Regulates Actin Organization and Contractility in the *Drosophila* Blastoderm Embryo.” *The Journal of Cell Biology* 168 (4): 575–85.

Palacios, Felipe, Jill K. Schweitzer, Rita L. Boshans, and Crislyn D’Souza-Schorey. 2002. “ARF6-GTP Recruits Nm23-H1 to Facilitate Dynamin-Mediated Endocytosis during Adherens Junctions Disassembly.” *Nature Cell Biology* 4 (12): 929–36.

Paluch, Ewa, and Carl-Philipp Heisenberg. 2009. “Biology and Physics of Cell Shape Changes in Development.” *Current Biology: CB* 19 (17): R790–99.

Park, J. A., J. H. Kim, D. Bi, J. A. Mitchel, N. T. Qazvini, K. Tantisira, C. Y. Park, et al. 2015. “Unjamming and Cell Shape in the Asthmatic Airway Epithelium.” *Nature Materials* 14 (10). https://doi.org/10.1038/nmat4357.

Paterson, Andrew D., Robert G. Parton, Charles Ferguson, Jennifer L. Stow, and Alpha S. Yap. 2003. “Characterization of E-Cadherin Endocytosis in Isolated MCF-7 and Chinese Hamster Ovary Cells: The Initial Fate of Unbound E-Cadherin.” *The Journal of Biological Chemistry* 278 (23): 21050–57.

Pelissier, Anne, Jean-Paul Chauvin, and Thomas Lecuit. 2003. “Trafficking through Rab11 Endosomes Is Required for Cellularization during *Drosophila* Embryogenesis.” *Current Biology: CB* 13 (21): 1848–57.

Pesacreta, T. C., T. J. Byers, R. Dubreuil, D. P. Kiehart, and D. Branton. 1989. “*Drosophila* Spectrin: The Membrane Skeleton during Embryogenesis.” *The Journal of Cell Biology* 108 (5): 1697–1709.

Pilot, Fanny, Jean-Marc Philippe, Céline Lemmers, and Thomas Lecuit. 2006. “Spatial Control of Actin Organization at Adherens Junctions by a Synaptotagmin-like Protein Btsz.” *Nature* 442 (7102): 580–84.

Pirraglia, Carolyn, Jenna Walters, and Monn Monn Myat. 2010. “Pak1 Control of E-Cadherin Endocytosis Regulates Salivary Gland Lumen Size and Shape.” *Development* 137 (24): 4177–89.

Porter, K., D. Prescott, and J. Frye. 1973. “Changes in Surface Morphology of Chinese Hamster Ovary Cells during the Cell Cycle.” *The Journal of Cell Biology* 57 (3): 815–36.

Postner, M. A., K. G. Miller, and E. F. Wieschaus. 1992. “Maternal Effect Mutations of the Sponge Locus Affect Actin Cytoskeletal Rearrangements in *Drosophila melanogaster*

Embryos." *The Journal of Cell Biology* 119 (5): 1205–18.

Qualmann, Britta, Michael M. Kessels, and Regis B. Kelly. 2000. "Molecular Links between Endocytosis and the Actin Cytoskeleton." *The Journal of Cell Biology* 150 (5): F111–16.

Quinones, Gabriel A., Janet Jin, and Anthony E. Oro. 2010. "I-BAR Protein Antagonism of Endocytosis Mediates Directional Sensing during Guided Cell Migration." *The Journal of Cell Biology* 189 (2): 353–67.

Ramanathan, Subramanian P., Matej Krajnc, and Matthew C. Gibson. 2019. "Cell-Size Pleomorphism Drives Aberrant Clone Dispersal in Proliferating Epithelia." *Developmental Cell* 51 (1): 49–61.e4.

Ravichandran, Yamini, Bruno Goud, and Jean-Baptiste Manneville. 2020. "The Golgi Apparatus and Cell Polarity: Roles of the Cytoskeleton, the Golgi Matrix, and Golgi Membranes." *Current Opinion in Cell Biology* 62 (February): 104–13.

Revenu, Céline, Rafika Athman, Sylvie Robine, and Daniel Louvard. 2004. "The Co-Workers of Actin Filaments: From Cell Structures to Signals." *Nature Reviews. Molecular Cell Biology* 5 (8): 635–46.

Reversi, Alessandra, Eva Loeser, Devaraj Subramanian, Carsten Schultz, and Stefano De Renzis. 2014. "Plasma Membrane Phosphoinositide Balance Regulates Cell Shape during *Drosophila* Embryo Morphogenesis." *The Journal of Cell Biology* 205 (3): 395–408.

Ridley, Anne J., Martin A. Schwartz, Keith Burridge, Richard A. Firtel, Mark H. Ginsberg, Gary Borisy, J. Thomas Parsons, and Alan Rick Horwitz. 2003. "Cell Migration: Integrating Signals from Front to Back." *Science* 302 (5651): 1704–9.

Riggs, Blake, Wendy Rothwell, Sarah Mische, Gilles R. X. Hickson, Johanne Matheson, Thomas S. Hays, Gwyn W. Gould, and William Sullivan. 2003. "Actin Cytoskeleton Remodeling during Early *Drosophila* Furrow Formation Requires Recycling Endosomal Components Nuclear-Fallout and Rab11." *The Journal of Cell Biology* 163 (1): 143–54.

Rikhy, Richa, Manos Mavrakis, and Jennifer Lippincott-Schwartz. 2015. "Dynamin Regulates Metaphase Furrow Formation and Plasma Membrane Compartmentalization in the Syncytial *Drosophila* Embryo." *Biology Open* 4 (3): 301–11.

Rodrigues, Francisco F., Wei Shao, and Tony J. C. Harris. 2016. "The Arf GAP Asap Promotes Arf1 Function at the Golgi for Cleavage Furrow Biosynthesis in *Drosophila*." *Molecular Biology of the Cell* 27 (20): 3143–55.

Rolo, Ana, Paul Skoglund, and Ray Keller. 2009. "Morphogenetic Movements Driving

Neural Tube Closure in Xenopus Require Myosin IIB." *Developmental Biology* 327 (2): 327–38.

Röper, Katja. 2012. "Anisotropy of Crumbs and aPKC Drives Myosin Cable Assembly during Tube Formation." *Developmental Cell* 23 (5): 939–53.

Saarikangas, Juha, Nazim Kourdougli, Yosuke Senju, Genevieve Chazal, Mikael Segerstråle, Rimante Minkeviciene, Jaakko Kuurne, et al. 2015. "MIM-Induced Membrane Bending Promotes Dendritic Spine Initiation." *Developmental Cell* 33 (6): 644–59.

Safari, Fatemeh, and Shiro Suetsugu. 2012. "The BAR Domain Superfamily Proteins from Subcellular Structures to Human Diseases." *Membranes* 2 (1): 91–117.

Salloum, Gilbert, Leila Jaafar, and Mirvat El-Sibai. 2020. "Rho A and Rac1: Antagonists Moving Forward." *Tissue & Cell* 65 (August): 101364.

Sathe, Mugdha, Gayatri Muthukrishnan, James Rae, Andrea Disanza, Mukund Thattai, Giorgio Scita, Robert G. Parton, and Satyajit Mayor. 2018. "Small GTPases and BAR Domain Proteins Regulate Branched Actin Polymerisation for Clathrin and Dynamin-Independent Endocytosis." *Nature Communications* 9 (1): 1835.

Satoh, A., F. Tokunaga, S. Kawamura, and K. Ozaki. 1997. "In Situ Inhibition of Vesicle Transport and Protein Processing in the Dominant Negative Rab1 Mutant of *Drosophila*." *Journal of Cell Science* 110 (Pt 23) (December): 2943–53.

Schmidt, Anja, and Jörg Grosshans. 2018. "Dynamics of Cortical Domains in Early Development." *Journal of Cell Science* 131 (7). https://doi.org/10.1242/jcs.212795.

Schmidt, Anja, Zhiyi Lv, and Jörg Großhans. 2018. "ELMO and Sponge Specify Subapical Restriction of Canoe and Formation of the Subapical Domain in Early Embryos." *Development* 145 (2). https://doi.org/10.1242/dev.157909.

Schroeder, T. E. 1978. "Microvilli on Sea Urchin Eggs: A Second Burst of Elongation." *Developmental Biology* 64 (2): 342–46.

Scott, Cameron C., Fabrizio Vacca, and Jean Gruenberg. 2014. "Endosome Maturation, Transport and Functions." *Seminars in Cell & Developmental Biology* 31 (July): 2–10.

Seetharaman, Shailaja, and Sandrine Etienne-Manneville. 2020. "Cytoskeletal Crosstalk in Cell Migration." *Trends in Cell Biology* 30 (9): 720–35.

Serra, Nicholas D., and Meera V. Sundaram. 2021. "Transcytosis in the Development and Morphogenesis of Epithelial Tissues." *The EMBO Journal* 40 (9): e106163.

Shahab, Jaffer, Manu D. Tiwari, Mona Honemann-Capito, Michael P. Krahn, and Andreas Wodarz. 2015. "Bazooka/PAR3 Is Dispensable for Polarity in *Drosophila* Follicular Epithelial Cells." *Biology Open* 4 (4): 528–41.

Sharma, Swati, and Richa Rikhy. 2021. “Spatiotemporal Recruitment of RhoGTPase Protein GRAF Inhibits Actomyosin Ring Constriction in *Drosophila* Cellularization.” *eLife* 10 (April). https://doi.org/10.7554/eLife.63535.

Sherlekar, Aparna, Gayatri Mundhe, Prachi Richa, Bipasha Dey, Swati Sharma, and Richa Rikhy. 2020. “F-BAR Domain Protein Syndapin Regulates Actomyosin Dynamics during Apical Cap Remodeling in Syncytial *Drosophila* Embryos.” *Journal of Cell Science* 133 (10): jcs235846.

Sherlekar, Aparna, and Richa Rikhy. 2016. “Syndapin Promotes Pseudocleavage Furrow Formation by Actin Organization in the Syncytial *Drosophila* Embryo.” *Molecular Biology of the Cell* 27 (13): 2064–79.

Shindo, Masayo, Housei Wada, Masako Kaido, Minoru Tateno, Toshiro Aigaki, Leo Tsuda, and Shigeo Hayashi. 2008. “Dual Function of Src in the Maintenance of Adherens Junctions during Tracheal Epithelial Morphogenesis.” *Development* 135 (7): 1355–64.

Shivas, Jessica M., Holly A. Morrison, David Bilder, and Ahna R. Skop. 2010. “Polarity and Endocytosis: Reciprocal Regulation.” *Trends in Cell Biology* 20 (8): 445–52.

Sidor, Clara, Tim J. Stevens, Li Jin, Jérôme Boulanger, and Katja Röper. 2020. “Rho-Kinase Planar Polarization at Tissue Boundaries Depends on Phospho-Regulation of Membrane Residence Time.” *Developmental Cell* 52 (3): 364–78.e7.

Silverman-Gavrila, Rosalind V., Karen G. Hales, and Andrew Wilde. 2008. “Anillin-Mediated Targeting of Peanut to Pseudocleavage Furrows Is Regulated by the GTPase Ran.” *Molecular Biology of the Cell* 19 (9): 3735–44.

Simunovic, Mijo, Gregory A. Voth, Andrew Callan-Jones, and Patricia Bassereau. 2015. “When Physics Takes Over: BAR Proteins and Membrane Curvature.” *Trends in Cell Biology* 25 (12): 780–92.

Sisson, J. C., C. Field, R. Ventura, A. Royou, and W. Sullivan. 2000. “Lava Lamp, a Novel Peripheral Golgi Protein, Is Required for *Drosophila* Melanogaster Cellularization.” *The Journal of Cell Biology* 151 (4): 905–18.

Skoglund, Paul, Ana Rolo, Xuejun Chen, Barry M. Gumbiner, and Ray Keller. 2008. “Convergence and Extension at Gastrulation Require a Myosin IIB-Dependent Cortical Actin Network.” *Development* 135 (14): 2435–44.

Sokac, Anna Marie, Natalie Biel, and Stefano De Renzis. 2023. “Membrane-Actin Interactions in Morphogenesis: Lessons Learned from *Drosophila* Cellularization.” *Seminars in Cell & Developmental Biology* 133 (January): 107–22.

Sokac, Anna Marie, and Eric Wieschaus. 2008. “Local Actin-Dependent Endocytosis Is

Zygotically Controlled to Initiate *Drosophila* Cellularization." *Developmental Cell* 14 (5): 775–86.

Stevenson, Victoria, Andrew Hudson, Lynn Cooley, and William E. Theurkauf. 2002. "Arp2/3-Dependent Pseudocleavage [correction of Psuedocleavage] Furrow Assembly in Syncytial *Drosophila* Embryos." *Current Biology: CB* 12 (9): 705–11.

St Johnston, Daniel, and Julie Ahringer. 2010. "Cell Polarity in Eggs and Epithelia: Parallels and Diversity." *Cell* 141 (5): 757–74.

St Johnston, Daniel, and Bénédicte Sanson. 2011. "Epithelial Polarity and Morphogenesis." *Current Opinion in Cell Biology* 23 (5): 540–46.

Stramer, Brian, Severina Moreira, Tom Millard, Iwan Evans, Chieh-Yin Huang, Ola Sabet, Martin Milner, Graham Dunn, Paul Martin, and Will Wood. 2010. "Clasp-Mediated Microtubule Bundling Regulates Persistent Motility and Contact Repulsion in *Drosophila* Macrophages in Vivo." *The Journal of Cell Biology* 189 (4): 681–89.

Sugimura, Kaoru, and Shuji Ishihara. 2013. "The Mechanical Anisotropy in a Tissue Promotes Ordering in Hexagonal Cell Packing." *Development*. https://doi.org/10.1242/dev.094060.

Su, Jing, Brenda Chow, Gabrielle L. Boulianne, and Andrew Wilde. 2013. "The BAR Domain of Amphiphysin Is Required for Cleavage Furrow Tip-Tubule Formation during Cellularization in *Drosophila* Embryos." *Molecular Biology of the Cell* 24 (9): 1444–53.

Sullivan, W., P. Fogarty, and W. Theurkauf. 1993. "Mutations Affecting the Cytoskeletal Organization of Syncytial *Drosophila* Embryos." *Development* 118 (4): 1245–54.

Sundd, Prithu, Maria K. Pospieszalska, Luthur Siu-Lun Cheung, Konstantinos Konstantopoulos, and Klaus Ley. 2011. "Biomechanics of Leukocyte Rolling." *Biorheology* 48 (1): 1–35.

Tanaka, Tsubasa, Naoki Tani, and Akira Nakamura. 2021. "Receptor-Mediated Yolk Uptake Is Required for Oskar mRNA Localization and Cortical Anchorage of Germ Plasm Components in the *Drosophila* Oocyte." *PLoS Biology* 19 (4): e3001183.

Thomas, C. M., and J. A. Williams. 1999. "Dynamic Rearrangement of the Spectrin Membrane Skeleton during the Generation of Epithelial Polarity in *Drosophila*." *Journal of Cell Science* 112 (Pt 17) (September): 2843–52.

Thompson, Barry J. 2013. "Cell Polarity: Models and Mechanisms from Yeast, Worms and Flies." *Development* 140 (1): 13–21.

Titus, Margaret A. 2018. "Myosin-Driven Intracellular Transport." *Cold Spring Harbor Perspectives in Biology* 10 (3). https://doi.org/10.1101/cshperspect.a021972.

Trylinski, Mateusz, and François Schweisguth. 2019. “Activation of Arp2/3 by WASp Is Essential for the Endocytosis of Delta Only during Cytokinesis in *Drosophila*.” *Cell Reports* 28 (1): 1–10.e3.

Turner, F. R., and A. P. Mahowald. 1976. “Scanning Electron Microscopy of *Drosophila* Embryogenesis. 1. The Structure of the Egg Envelopes and the Formation of the Cellular Blastoderm.” *Developmental Biology* 50 (1): 95–108.

Ullrich, O., S. Reinsch, S. Urbé, M. Zerial, and R. G. Parton. 1996. “Rab11 Regulates Recycling through the Pericentriolar Recycling Endosome.” *The Journal of Cell Biology* 135 (4): 913–24.

Ulrich, Florian, Michael Krieg, Eva-Maria Schötz, Vinzenz Link, Irinka Castanon, Viktor Schnabel, Anna Taubenberger, Daniel Mueller, Pierre-Henri Puech, and Carl-Philipp Heisenberg. 2005. “Wnt11 Functions in Gastrulation by Controlling Cell Cohesion through Rab5c and E-Cadherin.” *Developmental Cell* 9 (4): 555–64.

Unterseher, Frank, Joerg A. Hefele, Klaudia Giehl, Eddy M. De Robertis, Doris Wedlich, and Alexandra Schambony. 2004. “Paraxial Protocadherin Coordinates Cell Polarity during Convergent Extension via Rho A and JNK.” *The EMBO Journal* 23 (16): 3259–69.

Vicidomini, Giuseppe, Paolo Bianchini, and Alberto Diaspro. 2018. “STED Super-Resolved Microscopy.” *Nature Methods* 15 (3): 173–82.

Vishwakarma, Medhavi, Basil Thurakkal, Joachim P. Spatz, and Tamal Das. 2020. “Dynamic Heterogeneity Influences the Leader–follower Dynamics during Epithelial Wound Closure.” *Philosophical Transactions of the Royal Society of London. Series B, Biological Sciences* 375 (1807). https://doi.org/10.1098/rstb.2019.0391.

Wacker, S., K. Grimm, T. Joos, and R. Winklbauer. 2000. “Development and Control of Tissue Separation at Gastrulation in Xenopus.” *Developmental Biology* 224 (2): 428–39.

Wang, Hong-Rui, Yue Zhang, Barish Ozdamar, Abiodun A. Ogunjimi, Evguenia Alexandrova, Gerald H. Thomsen, and Jeffrey L. Wrana. 2003. “Regulation of Cell Polarity and Protrusion Formation by Targeting RhoA for Degradation.” *Science* 302 (5651): 1775–79.

Wang, Xun, Matthias Merkel, Leo B. Sutter, Gonca Erdemci-Tandogan, M. Lisa Manning, and Karen E. Kasza. 2020. “Anisotropy Links Cell Shapes to Tissue Flow during Convergent Extension.” *Proceedings of the National Academy of Sciences of the United States of America* 117 (24): 13541–51.

Wang, Yuan, Zhenchang Jia, Chenxi Liang, Yunfei He, Min Cong, Qiuyao Wu, Pu Tian, et al. 2023. “MTSS1 Curtails Lung Adenocarcinoma Immune Evasion by Promoting AIP4-

Mediated PD-L1 Monoubiquitination and Lysosomal Degradation." *Cell Discovery* 9 (1): 20.

Wang, Yu-Chiun, Zia Khan, Matthias Kaschube, and Eric F. Wieschaus. 2012. "Differential Positioning of Adherens Junctions Is Associated with Initiation of Epithelial Folding." *Nature* 484 (7394): 390–93.

Warn, R. M., B. Bullard, and R. Magrath. 1980. "Changes in the Distribution of Cortical Myosin during the Cellularization of the *Drosophila* Embryo." *Development* 57 (1): 167–76.

Warn, R. M., R. Magrath, and S. Webb. 1984. "Distribution of F-Actin during Cleavage of the *Drosophila* Syncytial Blastoderm." *The Journal of Cell Biology* 98 (1): 156–62.

Webster, N., J. R. Jin, S. Green, M. Hollis, and P. Chambon. 1988. "The Yeast UASG Is a Transcriptional Enhancer in Human HeLa Cells in the Presence of the GAL4 Trans-Activator." *Cell* 52 (2): 169–78.

Wei, Shu-Yi, Luis M. Escudero, Fengwei Yu, Li-Hsun Chang, Li-Ying Chen, Yu-Huei Ho, Chiao-Ming Lin, et al. 2005. "Echinoid Is a Component of Adherens Junctions That Cooperates with DE-Cadherin to Mediate Cell Adhesion." *Developmental Cell* 8 (4): 493–504.

Weng, Mo, and Eric Wieschaus. 2017. "Polarity Protein Par3/Bazooka Follows Myosin-Dependent Junction Repositioning." *Developmental Biology* 422 (2): 125–34.

West, Junior J., and Tony J. C. Harris. 2016. "Cadherin Trafficking for Tissue Morphogenesis: Control and Consequences." *Traffic* 17 (12): 1233–43.

White, Melanie D., Jennifer Zenker, Stephanie Bissiere, and Nicolas Plachta. 2018. "Instructions for Assembling the Early Mammalian Embryo." *Developmental Cell* 45 (6): 667–79.

Winter, C. G., B. Wang, A. Ballew, A. Royou, R. Karess, J. D. Axelrod, and L. Luo. 2001. "*Drosophila* Rho-Associated Kinase (Drok) Links Frizzled-Mediated Planar Cell Polarity Signaling to the Actin Cytoskeleton." *Cell* 105 (1): 81–91.

Wodarz, Andreas. 2002. "Establishing Cell Polarity in Development." *Nature Cell Biology* 4 (2): E39–44.

Xie, Yi, Rashmi Budhathoki, and J. Todd Blankenship. 2021. "Combinatorial Deployment of F-Actin Regulators to Build Complex 3D Actin Structures in Vivo." *eLife* 10 (May). https://doi.org/10.7554/eLife.63046.

Xie, Yi, and J. Todd Blankenship. 2018. "Differentially-Dimensioned Furrow Formation by Zygotic Gene Expression and the MBT." *PLOS Genetics*.

https://doi.org/10.1371/journal.pgen.1007174.

Yan, Shuling, Zhiyi Lv, Moritz Winterhoff, Christian Wenzl, Thomas Zobel, Jan Faix, Sven Bogdan, and Jörg Grosshans. 2013. “The F-BAR Protein Cip4/Toca-1 Antagonizes the Formin Diaphanous in Membrane Stabilization and Compartmentalization.” *Journal of Cell Science* 126 (Pt 8): 1796–1805.

Yu, Dan, Xiaoguo H. Zhan, Shuqiong Niu, Irina Mikhailenko, Dudley K. Strickland, Jianwei Zhu, Meng Cao, and Xi Zhan. 2011. “Murine Missing in Metastasis (MIM) Mediates Cell Polarity and Regulates the Motility Response to Growth Factors.” *PloS One* 6 (6): e20845.

Yu, D., X. H. Zhan, X. F. Zhao, M. S. Williams, G. B. Carey, E. Smith, D. Scott, et al. 2012. “Mice Deficient in MIM Expression Are Predisposed to Lymphomagenesis.” *Oncogene* 31 (30): 3561–68.

Zallen, Jennifer A. 2007. “Planar Polarity and Tissue Morphogenesis.” *Cell* 129 (6): 1051–63.

Zallen, Jennifer A., Yehudit Cohen, Andrew M. Hudson, Lynn Cooley, Eric Wieschaus, and Eyal D. Schejter. 2002. “SCAR Is a Primary Regulator of Arp2/3-Dependent Morphological Events in *Drosophila*.” *The Journal of Cell Biology* 156 (4): 689–701.

Zallen, Jennifer A., and Eric Wieschaus. 2004. “Patterned Gene Expression Directs Bipolar Planar Polarity in *Drosophila*.” *Developmental Cell* 6 (3): 343–55.

Zhang, Yixie, Jessica C. Yu, Tao Jiang, Rodrigo Fernandez-Gonzalez, and Tony J. C. Harris. 2018. “Collision of Expanding Actin Caps with Actomyosin Borders for Cortical Bending and Mitotic Rounding in a Syncytium.” *Developmental Cell* 45 (5): 551–64.e4.

Zhao, Hongxia, Anette Pykäläinen, and Pekka Lappalainen. 2011. “I-BAR Domain Proteins: Linking Actin and Plasma Membrane Dynamics.” *Current Opinion in Cell Biology* 23 (1): 14–21.

Zhao, Peng, Meng Cao, Lina Song, Hao Wu, Ke Hu, Bo Chen, Qiwei Wang, and Ning Gu. 2016. “Downregulation of MIM Protein Inhibits the Cellular Endocytosis Process of Magnetic Nanoparticles in Macrophages.” *RSC Advances* 6 (99): 96635–43.

Zhao, Peng, Bo Chen, Lushen Li, Hao Wu, Yan Li, Baxter Shaneen, Xi Zhan, and Ning Gu. 2019. “Missing-in-Metastasis Protein Promotes Internalization of Magnetic Nanoparticles via Association with Clathrin Light Chain and Rab7.” *Biochimica et Biophysica Acta, General Subjects* 1863 (2): 502–10.

Zobel, Thomas, Klaus Brinkmann, Nicole Koch, Katharina Schneider, Eric Seemann, Astrid Fleige, Britta Qualmann, Michael M. Kessels, and Sven Bogdan. 2015. “Cooperative

Functions of the Two F-BAR Proteins Cip4 and Nostrin in the Regulation of E-Cadherin in Epithelial Morphogenesis." *Journal of Cell Science* 128 (3): 499–515.

STAR Protocols

CellPress
OPEN ACCESS

Protocol

Imaging and quantification of apical microvilli in the syncytial blastoderm of *Drosophila* embryos

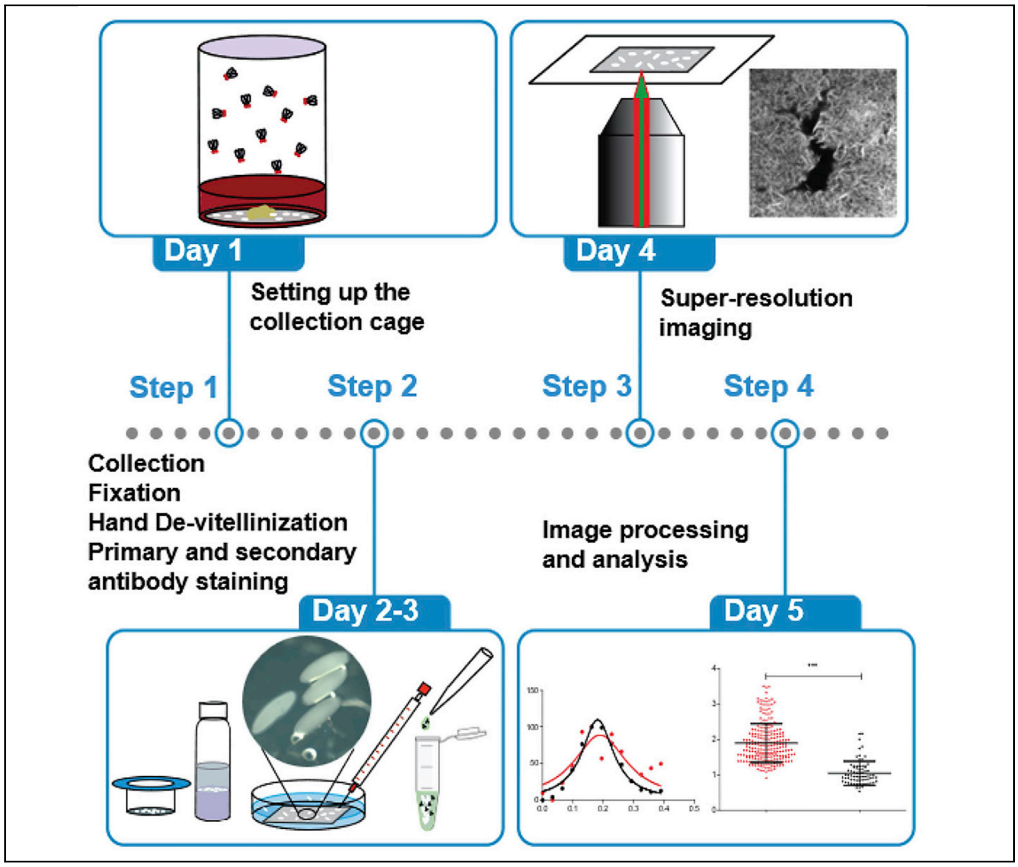

The syncytial *Drosophila* blastoderm embryo contains apical microvilli with filamentous actin that are remodeled during nuclear division cycles 10–13. Here, we describe a protocol for preparing whole embryo samples and capturing images of microvilli using confocal and super-resolution STED microscopy. This protocol enables visualization and quantification of lengths and numbers of microvilli oriented along the imaging plane. We provide information on identifying different nuclear division cycles and examples of quantification from the interphase and metaphase of cycle 12.

Publisher's note: Undertaking any experimental protocol requires adherence to local institutional guidelines for laboratory safety and ethics.

Debasmita Mitra, Amruta Swaminathan, Gayatri Mundhe, Richa Rikhy

mitra.debasmita@students.iiserpune.ac.in (D.M.)
richa@iiserpune.ac.in (R.R.)

Highlights

Embryo sample preparation for imaging microvilli using confocal and STED microscopy

Identification of interphase and metaphase stages for nuclear division cycles

Visualization of apical microvilli using confocal and STED microscopy

Quantification of microvilli lengths and numbers from confocal and STED images

Mitra et al., STAR Protocols *3*, 101736
December 16, 2022
https://doi.org/10.1016/j.xpro.2022.101736

STAR Protocols

CellPress
OPEN ACCESS

Protocol

Imaging and quantification of apical microvilli in the syncytial blastoderm of *Drosophila* embryos

Debasmita Mitra,[1,4,*] Amruta Swaminathan,[1,2] Gayatri Mundhe,[1,3] and Richa Rikhy[1,5,*]

[1]Biology, Indian Institute of Science, Education and Research, Pune 411008, India

[2]Present address: Stowers Institute for Medical Research, Kansas City, MO 64110, USA

[3]Present address: IBDM, Aix-Marseille Université, CNRS UMR 7288, Campus de Luminy, Marseille, France

[4]Technical contact

[5]Lead contact

*Correspondence: mitra.debasmita@students.iiserpune.ac.in (D.M.), richa@iiserpune.ac.in (R.R.)
https://doi.org/10.1016/j.xpro.2022.101736

SUMMARY

The syncytial *Drosophila* blastoderm embryo contains apical microvilli with filamentous actin that are remodeled during nuclear division cycles 10–13. Here, we describe a protocol for preparing whole embryo samples and capturing images of microvilli using confocal and super-resolution STED microscopy. This protocol enables visualization and quantification of lengths and numbers of microvilli oriented along the imaging plane. We provide information on identifying different nuclear division cycles and examples of quantification from the interphase and metaphase of cycle 12.

For complete details on the use and execution of this protocol, please refer to Sherlekar et al. (2020).

BEFORE YOU BEGIN

Drosophila embryo development begins as a syncytium wherein nuclei divide deep in the interior of the embryo until nuclear cycle 9. Nuclei then migrate to the periphery and nuclear cycle 10–13 occur at the cortex (Foe and Alberts, 1983). Each cortical nucleus is encompassed partially by the plasma membrane and an actin-rich cap is present between each nucleus and the plasma membrane during interphase of the syncytial division cycle. This actin cap bears filamentous actin protrusions termed apical microvilli (Turner and Mahowald, 1976; Warn et al., 1980; Foe and Alberts, 1983; Warn et al., 1984; Karr and Alberts, 1986; Mavrakis et al., 2009). The caps expand in area from interphase to metaphase of each nuclear division cycle (NC) and their microvilli are remodeled simultaneously, undergoing a concomitant reduction in lengths and numbers (Sherlekar et al., 2020). The apical cap remodeling is accompanied by extension of the plasma membrane in the form of furrows in between the nuclei and spindles. In this protocol, we use confocal and super-resolution STED microscopy to visualize apical microvilli present on the surface of embryos derived from the Canton-S wild-type strain of *Drosophila melanogaster*. We further show downstream image processing methods to resolve these structures using deconvolution. Finally, we demonstrate image analyses to elucidate the changes in microvilli architecture from interphase to metaphase in NC12.

Institutional permissions (if applicable)

Obtain appropriate institute biosafety permissions for import, maintenance and disposal of *Drosophila melanogaster* stocks and crosses.

Preparation of fly media and embryo collection cages

Timing: 45 min

1. Maintain the desired *Drosophila* stocks at 25°C in bottles containing fly media (see materials and equipment for the standard cornmeal agar recipe for fly media).
2. Prepare sucrose-agar plates for the embryo collection cages (see materials and equipment for the recipe).
3. Set up the embryo collection cages with at least 100 Canton-S flies per cage, as in shown in Figure 1A.
   a. Smear a dollop of yeast paste on the surface of a sucrose-agar plate.
4. Fix the plate on the mouth of the cage and invert the cage with the plate at the bottom.
5. Leave the cage undisturbed at 25°C for at least 24 h to allow the flies to acclimatize to the cage.

Preparation of fixative, buffers, blocking agent and mounting media

Timing: 3–4 h

Prepare the solutions listed below. See materials and equipment for recipes.

6. 10× PBS (Phosphate-buffered saline), pH 7.4.
   a. Dilute the 10× stock with deionized water to make a 1× working solution.
7. 0.3% PBST (Phosphate-buffered saline containing 0.3% [v/v] Triton X-100).
8. 2% PBTA (PBS containing 0.3% [v/v] Triton X-100, 2% [w/v] bovine serum albumin (BSA), and 0.02% [w/v] sodium azide), 4°C.
9. 4% [w/v] Paraformaldehyde (PFA) solution for fixation, 4°C.
10. Mowiol-DABCO solution for mounting embryo samples, −20°C.

KEY RESOURCES TABLE

REAGENT or RESOURCE	SOURCE	IDENTIFIER
Antibodies		
Phospho-histone H3 (pH3)	Invitrogen, Molecular Probes	RRID: AB_2533589
Alexa Fluor Anti-Rabbit 488 nm, 568 nm	Invitrogen, Molecular Probes	RRID: AB_2534114, AB_143157
Alexa Fluor Phalloidin 488 nm, 568 nm	Invitrogen, Molecular Probes	catalog number: A12379, A12380
Hoechst 33258 405 nm	Invitrogen, Molecular Probes	RRID: AB_2651133
Chemicals, peptides, and recombinant proteins		
Agar	local purchase	non-molecular biology grade
Yeast	local purchase	non-molecular biology grade
Malt	local purchase	non-molecular biology grade
Cornflour	local purchase	non-molecular biology grade
Sucrose	local purchase	non-molecular biology grade
Propionic acid	local purchase	non-molecular biology grade
Orthophosphoric acid	local purchase	non-molecular biology grade
5% methyl-para-hydroxybenzoate	Loba Chemie	catalog number: 04660
Ethanol	Jiangsu	catalog number: 1170
NaCl	Qualigens	catalog number: Q15918
KCl	Qualigens	catalog number: Q13305
Na_2HPO_4	HiMedia	catalog number: MB024
K_2HPO_4	HiMedia	catalog number: MB044
Triton X-100	Sigma	catalog number: T8787
Sodium Azide	Sigma	catalog number: S2002-25G
Paraformaldehyde	HiMedia	catalog number:GRM3660
BSA	HiMedia	catalog number: MB083
Mowiol	Sigma-Aldrich	Product number: 81381
DABCO	Sigma-Aldrich	catalog number: 290734
HCl	Fisher Scientific	catalog number: 29505

(*Continued on next page*)

Continued		
REAGENT or RESOURCE	SOURCE	IDENTIFIER
NaOH pellets	Qualigens	catalog number: Q15895
4% Sodium Hypochlorite (bleach)	Sigma	catalog number: 1056142500
Glycerol	HiMedia, India	catalog number: MB060
n-Heptane	Merck	catalog number: 1.04365.2521
Experimental models: Organisms/strains		
Canton-S strain of *Drosophila melanogaster*	L. S. Shashidhara, IISER Pune, India	RRID: DGGR_105666
Software and algorithms		
ImageJ/Fiji - Bio-Formats plugin	(Schindelin et al., 2012); (Rueden et al., 2017)	RRID: SCR_002285
Microsoft Excel	https://www.microsoft.com/en-in/microsoft-365/excel	RRID: SCR_016137
GraphPad Prism	https://www.graphpad.com/scientific-software/prism/	RRID: SCR_002798
Leica LAS X software (version 3.5.3)	Leica Microsystems	RRID: SCR_013673
Huygens Professional (version 17.04)	https://svi.nl/Huygens-Microscopy-Analysis-Software	RRID: SCR_014237
MATLAB R2021b	https://www.mathworks.com	RRID: SCR_001622
MATLAB code for calculating the Full-Width at Half-Maxima	Patrick Egan (2006). MATLAB Central File Exchange. Retrieved April 17, 2022	https://www.mathworks.com/matlabcentral/fileexchange/10590-fwhm
Other		
Incubator at 25°C for *Drosophila* stocks and crosses	Panasonic	MIR-554-PE
Stereomicroscope	Olympus	SZX10
STED microscope	Leica Microsystems, Mannheim, Germany	Inverted TCS SP8 3×
Embryo collection cages	Flystuff.com	Small (Cat # 59-100): 5.6 cm (D) × 7.6 cm (H)
Cell strainer	Corning	catalog number: CLS431751
Scintillation vials 6 mL or 20 mL	Sigma	catalog number: M1152 and V7130
Drosophila culture vials and bottles	Laxbro, India	catalog number: BT-30PSBK and FLBT-20
BD Ultra fine 40 IU/31G Syringe	Becton Dickinson (I) Pvt. Ltd.	Ref: 324902
Paintbrush	Camlin, India	00 number
Petri plates	Tarsons, India	60 mm
Soft tissue	Local purchase	non-molecular biology grade
Coverslips	VWR	22 mm × 22 mm, 22 mm × 40 mm #1.5
Glass slides	VWR	Slide Vista 25 × 75 mm
Micropipettes and tips	Tarsons	P1000, P200, P2
Conical tubes	Falcon	50 mL, 15 mL
Microcentrifuge tubes	Eppendorf	1.5 mL, 0.6 mL

MATERIALS AND EQUIPMENT

Fly Media (1 L)		
Reagent	Amount for 3% / 1 L	Amount for 6% / 1 L
Agar	10 g	10 g
Yeast	15 g	24 g
Malt	30 g	60 g
Cornflour	75 g	75 g
Sugar	80 g	80 g
Deionized water	900 mL	900 mL
Propionic acid	5 mL	5 mL
Orthophosphoric acid	1 mL	1 mL
Ethanol	5 mL	5 mL
5% Methyl-para-hydroxybenzoate	0.7 g in ethanol	1.7 g in ethanol

Weigh the required amounts of agar, yeast, malt, cornflour and sugar. Add them to deionized water and mix well by stirring. Autoclave the mixture of at 121°C and 15 psi for 15–20 min. Mix propionic

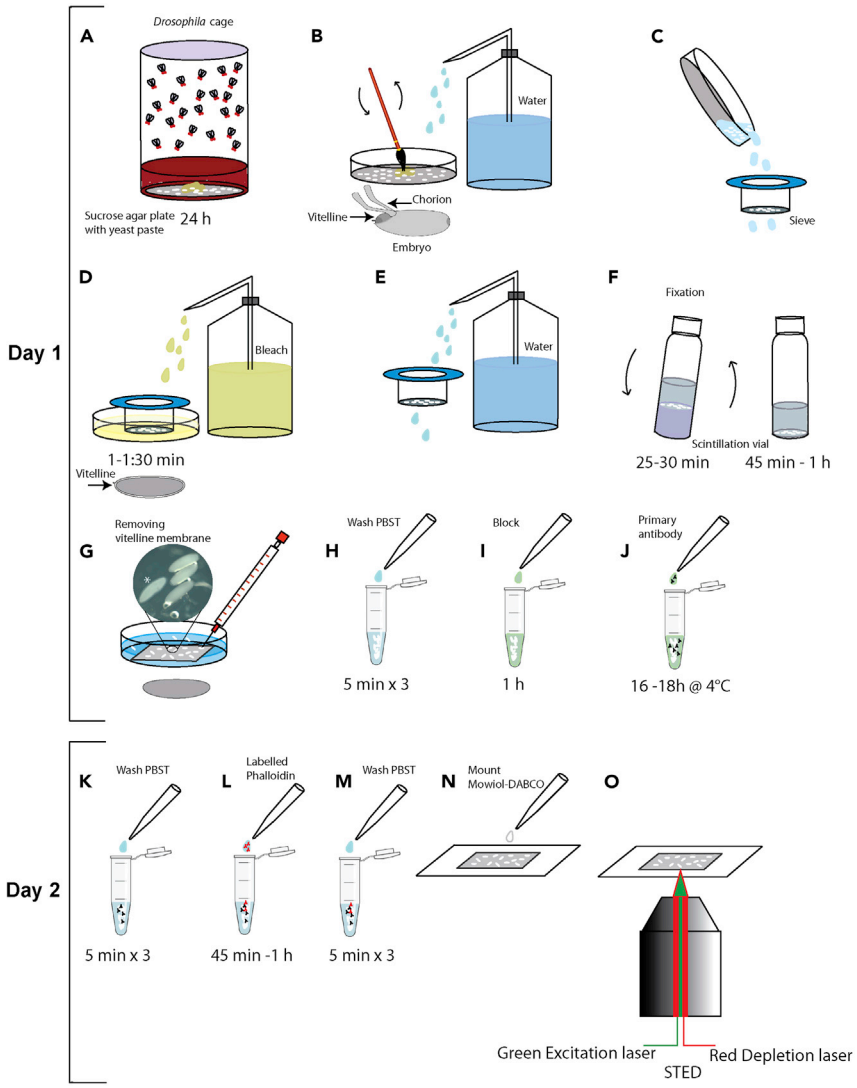

Figure 1. Schematics depicting the protocols for setting up cages, collecting embryos, hand-devitellinization, immunostaining and super-resolution imaging

(A) Carry out embryo collection in a sucrose agar plate containing yeast paste attached to a fly cage.

(B and C) Wash the embryos with water to remove residual yeast (B) and transfer the embryos into a sieve (C).

(D and E) Add bleach to dechorionate the embryos (D) and wash them in water (E).

(F) Transfer the embryos to a scintillation vial containing n-heptane. Add a 1:1 mixture of 4% PFA in PBS and n-heptane, cap the scintillation vial and shake it. The embryos settle at the interface of the two layers in the middle of the scintillation vial.

(G) Remove the PFA solution at the bottom. Transfer the embryos to a Whatman filter paper and overturn the filter paper on a double-sided sticky tape in a Petri plate and add PBS.

(H and I) Devitellinize the embryos (Methods video S1) using an insulin needle. Add the embryos in PBST in an Eppendorf tube, wash them 3 times (H) and add the blocking solution for 1 h (I).

(J) Add the anti-phospho histone antibody for 16–18 h at 4°C.

(K and L) Wash the embryos with PBST 3 times (K) and add fluorescently coupled phalloidin for 45 min to 1 h at room temperature (L).

(M and N) Finally wash with PBST 3 times (M) and mount in Mowiol-DABCO (N).

(O) Mount the slide on the 100× objective of the STED microscope. The time required for steps is mentioned below each schematic.

acid and orthophosphoric acid in a 15 mL conical tube and keep aside. Mix ethanol and methyl p-hydroxybenzoate in a 15 mL conical tube (to make a 5% solution) and keep aside. Mix the autoclaved media continuously for a few minutes, preferably with a motor-driven stirrer. Add the propionic acid and orthophosphoric acid mixture to the autoclaved media. Add the ethanol and methyl p-hydroxybenzoate mixture. Mix well and start pouring in vials/bottles. Cover the mouths of the vials/bottles with a thin clean cotton cloth and allow them to dry overnight.

Plug the mouths of the vials/bottles with tight cotton plugs and store at 4°C until further use.

Sucrose-Agar Plates (450 mL)

Reagent	Final concentration	Amount
Sucrose	3% [w/v]	13.50 g
Agar	2.5% [w/v]	11.25 g
Deionized water	N/A	Make up to 450 mL

Weigh the required amounts of sucrose and agar and dissolve them in deionized water. Make the volume up to 300 mL. Heat the solution in a microwave oven for 5–6 min. Add deionized water to the solution to make the volume up to 450 mL. Pour approximately 5 mL of the solution per 60 mm Petri plate. This will make approximately 90 plates. Let the sucrose-agar solution set in the plates at room temperature until it solidifies. Store the plates at 4°C for up to 3–4 days.

10× PBS, pH 7.4 (1 L)

Reagent	Final concentration	Amount
NaCl	1.37 M	80 g
KCl	27 mM	2 g
Na_2HPO_4	100 mM	14.4 g
KH_2PO_4	18 mM	2.4 g
Deionized water	N/A	Make up to 1 L
NaOH	N/A	As needed for pH adjustment to 7.4
HCl	N/A	As needed for pH adjustment to 7.4

Autoclave the solution and store it at room temperature for up to 3–4 months.

0.3% PBST (Phosphate-buffered saline containing 0.3% [v/v] Triton X-100) (200 mL)

Reagent	Final concentration	Amount
10× PBS	1×	20 mL
Triton X-100	0.3% [v/v]	600 µL
Deionized water	N/A	Make up to 200 mL

Add a magnetic bead to the solution and place it on a magnetic stirrer to ensure that the Triton X-100 dissolves completely. Store the solution at room temperature for up to 3–4 weeks.

2% PBTA (PBS containing 0.3% [v/v] Triton X-100, 2% [w/v] bovine serum albumin (BSA), and 0.02% sodium azide) (10 mL)

Reagent	Final concentration	Amount
0.3% PBST	0.3%	10 mL
Bovine serum albumin (BSA) powder	2% [w/v]	0.2 g
10 mg/mL Sodium Azide solution	1.2 [w/v]	#202122; 200 µL

Weigh the required amount of BSA powder and dissolve it in 0.3% PBST with sodium azide in a 15 mL conical tube. Place the tube on a rocker at 4°C to ensure that the BSA dissolves completely. Store the solution at 4°C for up to 1 week.

4% PFA (50 mL)		
Reagent	Final concentration	Amount
Paraformaldehyde	4% [w/v]	2 g
1× PBS	1×	to 50 mL

Weigh the required amount of PFA powder and dissolve it in 1× PBS in a glass beaker. Make the volume up to 50 mL. Cover sides and top of the beaker with aluminum foil. Add a magnetic bead to the solution and place the beaker on a hot plate magnetic stirrer set to 60°C and 100 rpm till the PFA powder dissolves completely. Allow the solution to cool to room temperature. Store the solution at −20°C in 1 mL aliquots.

⚠ CRITICAL: Paraformaldehyde is a potential carcinogen and a strong respiratory and skin irritant. Ensure you wear a lab coat, safety goggles, mask and gloves while handling PFA.

PFA is light-sensitive. Ensure that the PFA powder and the solution formed after dissolving it in PBS is protected from light exposure. Cover the glass beaker with aluminum foil from all sides.

Mowiol-DABCO (20 mL)		
Reagent	Final concentration	Amount
Mowiol	2.5% [w/v]	2.4 g
Glycerol	30% [w/v]	6 g
Tris-HCl (pH 8.5)	N/A	12 mL
DABCO	2.5% [w/v]	0.5 g
Deionized water	N/A	6 mL

Measure the required amounts of Mowiol powder and glycerol. Dissolve them in 6 mL of deionized water mixed with 12 mL of 0.2 M Tris-Cl (pH 8.5) in a 50 mL conical tube. Place the tube in a water bath set to 50°C for several hours. Centrifuge the solution at 5,000 g for 15 min and transfer the supernatant to a fresh 50 mL conical tube. Add DABCO to the supernatant to achieve a final concentration of 2.5% [w/v] of DABCO. Store the resultant solution at −30°C in 1 mL aliquots for up to 5–6 months.

STEP-BY-STEP METHOD DETAILS

Collection, fixation, and de-vitellinization of syncytial *Drosophila* embryos

Timing: 3–4 h

1. Place a fresh sucrose-agar plate smeared with fresh yeast paste on the mouth of a cage containing Canton-S flies.
2. Replace the cage at 25°C and collect the sucrose-agar plate after 2.5 h.

Note: The plate now contains embryos, the majority of which are in the syncytial blastoderm stages.

3. Pour deionized water into the plate and carefully with the help of a paint brush, dissolve the yeast, taking care not to break the sucrose-agar layer (as shown in Figure 1B).

Note: This dislodges embryos and suspends them in the water-yeast solution.

4. Carefully pour the contents of the plate into a cell strainer (as shown in Figure 1C).

Note: The water-yeast mixture passes through the strainer and the embryos remain in the strainer.

5. Wash the embryos multiple times with deionized water to get rid of any debris.
6. Pour 5–6 mL of 4% bleach into an empty 60 mm Petri plate. Immerse the cell strainer in bleach for 1–1.5 min such that the embryos are submerged, to remove the chorion, as shown in Figure 1D.

Note: Fly embryos are encased in two semi-transparent membranes - an outer chorion and an inner vitelline envelope, as shown in Figure 1B. These membranes need to be removed for this protocol.

⚠ CRITICAL: Avoid increased exposure to bleach as this may damage the embryos. Ensure that the bleach is fresh and unexposed to air and sunlight. Bleach loses its efficiency with time and exposure to air.

To ensure the chorion has been removed, observe the embryos under a stereomicroscope, once before adding bleach and once after the embryos have been soaked in bleach for 1 min. Each embryo possesses a pair of protrusions on the anterior end called the dorsal appendages which are part of the chorion. Before bleaching, the dorsal appendages are intact, whereas after bleaching, they are shed off along with the chorion.

7. Wash the embryos thrice with deionized water (Figure 1E).
8. Dry them by placing the cell strainer on a piece of soft tissue.
9. Add 1 mL of n-heptane to a scintillation vial.
10. Carefully, using a fine paint brush, swipe the embryos up from the walls of the strainer.
11. Transfer them into the scintillation vial containing n-heptane.

Note: The embryos sink to the bottom of the scintillation vial.

12. Add a 1: 1 mixture of 4% PFA and n-heptane (1 mL each) to the scintillation vial. 4% PFA and n-heptane are immiscible and separate into two phases - 4% PFA below and n-heptane above.

⚠ CRITICAL: The 4% PFA solution should be brought to room temperature before it is added to the scintillation vial to ensure efficient fixation.

13. The embryos come to rest at the interface of the two liquids, as shown in Figure 1F.
14. Place the scintillation vial on a rocker at room temperature for 25 min.
15. Carefully remove and discard the 4% PFA (bottom) layer of the solution in the scintillation vial.
16. Remove the n-heptane.
17. Add fresh n-heptane and incubate the embryos at 4°C for a minimum of 40 min.
18. Cut rectangular pieces of double-sided tape (~ 6 cm long) and Whatman filter paper (~ 6 cm long, and as wide as the double-sided tape).
19. Remove the plastic covering from one side of the tape and stick the tape to a 60 mm Petri plate along its diameter, as shown in Figure 1G.
20. Transfer the embryos and the n-heptane using a 200 µL pipette onto the filter paper rectangle.
21. Allow the n-heptane to evaporate, leaving the embryos on the filter paper.
22. Remove the plastic covering on the exposed surface of the tape.
23. Invert the filter paper rectangle such that the embryos face downwards, and touch it lightly on the sticky surface of the tape. The embryos will get immobilized on the tape.

24. Pour enough 1× PBS into the Petri plate containing the immobilized embryos so as to submerge the embryos.
25. Place the Petri plate under a stereomicroscope.
26. Using a 1 mL insulin syringe needle, poke each embryo at one end of its long axis to rupture its vitelline envelope (Figure 1G).
27. Give a slight push to each embryo with the needle to release it from its vitelline envelope as shown in the Methods video S1.

Note: The vitelline envelope remains stuck to the tape and the embryo floats in the 1× PBS. Embryos still encased in the vitelline envelope glisten under the light of the stereomicroscope, and are easily distinguished from de-vitellinized embryos. In Figure 1G, in the inset image, an asterisk marks the embryo that has been de-vitellinized whereas the others are not. If the embryos are soft and disintegrate when touched with the needle, please see troubleshooting step 2.

28. Transfer the de-vitellinized embryos in 1× PBS solution into a 0.6 mL microcentrifuge tube. Let the embryos settle at the bottom of the tube.
29. Without disturbing the embryos, remove the 1× PBS and add 300 μL 0.3% PBST to the tube.
30. The de-vitellinized embryos can be stored in 0.3% PBST solution for upto 24 h at 4°C.

Staining of microvilli and nuclei in syncytial *Drosophila* embryos

Timing: 18–20 h

31. Remove the 0.3% PBST from the microcentrifuge tube containing de-vitellinized embryos.
32. Add 300 μL of fresh 0.3% PBST.
33. Wash the embryos in 0.3% PBST for 5 min by placing the tube on a rocker at room temperature.
34. Allow the tube to stand so that the embryos settle at the bottom. Using a 200 μL pipette, remove the 0.3% PBST carefully without disturbing the embryos.
35. Add 300 μL of fresh 0.3% PBST and repeat the wash step twice more for a total of 3 washes.
36. Remove the 0.3% PBST after the last wash.
37. Add 300 μL of 2% PBTA to the tube.
38. Incubate the tube on a rocker at room temperature for 1 h for the blocking process.
39. Allow the tube to stand so that the embryos settle at the bottom. Using a 200 μL pipette, remove the 2% PBTA carefully without disturbing the embryos.
40. For the primary antibody staining, dilute the primary antibody in fresh 2% PBTA (1:200 for Phospho-Histone H3 in rabbit).
41. Remove the 2% PBTA used for the blocking step and add the diluted primary antibody solution to the tube containing the embryos.
42. Incubate on a rocker at 4°C for a minimum of 16 h.
43. Allow the tube to stand so that the embryos settle at the bottom. Using a 200 μL pipette, remove the primary antibody solution carefully without disturbing the embryos.
44. Add 300 μL of fresh 0.3% PBST to the tube.
45. Place the tube on a rocker at room temperature for 5 min. Repeat the wash step twice more for a total of 3 washes.
46. Dilute Alexa 488 phalloidin (1:100) and Alexa 568-coupled anti-rabbit secondary antibody (1:1,000) in 300 μL of 0.3% PBST.
47. Allow the tube to stand so that the embryos settle at the bottom. Using a 200 μL pipette, remove the 0.3% PBST carefully without disturbing the embryos.
48. Add the secondary antibody/dye solution to the tube.
49. Wrap the microcentrifuge tube in aluminum foil to protect the fluorophores (conjugated to the antibody/dye) from photobleaching.
50. Incubate the tube on a rocker at room temperature for 1 h.

51. During the incubation step, thaw an aliquot of Mowiol-DABCO on ice.
52. Allow the tube containing the embryos to stand so that the embryos settle at the bottom. Using a 200 μL pipette, remove the secondary antibody/dye solution carefully without disturbing the embryos.
53. Add 300 μL of fresh 0.3% PBST to the tube and place it on a rocker at room temperature for 5 min.
54. Allow the tube to stand so that the embryos settle at the bottom. Using a 200 μL pipette, remove the 0.3% PBST carefully without disturbing the embryos.
55. Repeat this wash step twice more for a total of 3 washes.
56. After removing the 0.3% PBST from the final wash, add 100 μL of fresh 0.3% PBST to the tube.
57. Transfer the solution with embryos onto a glass slide.
58. Drain the excess 0.3% PBST by standing the slide on its side.
59. Space the embryos on the slide by gently pushing them apart from each other using a fine brush.
60. Excess liquid can be drained out using a thin piece of Whatman filter paper by dabbing the paper lightly at the edges of each of the embryo(s).
61. Using a cut 1 mL pipette tip, add 2 drops of Mowiol-DABCO solution to the slide.
62. Carefully place a 22 × 40 mm, #1.5 coverslip on the slide, while avoiding formation of air bubbles and ensuring that the Mowiol-DABCO solution covers the embryos.
63. Seal the edges of the coverslip with transparent nail polish.
64. Protect the slide from light by covering it with aluminum foil and allow the nail polish to set for 15 min at room temperature.
65. Store the slide in an opaque box at 4°C and image them within 1–2 days of preparation to minimize the degradation of fluorophore signal.

Confocal and super-resolution STED imaging to obtain high-resolution images of microvilli

Timing: 3–4 h

66. Mount the slide on the stage of an inverted TCS SP8 3× microscope containing the super-resolution STED module (Leica Microsystems, Mannheim, Germany) operated by the Leica LAS X software (version 3.5.3).
67. Load the 100×/1.4 NA oil immersion (refractive index 1.518) objective (Leica HC PL APO CS2-STED WHITE).
68. Switch to fluorescence mode and toggle to the rhodamine/RHOD (red) filter while looking through the eyepiece.
69. Move the stage until an embryo becomes visible as an orange glow.
70. Use the coarse and fine focus knobs to bring the surface of the embryo in focus.
71. Identify the mitotic stage of the syncytial division cycle based on the phospho-histone H3 label as shown in Figure 2B.

⚠ CRITICAL: Hoechst 33258 cannot be used for labeling samples for super-resolution STED imaging as it might have a negative influence on image quality (background), especially with the 592 nm STED laser. Thus, for super-resolution STED imaging we have used phospho-histone H3 (green) only. We have shown nuclei co-labeled with phospho-histone H3 (green) and Hoechst 33258 (blue) using confocal microscopy in Figure 2B, for each of the mitotic stages (interphase, prophase and metaphase). Interphase nuclei appear as rounded and smooth with non-punctate chromatin in Hoechst, however phospho-histone H3 does not label interphase nuclei at all. Prophase nuclei in both appear as round structures with partially condensed chromatin resembling puncta. Metaphase nuclei in both cease to be rounded and have fully condensed chromatin that appears as thick coiled strands.

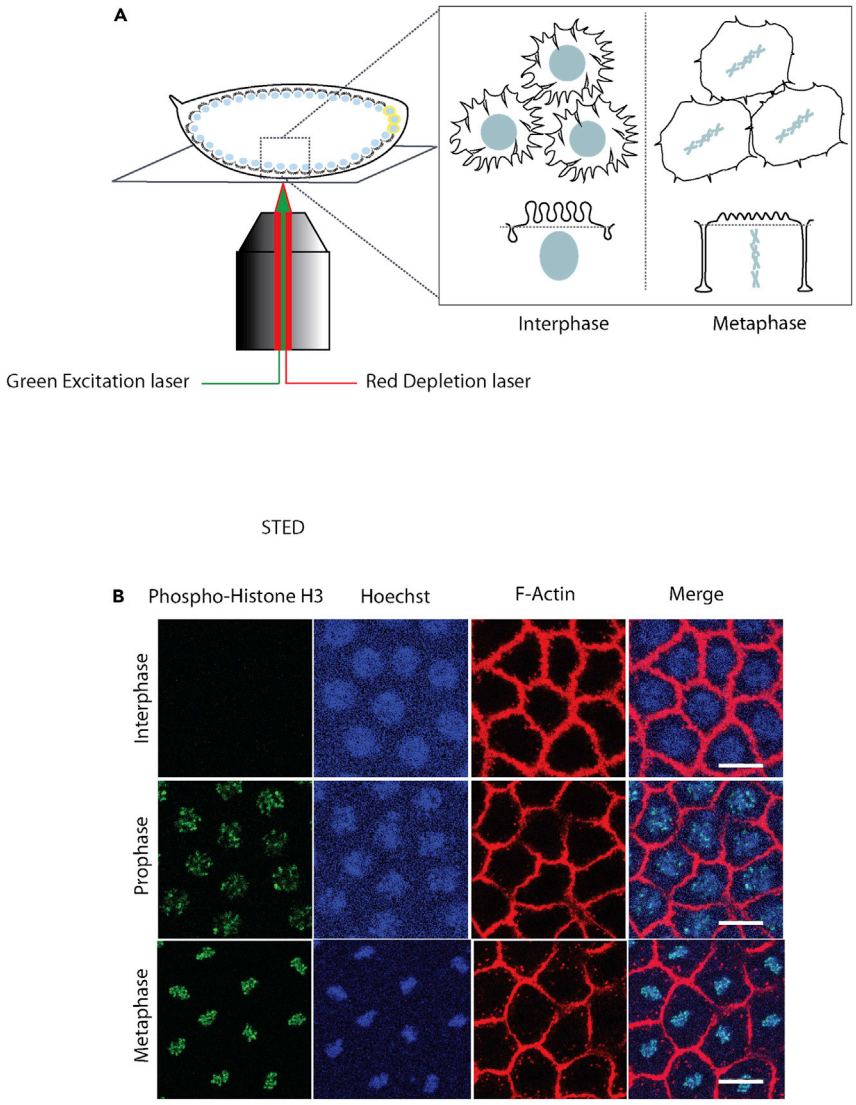

Figure 2. Setup for imaging and identification of the cell cycle stage in the syncytial blastoderm embryo

(A) Syncytial *Drosophila* embryos imaged using an inverted confocal and STED microscope (left). The schematic of the syncytial nuclear cycle (right, magnified inset), showing an apical view and a sagittal view (rotated by 180° to show the apical side on top) at interphase and metaphase. Interphase embryos possess short furrows between cortical nuclei (blue) and long apical microvilli (black) whereas metaphase embryos have long furrows and fewer and shorter microvilli. The dashed line indicates the plane of the membrane shown in the top panel.

(B) Grazing sections of confocal images showing the nuclei, labeled using both phospho-histone H3 (green) and Hoechst 33258 (blue), for each of the mitotic stages (interphase, prophase and metaphase). Cortical F-actin (red) is labeled using Alexa 568 phalloidin at different mitotic stages of a single nuclear division cycle 12. Scale bar: 5 μm.

Use the laser settings shown in Table 1 for exciting fluorophores and detecting emitted light for confocal imaging to identify the nuclear staining at different cell cycle stages.

72. Identify the nuclear division cycle number (10–13) based on the area of the apical caps as shown in Figure 3.
73. Apical caps are larger than 240 μm^2 during syncytial cycle 10, 120–240 μm^2 during syncytial cycle 11, 80–120 μm^2 during syncytial cycle 12 and 40–80 μm^2 during syncytial cycle 13. Cycle 14 is identified by small caps with area less than 40 μm^2.

Table 1. Laser settings for confocal microscopy

Fluorophore	Labels	Excitation wavelength	Excitation laser intensity	Detector	Spectral window for detection	Gain	Line averaging
Hoechst 33258	Dividing nuclei	405 nm	70% (90 MHz pulsed white light laser)	Photomultiplier tube (PMT)	443–466 nm	800–1,000	2
Phospho-Histone H3	Dividing nuclei	488 nm	70% (90 MHz pulsed white light laser)	Hybrid detector (HyD)	506–539 nm	100–200	2
Alexa 568 Phalloidin	Microvilli (F-actin)	561 nm	70% (90 MHz pulsed white light laser)	Hybrid detector (HyD)	585–623 nm	100–150	2

74. Move through a few z-planes near the surface of the embryo and find an optical plane which has the greatest number of microvilli in focus.
75. Set the pinhole size to 1.00 AU and capture a standard confocal image at the optical plane determined above. Use the standard mode with a zoom of 3.5× and scan speed 200 Hz.
76. To obtain STED images of the microvilli (labeled with Alexa 488 phalloidin), use the 592 nm pulsed depletion laser (Leica Microsystems) at 90% laser power in 2D STED mode.
77. Keep the gain at 100 and line averaging at 4.
78. Use the laser settings in Table 2 for exciting fluorophores and detecting emitted light for super-resolution STED imaging.
79. Export the images as 8 bit, 1024 × 1024 TIFF format images with a pixel size of about 30–40 nm.

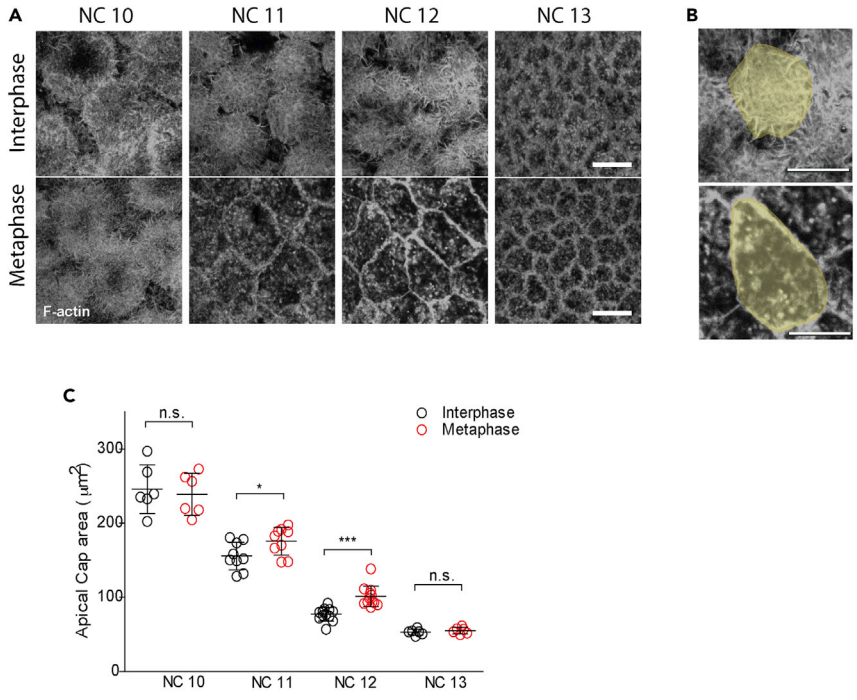

Figure 3. Apical villi images in the syncytial *Drosophila* blastoderm in interphase and metaphase of nuclear cycles 10–13

(A) Super-resolution STED images of apical actin caps at interphase and metaphase of nuclear cycles 10–13 in the syncytial *Drosophila* embryo. Scale bar: 5 μm.

(B) Image showing an ROI drawn (yellow) along the boundaries of the apical cap to measure its area using ImageJ. Scale bar: 5 μm.

(C) Quantification of apical cap areas at interphase and metaphase in nuclear division cycles 10–13 in the syncytial *Drosophila* embryo. Each circle represents the area obtained from individual caps from at least 3 embryos. NC 10, n = 6,3 caps from 2 embryos each, NC 11, n = 9,3 caps from 3 embryos each; NC 12, n = 12,3 caps from 4 embryos each, NC 13, n = 6,3 caps from 2 embryos each. Data are represented as mean ± SD, *p<0.05, **p<0.01, and ***p<0.001, two-tailed, unpaired Student's *t* test.

Table 2. Laser settings for STED super resolution microscopy

Fluorophore	Labels	Excitation wavelength	Excitation laser intensity	Detector	Time gate	Spectral window for detection	Gain	Line averaging
Alexa 488 Phalloidin	Microvilli (F-actin)	488 nm	70% (90 MHz pulsed white light laser)	Hybrid detector (HyD)	0.3–6 ns	507–542 nm	100–120	2
Phospho-Histone H3	Dividing nuclei	561 nm	70% (90 MHz pulsed white light laser)	Hybrid detector (HyD)	0.3–6 ns	584–633 nm	50–60	2

Deconvolution of images obtained from STED microscopy

Timing: 1–2 h

80. Deconvolve the images using the STED module on Huygens Professional version 17.04 (Scientific Volume Imaging, Netherlands).
81. Estimate the average background using the In/near object module by controlling the radius parameter.
82. Use the Classical Maximum Likelihood Estimation (CMLE) algorithm and set the maximum iterations at 40. Set the Signal to Noise Ratio at 7 and Quality Threshold at 0.1 in the 'fast' iteration mode with possible bleaching correction.
83. Save the deconvolved images as high-quality TIFF images.

EXPECTED OUTCOMES

This protocol describes the steps for staining and imaging microvilli composed of F-actin present on the apical caps of the syncytial *Drosophila* blastoderm embryo. A greater density of microvilli are visible at the periphery of each apical cap as compared to the center (Sherlekar et al., 2020). Microvilli are visible with both confocal and super-resolution STED microscopy. This protocol enables the documentation of density and length of microvilli in each actin cap, and recommends an analysis of microvilli remodeling in syncytial cycles 11 and 12. Since the remodeling process takes place from interphase to metaphase of each syncytial cycle, a comparison of density and length of microvilli in control and mutant animals at interphase and metaphase of syncytial cycles 11 and 12 provides an estimate of the extent of microvilli remodeling.

QUANTIFICATION AND STATISTICAL ANALYSIS

Identification of the nuclear division cycle number in fixed and stained embryos.

1. Draw a region of interest (ROI) as shown in Figure 3B, along the boundaries of the apical caps to form a closed area shown in yellow using the "Polygon Selection" tool in ImageJ.
2. Save the ROI and measure the area covered by the ROI using ROI Manager.

Measure at least 3–5 caps for each embryo and a minimum of 3 embryos at each stage.

3. Use the cap area information in Table 3 for estimating the apical cap areas in each nuclear cycle to determine the nuclear division cycle number for each embryo.

Note: Since the actin cap is a dome-shaped structure, the cap area will vary based on the optical plane of imaging.

Table 3. Apical cap area range in syncytial nuclear cycles 10–13

Nuclear cycle	10	11	12	13
Cap area range[a]	>240 μm^2	120–240 μm^2	80–120 μm^2	40–80 μm^2

[a]Area ranges identified are approximate.

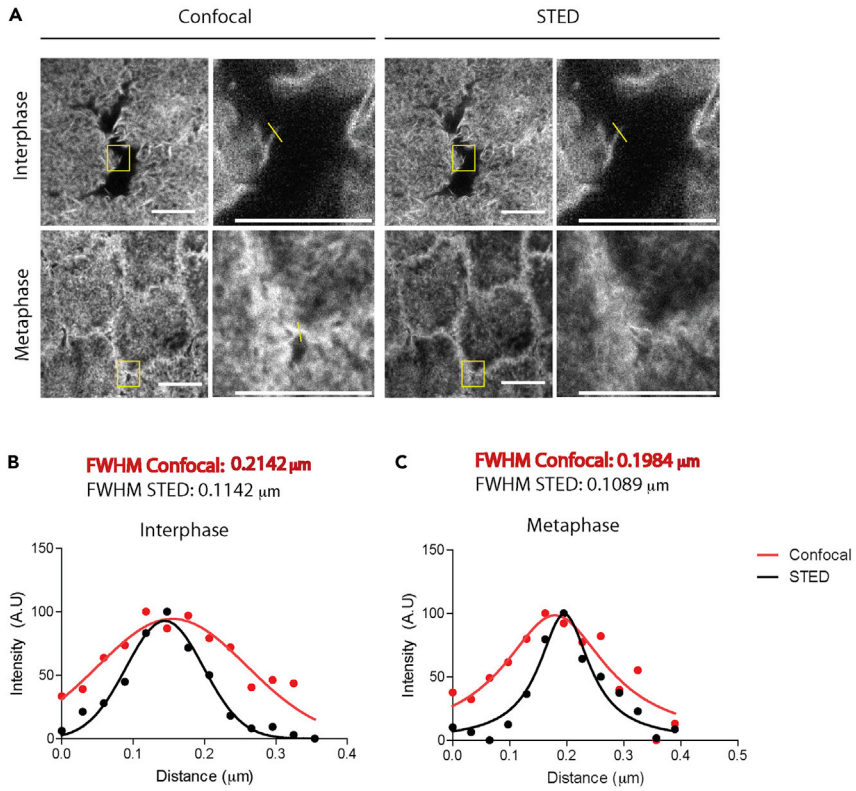

Figure 4. Comparison of confocal and STED super resolution images of apical caps

(A) Comparison of confocal and non-deconvolved super-resolution images of apical actin caps in nuclear cycle 12 of the syncytial *Drosophila* embryo, Scale bar: 5 µm. A section is zoomed in to show the apical microvilli. Scale bar: 5 µm. An ROI is drawn across a single microvillus and used to plot its intensity profile.

(B) Intensity profile of one microvillus at interphase obtained from confocal (red) and STED (black) imaging. Full-width at half-maximum (FWHM) values are calculated for both.

(C) Intensity profile of a microvillus at metaphase obtained from confocal (red) and STED (black) imaging. Full-width at half-maximum (FWHM) values are calculated for both.

Quantification of Full-Width at half maximum (FWHM)

4. Draw an ROI across a single microvillus (yellow line in Figures 4A and 5A) using the "Segmented Line" tool in ImageJ.
5. Select the "Plot Profile" option under the "Analyze" tab which plots the intensity of the pixels along the length of the ROI. Save the data of coordinates (x) and intensities (y).
6. Plot the data in GraphPad Prism as a scatter and fit a Gaussian distribution to the scatterplot (Figures 4B and 5B).
7. Input the data into MATLAB R2021b and run the code available publicly at https://www.mathworks.com/matlabcentral/fileexchange/10590-fwhm.

The output is the Full-Width at Half-Maximum (FWHM) of the Gaussian distribution waveform y(x) and its polarity.

Quantification of microvilli length and number

8. Draw an ROI along the length of the microvilli (yellow lines in Figure 6A) using the "Segmented Line " tool in ImageJ.
9. Count as many microvilli as can be observed in sharp focus emanating from one apical cap.

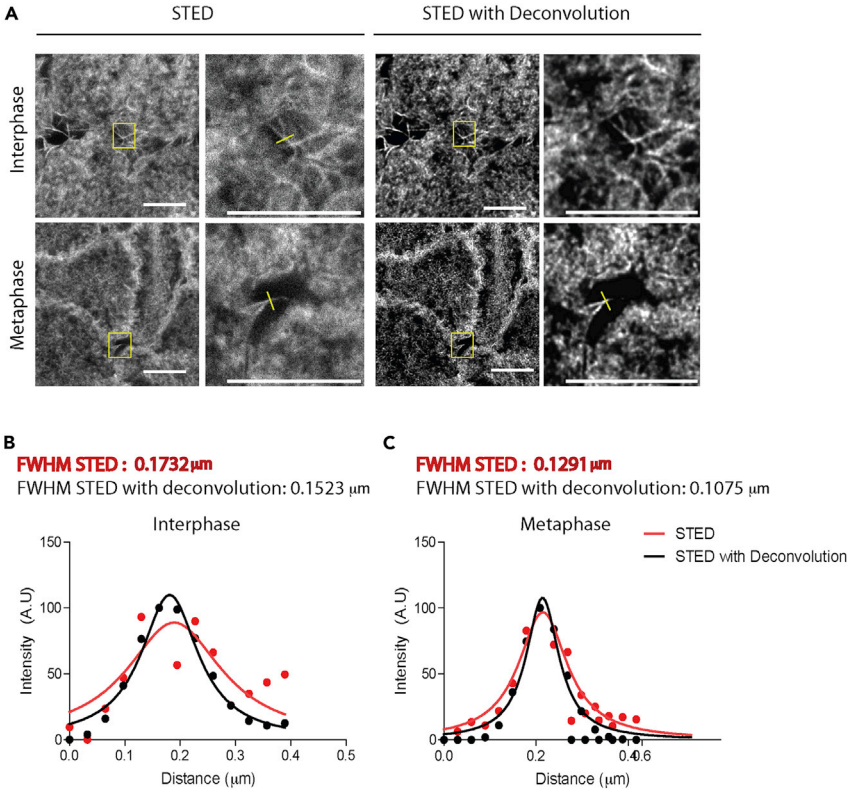

Figure 5. Analysis of STED super resolution images with deconvolution

(A) Comparison of acquired and deconvolved super-resolution images of apical actin caps in nuclear cycle 12 of the syncytial *Drosophila* embryo, Scale bar: 5 µm. A section is zoomed in to show the apical microvilli. Scale bar: 5 µm. An ROI is drawn across a single microvillus and is used to plot its intensity profile.

(B) Intensity profile of a microvillus at interphase obtained from STED imaging (red) and the STED image with deconvolution (black). Full-width at half-maximum (FWHM) values are calculated for both.

(C) Intensity profile of a microvillus at metaphase obtained from STED imaging (red) and the STED image with deconvolution (black). Full-width at half-maximum (FWHM) values are calculated for both.

Note: This quantification is possible from the deconvolved STED images and confocal images.

10. Repeat this for each apical cap that is fully visible in the image from the deconvolved super-resolution images and confocal images (Figure 6).
11. Save the ROIs and measure the length of each ROI. These are the length measurements for each microvillus.
12. Note also the number of ROIs per cap. These are the number of microvilli for each cap.
13. Save the measurements and plot the microvilli lengths and microvilli numbers per cap at interphase and metaphase in GraphPad Prism (Figures 6B–6E).

LIMITATIONS

The limitation of this method is the ability to only capture apical microvilli in a single focal plane of the apical cap which is a three-dimensional dome-shaped structure. The dimensions of the microvilli are dependent upon the orientation of the microvilli and the optical plane of imaging.

TROUBLESHOOTING

Problem 1

Very few embryos are obtained from embryo collections (step 1 of step-by-step method details: collection, fixation, and de-vitellinization of syncytial *Drosophila* embryos).

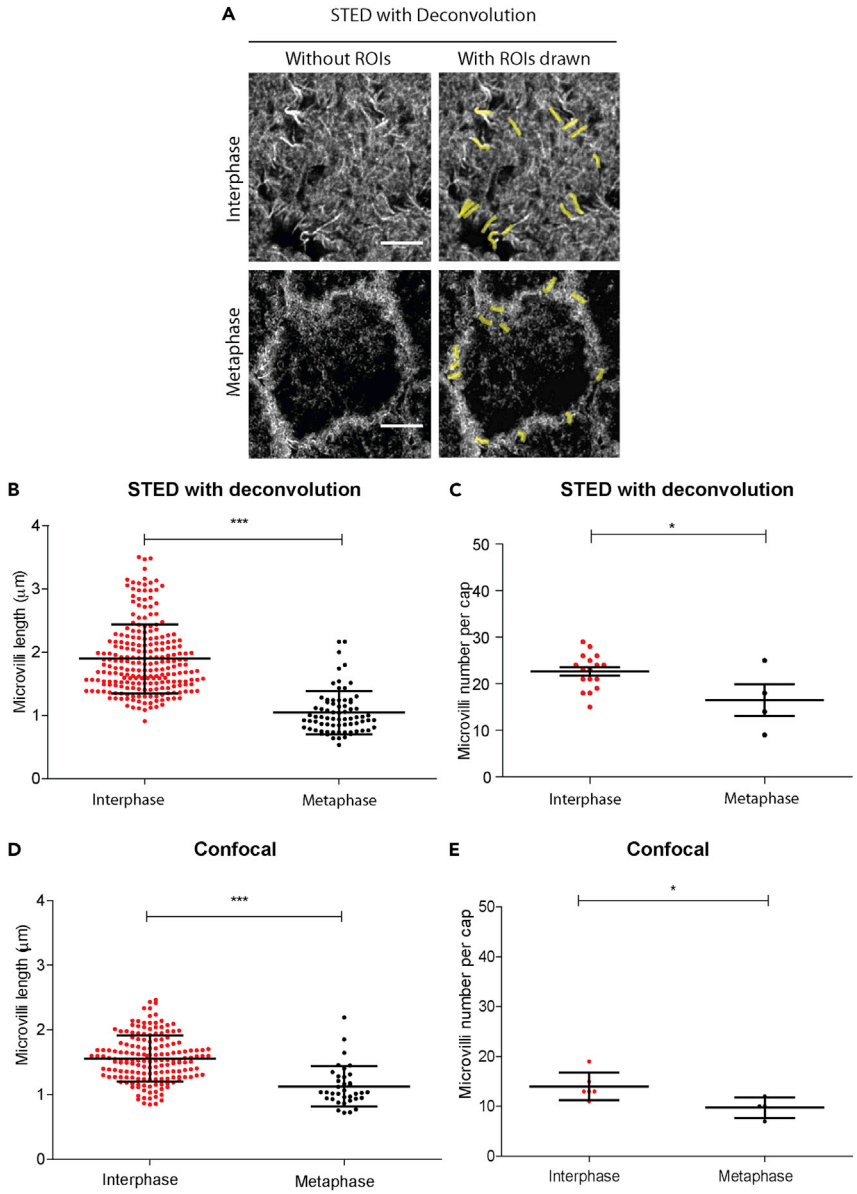

Figure 6. Quantification of microvilli lengths and number from deconvolved STED and confocal images

(A) Quantification of microvilli lengths and numbers using de-convolved super-resolution images of apical actin caps in nuclear cycle 12 of the syncytial *Drosophila* embryo. ROIs are drawn as shown in yellow along the length of each microvillus. (B and C) The lengths of microvilli (B) and numbers of microvilli per cap (C) are measured and plotted for interphase and metaphase in the deconvolved STED images. n= 2–4 cells each from 3 embryos. The range of microvilli length at interphase and metaphase as quantified from the de-convolved super-resolution images are 1.69 ± 0.342 µm and 1.04 ± 0.341 µm, respectively (B). The range of microvilli numbers at interphase and metaphase as quantified from the de-convolved super-resolution STED images are 21.17 ± 3.710 and 16.50 ± 6.758 respectively (C). Data are represented as mean ± SD, *p<0.05, **p<0.01, and ***p<0.001, two-tailed, unpaired Student's *t* test. Scale bar: 5 µm. (D and E) Quantification of microvilli lengths and numbers using confocal images of apical actin caps in nuclear cycle 12 of the syncytial *Drosophila* embryo. The lengths of microvilli (D) and numbers of microvilli per cap (E) are measured and plotted for interphase and metaphase. n= 2–3 cells each from 3 embryos. The range of microvilli length at interphase and metaphase as quantified from the confocal images are 1.45 ± 0.331 µm and 1.12 ± 0.312 µm (D). The range of microvilli numbers at interphase and metaphase as quantified from the confocal images are 14.00 ± 2.757 and 9.75 ± 2.062 respectively (E). Data are represented as mean ± SD, *p<0.05, **p<0.01, and ***p<0.001, two-tailed, unpaired Student's *t* test. Note that the numbers of villi and their lengths are reduced in the confocal images in interphase as compared to deconvolved STED images with a significance of p<0.001 possibly due to the reduced resolution.

Potential solution

Add more flies to the cage. The numbers of female flies may be increased to twice as many as the males in the cage for increasing the numbers of eggs in the collection. Also, transfer the flies into a fresh cage 6–7 days after the cage is set up. Post-transfer, allow the flies to get acclimatized to the cage for about 2–3 h before resuming egg collections.

Problem 2

Fixed embryos are too soft and disintegrate when touched by the syringe needle during de-vitellinization (step 18 of step-by-step method details: collection, fixation, and de-vitellinization of syncytial *Drosophila* embryos).

Potential solution

Allow the PFA solution to reach room temperature before using it to fix the embryos. Warmer temperatures are more likely to speed up the fixation process as the formaldehyde-methylene glycol equilibrium shifts towards formaldehyde. Formaldehyde is the active molecule that effectively facilitates tissue fixation (Winkelman et al., 2002). Fixing the embryos using a concentration of PFA that is greater than 4%, such as 8% PFA, can also be attempted. If the problem still persists, then prepare and use a fresh solution of 4% or 8% PFA.

Problem 3

The STED image has too much background noise (step 13 of step-by-step method details: confocal and super-resolution STED imaging to obtain high-resolution images of microvilli).

Potential solution

Increase the line averaging.

Problem 4

The STED image has been photobleached (step 13 of step-by-step method details: confocal and super-resolution STED imaging to obtain high-resolution images of microvilli).

Potential solution

Lower the power of the STED depletion laser by reducing its percentage.

Problem 5

The lateral resolution of microvilli in the STED images is not sufficient (step 13 of step-by-step method details: confocal and super-resolution STED imaging to obtain high-resolution images of microvilli).

Potential solution

This can be done by either increasing the line averaging up to 16 and power of STED depletion laser. Tweaking the STED beam like generating an azimuthally polarized light could also help achieve higher lateral resolution (Yang et al., 2016).

RESOURCE AVAILABILITY

Lead contact

Further information and requests for resources and reagents should be directed to and will be fulfilled by the lead contact, Richa Rikhy, richa@iiserpune.ac.in.

Materials availability

The materials used in the protocol are listed along with their source of procurement.

Data and code availability

The protocol includes all datasets generated or analyzed during this study.

SUPPLEMENTAL INFORMATION

Supplemental information can be found online at https://doi.org/10.1016/j.xpro.2022.101736.

ACKNOWLEDGMENTS

We thank the IISER, Pune, India *Drosophila* and Microscopy facility for their help with fly work and maintenance of microscopes. D.M. thanks the Council of Scientific and Industrial Research for funding her graduate fellowship. A.S. thanks the Department of Science and Technology for INSPIRE-SHE fellowship. R.R. thanks the Department of Biotechnology BT/PR17317/BRB/10/1521/2016 for funding this project.

AUTHOR CONTRIBUTIONS

D.M., A.S., G.M., and R.R. designed the experiments, performed experiments, and carried out the data analysis for the project. D.M., A.S., and R.R. wrote the manuscript. R.R. obtained funding for the project.

DECLARATION OF INTERESTS

The authors declare no competing interests.

REFERENCES

Foe, V.E., and Alberts, B.M. (1983). Studies of nuclear and cytoplasmic behaviour during the five mitotic cycles that precede gastrulation in *Drosophila* embryogenesis. J. Cell Sci. *61*, 31–70.

Karr, T.L., and Alberts, B.M. (1986). Organization of the cytoskeleton in early *Drosophila* embryos. J. Cell Biol. *102*, 1494–1509.

Mavrakis, M., Rikhy, R., and Lippincott-Schwartz, J. (2009). Plasma membrane polarity and compartmentalization are established before cellularization in the fly embryo. Dev. Cell *16*, 93–104.

Rueden, C.T., Schindelin, J., Hiner, M.C., DeZonia, B.E., Walter, A.E., Arena, E.T., and Eliceiri, K.W. (2017). ImageJ2: ImageJ for the next generation of scientific image data. BMC Bioinf. *18*, 529.

Schindelin, J., Arganda-Carreras, I., Frise, E., Kaynig, V., Longair, M., Pietzsch, T., Preibisch, S., Rueden, C., Saalfeld, S., Schmid, B., et al. (2012). Fiji: an open-source platform for biological-image analysis. Nat. Methods *9*, 676–682.

Sherlekar, A., Mundhe, G., Richa, P., Dey, B., Sharma, S., and Rikhy, R. (2020). F-BAR domain protein Syndapin regulates actomyosin dynamics during apical cap remodeling in syncytial *Drosophila* embryos. J. Cell Sci. *133*, jcs235846. https://doi.org/10.1242/jcs.235846.

Turner, F.R., and Mahowald, A.P. (1976). Scanning electron microscopy of Drosophila embryogenesis. 1. The structure of the egg envelopes and the formation of the cellular blastoderm. Dev. Biol. *50*, 95–108.

Warn, R.M., Bullard, B., and Magrath, R. (1980). Changes in the distribution of cortical myosin during the cellularization of the Drosophila embryo. Development *57*, 167–176. https://doi.org/10.1242/dev.57.1.167.

Warn, R.M., Magrath, R., and Webb, S. (1984). Distribution of F-actin during cleavage of the *Drosophila* syncytial blastoderm. J. Cell Biol. *98*, 156–162. https://doi.org/10.1083/jcb.98.1.156.

Winkelman, J.G.M., Voorwinde, O.K., Ottens, M., Beenackers, A.A.C.M., and Janssen, L.P.B.M. (2002). Kinetics and chemical equilibrium of the hydration of formaldehyde. Chem. Eng. Sci. *57*, 4067–4076. https://doi.org/10.1016/s0009-2509(02)00358-5.

Yang, H., Zhang, Y., Xiao, Y., Gao, F., Chang, J., Wei, T., and Jiang, S. (2016). Generation and comparison of donut-shaped depletion beams in STED microscopy. Optik *127*, 3735–3739. https://doi.org/10.1016/j.ijleo.2015.12.151.

Biophysical *Journal*
Article

Biophysical Society

Pseudocleavage furrows restrict plasma membrane-associated PH domain in syncytial *Drosophila* embryos

Sameer Thukral,[1] Bivash Kaity,[2] Debasmita Mitra,[1] Bipasha Dey,[1] Pampa Dey,[2] Bhavin Uttekar,[1] Mithun K. Mitra,[2,*] Amitabha Nandi,[2,*] and Richa Rikhy[1,*]

[1]Biology, Indian Institute of Science Education and Research, Pashan, Pune, India and [2]Department of Physics, Indian Institute of Technology Bombay, Mumbai, India

ABSTRACT Syncytial cells contain multiple nuclei and have local distribution and function of cellular components despite being synthesized in a common cytoplasm. The syncytial *Drosophila* blastoderm embryo shows reduced spread of organelle and plasma membrane-associated proteins between adjacent nucleo-cytoplasmic domains. Anchoring to the cytoarchitecture within a nucleo-cytoplasmic domain is likely to decrease the spread of molecules; however, its role in restricting this spread has not been assessed. In order to analyze the cellular mechanisms that regulate the rate of spread of plasma membrane-associated molecules in the syncytial *Drosophila* embryos, we express a pleckstrin homology (PH) domain in a localized manner at the anterior of the embryo by tagging it with the *bicoid* mRNA localization signal. Anteriorly expressed PH domain forms an exponential gradient in the anteroposterior axis with a longer length scale compared with Bicoid. Using a combination of experiments and theoretical modeling, we find that the characteristic distribution and length scale emerge due to plasma membrane sequestration and restriction within an energid. Loss of plasma membrane remodeling to form pseudocleavage furrows shows an enhanced spread of PH domain but not Bicoid. Modeling analysis suggests that the enhanced spread of the PH domain occurs due to the increased spread of the cytoplasmic population of the PH domain in pseudocleavage furrow mutants. Our analysis of cytoarchitecture interaction in regulating plasma membrane protein distribution and constraining its spread has implications on the mechanisms of spread of various molecules, such as morphogens in syncytial cells.

SIGNIFICANCE Syncytial cells are large cells containing multiple nuclei formed by cell fusion or incomplete cytokinesis. Syncytial cells of the *Drosophila* embryo do not have complete plasma membrane boundaries around each nucleus and show a restricted spread of molecules around each nucleo-cytoplasmic domain. In this study, we express the plasma membrane-associated PH domain in a localized manner in the anterior of syncytial *Drosophila* embryos. The plasma membrane association produces an anteroposterior gradient of the PH domain, and this distribution is disrupted in pseudocleavage furrow remodeling mutants. Our experimental and theoretical results show that loss of restriction of diffusion of the cytoplasmic pool of the PH domain in these mutants leads to an increase in its spread across the embryo.

INTRODUCTION

Syncytial cells in plant and animal tissue are large cells containing multiple nuclei formed by incomplete cell division or cell fusion. Even though plasma membrane boundaries do not separate the syncytial nuclei, each nucleus has a nucleo-cytoplasmic region of influence with discrete function. Muscle cells show myo-nuclear domains of restricted diffusion, where proteins and mRNA produced by one nucleus are constrained near its vicinity (1,2). In fungi, sister nuclei in syncytial cells formed after a division maintain synchrony despite losing proximity and being present in a common cytoplasm (3,4). Nuclei and organelles are inherited from mother to daughter nucleo-cytoplasmic domains in a lineage-specific manner in syncytial *Drosophila* embryos (5–7). Thus, key molecules such as activated receptors, transcription factors, cell cycle molecules, and mRNA are locally produced and inhomogeneously maintained in syncytia.

Submitted November 23, 2021, and accepted for publication May 13, 2022.

*Correspondence: mithun@phy.iitb.ac.in or amitabha@phy.iitb.ac.in or richa@iiserpune.ac.in

Editor: Dimitrios Vavylonis.

https://doi.org/10.1016/j.bpj.2022.05.015

Various cellular mechanisms are likely to restrict molecular spread between adjacent nucleo-cytoplasmic domains, also called energids, in syncytial cells. In syncytial fungal hyphae, nuclear asynchrony is regulated by the inhomogeneous distribution of unstructured aggregation-prone proteins and cyclin transcripts (8). Molecules within lumens of subcellular organelles such as endoplasmic reticulum (ER) and associated with the plasma membrane above each nucleus mix freely within each energid of syncytial *Drosophila* embryos and show decreased diffusion across neighboring domains (5,6,9). Disruption of the microtubule and actin cytoskeleton leads to loss of restriction of ER lumenal molecules and plasma membrane-associated molecules respectively (5,9). However, it remains to be tested whether this increase in spread occurs due to an increase in the diffusion of free or bound populations of the molecule.

The apical and lateral plasma membrane domains belonging to each nucleo-cytoplasmic domain of the syncytial *Drosophila* blastoderm embryo show distinct morphology and localization of molecules (9). Moreover, photobleaching and photoactivation experiments show a restricted diffusion of plasma membrane-associated molecules across adjacent nucleo-cytoplasmic domains. Association with the plasma membrane and restriction of diffusion due to the presence of lateral furrows is likely to constrain the spread of plasma membrane-associated molecules and has not yet been analyzed. Metaphase furrows are likely to be important for constraining the spread of morphogens such as Dorsal, which is in the nucleus in interphase and cytoplasm in metaphase of the syncytial cycles (10). In this study, we use the syncytial *Drosophila* embryo to assess the rate of spread of plasma membrane-associated molecules by a new method by expressing them from a localized anterior source in the anteroposterior (AP) axis. We analyzed the role of lateral furrows in constraining its spread.

The Bicoid (Bcd) gradient is produced in the AP axis from the anteriorly localized *bcd* mRNA with the *bcd*-3′ UTR sequence in oogenesis and embryogenesis (11,12). Adding the *bcd*-3′ UTR to another transcription factor, Smaug, results in an AP gradient of Smaug (13). Contrarily, adding the *bcd*-3′ UTR to cytoplasmic GFP and mCherry leads to the uniform spread of GFP and mCherry and fails to form a gradient (14,15). Therefore, anchoring genes with the *bcd*-3′ UTR can be used to create an anteriorly localized protein source and study its kinetics and mechanisms of spread in the AP axis during syncytial cycles. Here, we analyze the AP spread of fluorescently tagged plasma membrane-associated pleckstrin homology (PH) domain produced from mRNA localized anteriorly using the *bcd*-3′ UTR sequence. We find that the anteriorly expressed PH domain associated with the plasma membrane forms an exponential gradient with a longer length scale than Bicoid. Using a combination of experiments and theory, we find that restriction of plasma membrane-bound and cytoplasmic pools of PH domain to an energid contribute to an effective diffusion, leading to the observed gradient. Disruption of pseudocleavage furrows in mutants leads to increased spread of the PH domain in the AP axis. Computational modeling shows that the flattening of the anteriorly expressed PH-domain gradient on the loss of furrows occurs due to the loss of cytoplasmic restriction.

MATERIALS AND METHODS

Drosophila stocks

Fly stocks were maintained at 25°C on standard cornmeal agar. All crosses were at 25°C except with *ralA* RNAi (29°C). *mat-gal4-vp16*; *mat-gal4-vp16* (made using w[*]; P{w[+mC] = matalpha4-GAL-VP16}V2H, Bloomington stock number #7062) and *nanos*-Gal4 (w1118; P{GAL4:VP16-nos.UTR}CG6325^{MVD1}, #4937) were used for *ralA* RNAi and RhoGEF2 overexpression studies. *ralA* RNAi (y[1] sc[*] v[1] sev [21]; P{y[+t7.7] v[+t1.8] = TRiP.HMS01365}attP2/TM3, Sb[1] #34375) and RhoGEF2-OE (y[1] w[*]; P{w[+mC] = UASp-T7.RhoGEF2}5, #9386) were obtained from consultation with Flybase (16) and Bloomington stock center, Indiana, USA (17). Bicoid-Venus was provided by Eric Wieschaus and Thomas Gregor (Princeton, PA, USA). Transgenic flies containing the construct UASp-PH-PLC-CFP-*bcd*-3′ UTR were created as described below.

Transgenic flies

PH-PLC-CFP was cloned in pUASp previously using the primers CGGGGTACCATGGACTCGGGCCGGGACTTCC and ATAAGAATGC GGCCGCTTTACTTGTACAGCTCGTCCATGC (9) and cut using KpnI and NotI and inserted into UASp.

mRFP (RFP) was inserted into the UASp construct at the Kpn1 and Not1 restriction site using primers GGGGTACCATGGCCTCCTCCGAGGAC and ATTTGCGGCCGCTTAGGCGCCGGTGGAGTG.

The *bcd* gene-containing plasmid with the 3′ UTR was a kind gift from Elizabeth Gavis (Princeton, PA, USA). The *bcd*-3′ UTR was PCR amplified using primers CATGGCGGCCGCTGGACGAGAGGCGTGTT or CATG TCTAGATGGACGAGAGGCGTGTT and CACTTCTAGAGGACGGAA ATATGGGCTA and cut using NotI and/or XbaI and inserted in the UASp constructs containing mRFP/PH-PLC-CFP obtained as described above. All constructs were confirmed by sequencing. Injection of UASp plasmids into *Drosophila* embryos and selection of transgenic animals was done by the NCBS transgenic injection facility, Bangalore, India.

Imaging

The 1.5-h-old embryos were collected on sucrose agar plates, washed, dechorionated using 100% bleach, mounted on coverglass chambers (LabTek, Germany) in PBS, and imaged on Plan-Apochromat 25×/0.8 oil immersion to obtain whole-embryo images or Plan-Neofluar 40×/1.30 oil objective to obtain zoomed-in images from embryos and fluorescence recovery after photobleachings (FRAPs) on Zeiss LSM780 or LSM710 systems. CFP and Venus tags were excited using 458- and 514-nm laser lines respectively. Scan speed was maintained at 0.7 to 2 s per frame. Mid-sagittal sections were imaged for both live and fixed embryos. The laser power was maintained in a similar range between controls and mutants. Eight-bit images were acquired with a line averaging of two, with a minimum interval between images until cellularization was completed for each embryo. Gain and laser power were adjusted to cover the dynamic range of each fluorescent tag. The pinhole was kept open at 170 μm with an optical thickness of

33.2 μm for Venus based tags, or 90 μm with an optical thickness of 17.6 μm for fixed imaging.

For each of the gradients (Bicoid-Venus and PH-PLC-CFP), we imaged multiple embryos sequentially using the multiple position imaging. The imaged embryos were then screened visually for the presence of the gradient and the gradient was quantified as illustrated (Fig. S1). In the case of PH-PLC-CFP gradients, we selected embryos that showed a consistent length scale along both the dorsal and ventral sides of the embryo, and whose corresponding Bicoid profiles yielded length scales comparable with previous estimates in the literature. There was a sub-population that yielded extremely large length scales in one direction for both Bicoid and PH-PLC-CFP, which were excluded from our analysis. Briefly, line profiles (10 or 20 pixels/1 or 2 μm wide) were drawn across the cortex in the AP axis in the dorsal and ventral sides. The two profiles were fitted independently to extract length scales. Embryos with the two length scales within 20% of each other were selected to be included for analysis.

For analysis of gradients (PH-PLC-CFP and Bicoid-Venus) with mutant backgrounds, we imaged multiple embryos using multiple position imaging. Imaged embryos were screened visually for the presence of a gradient. Mutant embryos with loss of pseudocleavage furrows showed embryo-wide contractions and gradients were quantified after selection of live mutant embryos containing this phenotype. The length scale for all gradients was observed to evolve across syncytial cycles.

Immunohistochemistry

F1 flies were selected from Gal4 and fluorescent construct/mutant crosses and transferred to embryo collection cages (Genesee Scientific, CA, USA) with 2.5% sucrose agar supplemented with yeast paste. Embryos were washed, dechorionated using 100% bleach for 1 min, washed, and fixed in heptane: 4% paraformaldehyde (PFA) (1:1) in PBS (137 mM NaCl, 2.7 mM KCl, 10 mM Na_2HPO_4, 1.8 mM KH_2PO_4) for 20 min at room temperature. Ovaries were dissected in Schnieders medium and fixed with 4% PFA in PBS for 20 min. Embryos were devitellinized by vigorously shaking in heptane:methanol (1:1) for anti-Bicoid immunostaining or hand devitellinized for actin staining with fluorescently tagged phalloidin. Blocking for embryos and ovaries was done using 2% bovine serum albumin (BSA) in PBS with 0.3% Triton X-100 (PBST). The following primary antibodies were diluted in the block solution: anti-Bicoid (rabbit, SantaCruz, 1:500), anti-GFP (chicken, Life Technologies, 1:1,000). Fluorescently coupled secondary antibodies (Alexa Fluor 488, 568, 647 coupled anti-rabbit and anti-chicken, Molecular Probes, Bangalore, India) were used at 1:1,000 dilution in PBST. Fluorescently tagged phalloidin (1:100, Molecular Probes, Bangalore, India) was added with secondary antibodies. DNA was labeled using Hoechst 33342 (1:1,000, Molecular Probes, Bangalore, India). Embryos were imaged using LD LCI Plan-Apochromat 25×/0.8 Imm Korr DIC M27 objective on the Zeiss LSM710/780.

Quantification of furrow length, cap area, and oocyte fluorescence

Four-dimensional videos of PH-PLC-CFP-expressing embryos were used for quantification of furrow length and cap area. Cap area was measured using the segmented tool in ImageJ from projected views for five caps for time point from interphase to metaphase of syncytial cycle 13 from each embryo. Furrow length was measured from five furrows from each embryo at cap edges from each time point from interphase to metaphase and plotted.

Anteriorly expressing PH-PLC-CFP containing oocytes between stage 7 and 9 egg chambers were stained with fluorescently coupled phalloidin and used to quantify mean CFP and phalloidin fluorescence intensity in the anterior and posterior membrane of each oocyte respectively. A ratio of the anterior membrane fluorescence to the posterior membrane fluorescence was obtained for each oocyte and plotted.

Quantitation of gradient profiles

For quantification of gradient profiles, segmented lines of 10 or 20 pixels (1 or 2 μm width) were drawn across the cortex from the anterior to the posterior, either on the dorsal side or the ventral side of the embryo. Line profile measurements for embryo length and intensity values were obtained using ImageJ and Fiji (18–20). The process was multiplexed across multiple embryos using ImageJ macros. A MATLAB script was used to extract the gradients from the generated files. Normalized intensity (arbitrary units [a.u.]) refers to values obtained after processing raw fluorescent intensity values using the MATLAB script. The script was written to 1) normalize the embryo length on a 0 to 1 scale in the AP axis to represent multiple embryos, 2) rescale the fluorescence intensity to the maximum value followed by smoothening of the intensity values using a sliding window averaging method to represent multiple embryos (Figs. 1 *F* and *G*, and S5 *B* and *D*).

The actual intensity is displayed in Figs. 1 *E* (inset) and 3 *B*.

Fitting and length scale estimation

The experimental intensity profiles for all gradients were analyzed after excluding the anterior-most region that had significant fluctuations, as suggested previously (21) (the method is shown in Fig. S1). Gradient profiles for the PH-PLC-CFP were initially analyzed using a simple exponential decay of the form $Ae^{-x/\lambda} + B$ to the profile during nuclear cycle (n.c.) 13 to extract an instantaneous length scale λ (Fig. 1 *G*).

Sampling and statistics

Terminal or multiple time points from across the syncytial cycles from at least three (or more) embryos were imaged and quantified for each experiment, as indicated in the corresponding figure legends. Two-tailed nonparametric Mann-Whitney test was used. Graphpad Prism 5.0 was used for statistical analysis and plotting.

Estimation of energid length and furrow length

In order to determine the energid length, we calculate the separation between adjacent furrows (denoted by local peaks in the intensity profile) through two different methods:

- Direct identification of peaks: from an experimentally determined intensity profile, we use the MATLAB function "findpeaks" to determine the locations of local maximum intensity. In order to identify the peaks, we set a minimum peak separation (MinPeakDistance) at 3 μm and minimum peak prominence (MinPeakProminence) varies from 0.13 to 0.2 depending on the nuclear cycle. The peak prominence of intensity profile is high at n.c.11 compared with n.c.13. Therefore, we used MinPeakProminence of 0.2 for cycle 11, 0.15 for cycle 12, and 0.13 for cycle 13.

The combined peak-to-peak separation values for all furrows for both the dorsal and ventral profiles across all embryos ($n = 5$) are used to calculate the mean and standard deviation values using this method.

- Fast Fourier transform (FFT) of intensity profile: an alternate method to identify the energid length is to compute the Fourier transform of the experimentally measured intensity profiles. In comparison with the direct method, this method has the advantage that no a priori assumptions regarding minimum peak separations or peak prominences are required. The discrete Fourier transform was calculated using the MATLAB function "fft" on the experimental intensity profiles. In order to remove the mean value or linear trend present in the intensity profile, we performed the moving mean on a sliding window using the MATLAB function "movmean" and subtracted it from the experimentally determined profile. The location of the peak of the FFT signal for a given intensity profile along the dorsal/ventral side yields a single value for the energid

length for each embryo. The energid lengths are then averaged across all embryos (n = 5) to calculate the mean and standard deviation values.

Both methods yield comparable estimates of the average energid length across cycles. Note the peak of the FFT signal corresponds to the dominant energid length. The FFT signal also shows secondary peaks that can arise due to the contribution from furrows below and above the focal plane. The direct identification method performs an average over all identified energid lengths and hence leads to a slightly lower value than the FFT.

Furrow length estimation in n.c.13 was carried out from high-resolution videos of PH-PLC-CFP taken in the x-y direction across time. The furrow lengths were estimated across the Z axis from interphase to metaphase by drawing a region of interest (ROI) in sagittal sections from interphase to metaphase of n.c.13. Apical area was estimated by drawing an ROI on each cap and estimating the area in n.c.13 from interphase to metaphase.

Numerical solution of model equations

The partial differential equations for the free and bound sub-populations (Eq. 1) were numerically solved using MATLAB in a one-dimensional domain with a sufficiently high spatial resolution $\Delta x = 0.005\mu m$. For the bound species, we use zero-flux boundary conditions at both left and right boundaries,

$$\left.\frac{\partial C_{bound}}{\partial x}\right|_{x=0} = \left.\frac{\partial C_{bound}}{\partial x}\right|_{x=L} = 0$$

For the free species, the source boundary condition is considered at the left boundary and zero flux at the right boundary of the domain,

$$-D^{\alpha}_{free}\left.\frac{\partial C_{free}}{\partial x}\right|_{x=0} = Q \text{ and } \left.\frac{\partial C_{free}}{\partial x}\right|_{x=L} = 0$$

Further, at each furrow interface, flux balance is satisfied individually for the free and bound species.

Initial conditions for wild-type simulations

The experimental intensity profile measures the total intensity due to the sum of the free and bound PH-PLC populations. In order to solve the coupled equations for C_{free} and C_{bound}, we need an estimate of the initial concentration profile. For the wild-type (WT) simulations, since our model does not incorporate the effects of nuclear cycles, we simulate the equations within the single nuclear cycle, n.c.13. We start with the experimentally determined intensity profile at the beginning of n.c.13 as the initial condition for our simulation. To obtain the initial gradient profile for both free and bound populations from this total intensity profile (Fig. 3 *C*), we decomposed it using the following method. We use the MATLAB function "findpeaks" on the inverted intensity profile (using the same protocol as mentioned for the direct identification of peaks) to construct the lower envelope, which is then assumed to be the gradient profile for the free population. This is based on the assumption that the lower envelope roughly approximates the free concentration profile, motivated by the argument that the inter-conversion between free and bound species occurs over a timescale that is much faster compared with the timescale of gradient formation. Hence, to a first approximation, one can assume a quasi-equilibrium between the free and the bound species, which then leads to a relation between the concentrations of the free and bound species. Specifically, in the apical (non-furrow) regions, we have $\frac{C_{bound}}{C_{free}} \simeq \frac{k^a_b}{k_{ub}}$. Note that, in the apical region, this ratio is necessarily much less than 1, or else this leads to unphysically high peaks in the furrow regions. This implies that in the non-furrow regions, the total concentration profile is dominated by contributions from the free cytoplasmic component, and hence the free profile is constructed using the troughs of the experimental concentration profile, which correspond to the concentrations in the non-furrow regions.

In order to determine the bound concentration, we first determine the upper envelope of the measured profile, again using the MATLAB function findpeaks. Then the bound concentration at the furrow locations is obtained by the difference between the upper envelope and the free concentration, while, at the apical region, it is assumed to be zero. We note that our results are not significantly sensitive to this decomposition to free and bound species. The model is simulated numerically using a pdepe solver in MATLAB 2018a.

Parameter values

Measurement of the cytoplasmic diffusion coefficient for fluorescent dextrans of similar size diffusion is $D^{\alpha}_{free} = 17.5\mu m^2/s$ (22). Diffusion coefficient for the membrane-bound PH-domain proteins has been measured to be in the range of $0.8 \pm 0.2\mu m^2/s$ (23, 24) to $3.79 \pm 2.22\mu m^2/s$ (25). In our simulations, we use an approximate average of these values at $D^{\alpha}_{bound} = 2.5\mu m^2/s$. In order to incorporate compartmentalization properties leading to decrease in diffusion across adjacent energids, we use a 10-fold reduction in the diffusivities for both cytoplasmic and membrane-bound PH-PLC across energids, $D^{\beta}_{free} = 1.75\mu m^2/s$, and $D^{\beta}_{bound} = 0.25\mu m^2/s$. The total length of the one-dimensional simulation box is taken to be the average embryo length, $L = 500\mu m$. The length of a single energid is $l_E = 7\mu m$ as estimated from the embryos expressing PH-PLC-CFP (Fig. 2), while the width of the furrow (slow) region is $l_f = 1\mu m$. We assumed the degradation rate to be zero. The enhanced effective binding in the furrow regions is proportional to the excess lateral membrane, $k^l_b = k^a_b\left(1 + \frac{2h}{l_f}\right)$, where $h = 10\mu m$ is the approximate furrow length estimated from experiments (Fig. 2). The above equation is consistent with PH-PLC-CFP binding to membrane area proportional to $(l_f + 2h)$ when crossing a distance l_f in the effective one-dimensional model.

To compare our theoretical model with the experiment, we fitted our simulation results to the gradient profiles and the relative peak height obtained from the experiments at the end of the n.c.13. The strength of the source was chosen to be $Q = 1s^{-1}$, in order to match the fluorescent intensity values of the experimental profile at the end of the n.c.13. In our model, we have three free parameters: the free and bound diffusion coefficient across the energids (D^{β}_{free} and D^{β}_{bound}), and the ratio of the binding to unbinding coefficients, k^a_b/k_{ub}. To identify the right set of parameters, we performed an extensive parameter space study. For a given value of D^{β}_{bound}, which was chosen to be 10%, 25%, and 50% respectively of the D^{α}_{bounnd} value, we varied $k^a_b/k_{ub} \in [0.001, 1]$, and $D^{\beta}_{free} \in [D^{\beta}_{bound}, D^{\beta}_{free}]$. The lower bound of the compartmentalized diffusion coefficient reflects the fact that the cytoplasmic diffusion is always expected to be higher than the membrane diffusion, while the upper bound is set by the compartmentalization condition. We computed the error in the estimation of the length scale as $\Delta\lambda = \left|\frac{\lambda_{th} - \lambda_{exp}}{\lambda_{exp}}\right|$. For computing the error in the estimation of relative peak height, we first fitted the upper and lower envelopes of the experimental intensity profile with a spline function (MATLAB function "csaps" with smoothness parameter $p = 10^{-5}$). The experimental relative peak height was obtained by taking the difference between the two spline functions. The root-mean-square error (RMSE) was then computed as $\Delta peak = \sqrt{\frac{1}{N_p}\sum_{i=1}^{N_p}\left(\frac{y^i_{th} - y^i_{exp}}{y^i_{exp}}\right)^2}$, where the sum is over N_p peaks and $y^i_{th/exp}$ represents the theoretical/experimental peak height at the location of the i^{th} peak. The results are shown in Fig. S5, where, in the $k^a_b/k_{ub} - D^{\beta}_{free}$ parameter space, we have plotted $\Delta\lambda$ using a color heatmap, and $\Delta peak$ using contours lines. Our parameter space study reveals several important features. First, we note that the gradient length scale λ is mainly controlled by the cytoplasmic diffusion coefficients, while the accumulation at the furrows (relative peak heights) is mainly controlled by k^a_b/k_{ub}. Second, the bound diffusion coefficient does affect λ, but has a weak effect in the accumulation at the furrows. Finally, we note that there exists a very narrow parameter range, where the comparison with

the experiment is the best. This indicates that, within the current model framework, the choice of the parameters is not arbitrary. Based on this analysis, we choose $D^{\beta}_{bound} = 0.25\mu m^2/s$, $D^{\beta}_{free} = 1.75\mu m^2/s$, and $k^{a}_{i}/k_{ub} = 0.05 - 0.08$.

Mutant simulations

To analyze the effect of furrow mutants, we do not make a direct comparison with experimental intensity profiles, but rather compare the relative contributions of the different mechanisms by studying various limiting cases in an idealized setting. In this case, we start with an initial condition $C_{free}(t = 0) = C_{bound}(t = 0) = 0$, and evolve the system of equations for a time $T = 3$ h. Note that we neglect changes in furrow separation due to nuclear divisions in our model.

RESULTS

Anteriorly expressed fluorescently tagged PH domain shows an AP gradient

The *Drosophila* embryo begins as a syncytium with 13 nuclear division cycles occurring without cytokinesis. n.c.10–13 take place at the cortex, followed by the formation of complete cells in a process called cellularization in the interphase of n.c.14 (26,27). n.c.10–13 contain short ingressions of the plasma membrane in the form of nascent furrows between adjacent nuclei in interphase. The plasma membrane extends further to form pseudocleavage furrows in metaphase (Fig. 1 *A*). We assessed the gradient formation of an anteriorly expressed fluorescently tagged protein containing a phospholipid-binding domain. The PH domain of phospholipase C-δ (PH-PLC-δ) binds PIP2 and dynamically associates with the plasma membrane (9,28). A transgenic construct containing PH-PLC-CFP (∼48 kDa) in tandem with the *bcd*-3′ UTR, under the control of the UASp promoter, was generated and expressed in the embryo using *mat-gal4-vp16* (Fig. 1 *B*). Like Bicoid, the anteriorly expressed PH-PLC-CFP formed a gradient in the AP axis (Fig. 1 *C*; Video S1). PH-PLC-CFP with the *bcd* 3′ UTR localized to the plasma membrane in n.c.12–14 similar to the PH-PLC-CFP transgene generated without any mRNA localization sequence as reported previously (Fig. 1 *D*) (9). PH-PLC-CFP marked the apical plasma membrane and short furrows in interphase and longer pseudocleavage furrows in metaphase (Video S1). At the same time, Bicoid-Venus was present in nuclei in interphase and the cytoplasm in metaphase respectively (Fig. 1 *D*). Therefore PH-PLC-CFP binding to the plasma membrane restricts its spread and produces a gradient. This system can therefore be used to test the dependence of its spread on cytoarchitecture components.

To quantify the distribution of anteriorly expressed PH-PLC-CFP, an ROI was drawn at the cortex of the embryo across the AP axis to estimate the fluorescence in the syncytial cycles (Fig. S1 *A–D* for Bicoid and Fig. S1E–H for PH-PLC-CFP). The PH-PLC-CFP fluorescence increased in amplitude across n.c.11–13 (Fig. 1 *E*). Since PH-PLC-CFP was present on ingressing furrows, the fluorescence increased at the furrow positions in the AP axis, and the cytoplasmic intensity was seen in between adjacent furrows (Fig. 1 *E*, inset). The decrease in fluorescence was comparable when measured on the top or bottom of the embryo in AP axis (Fig. 1 *F*). It is interesting to note that, when GFP or mCherry is expressed in a similar manner with the *bcd*-3′ UTR, it distributes uniformly across the AP axis and does not form a gradient (14,15). Our repetition of the experiment with mRFP transgene containing a 3′*bcd* UTR sequence also showed a uniform distribution of mRFP and no gradient was formed (Fig. 1 *G*). The Bicoid gradient was steeper than anteriorly expressed PH-PLC-CFP in living embryos (Fig. 1 *G*; Videos S1 and S2). We calculated the gradient length scale for anteriorly expressed PH-PLC-CFP (Fig. S1). The PH-PLC-CFP and Bicoid gradients were fitted to an exponential equation $C(x) = Ae^{-x/\lambda} + B$ to obtain the instantaneous length scale λ in n.c.13 (Fig. 1 *H*). This length scale of the PH-PLC-CFP gradient was found to be significantly higher than the Bicoid gradient ($\lambda_{Bicoid} = 106 \pm 4.2\mu m$, $\lambda_{PHPLC} = 166 \pm 5.2$ μm) (Fig. 1 *I*). In summary, the anteriorly expressed plasma membrane-associated PH-PLC-CFP produces a gradient in the AP axis.

Analysis of furrow distribution in the AP axis in embryos containing the anteriorly expressed PH-PLC-CFP gradient

In order to determine the dimensions of the energid across which the PH-PLC-CFP gradient spreads in the AP axis, we estimated the distance between adjacent metaphase furrows in the AP axis and the furrow length at metaphase in energids from embryos containing PH-PLC-CFP. The intensity profile in the AP axis shows peaks of fluorescence intensity at the location of metaphase furrows indicating enrichment of PH-PLC-CFP at these locations (Figs. 2 *A* and 1 *E* inset). We observed that the number of peaks, corresponding to the number of furrows, increased across nuclear cycles with an average of 58 ± 3 peaks in n.c.13 across the AP axis in the visible plane from live embryos (Fig. 2 *B*). We estimated the distance between successive furrows in metaphase, i.e., energid length (l_E), using two different methods: a direct estimation of the distance between adjacent peaks and an FFT of the experimentally measured intensity profiles. Direct estimation of the distance between adjacent furrows as $l_E = 7.8 \pm 0.4\mu m$ for n.c.13 (Fig. 2 *C* and *D*). The FFT method yielded $l_E = 9.2 \pm 0.5\mu m$ (Fig. 2 *E* and *F*). Both the methods yielded a decrease in the energid lengths across successive nuclear cycles (Fig. 2 *D* and *F*).

To estimate the furrow length across the syncytial cycle, we imaged PH-PLC-CFP-expressing embryos in three

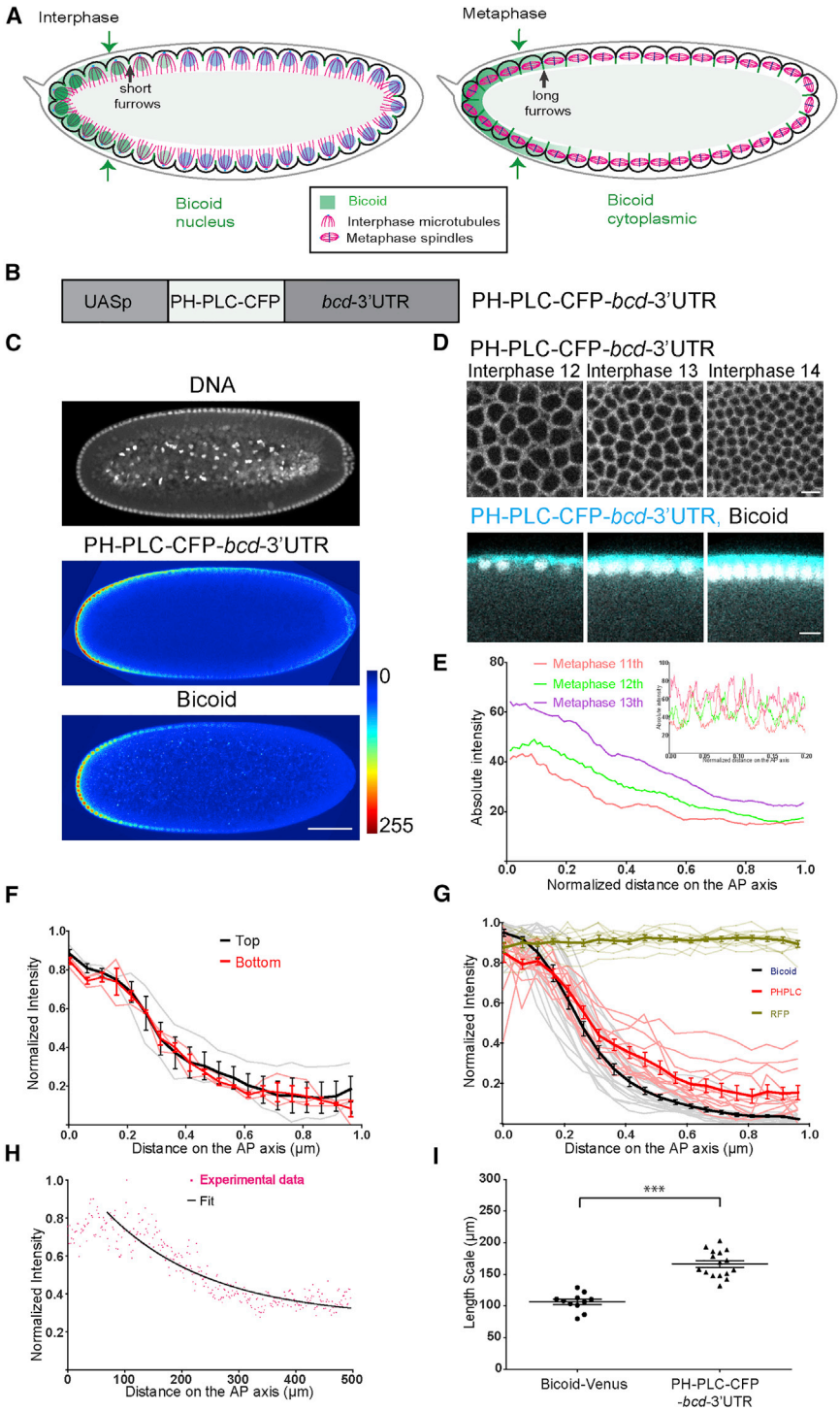

FIGURE 1 Anteroposterior (AP) gradient of anteriorly expressed PH-PLC-CFP. (*A*) Schematic of the *Drosophila* syncytial cycle showing interphase and metaphase stage of n.c.11–13. The interphase stage has plasma membrane ingressions (black) forming short furrows with the centrosome in apical regions. The metaphase stage has longer furrows (apical black and lateral green) separating adjacent spindles (magenta). The centrosome (blue) is present apically in the interphase and spindles are oriented horizontally in metaphase. Bicoid (green gradient, more intense in the nucleus compared with the cytoplasm in interphase and in the cytoplasm in metaphase) is present in the anterior region up to approximately 40% of the AP axis in the nucleus in interphase and cytoplasm in metaphase. The green arrow represents the length scale of the Bicoid gradient. (*B*) Schematic shows the anteriorly localized PH-PLC-CFP construct containing UASp promoter, PH domain of PH-PLC fused to CFP, and the *bcd*-3′ UTR sequence. (*C*) Anteriorly expressed PH-PLC-CFP shows a gradient in the AP axis. Embryos expressing anteriorly localized PH-PLC-CFP are immunostained with Bicoid antibodies and representative images are shown in the 16-color rainbow scale. (*D*) Images from the surface and sagittal views of anteriorly expressed, PH-PLC-CFP, which localizes to the apical membrane and lateral furrows, and Bicoid-Venus, which is present in the nucleus in interphase during n.c.12–14. Scale bar, 10 μm. (*E*) Smoothened fluorescence intensity of anteriorly expressed PH-PLC-CFP is shown with a normalized AP axis in metaphase of n.c.11–13. Inset shows the fluorescence intensity traces across approximately 100 μm. The profiles were similar in n = 6 embryos. (*F*) Graph shows the gradient of anteriorly expressed PH-PLC-CFP in the AP axis measured in the axis on the top of the embryo versus the bottom of the embryo (n = 3 embryos at the top and bottom each). (*G*) Graph shows normalized averaged intensity profiles of anteriorly expressed mRFP, PH-PLC-CFP, and Bicoid-Venus in the AP axis (individual embryos shown in light red for PH-PLC-CFP, light gray for Bicoid; mean ± SEM shown in red for PH-PLC-CFP; black for Bicoid) (n = 10, 5 embryos containing anteriorly expressed mRFP, n = 12, 7 embryos containing anteriorly expressed PH-PLC-CFP, 17, 9 embryos marked for Bicoid; a.u., arbitrary units). (*H* and I) Normalized fluorescence intensity (red dots) is plotted on the AP axis (μm) for n.c.13 for anteriorly expressed PH-PLC-CFP and the fit of the data (black line) with exponential decay equation (*G*). Length scale values for Bicoid and PH-PLC-CFP are plotted (*H*) (mean ± SEM, n = 11, 6 Bicoid, 16, 8 PH-PLC-CFP, two-tailed non-parametric Mann-Whitney test, $p < 0.0001$).The 16-color-intensity rainbow scale contains blue as the lowest intensity and red as the highest intensity.

dimensions over time at a higher resolution (Fig. 2 *G*). The furrow length and apical area increased from interphase to metaphase in n.c.13 (Figs. 2 *H*, and S2 *A* and *B*). Furrow length was $9.6 \pm 0.3 \mu m$ in the metaphase compared with $3.7 \pm 0.2 \mu m$ during the interphase of n.c.13 (Fig. 2 *I*). These morphometric observations were used as input parameters to model the gradient formation (see section "materials and methods").

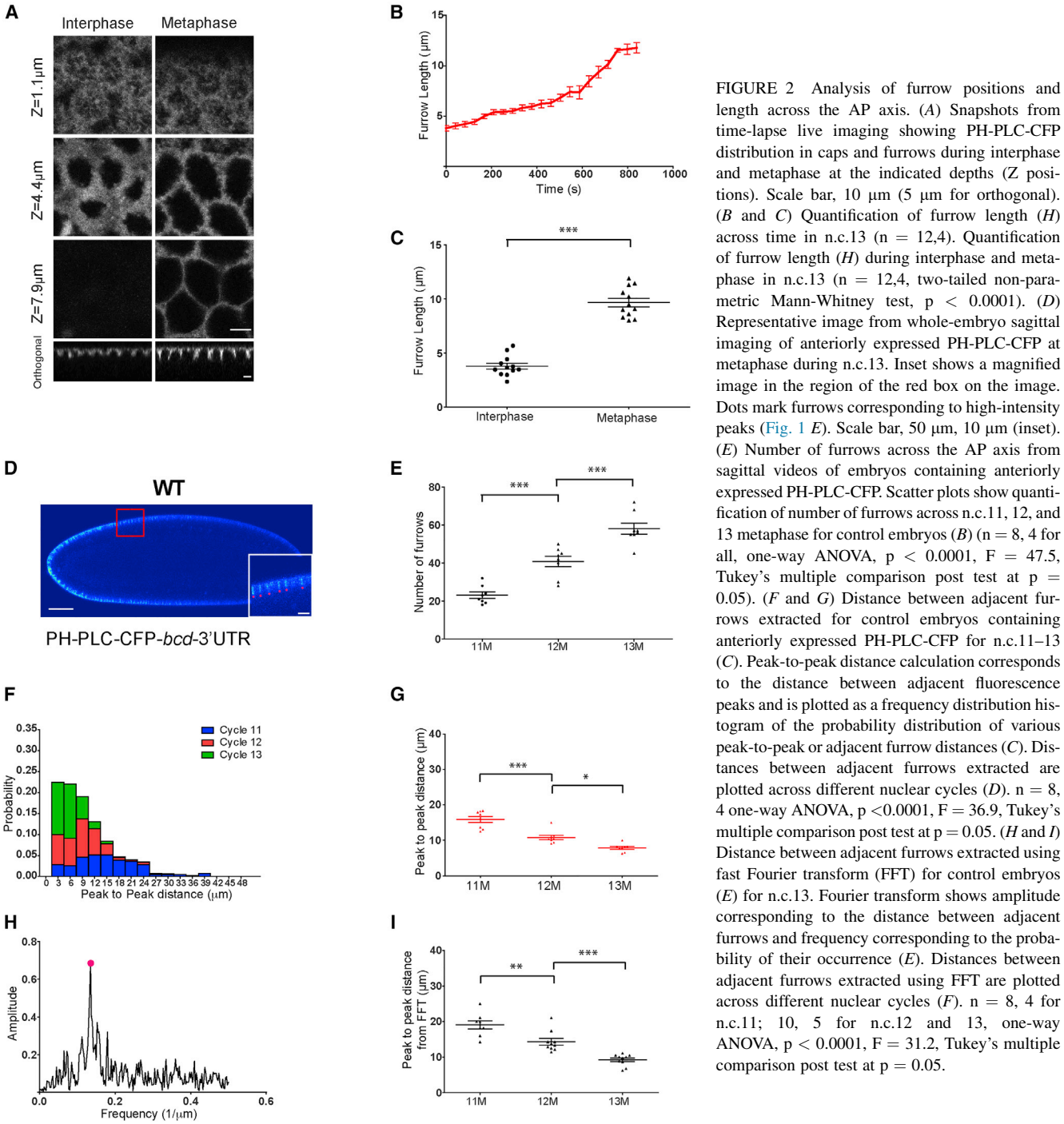

FIGURE 2 Analysis of furrow positions and length across the AP axis. (*A*) Snapshots from time-lapse live imaging showing PH-PLC-CFP distribution in caps and furrows during interphase and metaphase at the indicated depths (Z positions). Scale bar, 10 μm (5 μm for orthogonal). (*B* and *C*) Quantification of furrow length (*H*) across time in n.c.13 (n = 12,4). Quantification of furrow length (*H*) during interphase and metaphase in n.c.13 (n = 12,4, two-tailed non-parametric Mann-Whitney test, $p < 0.0001$). (*D*) Representative image from whole-embryo sagittal imaging of anteriorly expressed PH-PLC-CFP at metaphase during n.c.13. Inset shows a magnified image in the region of the red box on the image. Dots mark furrows corresponding to high-intensity peaks (Fig. 1 *E*). Scale bar, 50 μm, 10 μm (inset). (*E*) Number of furrows across the AP axis from sagittal videos of embryos containing anteriorly expressed PH-PLC-CFP. Scatter plots show quantification of number of furrows across n.c.11, 12, and 13 metaphase for control embryos (*B*) (n = 8, 4 for all, one-way ANOVA, $p < 0.0001$, $F = 47.5$, Tukey's multiple comparison post test at $p = 0.05$). (*F* and *G*) Distance between adjacent furrows extracted for control embryos containing anteriorly expressed PH-PLC-CFP for n.c.11–13 (*C*). Peak-to-peak distance calculation corresponds to the distance between adjacent fluorescence peaks and is plotted as a frequency distribution histogram of the probability distribution of various peak-to-peak or adjacent furrow distances (*C*). Distances between adjacent furrows extracted are plotted across different nuclear cycles (*D*). n = 8, 4 one-way ANOVA, $p < 0.0001$, $F = 36.9$, Tukey's multiple comparison post test at $p = 0.05$. (*H* and *I*) Distance between adjacent furrows extracted using fast Fourier transform (FFT) for control embryos (*E*) for n.c.13. Fourier transform shows amplitude corresponding to the distance between adjacent furrows and frequency corresponding to the probability of their occurrence (*E*). Distances between adjacent furrows extracted using FFT are plotted across different nuclear cycles (*F*). n = 8, 4 for n.c.11; 10, 5 for n.c.12 and 13, one-way ANOVA, $p < 0.0001$, $F = 31.2$, Tukey's multiple comparison post test at $p = 0.05$.

Analysis of the role of membrane binding and cytoplasmic pools of anteriorly expressed PH-PLC-CFP in gradient formation

PH-PLC-CFP binds to PIP2-rich regions in the plasma membrane, leading to a sub-population of membrane-bound PH-PLC-CFP. This bound species has enhanced accumulation at the apical and lateral membrane, likely contributing to the gradient shape (29). Furrows also serve as barriers leading to reduced exchange of plasma membrane-associated proteins and cytoplasmic proteins between neighboring energids (9,10,30). Previous modeling using particle-based simulation approaches suggests that an increase in pseudocleavage furrows in the syncytial division cycles in metaphase can produce a corresponding decrease in the diffusion of cytoplasmic

molecules (10). These data together show that diffusion within an energid will occur at a faster rate compared with across neighboring energids, and furrows decrease the diffusion of plasma membrane-associated and cytoplasmic molecules.

In order to explain the observed gradient for PH-PLC-CFP, we introduced a one-dimensional theoretical model (Fig. 3 *A*). The lateral furrow is at its maximum length in metaphase and two such furrows are a part of each energid. In n.c.13, the lateral area available for binding PH-PLC-CFP is almost twice that of the apical area (Fig. 3 *A*, lower panel). Further, since PH-PLC is present on the membrane, membrane-associated structures, and cytoplasm (28,31), we consider two sub-populations of PH-PLC-CFP: the cytoplasmic (or free) pool and the membrane-bound pool. The concentrations of the two species are denoted by $C_{free}(x,t)$ and $C_{bound}(x,t)$ respectively, and their time evolution can be described by,

$$\frac{\partial C_{free}}{\partial t} = \frac{\partial}{\partial x}\left[D_{free}(x)\frac{\partial C_{free}}{\partial x}\right] + k_{ub}C_{bound} - k_b(x)C_{free}, \tag{1a}$$

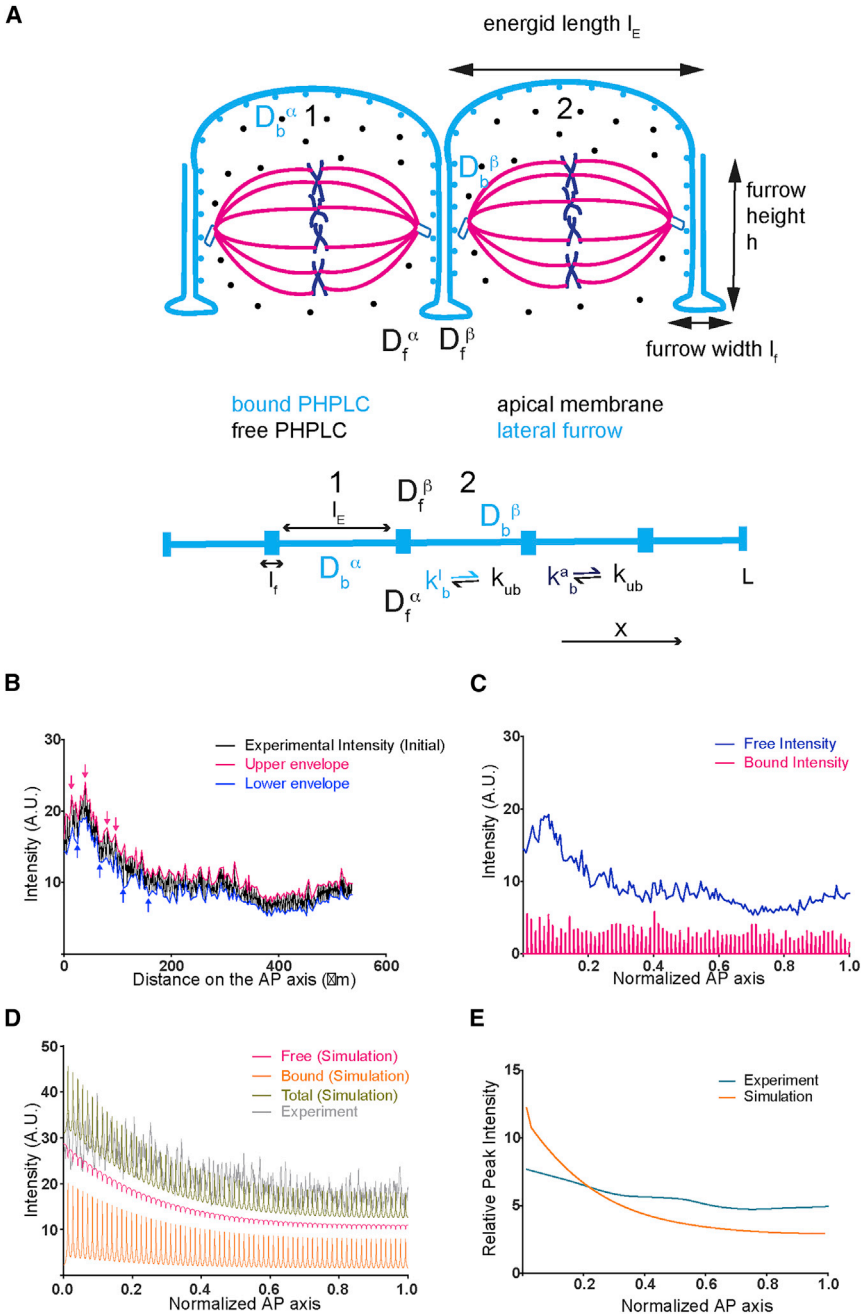

FIGURE 3 Analysis of the role of membrane binding and energid restriction in the spread of anteriorly expressed PH-PLC-CFP. (*A*) Schematic illustrating the parameters for the formation of the gradient of anteriorly expressed PH-PLC-CFP (top) under the modified SDD model involving membrane and cytoplasmic populations and a rate for binding and unbinding from the membrane (k_b, k_{ub}). D_f (D_{free}), diffusion of free species; D_b (D_{bound}), diffusion of bound species. One-dimensional model for the spread of the PH-PLC-CFP gradient. l_f is the thickness of the lateral furrow represented by a thick bar signifying the increased accumulation of PH-PLC-CFP in positions of the lateral furrow, l_E is the width of the energid. (*B*) Fluorescence intensity (a.u.) is plotted on the AP axis for anteriorly expressed PH-PLC-CFP. Graph shows upper (magenta) and lower envelope (blue), corresponding to the high-intensity peaks and the low intensity troughs respectively. The upper envelope (high-intensity peaks, magenta arrows) corresponds to bound fraction, while the lower envelope (lowest-intensity troughs, blue arrows) corresponds to the cytoplasmic or free fraction of PH-PLC-CFP often present in the energid in between adjacent furrows. (*C*) Graph shows the two pools of PH-PLC-CFP intensity after subtraction from the gradient profile across the AP axis. The cytoplasmic (free) and membrane-bound intensity profiles across the AP axis are used as input in the simulation. (*D*) Intensity across the AP axis as predicted by a simulation run for ~20 min using free, bound, and total PH-PLC-CFP gradient (Fig. 4 *B*) as input and compared with the experimental gradient profile. The experimental profile is taken from a time point after a similar time duration (~20 min) from the same embryo as Fig. 4 *B*. (*E*) Comparison of relative peak height (difference in intensity between furrow and non-furrow locations) as computed using simulation with an average of experimentally determined peak heights.

$$\frac{\partial C_{bound}}{\partial t} = \frac{\partial}{\partial x}\left[D_{bound}(x)\frac{\partial C_{bound}}{\partial x}\right] - k_{ub}C_{bound} + k_b(x)C_{free}, \tag{1b}$$

Here, $D_{free}(x)$ is the cytoplasmic diffusion coefficient of PH-PLC-CFP, and $D_{bound}(x)$ is the membrane diffusion coefficient. Experimentally, it has been observed that there is the restriction of diffusion for both membrane-bound and cytoplasmic proteins, and the plasma membrane and cytoplasmic populations of membrane-associated proteins are restricted to an energid (9,10,30,32,33). This results in an effective slower diffusion of both sub-populations across neighboring energids. In our one-dimensional model, this is modeled by diffusion coefficients that vary periodically along the AP axis, with a periodicity corresponding to the energid length (l_E),

$$D_{free}(x) = \begin{cases} D^{\alpha}_{free} & if\ x \in\ within\ energids \\ D^{\beta}_{free} & if\ x \in\ across\ energids \end{cases} \tag{2a}$$

$$D_{bound}(x) = \begin{cases} D^{\alpha}_{bound} & if\ x \in\ within\ energids \\ D^{\beta}_{bound} & if\ x \in\ across\ energids \end{cases} \tag{2b}$$

The restricted diffusion across energids necessarily implies that $D^{\beta} < D^{\alpha}$ for both sub-populations. Further, the two sub-populations can inter-convert due to binding to and unbinding from the membrane. The presence of furrows between adjacent energids results in a spatially heterogeneous binding rate $(k_b(x))$, given by,

$$k_b(x) = \begin{cases} k^a_b\ if\ x \in\ apical\ membrane \\ k^l_b\ if\ x \in\ lateral\ membrane \end{cases} \tag{3}$$

Note that, in the one-dimensional model, the dense regions represent the two lateral membranes corresponding to each energid and thereby leading to an increased accumulation of PH-PLC-CFP (Fig. 3 *A*). Additionally, the excess membrane in the lateral furrows necessarily implies $k^l_b > k^a_b$ (see Supporting Materials for details). The unbinding rate k_{ub} was assumed to be constant, independent of the spatial location. Note that the different parameters at the furrow locations $(D^{\beta}_{free}, D^{\beta}_{bound}, k^l_b)$ should be interpreted as time-averaged values that incorporate the variation in the furrow length across a nuclear division cycle.

These equations were solved subject to a source boundary condition at the anterior end $(x = 0)$, and reflecting boundary conditions at the posterior end $(x = L)$ for the free sub-population. The bound sub-population obeyed reflecting boundary conditions at both $x = 0$ and $x = L$.

We simulate this theoretical model with the experimental intensity profile at the start of n.c.13 as the initial condition (Fig. 3 *B*). To obtain the initial gradient profile for both free and bound sub-populations from this total intensity profile, we decomposed it to free and bound species (see section "materials and methods" for details) (Fig. 3 *B* and *C*).

For evaluating the extent of restriction across energids, and the (un)binding rates, we varied D^{β} (both cytoplasmic and bound sub-populations), and the ratio of the binding to unbinding rates to match the simulation and experimental profile at the end of n.c.13 (Fig. S3 *A–C*). Experimental estimates of D^{α} were taken from the literature (see section "materials and methods" for details). The experimental intensity profile was characterized by two quantitative measures: the overall gradient length scale (Fig. 3 *D*), and the relative peak intensity; i.e., the excess intensity at the furrow locations compared with non-furrow locations (Fig. 3 *C* and *E*). We found that the overall gradient length scale was controlled by the cytoplasmic diffusion coefficient D_{free}. In contrast, the strength of the local accumulation at the furrow locations was controlled by an interplay of the bound diffusion coefficients and the (un)binding rates (Fig. S3 *A–C*). The details of the simulations can be found in the section "materials and methods."

Thus a simplified model, which incorporates membrane and cytoplasmic restriction to an energid due to architectural features in the syncytium and binding-unbinding kinetics in the absence of degradation, can qualitatively capture the main features of the anteriorly expressed PH-PLC-CFP gradient. The analysis also allows us to identify and perturb biologically relevant features contributing to the experimentally observed gradient.

Overexpression of RhoGEF2 leads to disruption of pseudocleavage furrows and increased spread of the anteriorly expressed PH-PLC-CFP gradient

To assess the role of lateral furrows in regulating the spread of the PH-PLC-CFP gradient, we analyzed the gradient of anteriorly expressed PH-PLC-CFP in embryos with perturbed pseudocleavage furrows. Pseudocleavage furrow extension requires the GTPase exchange factor RhoGEF2. RhoGEF2 is localized at pseudocleavage furrows, and its loss shows decreased myosin II at the furrow leading to cap expansion and a slight decrease in the furrow length (34–38). RhoGEF2 overexpression, on the other hand, shows increased myosin II throughout the syncytial division cycle leading to cap constriction and loss of furrows (34,35). We tested embryos containing an overexpression of RhoGEF2 (RhoGEF2-OE) for perturbation of the anteriorly expressed gradient in oogenesis and embryogenesis. Control oocytes expressing anteriorly expressed PH-PLC-CFP contained a greater level of PH-PLC-CFP fluorescence on the anterior membrane compared with the posterior membrane (Fig. S4 *A* and *B*). F-actin distribution did not show this varied distribution between the anterior and posterior membranes. This increased anterior distribution was also seen in RhoGEF2 overexpression. This suggested that the anterior localization of the construct was similar in controls

and RhoGEF2-OE embryos, allowing us to test the effect of furrow perturbation in embryos.

Flies containing RhoGEF2-OE with *mat*-Gal4 gave embryos that were 87% lethal (n = 300 embryos). RhoGEF2-OE led to short furrows (100%) throughout with patches of complete loss of furrows (Fig. 4 *A*). The density of energids in the RhoGEF2-OE embryos was comparable with controls in optical sections shown (Fig. 4 *A*). Since the number of furrows appeared distinctly reduced, we quantified the number of furrows in embryos containing anteriorly expressed PH-PLC-CFP (Fig. 4 *B*). We observed a decrease in the number of furrows in the AP axis to 28 ± 1.8 peaks for n.c.13 (Fig. 4 *C*) compared with controls (Fig. 2 *B*). Moreover, the number of furrows did not increase significantly from n.c.11 to n.c.12 to n.c.13 (Fig. 4 *C*) compared with controls (Fig. 2 *B*). As expected, the distance between adjacent peaks also increased and was found to be $15 \pm 1.02\mu m$ compared with $7.8 \pm 0.4\mu m$ in controls in n.c.13 as calculated via the direct method (Fig. 4 *D* and *E*). This increase in distance between adjacent peaks was also seen in FFT measurements (Fig. S4 *C* and *D*).

Analysis of the PH-PLC-CFP gradient across multiple embryos showed that the profiles were considerably varied with an increase in the spread of the fluorescence toward the posterior of the embryo compared with the controls, and hence the length scales could not be calculated (Fig. 4 *F* compared with control in Fig. 1 *G*; Video S3). We also tested the Bicoid gradient by expressing Bicoid-Venus in embryos with RhoGEF2-OE. Bicoid-Venus showed a gradient similar to controls in RhoGEF2-OE embryos (Fig. S5 *A* and *B*; and Video S5). The Bicoid-Venus gradient length scale did not change significantly in embryos containing RhoGEF2-OE compared with controls (Fig. S5 *E*). Therefore RhoGEF2-OE led to the loss

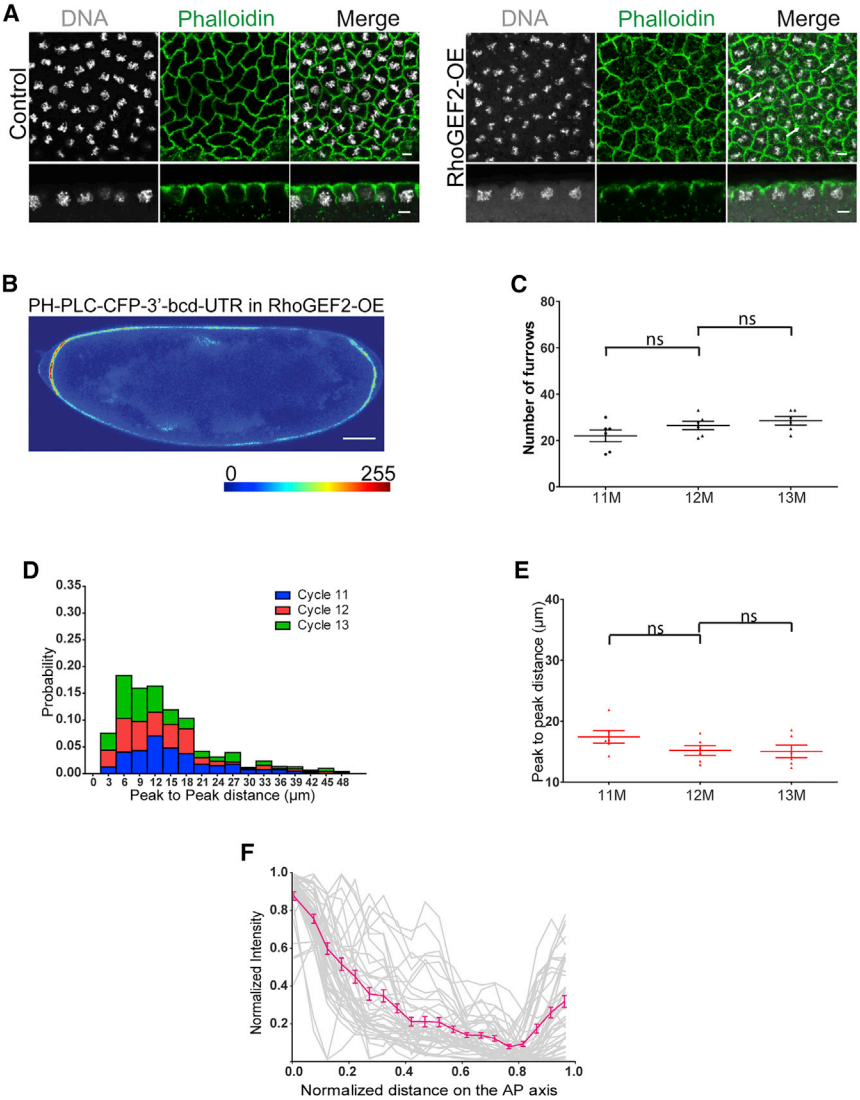

FIGURE 4 Anteriorly expressed PH-PLC-CFP gradient is disrupted in embryos deficient for pseudocleavage furrows due to RhoGEF2 overexpression. (*A*) RhoGEF2-OE gives rise to shorter metaphase furrows. Sagittal and surface views of fixed control (*mat*-Gal4/+) or RhoGEF2-OE embryos, stained with DNA (gray) and phalloidin (green). Arrows mark missing furrows (100% n = 30). Scale bar, 10 μm. (*B*) Anteriorly expressed PH-PLC-CFP gradient in RhoGEF2-OE embryos is shown in a snapshot from a time-lapse video (*B*). Scale bar, 50 μm. (*C*) Number of furrows across the AP axis, calculated from distance between adjacent fluorescence peaks obtained from RhoGEF2-OE embryos containing anteriorly expressed PH-PLC-CFP. Scatter plots show quantification of the number of furrows across n.c 11, 12, and 13 metaphases for RhoGEF2-OE embryos. n = 6, 3; one-way ANOVA, p = 0.11, F = 2.52, Tukey's multiple comparison post test at p = 0.05. (*D* and *E*) Distance between adjacent furrows extracted by direct calculation of distance between adjacent fluorescence peaks for embryos overexpressing RhoGEF2 for n.c.11–13 (*D*). Peak-to-peak distance calculation is plotted as a histogram of the probability distribution of various peak-to-peak or adjacent furrow distances (*D*). Distances between adjacent furrows extracted are plotted across different nuclear cycles (*E*). n = 6, 3; one-way ANOVA, p = 0.17, F = 1.9, Tukey's multiple comparison post test at p = 0.05. (*F*) Quantification shows individual gradient profiles data across syncytial cycles 11 to 13 in different embryos with gray lines and average ± SEM in red (*I*) (n = 49, 26). The 16-color-intensity rainbow scale contains blue as the lowest intensity and red as the highest intensity.

of pseudocleavage furrows and disruption of the anteriorly expressed PH-PLC-CFP gradient but not the Bicoid gradient.

RalA depletion leads to disruption of pseudocleavage furrows and increased spread of the anteriorly expressed PH-PLC-CFP gradient

RalA is a component of the Ras signaling pathway (39,40). In syncytial *Drosophila* embryos, RalA functions through the exocyst complex to form pseudocleavage furrows. RalA depletion leads to loss of furrow extension in the syncytial division cycles (41). Anteriorly expressed PH-PLC-CFP was monitored in *ralA* RNAi-expressing oocytes. There was a decrease in fluorescence of anteriorly expressed PH-PLC-CFP in *ralA* RNAi compared with controls. However an increased accumulation of PH-PLC-CFP on the anterior membrane was seen in 100% of the oocytes. In addition, among these, 50% of the oocytes showed levels similar to controls (Fig. S4 *A* and *B*). These results in turn suggested that the PH-PLC-CFP mRNA distributed to the anterior membrane of the oocyte.

We further expressed RNAi against RalA with *mat*-Gal4 and found that 60% of the embryos (n = 300) were lethal at 24 h. The density of energids did not change on RalA depletion compared with controls in optical sections shown (Fig. 5 *A*). We saw phenotypes of short furrows (100%) and loss of furrows in patches during the metaphase of the syncytial division cycle, similar to the previous reports (41) (Fig. 5 *A*). We further assessed the anteriorly expressed PH-PLC-CFP gradients in embryos expressing *ralA* RNAi (Fig. 5 *B*). We observed a decrease in the number of furrows in the AP axis to 22 ± 7 peaks for n.c.13 (Fig. 5 *C*) compared with controls (Fig. 2 *B*). Like RhoGEF2-overexpressing embryos, we found no significant difference between the numbers of furrows across n.c.11, 12, and

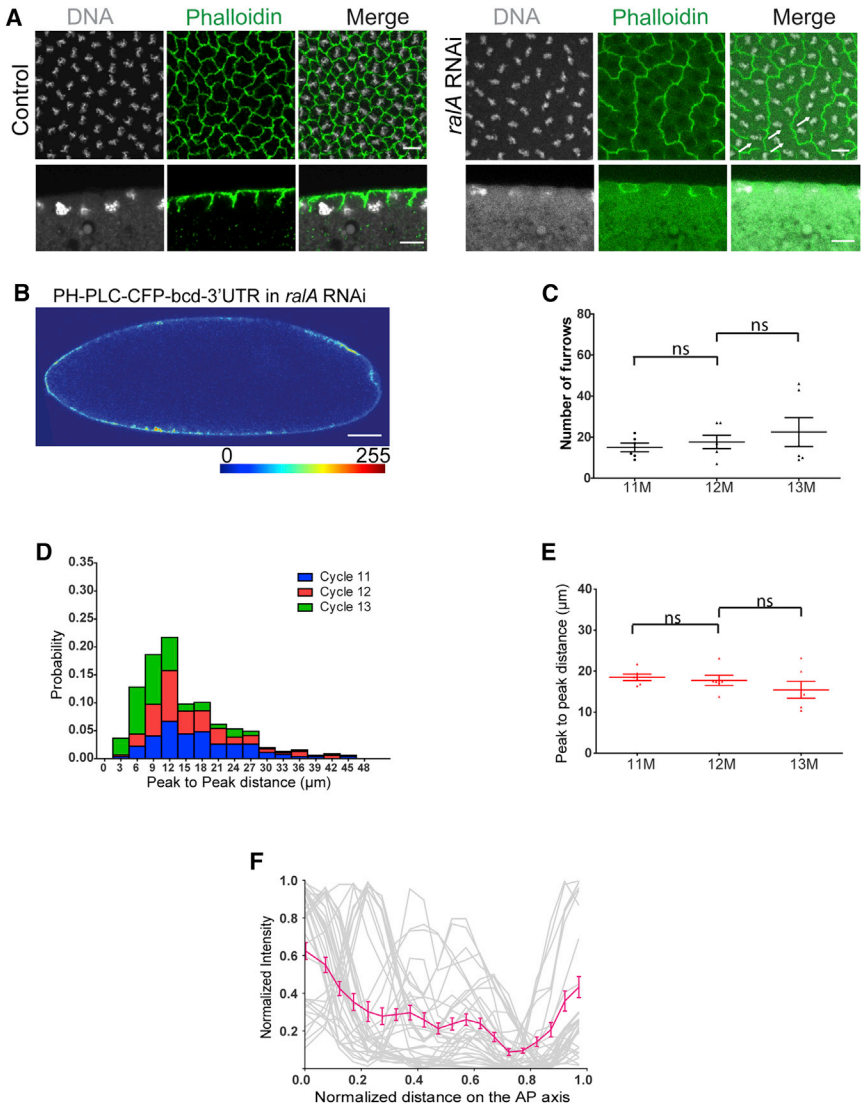

FIGURE 5 Anteriorly expressed PH-PLC-CFP gradient is disrupted in embryos deficient for pseudocleavage furrows due to *ralA* RNAi. (*A*) *ralA* RNAi expressed with *mat*-Gal4 show loss of metaphase furrows: sagittal and surface views of fixed control (*mat*-Gal4/+) or *ralA* RNAi-expressing embryos, stained with DNA (gray) and phalloidin (green). Arrows point to intermittent loss of furrows upon *ralA* RNAi expression (80% of n = 30 embryos). Scale bar, 10 μm. (*B*) Anteriorly expressed PH-PLC-CFP is shown in a snapshot from a time-lapse video of an embryo expressing *ralA* RNAi (*B*). Scale bar, 50 μm. (*C*) Number of furrows across the AP axis, calculated by estimating the distance between adjacent fluorescence peaks obtained from *ralA* RNAi embryos containing anteriorly expressed PH-PLC-CFP. Scatter plots show quantification of the number of furrows across n.c.11, 12, and 13 metaphases for *ralA* RNAi embryos. n = 6, 3; one-way ANOVA, p = 0.52, F = 0.67, Tukey's multiple comparison post test at p = 0.05. (*D* and *E*) Distance between adjacent furrows extracted by a direct calculation of distance between adjacent fluorescence peaks for embryos expressing *ralA* RNAi for n.c. 11–13 (*D*). Peak-to-peak distance calculation is plotted as a histogram of the probability distribution of various peak-to-peak or adjacent furrow distances (*D*). Distances between adjacent furrows extracted are plotted across n.c.11 to 13 (*E*). n = 6, 3; one-way ANOVA, p = 0.33, F = 1.18, Tukey's multiple comparison post test at p = 0.05. (*F*) Quantification shows individual data across syncytial cycles 11 to 13 in different embryos with gray lines and average ± SEM in red (*C*) (n = 42, 23) .The 16-color-intensity rainbow scale contains blue as the lowest intensity and red as the highest intensity.

13 in *ralA* RNAi-expressing embryos (Fig. 5 *C*). As expected, the distance between adjacent peaks increased to 15.4 ± 2μm compared with $7.8 \pm 0.4 \mu m$ for controls in cycle 13 as calculated via the direct method (Fig. 5 *D* and *E*). This increase in distance between adjacent peaks was also seen in FFT measurements (Fig. S4 *E* and *F*).

The anteriorly expressed PH-PLC-CFP fluorescence appeared to spread to a greater extent in the AP axis in *ralA* RNAi-expressing embryos (Fig. 5 *F* and Video S4) compared with the control (Fig. 5 *F* compared with control in Fig. 1 *G*). The fluorescent intensity profiles were considerably varied across embryos, and hence length scales could not be calculated. We also tested the Bicoid gradient by expressing Bicoid-Venus in embryos with RalA depletion. Bicoid-Venus showed a gradient similar to controls in embryos with *ralA* RNAi (Fig. S5 *C* and *D*; and Video S6). The Bicoid-Venus gradient length scale did not change significantly in both cases compared with controls (Figure S5 *E*). Thus, RalA depletion led to the loss of pseudocleavage furrows and disruption of the anteriorly expressed PH-PLC-CFP gradient but not the Bicoid gradient.

Taken together, the observations from both the RhoGEF2-OE and *ralA* RNAi-expressing embryos showed a decrease in the numbers of pseudocleavage furrows and disruption of the anteriorly expressed PH-PLC-CFP gradient. The RhoGEF2-OE and *ralA* RNAi-expressing embryos did not show a significant effect on the spread of the Bicoid gradient (Fig. S5). This lack of effect on the spread of the Bicoid gradient is likely due to the absence of its regulation by furrows or incomplete loss of furrows seen in these embryos.

Numerical simulations show loss of restriction of the cytoplasmic pool of PH-PLC-CFP as a cause for gradient disruption in furrow mutants

The anteriorly expressed PH-PLC-CFP gradient was formed due to restriction of membrane-bound and cytoplasmic pools of PH-PLC-CFP to an energid (Fig. 3). Removal of pseudocleavage furrows is likely to allow membrane diffusion of PH-PLC-CFP and increase the spread of cytoplasmic PH-PLC-CFP molecules across the energids. Having observed that pseudocleavage furrows regulate the formation of the PH-PLC-CFP gradient, we investigated the role of membrane binding versus decreased exchange or compartmentalization of membrane-bound and cytoplasmic pools of PH-PLC-CFP in gradient formation in different idealized furrow mutant simulations. Our theoretical model, proposed for the control embryos expressing anteriorly expressed PH-PLC-CFP, has three key features: an enhanced binding at furrow locations, compartmentalization of the membrane-bound sub-population, and compartmentalization of the cytoplasmic sub-population (Fig. 3). We attempted to determine which of these factors contribute to gradient disruption in the furrow mutants.

We conceptualized three variations of our model: 1) an enhanced binding (EB) model, where there is an enhanced binding at furrow locations, but neither the membrane-bound nor the cytoplasmic sub-species is compartmentalized; 2) a compartmentalized membrane (CM) model, where, along with enhanced binding at furrows, the membrane-bound species is compartmentalized, but cytoplasmic species have a spatially uniform diffusivity with no compartmentalization; and 3) the WT model, with the compartmentalization of both membrane-bound and cytoplasmic species, and enhanced binding at furrows (Fig. 6 *A–C*). We evolved our system of equations for 3 h, starting from zero concentrations of both free and bound species. The furrow numbers and other parameters are taken from the WT fits for n.c.13 and are kept constant for the length of the simulation (Fig. 2 *B*, *D*, and *I*). Note that the absence of the nuclear cycle kinetics implies that the resultant simulation profiles should not be compared directly with experiments but are meant to test the role of the different parameters in disrupting the gradient profile. Upon comparing the reference intensity profiles for the three models, we observed that EB and CM models provided similar gradient shapes, while the WT model had the steepest gradient profile (Fig. 6 *D*).

We next simulated loss of 70% furrows randomly in each of these cases to identify the mechanism behind gradient disruption in the furrow mutants. In the EB model, there is an enhanced accumulation at the furrow due to differential binding kinetics. Upon 70% furrow disruption, the enhanced accumulation at the furrows was also disrupted, as shown by the reduction in intensity on the furrow peaks (Fig. 6 *E*). However, there was no change in the overall gradient length scale, implying that differential binding kinetics is not sufficient to explain gradient disruption in the furrow mutants (Fig. 6 *E*). In the CM model, the disruption of furrows changed local accumulation at the affected sites but was not sufficient to change the overall gradient length scale (Fig. 6 *F*). The loss of furrows leading to a decrease of both cytoplasmic and membrane compartmentalization led to a drastic change in gradient length scale in the WT model (Fig. 6 *G*). This loss of cytoplasmic restriction gave rise to gradient disruption similar to that seen in RhoGEF2-OE- and *ralA* RNAi-expressing embryos. Our theoretical model containing binding-unbinding kinetics and compartmentalization of membrane-bound and cytoplasmic PH-PLC-CFP qualitatively captured the gradient in control embryos and gradient disruption in *ralA* RNAi and RhoGEF2-OE embryos.

DISCUSSION

In this study, we expressed a fluorescently tagged PH domain in the form of a gradient in the AP axis in the syncytial *Drosophila* embryo to examine the role of pseudocleavage furrows in its restriction. Our analysis of gradient

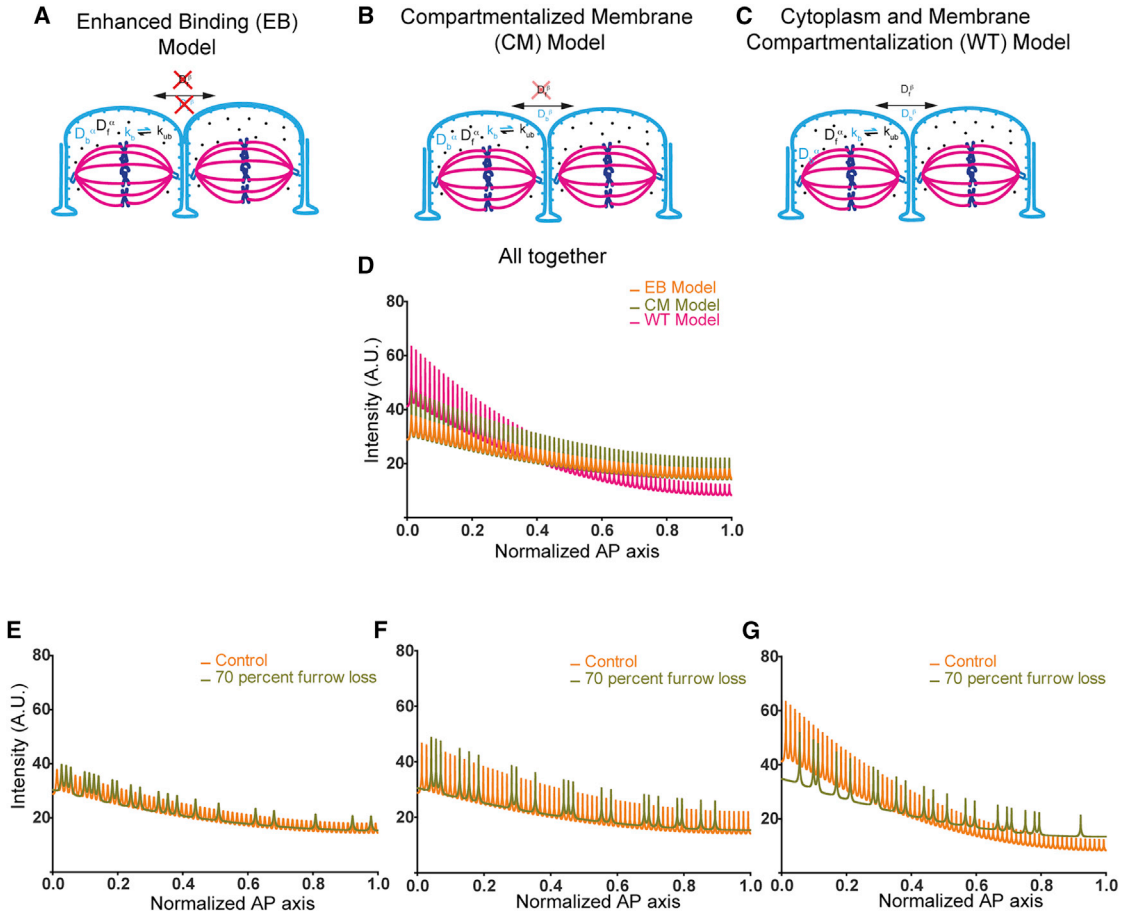

FIGURE 6 Simulations show disruption of anteriorly expressed PH-PLC-CFP gradient by loss of furrow membrane binding and cytoplasmic compartmentalization. (*A–D*) Schematic showing simulations for the EB, CM, and WT models from control embryos containing anteriorly expressed PH-PLC-CFP results of the AP intensity gradient (*A–C*). Graph shows that the WT model has a steeper gradient compared with the CM and EB models (*D*). (*E*) Simulation results of the AP intensity gradient using the EM model for control embryos containing anteriorly expressed PH-PLC-CFP and embryos lacking 70% of the furrows. (*F*) Simulation results of the AP intensity gradient using the CM model for control embryos containing anteriorly expressed PH-PLC-CFP and embryos lacking 70% of the furrows. (*G*) Simulation results of the AP intensity gradient using the WT model for control embryos containing anteriorly expressed PH-PLC-CFP and embryos lacking 70% of the furrows. Loss of cytoplasmic compartmentalization leads to increased PH-PLC-GFP spread of the gradient in the AP axis.

properties and simulations shows that anteriorly expressed PH-PLC-CFP forms an exponential gradient regulated by membrane association and cytoplasmic restriction by pseudocleavage furrows during n.c.11 to 13 (Fig. 7 *A*). Loss of pseudocleavage furrows in RhoGEF2-OE and *ralA* RNAi-expressing embryos did not affect the Bicoid gradient (Fig. 7 *B*). We discuss our results in the light of concepts of molecular restriction mediated by interactions with the cellular architecture and the impact of our findings on the spread of morphogen gradients.

Restriction of molecules based on cellular localization

To what extent and by what means do molecules restrict their localizations to particular energids within syncytia? Restriction of molecules in syncytia could occur due to their subcellular localization and partitioning. F-actin and plasma membrane reduce lateral movement of the *fushi tarazu* mRNA in the syncytial *Drosophila* embryo, while microtubules are involved in confining it above the nucleus in the absence of plasma membrane boundaries (42). Depolymerization of microtubules by nocodazole leads to increased spread of molecules in the ER lumen across adjacent energids (5). Disruption of actin dynamics and trafficking leads to an increased diffusion of plasma membrane-associated proteins across energids (9,30). Modeling studies show that transient binding to microtubules is sufficient for segregating and restricting cytoplasmic components to spindle poles in the absence of plasma membrane-based boundaries (43).

Our study further suggests the restriction of molecules between energids due to the presence of plasma membrane furrows. We observe a change in the gradient shape of anteriorly expressed PH-PLC-CFP when pseudocleavage furrows are shorter or lost. We initially expected that

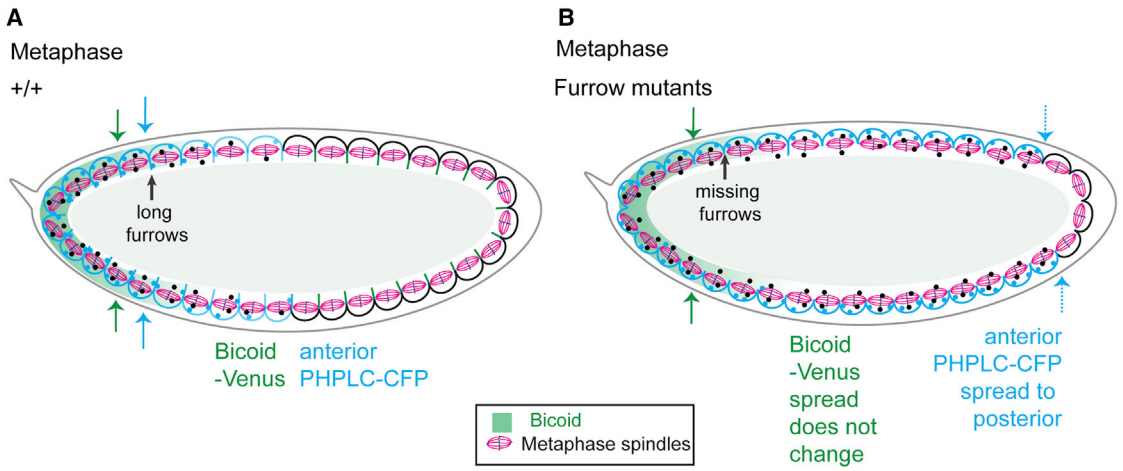

FIGURE 7 Summary of anteriorly expressed PH-PLC-CFP and Bicoid gradient in control and mutant embryos. Schematic summarizing the distribution of anteriorly expressed PH-PLC-CFP and Bicoid. Anteriorly expressed PH-PLC-CFP has a longer length scale compared with Bicoid (*A*). The length scale for the PH-PLC-CFP arises due to cytoplasmic and membrane-bound pools of the protein. Anteriorly expressed PH-PLC-CFP gradient is disrupted by the loss of furrows and spreads to a greater extent in the AP axis in *ralA* RNAi and RhoGEF-OE (*B*). The cytoplasmic pool of PH-PLC-CFP spreads across the embryo to a greater distance and causes a spread in the gradient.

molecular restriction of PH-PLC-CFP is governed primarily by membrane binding. However, our simulation results show the role of both membrane binding and cytoplasmic restriction contributing to molecular restriction. While the membrane restriction is governed by the kinetics of binding/unbinding of PH-PLC-CFP, our simulation results suggest that cytoplasmic restriction may be passively caused due to physical restriction of molecules across energids by the furrows and independent of the molecule under consideration. Membrane-associated proteins such as H-Ras have been found to exchange via lateral diffusion and with molecules in the cytoplasm. Diffusion analysis by the FRAP beam size analysis method showed that the exchange with the cytoplasm is 2- to 3-fold faster than diffusion within the membrane (44). Our simulation results show that an increase in diffusion of the free population of PH-PLC-CFP molecules to at least 10-fold on the loss of compartmentalization provides an explanation of the spread of the anteriorly expressed PH-PLC-CFP gradient in the AP axis.

Our recent analysis of AP protein gradients of photoactivatable cytoplasmic GFP (PA-GFP) and PA-GFP-Tubulin shows that PA-GFP-Tubulin has a shorter length scale and is more constrained than PA-GFP. Loss of tubulin polymerization and furrows leads to increased diffusion of PA-GFP-Tubulin, which approaches PA-GFP diffusion (45). Thus molecular associations of plasma membrane or cytoskeletal proteins become confined to each energid due to the presence of pseudocleavage furrows. Our observation of cytoplasmic restriction as a way to confine PH-PLC-CFP spread is consistent with previous experimental observations of restriction of diffusion of both the membrane and cytoplasmic components of plasma membrane-associated proteins in photobleaching experiments (9). This suggests a possibility of restriction of cytoplasmic constituents within each energid due to enclosure within the nucleus and binding to DNA, enclosure within other organelles, binding to the microtubule cytoskeleton, and restriction due to the presence of furrows (10,33,43). It is also possible that increased cytoplasmic movement in mitosis during the syncytial cycles due to the characteristic yo-yo movement of nuclei is responsible for increased cytoplasmic mixing when pseudocleavage furrows are lost (46). In our study, these movements have differential impacts on the spread of the anteriorly expressed PH-PLC-CFP and Bicoid.

We further find that the profiles of anteriorly expressed PH-PLC-CFP are sensitive to variations in binding-unbinding kinetics. Future studies that discern the binding-unbinding kinetics, spatial dynamics of the PH-PLC-CFP association to the apical versus the lateral furrow membrane, as well as changes in the spatial organization of furrows in syncytial cycles will reveal a more precise depiction of the extent of dependence of each parameter on the anteriorly expressed PH-PLC-CFP gradient.

Implications for morphogen gradients

Loss of pseudocleavage furrows did not affect the Bicoid gradient in our study. However, other components of the cytoarchitecture may affect the Bicoid gradient. Transient binding or trapping of molecules, in general, is likely to lead to a reduction in the number of molecules undergoing free diffusion across the embryo, and this will have implications for the spread of morphogen gradients. For Bicoid, interactions with various cyto-architectural components in the early embryo, such as transient localization with actin (47), may affect its gradient formation more strongly than restriction by pseudocleavage furrows. Nuclear shuttling has been

ruled out as a mechanism regulating Bicoid gradient formation since a Bicoid mutant deficient in nuclear shuttling forms a WT gradient (48,49). The homeobox transcription factors Engrailed-1 and Engrailed-2 have shown specific non-nuclear subcellular localization signals in the homeodomain (50,51), suggesting similar signals may be present in Bicoid, another homeobox transcription factor. Bicoid is also associated with chromatin across the AP axis creating hubs of local concentration, which may lead to its restricted diffusion and confinement to one energid (52). Moreover, the presence of Bicoid and PH-PLC-CFP near the cortex across nuclear cycles suggests that the effective volume in which these molecules are diffusing is restricted to the cortex, similar to other cytoplasmic components (45). Future analysis of disruption of organelles and cytoskeleton components will reveal their impact on the Bicoid gradient. Further analysis of the Bicoid protein could be carried out to elucidate the domains responsible for its association with cytoarchitecture and generation of the gradient.

Differential interactions of gradient molecules with nuclear, cytoplasmic, and extracellular components have implications for other gradients. Dorsal, the dorso-ventral morphogen, is compartmentalized to nuclei in the syncytial *Drosophila* embryo (33). Plasma membrane furrows, microtubules, and size of Dorsal are predicted to be important for the gradient (10,43,53). Nuclei are obligately required for the shape of dpERK gradient caused by the Torso-mediated terminal patterning pathway in the syncytial *Drosophila* embryo. Disrupting nuclear patterning using *shakleton* mutants leads to a change in dpERK gradient shape (54). Fibroblast growth factor (FGF) gradient in zebrafish and cultured fibroblasts depends on binding to extracellularly present heparan sulfate proteoglycans (HPSGs) (55). The Dpp gradient is also postulated to be dependent upon binding to HSPG. Similar to our study, an engineered GFP gradient sequestered near the tissue surface was sufficient to pattern the wing primordia, replacing the natural *dpp* gradient (56). Our study provides an intracellular perspective to the rapidly growing understanding of the effects of binding and physical restriction on morphogen gradients.

In summary, our study evaluates the significance of membrane binding and cytoplasmic restriction in regulating diffusion in the syncytial *Drosophila* embryo. Future studies evaluating the role of weak binding, molecular size, and crowded cytoplasm due to cytoskeletal, cytoplasmic, and organellar organization on the spread of gradients in different contexts will help generalize the model in different paradigms of development.

SUPPORTING MATERIAL

Supporting material can be found online at https://doi.org/10.1016/j.bpj.2022.05.015.

AUTHOR CONTRIBUTIONS

S.T., B.K., A.M., M.M., and R.R. designed the study, executed the experiments, analyzed the experiments, and wrote the manuscript. D.M., B.D., and B.U. performed experiments and analyzed data for the study. P.D. analyzed the experiments for the study.

ACKNOWLEDGMENTS

We thank Girish Deshpande, Girish Ratnaparkhi, Thomas Pucadyil, and RR laboratory members for discussions on this project. M.K.M. and A.N. thank Varun Bhalerao for helpful discussions on the error analysis. Stocks obtained from the Bloomington *Drosophila* Stock Center (NIH P40OD018537) were used in this study. S.T. thanks CSIR, R.R. thanks DBT and IISER Pune, M.K.M. thanks IIT Bombay (IRCC-SG13/009), and A.N. thanks SERB, DST, India (project no. ECR/2016/001967) for financial support.

DECLARATION OF INTERESTS

The authors declare no competing interests.

REFERENCES

1. Hardy, K. M., R. M. Dillaman, …, S. T. Kinsey. 2009. A skeletal muscle model of extreme hypertrophic growth reveals the influence of diffusion on cellular design. *Am. J. Physiol. Regul. Integr. Comp. Physiol.* 296:R1855–R1867. https://doi.org/10.1152/ajpregu.00076.2009.
2. Cutler, A. A., J. B. Jackson, …, G. K. Pavlath. 2018. Non-equivalence of nuclear import among nuclei in multinucleated skeletal muscle cells. *J. Cell Sci.* 131:jcs207670. https://doi.org/10.1242/jcs.207670.
3. Dundon, S. E. R., S.-S. Chang, …, M. Roper. 2016. Clustered nuclei maintain autonomy and nucleocytoplasmic ratio control in a syncytium. *Mol. Biol. Cell.* 27:2000–2007. https://doi.org/10.1091/mbc.e16-02-0129.
4. Anderson, C. A., U. Eser, …, J. Skotheim. 2013. Nuclear Repulsion Enables Division Autonomy in a Single Cytoplasmrepulsion enables division autonomy in a single cytoplasm. *Curr. Biol.* 23:1999–2010. https://doi.org/10.1016/j.cub.2013.07.076.
5. Frescas, D., M. Mavrakis, …, R. DeLotto. 2006. The secretory membrane system in the Drosophila syncytial blastoderm embryo exists as functionally compartmentalized units around individual nuclei. *J. Cell Biol.* 173:219–230. https://doi.org/10.1083/jcb.200601156.
6. Chowdhary, S., D. Tomer, …, D. Sambre. 2017. Analysis of mitochondrial organization and function in the Drosophila blastoderm embryo. *Sci. Rep.* 7:5502. https://doi.org/10.1038/s41598-017-05679-1.
7. Minden, J. S., D. A. Agard, …, B. M. Alberts. 1989. Direct cell lineage analysis in Drosophila melanogaster by time-lapse, three-dimensional optical microscopy of living embryos. *J. Cell Biol.* 109:505–516. https://doi.org/10.1083/jcb.109.2.505.
8. Lee, C., P. Occhipinti, and A. S. Gladfelter. 2015. PolyQ-dependent RNA–protein assemblies control symmetry breaking. *JCB (J. Cell Biol.).* 208:533–544. https://doi.org/10.1083/jcb.201407105.
9. Mavrakis, M., R. Rikhy, and J. Lippincott-Schwartz. 2009. Plasma membrane polarity and compartmentalization are established before cellularization in the fly embryo. *Dev. Cell.* 16:93–104. https://doi.org/10.1016/j.devcel.2008.11.003.
10. Daniels, B. R., R. Rikhy, …, T. M. Dobrowsky. 2012. Multiscale diffusion in the mitotic Drosophila melanogaster syncytial blastoderm. *Proc. Natl. Acad. Sci. U. S. A.* 109:8588–8593. https://doi.org/10.1073/pnas.1204270109.
11. Ephrussi, A., and R. Lehmann. 1992. Induction of germ cell formation by oskar. *Nature.* 358:387–392. https://doi.org/10.1038/358387a0.

12. Berleth, T., M. Burri, …, M. Noll. 1988. The role of localization of bicoid RNA in organizing the anterior pattern of the Drosophila embryo. *EMBO J.* 7:1749–1756. https://doi.org/10.1002/j.1460-2075.1988.tb03004.x.

13. Benoit, B., C. H. He, …, H. D. Lipshitz. 2009. An essential role for the RNA-binding protein Smaug during the Drosophila maternal-to-zygotic transition. *Development.* 136:923–932. https://doi.org/10.1242/dev.031815.

14. Gregor, T., A. P. McGregor, and E. F. Wieschaus. 2008. Shape and function of the Bicoid morphogen gradient in dipteran species with different sized embryos. *Dev. Biol.* 316:350–358. https://doi.org/10.1016/j.ydbio.2008.01.039.

15. Durrieu, L., D. Kirrmaier, …, T. E. Saunders. 2018. Bicoid gradient formation mechanism and dynamics revealed by protein lifetime analysis. *Mol. Syst. Biol.* 14:e8355. https://doi.org/10.15252/msb.20188355.

16. Gramates, L. S., S. J. Marygold; …, the FlyBase Consortium. 2017. FlyBase at 25: looking to the future. *Nucleic Acids Res.* 45:D663–D671. https://doi.org/10.1093/nar/gkw1016.

17. Whitworth, C. 2019. *In* The Bloomington Drosophila Stock Center. *The Biological Resources of Model Organisms*, R. L. Jarret and K. McCluskey, eds. CRC Press, pp. 145–162. https://doi.org/10.1201/9781315100999-8.

18. Schneider, C. A., W. S. Rasband, and K. W. Eliceiri. 2012. NIH Image to ImageJ: 25 years of image analysis. *Nat. Methods.* 9:671–675. https://doi.org/10.1038/nmeth.2089.

19. Rueden, C. T., J. Schindelin, …, E. T. Arena. 2017. ImageJ2: ImageJ for the next generation of scientific image data. *BMC Bioinf.* 18:529. https://doi.org/10.1186/s12859-017-1934-z.

20. Schindelin, J., I. Arganda-Carreras, …, P. Tomancak. 2012. Fiji: an open-source platform for biological-image analysis. *Nat. Methods.* 9:676–682. https://doi.org/10.1038/nmeth.2019.

21. Houchmandzadeh, B., E. Wieschaus, and S. Leibler. 2005. Precise domain specification in the developing Drosophila embryo. *Phys. Rev. E Stat. Nonlin. Soft Matter Phys.* 72:061920. https://doi.org/10.1103/physreve.72.061920.

22. Gregor, T., W. Bialek, …, D. W. Tank. 2005. Diffusion and scaling during early embryonic pattern formation. *Proc. Natl. Acad. Sci. U. S. A.* 102:18403–18407. https://doi.org/10.1073/pnas.0509483102.

23. Knight, J. D., M. G. Lerner, …, R. W. Pastor. 2010. Single molecule diffusion of membrane-bound proteins: window into lipid contacts and bilayer dynamics. *Biophys. J.* 99:2879–2887. https://doi.org/10.1016/j.bpj.2010.08.046.

24. Golebiewska, U., M. Nyako, …, I. Zaitseva. 2008. Diffusion coefficient of fluorescent phosphatidylinositol 4,5-bisphosphate in the plasma membrane of cells. *Mol. Biol. Cell.* 19:1663–1669. https://doi.org/10.1091/mbc.e07-12-1208.

25. Brough, D., F. Bhatti, and R. F. Irvine. 2005. Mobility of proteins associated with the plasma membrane by interaction with inositol lipids. *J. Cell Sci.* 118:3019–3025. https://doi.org/10.1242/jcs.02426.

26. Foe 1993. Mitosis and morphogenesis in the Drosophila embryo: point and counterpoint. *In* The Development of Drosophila melanogaster. A. M. A. Michael Bates, ed. Cold Spring Harbor Laboratory Press, pp. 149–300.

27. Mazumdar, A., and M. Mazumdar. 2002. How one becomes many: blastoderm cellularization in Drosophila melanogaster. *Bioessays.* 24:1012–1022. https://doi.org/10.1002/bies.10184.

28. Várnai, P., and T. Balla. 1998. Visualization of phosphoinositides that bind pleckstrin homology domains: calcium- and agonist-induced dynamic changes and relationship to myo-[3H]inositol-labeled phosphoinositide pools. *J. Cell Biol.* 143:501–510. https://doi.org/10.1083/jcb.143.2.501.

29. Claret, S., J. Jouette, …, K. Legent. 2014. PI(4,5)P2 produced by the PI4P5K SKTL controls apical size by tethering PAR-3 in Drosophila epithelial cells. *Curr. Biol.* 24:1071–1079. https://doi.org/10.1016/j.cub.2014.03.056.

30. Rikhy, R., M. Mavrakis, and J. Lippincott-Schwartz. 2015. Dynamin regulates metaphase furrow formation and plasma membrane compartmentalization in the syncytial Drosophila embryo. *Biol. Open.* 4:301–311. https://doi.org/10.1242/bio.20149936.

31. Balla, T. 2007. Imaging and manipulating phosphoinositides in living cells. *J. Physiol.* 582:927–937. https://doi.org/10.1113/jphysiol.2007.132795.

32. Kanodia, J. S., R. Rikhy, …, J. Lippincott-Schwartz. 2009. Dynamics of the Dorsal morphogen gradient. *Proc. Natl. Acad. Sci. U. S. A.* 106:21707–21712. https://doi.org/10.1073/pnas.0912395106.

33. DeLotto, R., Y. DeLotto, …, J. Lippincott-Schwartz. 2007. Nucleocytoplasmic shuttling mediates the dynamic maintenance of nuclear Dorsal levels during Drosophila embryogenesis. *Development.* 134:4233–4241. https://doi.org/10.1242/dev.010934.

34. Dey, B., and R. Rikhy. 2020. DE-cadherin and Myosin II balance regulates furrow length for onset of polygon shape in syncytial Drosophila embryos. *J. Cell Sci.* https://doi.org/10.1242/jcs.240168.

35. Zhang, Y., J. C. Yu, …, R. Fernandez-Gonzalez. 2018. Collision of expanding actin caps with actomyosin borders for cortical bending and mitotic rounding in a syncytiumexpanding actin caps with actomyosin borders for cortical bending and mitotic rounding in a syncytium. *Dev. Cell.* 45:551–564.e4. https://doi.org/10.1016/j.devcel.2018.04.024.

36. Sherlekar, A., and R. Rikhy. 2016. Syndapin promotes pseudocleavage furrow formation by actin organization in the syncytial *Drosophila* embryo. *Mol. Biol. Cell.* 27:2064–2079. https://doi.org/10.1091/mbc.e15-09-0656.

37. Großhans, J., C. Wenzl, …, H. A. Müller. 2005. RhoGEF2 and the formin Dia control the formation of the furrow canal by directed actin assembly during Drosophila cellularisation. *Development.* 132:1009–1020. https://doi.org/10.1242/dev.01669.

38. Padash Barmchi, M., S. Rogers, and U. Häcker. 2005. DRhoGEF2 regulates actin organization and contractility in the Drosophila blastoderm embryo. *J. Cell Biol.* 168:575–585. https://doi.org/10.1083/jcb.200407124.

39. Harden, N. 2002. Signaling pathways directing the movement and fusion of epithelial sheets: lessons from dorsal closure in Drosophila. *Differentiation.* 70:181–203. https://doi.org/10.1046/j.1432-0436.2002.700408.x.

40. Colicelli, J. 2004. Human RAS Superfamily Proteins and Related GTPasessuperfamily proteins and related GTPases. *Sci. Signal.* 2004:re13. https://doi.org/10.1126/stke.2502004re13.

41. Holly, R. M., L. M. Mavor, …, J. T. Blankenship. 2015. A rapid, membrane-dependent pathway directs furrow formation through RalA in the early Drosophila embryo. *Development.* 142:2316–2328. https://doi.org/10.1242/dev.120998.

42. Edgar, B. A., G. M. Odell, and G. Schubiger. 1987. Cytoarchitecture and the patterning of fushi tarazu expression in the Drosophila blastoderm. *Genes Dev.* 1:1226–1237. https://doi.org/10.1101/gad.1.10.1226.

43. Chen, J., J. Lippicott-Schwartz, and J. Liu. 2012. Intracellular spatial localization regulated by the microtubule network. *PLoS One.* 102:698a. https://doi.org/10.1016/j.bpj.2011.11.3790.

44. Henis, Y. I., B. Rotblat, and Y. Kloog. 2006. FRAP beam-size analysis to measure palmitoylation-dependent membrane association dynamics and microdomain partitioning of Ras proteins. *Methods.* 40:183–190. https://doi.org/10.1016/j.ymeth.2006.02.003.

45. Thukral, S., B. Kaity, …, M. K. Mitra. 2020. Cyto-architecture constrains the spread of photoactivated tubulin in the syncytial Drosophila embryo. *Int. J. Dev. Biol.* 64:275–287. https://doi.org/10.1387/ijdb.190172rr.

46. Lv, Z., J. Rosenbaum, …, J. GroBhans. 2020. The emergent yo-yo movement of nuclei driven by cytoskeletal remodeling in pseudo-synchronous mitotic cyclesemergent yo-yo movement of nuclei driven by cytoskeletal remodeling in pseudo-synchronous mitotic cycles. *Curr. Biol.* 30:2564–2573.e5. https://doi.org/10.1016/j.cub.2020.04.078.

47. Lucchetta, E. M., M. E. Vincent, and R. F. Ismagilov. 2008. A Precise Bicoid Gradient Is Nonessential during Cycles 11–13 for Precise

Patterning in the Drosophila Blastoderm. *PLoS One.* 3:e3651. https://doi.org/10.1371/journal.pone.0003651.

48. Kavousanakis, M. E., J. S. Kanodia, …, I. G. Kevrekidis. 2010. A compartmental model for the bicoid gradient. *Dev. Biol.* 345:12–17. https://doi.org/10.1016/j.ydbio.2010.05.491.
49. Grimm, O., and E. Wieschaus. 2010. The Bicoid gradient is shaped independently of nuclei. *Development.* 137:2857–2862. https://doi.org/10.1242/dev.052589.
50. Joliot, A., A. Maizel, …, M. Volovitch. 1998. Identification of a signal sequence necessary for the unconventional secretion of Engrailed homeoprotein. *Curr. Biol.* 8:856–863. https://doi.org/10.1016/s0960-9822(07)00346-6.
51. Joliot, A., A. Trembleau, …, M. Volovitch. 1997. Association of Engrailed homeoproteins with vesicles presenting caveolae-like properties. *Development.* 124:1865–1875.
52. Mir, M., A. Reimer, …, M. B. Eisen. 2017. Dense Bicoid hubs accentuate binding along the morphogen gradient. *Genes Dev.* 31:1784–1794. https://doi.org/10.1101/gad.305078.117.
53. Carrell, S. N., M. D. O'Connell, …, S. M. Hayes. 2017. A facilitated diffusion mechanism establishes the drosophila dorsal gradient. *Development.* 144:4450–4461. https://doi.org/10.1242/dev.155549.
54. Coppey, M., A. N. Boettiger, …, S. Y. Shvartsman. 2008. Nuclear trapping shapes the terminal gradient in the Drosophila embryo. *Curr. Biol.* 18:915–919. https://doi.org/10.1016/j.cub.2008.05.034.
55. Balasubramanian, R., and X. Zhang. 2016. Mechanisms of FGF gradient formation during embryogenesis. *Semin. Cell Dev. Biol.* 53:94–100. https://doi.org/10.1016/j.semcdb.2015.10.004.
56. Stapornwongkul, K. S., M. de Gennes, …, J.-P. Vincent. 2020. Patterning and growth control *in vivo* by an engineered GFP gradient. *Science.* 370:321. https://doi.org/10.1126/science.abb8205.

OXFORD GENETICS

GENETICS, 2023, 225(4), iyad184
https://doi.org/10.1093/genetics/iyad184
Advance Access Publication Date: 7 October 2023
Investigation

Adhesion and Polarity protein distribution-regulates hexagon dominated plasma membrane organization in *Drosophila* blastoderm embryos

Bipasha Dey,[1,2,†] Debasmita Mitra,[1,†] Tirthasree Das,[1,3] Aparna Sherlekar,[1,4] Ramya Balaji,[1,5] Richa Rikhy[1,*]

[1]Biology, Indian Institute of Science Education and Research, Homi Bhabha Road, Pashan, Pune 411008, India
[2]Present address: Biosystems Dynamics Research Center, Riken, Kobe 650-0047, Japan
[3]Present address: Department of Ophthalmology, University of California San Francisco, San Francisco, CA 94115, USA
[4]Present address: Department of Molecular and Cellular Physiology, Stanford University School of Medicine, Stanford, CA 94305, USA
[5]Present address: Biology, Hilde-Mangold-Haus, University of Freiburg, Freiburg, Germany

*Corresponding author: Biology, Indian Institute of Science Education and Research, Dr. Homi Bhabha Road, Pashan, Pune 411008, India. Email: richa@iiserpune.ac.in
[†]Equal contribution.

Epithelial cells contain polarity complexes on the lateral membrane and are organized in a hexagon-dominated polygonal array. The mechanisms regulating the organization of polygonal architecture in metazoan embryogenesis are not completely understood. *Drosophila* embryogenesis enables mechanistic analysis of epithelial polarity formation and its impact on polygonal organization. The plasma membrane (PM) of syncytial *Drosophila* blastoderm embryos is organized as a polygonal array with pseudocleavage furrow formation during the almost synchronous cortical division cycles. We find that polygonal (PM) organization arises in the metaphase (MP) of division cycle 11, and hexagon dominance occurs with an increase in furrow length in the metaphase of cycle 12. There is a decrease in cell shape index in metaphase from cycles 11 to 13. This coincides with *Drosophila* E-cad (DE-cadherin) and Bazooka enrichment at the edges and the septin, Peanut at the vertices of the furrow. We further assess the role of polarity and adhesion proteins in pseudocleavage furrow formation and its organization as a polygonal array. We find that DE-cadherin depletion leads to decreased furrow length, loss of hexagon dominance, and increased cell shape index. Bazooka and Peanut depletion lead to decreased furrow length, delay in onset of hexagon dominance from cycle 12 to 13, and increased cell shape index. Hexagon dominance occurs with an increase in furrow length in cycle 13 and increased DE-cadherin, possibly due to the inhibition of endocytosis. We conclude that polarity protein recruitment and regulation of endocytic pathways enable pseudocleavage furrow stability and the formation of a hexagon-dominated polygon array.

Keywords: syncytium; embryo; epithelia; polygon; *Drosophila*; DE-cadherin; Bazooka; septin

Introduction

Epithelial tissues consist of adherent cells that line the internal and external surfaces of various metazoans. These cells are classified by the presence of 3 major hallmark features. First, epithelial cells show the asymmetric distribution of polarity protein complexes on the plasma membrane (PM), thereby dividing it into the apical, lateral, and basal domains. These polarity complexes are important for cell shape, tissue integrity, and tissue remodeling (Bilder et al. 2000; Hayashi and Carthew 2004; Letizia et al. 2013; Laprise and Tepass 2011). Second, epithelial cells adhere to each other via junctional complexes that enable them to form a leak-proof sheet that functions as a barrier to seal off either an organism's or an organ's interior from the external environment. Third, epithelial tissues across metazoans exhibit a polygonal cell shape distribution with a predominance of hexagonal shapes. Though the functional and molecular details of polarity and junctions in epithelia have been extensively laid out, their role in regulating hexagon dominance is not fully understood.

Hexagon dominance is a conserved property of epithelia seen in organisms ranging from the diploblastic *Hydra* to the triploblastic *Xenopus* (Gibson et al. 2006; Farhadifar et al. 2007) and, in some cases, exhibits dynamic evolution over developmental stages (Classen et al. 2005; Sánchez-Gutiérrez et al. 2013). One of the fundamental ideas in theoretical studies is that hexagon dominance results simply from surface energy minimization. Similar to the arrangement of soap bubbles being driven by surface tension, epithelial cells organize into a polygonal array by maximizing the cell area in contact with the neighbors while minimizing the surface area exposed to the environment. Additionally, asynchronous divisions, cell mechanical properties defined by adhesion and contractility, cellular rearrangements as well as global tissue level forces have also been implicated in regulating this distribution (Gibson et al. 2006; Farhadifar et al. 2007; Aegerter-Wilmsen et al. 2010; Sugimura and Ishihara 2013). On the other hand, molecular factors that facilitate this energy-minimized organization are just beginning to be explored. For example, lowered *Drosophila* E-cad (DE-cad) turnover in endocytic mutants results in a decrease

Received on 29 August 2023; accepted on 25 September 2023

in the frequency of hexagons in *Drosophila* wing discs. DE-cad recycling is, in turn, regulated by planar cell polarity (PCP) proteins, therefore, an interplay of adhesion and PCP proteins regulates the frequency of hexagons in wing disc epithelium (Classen et al. 2005; Iyer et al. 2019). In human keratinocytes, loss of MyosinII activity in ROCK1 and ROCK2 mutants also results in a low percentage of hexagonally shaped cells (Kalaji et al. 2012). Cell shape index, which is a measure of jammed epithelia, increases with the onset of germ band extension on the increase of elongated and pentagonal cells (Wang et al. 2020). These examples corroborate the theoretical studies suggesting that molecules regulating adhesion, contractility, and polarity could be important determinants of hexagon dominance. However, how the temporal onset of polarity correlates with the onset of hexagon dominance in epithelia is not well understood.

Metazoan embryogenesis shows the onset of epithelial-like polarity and formation of a polygonal array and, therefore, provides the opportunity to address the mechanisms that regulate the onset of hexagon dominance (Nance 2014). An analysis of the onset of polygonal PM packing and the factors that determine this in embryogenesis has not been characterized thus far. In this study, we use the syncytial *Drosophila* blastoderm embryo to characterize the temporal onset of polygonal packing and the role of polarity and adhesion proteins in regulating its dynamics. *Drosophila* embryogenesis begins with nuclear division cycles (NC) 1–8 occurring deep in the interior of the embryo followed by nuclear migration to the cortex during NC9 (Foe and Alberts 1983; Miller et al. 1985). The arrival of the nuclei can be seen as buds called caps at the cortex (Foe and Alberts 1983; Miller et al. 1985). The NCs10–14 occur in an almost synchronous manner near the cortex without undergoing complete cytokinesis, thereby, resulting in the formation of a syncytial blastoderm. The PM is organized as circular caps in the interphase and converts to a polygonal array with furrow extension, showing a cyclical behavior of circular to polygonal transition during each syncytial division cycle (Dey and Rikhy 2020). Cytoskeletal and PM dynamics help maintain a hexagon-dominated polygonal arrangement of nuclei during these syncytial cycles (Kanesaki et al. 2011; Kaiser et al. 2018; Lv et al. 2020).

The syncytial blastoderm embryo shows the asymmetric distribution of various polarity and cytoskeletal proteins on the PM (Schmidt and Grosshans 2018). To begin with, the *Drosophila* embryo is cortically uniform at the preblastoderm stage. The first cortical differentiation occurs during NC10 where the cortex is divided into 2 domains during interphase; the cap and intercap regions. The cap region is enriched in F-actin and actin-associated proteins such as Arp2/3, SCAR, Moesin, ELMO, Sponge, and α-spectrin, while the intercap region is marked by Myosin II, Toll and Slam. The PM begins to be organized into a polygonal array with furrow extension during syncytial division cycles 11 to 14. Particularly at metaphase (MP), the PM is segregated into 3 domains; apical, lateral, and basal domain. In the syncytial system, the basal domain refers to the tip of the pseudocleavage furrow. The lateral region is occupied by Canoe, Peanut (Pnut), Scrambled, DE-cad, Bazooka (Baz), Dlg, and Toll; and the furrow tip shows enrichment of PatJ, Amphiphysin, Anilin, Diaphanous, and Syndapin (Pesacreta et al. 1989; Thomas and Williams 1999; Foe et al. 2000; Stevenson et al. 2002; Zallen et al. 2002; Mavrakis et al. 2009; Rikhy et al. 2015; Sherlekar and Rikhy 2016; Schmidt et al. 2018; Schmidt and Grosshans 2018; Dey and Rikhy 2020). Therefore, the syncytial *Drosophila* blastoderm embryo shows molecular and morphological asymmetries in the PM along with the formation of a polygonal array at MP during the syncytial cycles. However, how these asymmetries impact the onset, distribution, and dynamics of the polygonal array remains to be investigated.

In our previous study, we showed that the extension of the furrow in between adjacent nuclei leads to the onset of polygonal organization in syncytial division cycles 11 to 14 (Dey and Rikhy 2020; Sherlekar et al. 2020). In this study, we assess the role of polarity and adhesion proteins in regulating the polygonal PM organization on the increase in furrow extension and in MP of the cortical syncytial cycles. We find that the PM of the embryo is organized as a hexagon-dominated polygonal array for the first time in NC12 at the final furrow length achieved at MP. There is a decrease in the anisotropy of shapes and cell shape index with the progression of the syncytial division cycles. DE-cad and Baz are enriched at the edges while Peanut is enriched at the vertices in these polygonal cells. DE-cad depletion leads to a short furrow, loss of hexagon dominance, and an increase in cell shape index. Baz and Pnut depletion also leads to a minor decrease in furrow length, an increase in cell shape index, and a delay in hexagon dominance when the furrow length increases in NC13. This is accompanied by the accumulation of key endocytic proteins and DE-cad at the furrow.

Materials and methods

Fly stocks, crosses, and lethality estimation

Drosophila melanogaster stocks were raised in standard cornmeal agar at 25°C and 29°C for RNAi experiments. Embryos obtained from CantonS flies or CantonS flies crossed to *maternal α-tubulin* Gal4-VP16 (*mat*-Gal4) or *nanos*-Gal4 (*nos*-Gal4) were used as control. The information on fly genes and stocks was obtained from Flybase (Gramates et al. 2022). Maternal driver line *mat67; mat15* carrying *maternal α4 tubulin*-Gal4-*VP16* (obtained from Girish Ratnaparkhi, IISER, Pune, India), homozygous for chromosome II and III was used for all RNAi and overexpression experiments except for shg^{i} for which *nos*-Gal4 was used. Baz RNAi (Bloomington Stock number #35002), Pnut RNAi (#65157), DE-cad RNAi (#38207), tGPH (#8163), UASp-Baz-GFP (#65845), endo-DE-cad-GFP (#60584), and baz^{G0484} lines were obtained from the Bloomington Stock Center, Indiana, Bloomington, USA. ubi-cad-GFP was obtained from the Maithreyi Narasimha lab from TIFR, Mumbai, India. $pnut^{XP}$ FRTG13/CyO and *UASp*-Pnut-mCherry stocks were obtained from Manos Mavrakis, Fresnel University, Marseilles, France. Baz truncation domain constructs were obtained from Andreas Wodarz, Goettingen University, Germany. *Sqh*-Sqh Cherry, *mat67*-Gal4; *ubi*-DE-cad-GFP, *mat15*-Gal4/TM3Sb was obtained from Adam Martin's lab, MIT, Massachusettes, USA. *Sqh*-Sqh GFP, *mat67*-Gal4 from Thomas Lecuit, IBDM, Marseilles, France.

F1 flies were put in a cage for egg collection to perform immunostaining or live imaging. Germline clones of $pnut^{XP}$ were made by crossing ovo^{D} FRTG13 males to *hsflp; GlaBlc* females to obtain hsflp; ovo^{D} FRTG13/*GlaBlc* males. These males were then crossed to $pnut^{XP}$ FRTG13/*Cyo* females. Larvae, pupae, and adults emerging from this cross were heat-shocked at 37.5°C. hsflp; ovo^{D} FRTG13/$pnut^{XP}$ FRTG13 adults were then put in a cage to collect embryos depleted of *pnut*. shg^{i} was crossed to a single chromosomal copy of *nos*-Gal4 and maintained at 18°C to lower the severity of phenotype and obtain fertilized eggs to perform experiments. F1 flies expressing shg^{i} with *nos*-Gal4 when grown at 25 or 29°C, laid embryos that were arrested early in the pre-blastoderm stage of development and, hence, the experiments were performed at 18°C to allow for Gal4 dilution. This cross at 18°C gave enough embryos that entered the syncytial cycles. The lethality of shg^{i} embryos

was 100% ($n = 150$) at 25°C and 29°C and 70% ($n = 200$) at 18°C after 24 hrs. The lethality of *pnut*^{i} and *baz*^{i} expressing embryos and *pnut*^{XP} germline clones was 100% ($n = 300$ embryos each).

Immunostaining

0–2.5 hr old embryos were collected on sucrose agar plates, washed, and dechorionated with 100% bleach for 1 min. Embryos were fixed using a 1:1 mixture of 4% paraformaldehyde in PBS and Heptane for 20 min. Fixed embryos were either hand-de-vitellinized for phalloidin staining or MeOH de-vitellinized, washed thrice in 1× PBST (1× PBS with 0.3% Triton ×100), and blocked in 2% BSA (Sigma-Aldrich, India) in 1× PBST for 1 hr. Primary antibody was then added at an appropriate dilution and incubated overnight, followed by 3 1× PBST washes, and 1 hr incubation in appropriate fluorescently coupled secondary antibodies at 1:1000 (Molecular probes, Bangalore, India). Hoechst 33,258 was added for 10 min in 1× PBST. Finally, the embryos were washed 3 times in 1× PBST and mounted in Slow fade Gold antifade reagent (Molecular Probes). The primary antibodies used were: rabbit anti-Baz (1:1000 from Andreas Wodarz, Germany), mouse anti-Pnut (1:5, DSHB), mouse anti-Dlg (1:100 DSHB), rabbit anti-Patj (1:1000 from Hugo Bellen, USA), rat Sep1 (1:250 from Manos Mavrakis, France), guinea pig Sep2 (1:250 from Manos Mavrakis, France), rat anti-DE-cad (1:5, DSHB), guinea pig anti-Rab5 (1:500 from Akira Nakamura, Japan) (Tanaka et al. 2021), mouse anti-Dynamin (1:200 BD Transduction Laboratories). DNA was stained with Hoechst 33258 (1:1000, Molecular Probes, Bangalore, India).

Live imaging of *Drosophila* embryos

1–1.5 hr old embryos expressing the membrane marker tGPH or Sqh-GFP or Sqh-mCherry; DE-cad-GFP were collected and dechorionated with 100% bleach for 1 min and mounted on coverslip-bottomed LabTek chambers (Mavrakis et al. 2008). The chambers were then filled with 1× PBS and imaged on Zeiss Plan Apochromat 40X/1.4 NA oil objective.

Microscopy

Live or fixed embryos were imaged on any of the following laser scanning confocal microscopes: Zeiss LSM710, LSM780, and Leica SP8. The 40× objective with NA 1.4 was used to image living and fixed embryos. The Argon laser was used to image GFP in tGPH, DE-cad-GFP, Baz-GFP, and Sqh-GFP. The Diode 561 laser was used to image the Sqh-mCherry and Pnut-mCherry. Care was taken to maintain the laser power and gain with the range indicator mode such that the 8-bit image acquired did not show any saturation and was within the 0–255 range. Averaging of 2 was used for both fixed and live imaging. Images were acquired with an optical section of 1.08 microns in all except F-actin stainings, where an optical section of 0.34 microns was used.

Embryo lethality

3–4 hr old embryos were collected, washed, and arranged into a 10 × 10 matrix on a sugar-agar plate using a brush. The number of unhatched embryos was counted after 24 hrs. This procedure was repeated 3 times for each genotype tested.

Quantification and statistical analysis

Image quantification

Polygon analysis. The most taut and bright grazing section from MP (usually at the base of the furrow) of each NC per embryo was used to quantify polygons using the Packing analyzer software (Benoit Aigouy, Classen et al. 2005). The software allows the segmentation of the PM surrounding each cell (Fig. 1a). Note that the segmented edges have curved edges similar to the actual images. The cell area and perimeter are estimated from each cell in the rendered image. The image is color-coded according to polygon type. It is important to note that represented color-coded polygon-rendered images contain straight edges. The output is available in an Excel sheet with the area, perimeter, and polygon type of each cell in the field. Three or more embryos were used per NC and all the cells in the field were analyzed this way to obtain the polygon distribution per cycle.

Quantification of cell shape index

Based on the cell segmentation data obtained from the Packing analyzer software (Fig. 1a) and from the area (A) and perimeter (P) data obtained as an output, cell shape index was calculated using the formula: $P/\sqrt{A}$ (Bi et al. 2015). It is important to note that the cell shape index is estimated from the segmented images and not the color-coded images used to document the polygon distribution shown in each figure. Three or more embryos were used for each NC and all the cells in the field were analyzed to calculate the average cell shape index.

Quantification of relative fluorescent signal across the depth and in planar sections of the plasma membrane

The grazing sections at MP across depth expressing various polarity proteins were used for this analysis. A region of interest (ROI) was drawn at 5 edges and 5 vertices for MP11, and 10 edges and 10 vertices for MP12-13, in each optical section from apical to basal sections. Optical sections were taken at approximately 1 µm depth across the entire furrow. The mean intensities from these ROIs were measured using ImageJ (Schneider et al. 2012). The intensities from each stack were background subtracted. The graphs shown in Fig. 2 represent mean intensities obtained across the depth of the furrow normalized to the mean intensity of the apical-most optical section in NC11.

Quantification for Sep1 and Sep2 was done by creating 5 ROIs on the edge and the vertex as mentioned above. The mean intensities were normalized by dividing by the mean intensity of the entire field.

Enrichment in the basal furrow region and edge/vertex was computed by performing statistical analysis for the fluorescence values on the length of the furrow using 2-way ANOVA to test how the intensity of signals varied with either edge/vertex or apical/basal regions of the furrow.

The change in the fluorescence intensity at the furrow membrane was estimated at MP11, MP12, and MP13 by measuring 5 different ROIs corresponding to the furrow membrane and divided by the fluorescence in the neighboring cytosol.

Quantification of the MP furrow length

Metaphase furrow lengths were quantified from the orthogonal sections for different time points and NCs using the Zen Blue software. Five to eight furrows were measured per time point per embryo. These lengths were further confirmed with the number of z-stacks taken to cover the entire furrow length of syncytial cells in the field of view.

Quantification of fluorescence from antibody stainings

Baz, Pnut, DE-cad, Dynamin, and Rab5 antibody and DE-cad-GFP staining were quantified by estimating the fluorescence at 5

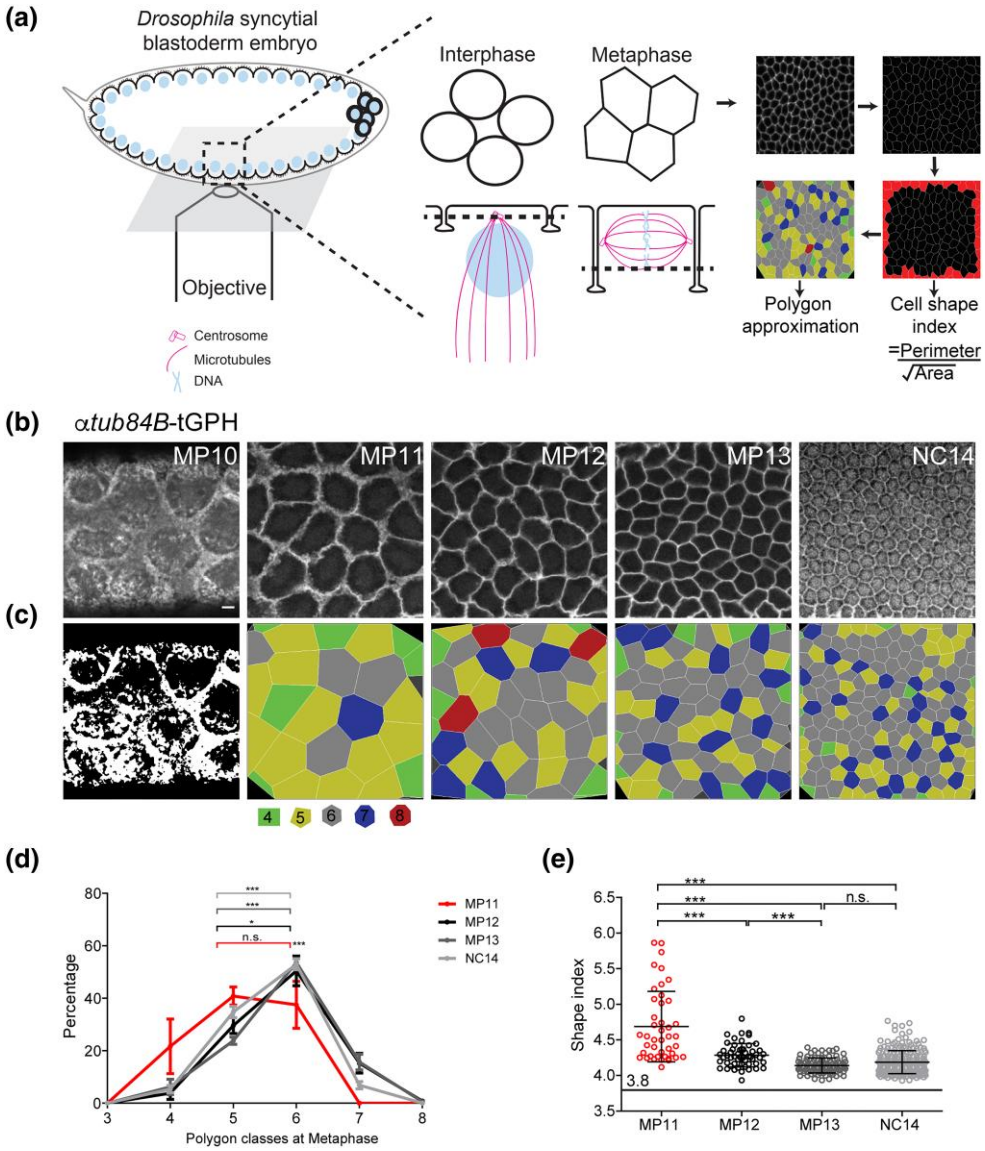

Fig. 1. Hexagon dominated PM organization emerges in NC12. Schematic showing the syncytial *Drosophila* blastoderm embryo in interphase being imaged by an objective at the bottom on an inverted confocal microscope. The zoomed inset shows sagittal and XY views of syncytial cells in both interphase and MP turned 180° with the PM at the top. XY views are the cross-sections along the MP furrow at a length represented by the dotted lines. The PM shows polygonal organization in MP. The right-hand side of the schematic shows the pipeline for image analysis. The acquired fluorescent images are segmented in packing analyzer for obtaining cell boundaries which are used to estimate the cell shape index. Note that the cells have wavy edges in the MP13 image shown. The cells at the edges are omitted for calculations. The segmented images are rendered for estimation of polygon distribution across the MP10–14. Note that the representation has straight edges rendered in the polygon distribution images (a). Grazing sections of *αtub84B*-tGPH expressing embryos from MP10–13 and NC14, tGPH labels the entire membrane in MP10–13 and enters the nucleus in NC14 in addition to being at the PM (b). Color-coded polygon rendering of the respective images in B using the packing analyzer software (c). Quantitative analysis of polygon distribution in MP11–13 and NC14 ($n = 20$–60 cells from NC11–14 per embryo, 4 embryos). Each curve represents a single NC (d). Pentagons and hexagons are compared using the unpaired, 2-tailed, Student's *t* test. Data is represented as mean ± SEM, $^{*}P < 0.05$, $^{**}P < 0.01$, and $^{***}P < 0.001$. Graph shows the average shape index of all the cells in the field for control embryos (e) ($n = 20$–60 cells from MP11–13 and NC14 per embryo, 4 embryos). Data is represented as mean ± SEM, $^{*}P < 0.05$, $^{**}P < 0.01$, and $^{***}P < 0.001$, 2-tailed, unpaired Student's *t*-test. Scale bar: 5 μm.

furrow membranes from each embryo as compared to the cytosol in controls and mutants at the same stage.

Statistical analysis

All data are represented as mean ± SD or SEM. Statistical significance was determined using the 2-tailed, unpaired, Student's *t*-test in most cases, to compare between 2 means. One-way ANOVA was used when comparing 3 or more means together, with Dunnett's Multiple Comparison Test as a post-test to compare all means to control. Student's *t*-test was used to compare hexagons to pentagons in each NC per genotype to determine hexagon dominance.

Results

Onset of hexagon-dominated plasma membrane architecture occurs during nuclear cycle 12 in syncytial *Drosophila* blastoderm embryos

To assess the syncytial NC at which optimal packing and hexagon-dominated polygon organization emerge during the syncytial

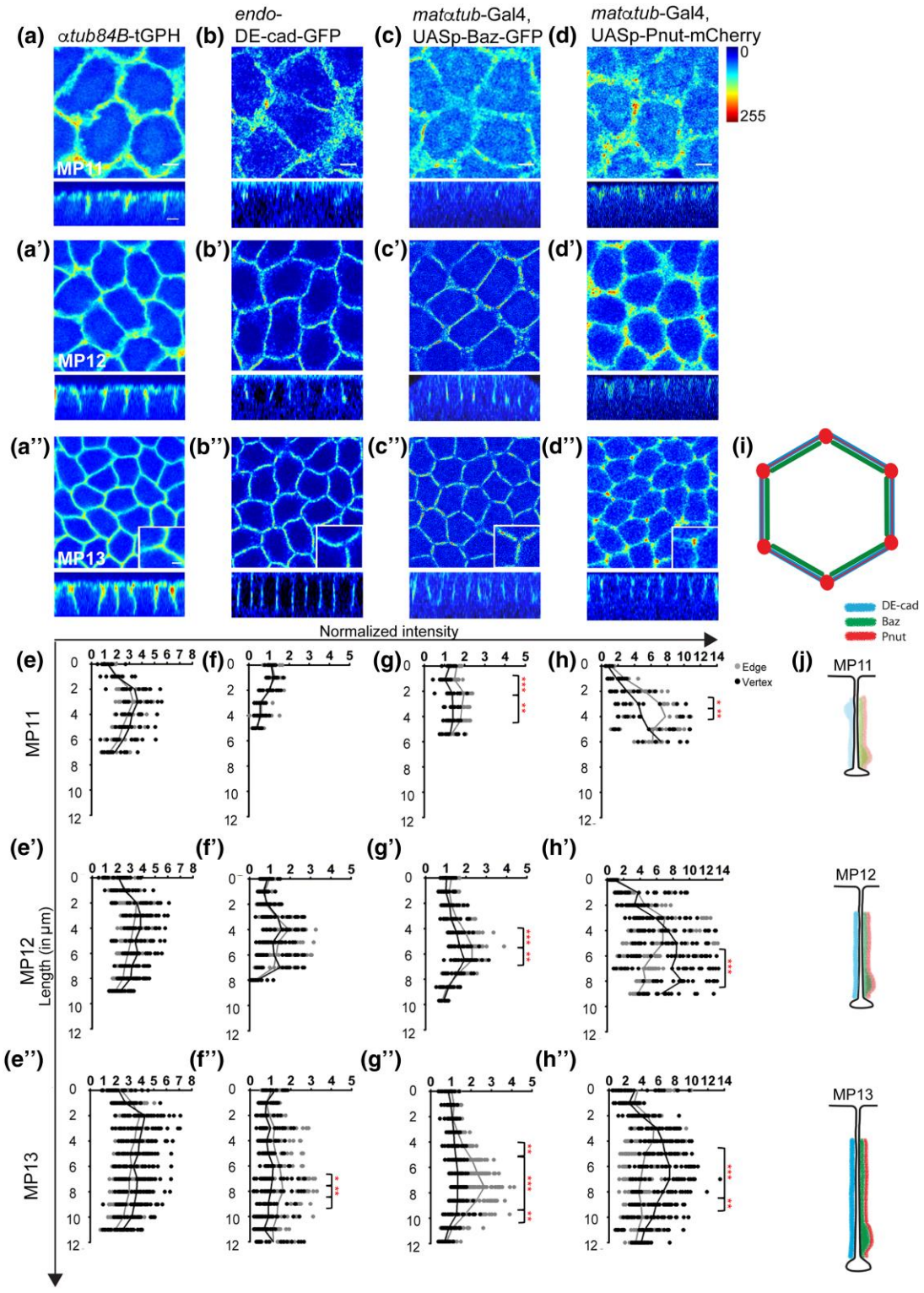

Fig. 2. DE-cad, Baz and Pnut show polarized distribution in the syncytial cells. a–b) Distribution of *atub84B*-tGPH (a: MP11, a′: MP12 and a″: MP13), *endo*-DE-cad-GFP (b: MP11, b′: MP12, and b″: MP13), *matatub*-Gal4; Baz-GFP (c: MP11, c′: MP12, and c″: MP13) and *matatub*-Gal4; Pnut-mCherry (d: MP11, d′: MP12, and d″: MP13) in grazing and sagittal views in syncytial MP11–13. The Jet rainbow scale from ImageJ is used to show fluorescent intensities. tGPH labels the entire PM, DE-cad is enriched at edges in MP13 (a″-b″ insets show zoomed-in images), Baz is enriched at edges MP11 onward while Pnut is enriched on the vertex MP12 onward (c″-d″ insets show zoomed in images). e–h) Quantification of intensities normalized to the apical section of NC11 in edges (black) and vertices (gray) along the MP furrow length for *atub84B*-tGPH (E: NC11, E′: NC12, E″: NC13), *endo*-DE-cad-GFP (F: MP11, F′: MP12, F″: MP13), *matatub*-Gal4; Baz-GFP (G: MP11, G′: MP12, G″: MP13′), and *matatub*-Gal4; Pnut-mCherry (H: MP11, H′: MP12, H″: MP13) in NC11–13 ($n = 3$ embryos each). i and j) Schematic representing the polarized localization of proteins in XZ and XY planes. Asymmetric distribution of DE-cad, Baz, and Pnut between edges and vertices in the XY plane (i). Asymmetric distribution of DE-cad, Baz, and Pnut across MP11–13 along the apico-basal axis in the XZ plane (j). While DE-cad spreads all across the length, Baz, and Pnut are enriched in the basal part of the furrow region. The scatter plots contain a line connecting the means, $^{*}P < 0.05$, $^{**}P < 0.01$, and $^{***}P < 0.001$, 2-way ANOVA with Bonferroni post-tests. The stars show significance between edge and vertex intensities at the indicated length based on the post test. Scale bar = 5 µm. The zoomed-in insets show a scale bar of 2 µm.

blastoderm development, we performed live imaging of tGPH (*atub84B*-tGPH) expressing embryos. tGPH contains the PH domain of GRP fused to GFP (GPH). The tGPH PH domain binds phospholipid PIP3 and labels the PM uniformly in the syncytial *Drosophila* embryo (Britton et al. 2002; Sherlekar and Rikhy 2016; Dey and Rikhy 2020). We used the packing analyzer software to segment the polygonal array to estimate the polygon distribution and the shape index from the MP stage of NC10, 11, 12, and 13 and in the interphase of NC14 (referred to as MP10, MP11, MP12, MP13, and NC14, respectively) (Fig. 1a). The nucleo-cytoplasmic domains seen as caps at the cortex were relatively far apart in MP10 (Fig. 1b, Supplementary Video 1). The furrow length increases during each cycle from NC11 to 13 from interphase to MP in between adjacent nucleo-cytoplasmic domains and it reaches a maximum in MP13 (Foe and Alberts 1983; Holly et al. 2015; Xie and Blankenship 2018; Dey and Rikhy 2020). During *Drosophila* embryogenesis, the PM was organized into a polygonal array for the first time in NC11 (Fig. 1b). The polygonally organized PM in MP13 and NC14 was more taut as compared to MP11 and MP12. MP11 showed almost equal numbers of pentagons and hexagons in the polygonal array. The polygonal array then became dominated by hexagons in MP12. This hexagon dominance persisted in MP13 and NC14 (Fig. 1c and d). While observing the onset of the formation of the polygonal array, we noted that edges formed before vertices in NC11 (Supplementary Fig. 1a).

A theoretical framework for confluent epithelial monolayers defines a non-dimensional parameter called the shape index estimated from the ratio of the perimeter and area of each cell as a predictor of tissue material properties (see materials and methods) (Bi et al. 2015; Park et al. 2015). Below a critical value of 3.81, the tissue becomes jammed or solid-like with cells displaying isotropic shapes and being caged within their radii (Bi et al. 2015). In *Drosophila* germ band extension, the tissue elongation phase shows an increase in anisotropic cell shapes and an increase in cell shape index along with an increase in the fraction of pentagons (Wang et al. 2020). We estimated the cell shape index in MP11, MP12, MP13, and NC14 from the perimeter and area output from segmented images from the movies of embryos expressing tGPH (Fig. 1e). First, we found that the cell shape index was greater than 3.81 in MP11, MP12, MP13, and NC14 suggesting that the syncytial epithelium at MP has a more fluid-like property. Additionally, we found that there was a decrease in the cell shape index from MP11 (average of 4.67) to MP12 (4.28) to MP13 (4.14) and NC14 (4.19). This result is consistent with the observations in a previous study in mammalian epithelial cells that show a decrease in the shape index with an increase in cell density with proliferation (Vishwakarma et al. 2020). This shows that the PM organization in the syncytial *Drosophila* embryo in MP forms a soft network that could facilitate the fast dynamics of cellular organization seen in each syncytial cycle. It also suggests that with each division cycle, the cell shapes become more isotropic and the system moves closer to a more rigid or solid-like phase.

Similar to previous studies (Holly et al. 2015; Dey and Rikhy 2020), we found that the furrow length increases across syncytial cycles 11 to 13 and was approximately 7 μm in MP11, 9 μm in MP12 and 11 μm in MP13 with tGPH. Our previous studies show that the onset of polygon architecture occurs at the furrow length of approximately 6 μm during each syncytial division (Dey and Rikhy 2020). Therefore, we analyzed the polygon distribution at a lower length of approximately 6.5 μm in NC12 and NC13 when polygonal architecture was visible across the embryo. We found that at this lower furrow length in NC12, the average number of pentagons was more than hexagons but this was not statistically significant, whereas in NC13 hexagons were dominant at 6.5 μm (Supplementary Fig. 1b–d). Therefore, hexagon dominance was first seen in NC12 at increased furrow lengths in MP (furrow length 9 μm) and hexagon dominance was already seen at the short furrow length of 6.5 μm in NC13. The cell shape index was significantly increased at 6.5 μm in the NC12 (4.38) and NC13 (4.25) as compared to the longest furrow length in MP (Supplementary Fig. 1e). Together, these data show that epithelial-like hexagon dominance first occurs in syncytial NC12 at longer furrow lengths in MP, even before complete cells are formed in the *Drosophila* blastoderm embryo. Coincident with an increase in hexagons, the cell shape index decreases indicating a more stable epithelial-like network. This organization is also consistent with the observation of nuclei present in a hexagon-dominated polygonal array shown previously (Kanesaki et al. 2011; Kaiser et al. 2018).

DE-cadherin, Bazooka, and Peanut are asymmetrically distributed along the furrow in the *Drosophila* syncytial blastoderm

Since the syncytial embryo PM was organized into an epithelial-like polygonal array starting from NC11 and became hexagon dominant during NC12 with an increase in furrow length, we tested if polarity proteins were progressively enriched in the lateral furrows from NC11 to NC13. DE-cad and Baz have been found in the syncytial furrow and form apical spot junctions in cellularization (Harris and Peifer 2004). To characterize the temporal distribution of DE-cad and Baz as compared to tGPH in NC11–13, we performed live imaging of embryos expressing DE-cad-GFP under the endogenous promoter (Huang et al. 2009) and Baz-GFP in control and mutant backgrounds with *matatub*-Gal4 (Benton and St Johnston 2003). The PM in epithelial cells shows a distinct distribution of proteins along tricellular junctions, which function in sealing the intercellular space (Schulte et al. 2003; Ikenouchi et al. 2005); as well as along the lateral domain. We quantified the intensity of the fluorescently tagged DE-cad and Baz and the PM marker tGPH in edges and vertices of the polygonal array along with different optical sections along the length of the furrow in MP11, MP12, and MP13 (Fig. 2a–c). The total intensities obtained at the furrow were plotted as a fold change with respect to the apical section of NC11 in each embryo (Fig. 2e–g). tGPH was distributed evenly across the furrow in edges and vertices and marked the entire length of the furrow in the lateral views (Fig. 2a-a″, e-e″). For DE-cad, we quantified the intensities using the DE-cad-GFP expressed at the endogenous gene location (Huang et al. 2009). We found that DE-cad was uniform across edges and vertices in MP11 and MP12 and was enriched at edges in MP13 (Fig. 2b-b″, f-f″). DE-cad was present along the entire MP furrow in MP11 and MP12, while in MP13 it was enriched in the basal part of the furrow from 7 to 10 μm (Fig. 2b-b″, f-f″). For Baz-GFP, we have expressed the GFP in the control and mutant (baz^{G0484}) background with *matatub*-Gal4 (see materials and methods, Fig. 2 and Supplementary Fig. 2). Baz-GFP was present along the entire membrane with enrichment at edges in MP12 and MP13 when present in the control and mutant background (Fig. 2c-c″, Supplementary Fig. 2e). Baz was enriched at the furrow between 2 and 5 μm in MP11 and toward the basal part of the furrow from 4 to 6 μm in MP12 and from 6 to 10 μm in MP13 (Fig. 2c-c″, g-g″).

The septin family proteins Pnut, Sep1, and Sep2 were also studied because Pnut is present at the furrow in syncytial stages and functions in actin organization and furrow extension (Silverman-Gavrila and Silverman-Gavrila 2008). Pnut-mCherry (Guillot and Lecuit 2013) expressed in control embryos was used

to assess the distribution of Pnut on the membrane in edges and vertices and along the length of the furrow across the syncytial cycles. Pnut was present throughout the membrane and was enriched at vertices in MP11. Pnut was concentrated toward the basal part of the furrow at 5–8 μm in MP12 and 5–10 μm in MP13 (Fig. 2d-d″, h-h″). Vertex enrichment was also observed for Sep1 and Sep2 using Sep1-GFP, Sep2-GFP (Supplementary Fig. 2a–d). Immunostainings against endogenous Sep1 and Sep2 showed an increase at vertices (Supplementary Fig. 2a–d). Pnut was also found to be enriched at vertices in immunostainings against the endogenous protein (Supplementary Fig. 3a).

We estimated the fold change of total DE-cad, Baz, and Pnut fluorescence on the PM across the syncytial cycles as compared to MP11 (Supplementary Fig. 2e and f). We found that DE-cad successively increased from MP11 to MP12 to MP13 (Supplementary Fig. 2f). Pnut-mCherry was present at a significantly higher intensity on the furrow membrane in MP13 as compared to MP11 and MP12 (Supplementary Fig. 2f). Baz was present at a higher intensity in NC12 as compared to NC11 when Baz-GFP was expressed in the control and mutant background. Baz did not change significantly from MP12 to MP13 in both the control and the *baz*^{G0484} mutant background (Supplementary Fig. 2f). This progressive increase in the distribution of DE-cad, Baz, and Pnut across the syncytial cycles implied a function of these proteins in the formation and stabilization of furrows along with polygonal architecture. The syncytial PM showed asymmetries in the planar axis of the polygon at edges (DE-cad, Baz) and vertices (Pnut) and enrichment of proteins along the base of lateral furrow from MP12 to MP13 (Fig. 2i and j).

DE-cad regulates both Baz and Pnut distribution and Baz regulates Pnut distribution at the syncytial furrow membrane

Since polarity proteins are known to regulate cell shape and hexagon dominance, we dissected the role of DE-cad, Baz, and Pnut on furrow formation and hexagon dominance. We first investigated their loss-of-function effects on the distribution of the polarity proteins in the syncytial cycles. We assessed the role of DE-cad in the recruitment of Baz and Pnut by maternally expressing DE-cad RNAi (*shg*^{i}). Similar to our previous studies, DE-cad depletion showed a decrease in DE-cad immunostaining as compared to controls (Fig. 3a) (Dey and Rikhy 2020). DE-cad-depleted embryos also showed a significant decrease in the localization of Baz and Pnut on the syncytial furrows and an increase in their cytoplasmic distribution (Fig. 3b–d). The enrichment of Pnut at vertices as compared to controls was not seen upon DE-cad depletion (Fig. 3b).

Next, we assessed the role of Baz on Pnut distribution by maternally expressing *baz* RNAi (*baz*^{i}) (see *Material and methods* for details). Baz protein levels as assessed by an antibody against the N-terminus of the protein (Wodarz et al. 1999) were lower in these embryos as compared to controls (Fig. 3e and f). Interestingly, with the knockdown of Baz, Pnut was also lowered (Fig. 3e and g) suggesting a possible role of Baz in the stabilization of Pnut on the membrane. To determine the effect of the loss of Pnut on Baz and Pnut localization, we generated germline clone embryos of null mutants of Pnut (*pnut*^{XP}) (Neufeld and Rubin 1994). *pnut*^{XP} embryos showed a significant reduction of Pnut while Baz localization remained unaffected (Fig. 3e–g). Thus, the presence of Pnut was not important for Baz localization on the syncytial PM.

To further verify if Pnut localization depended on Baz association with the syncytial PM, we maternally overexpressed truncated transgenes of Baz containing the N terminus oligomerization domain or the C terminus phospholipid membrane-binding domain fused to GFP. A GFP-tagged C-terminal truncation mutant of Baz, BazΔ969-1464-GFP, which is defective in PM recruitment (Krahn et al. 2010) was expressed maternally in the presence of wild-type protein. The GFP fluorescence pattern could be used to ascertain the distribution of the truncated transgene and the antibody against the N terminus could be used to identify the distribution of the total Baz protein. BazΔ969-1464-GFP showed a cytosolic pattern in the MP stage of NC13 showing that the C terminal truncation leads to loss of association with the furrow. Baz antibody staining against the N-terminus of the protein also showed an increased cytosolic distribution and a diffused membrane localization as compared to controls (Supplementary Fig. 3a and b). Since Baz forms oligomers in vivo (Benton and St Johnston 2003), we speculate that the N-terminal domain oligomerizes in this overexpression mutant, leading to the reduction of Baz from PM and an increase in the cytosol, in addition to the attenuated levels of Pnut. On the other hand, when a GFP-tagged Baz N-terminal truncation mutant, BazΔ1-904-GFP was maternally overexpressed, both the truncated and endogenous Baz could localize on the membrane. Pnut distribution was weaker than that seen in controls but it was present on the membrane (Supplementary Fig. 3a and c). Thus, the C-terminal domain of Baz was important not only for its own recruitment on the PM but also for Pnut membrane localization.

In summary, these observations show that DE-cad regulates the recruitment of Baz and Pnut, and Baz, in turn, regulates the distribution of Pnut on the syncytial furrow.

DE-cad, Baz, and Pnut-depleted embryos show decreased furrow length and skewed polygon distributions

So far we found that DE-cad, Baz, and Pnut distributed asymmetrically on the syncytial furrow PM (Fig. 2). Further, DE-cad depletion led to decreased levels of Pnut and Baz, while Baz depletion reduced the levels of Pnut on the syncytial furrow (Fig. 3). Previous reports show that DE-cad and Pnut loss leads to shorter MP furrows (Silverman-Gavrila et al. 2008; Sherlekar and Rikhy 2016; Dey and Rikhy 2020). Therefore, we further assessed the furrow length, polygon distribution, and cell shape index in DE-cad, Baz, and Pnut-depleted embryos. We found that *shg*^{i}-expressing embryos showed a significant decrease in furrow length in MP11, MP12, and MP13 as compared to control tGPH embryos. *baz*^{i}, and *pnut*^{i} expressing embryos showed a slight decrease in furrow length in MP11 and MP12 but not in MP13 (Fig. 4a and b, Supplementary Video 2–4). The furrow length in *shg*^{i} was approximately 6 in MP12 (approximately 34% decrease as compared to control which is approximately 9 μm) and approximately 9 in MP13 (approximately 30% decrease as compared to control which is approximately 13 μm). The furrow lengths in *baz*^{i} decreased to approximately 6 and *pnut*^{i} decreased to approximately 7 in the MP of NC12 (approximately 22% decrease as compared to control which is approximately 9 μm) (Fig. 4a and b). The furrow lengths in *baz*^{i} and *pnut*^{i} expressing embryos were longer in MP13 than MP12. The average furrow length reached approximately 11 μm and was not statistically different from control embryos (Fig. 4a and b). *shg*^{i} embryos showed shorter furrow lengths than the control in MP12 and MP13, and *baz* and *pnut* knockdowns especially in MP13 (Fig. 4a and b). Double depletion of Baz and Pnut also showed a decrease in furrow length similar to each of the single depletions (Supplementary Fig. 4d and e). We found that the rates of furrow ingression between Baz and Pnut depleted embryos were similar to controls (Supplementary Fig. 4c).

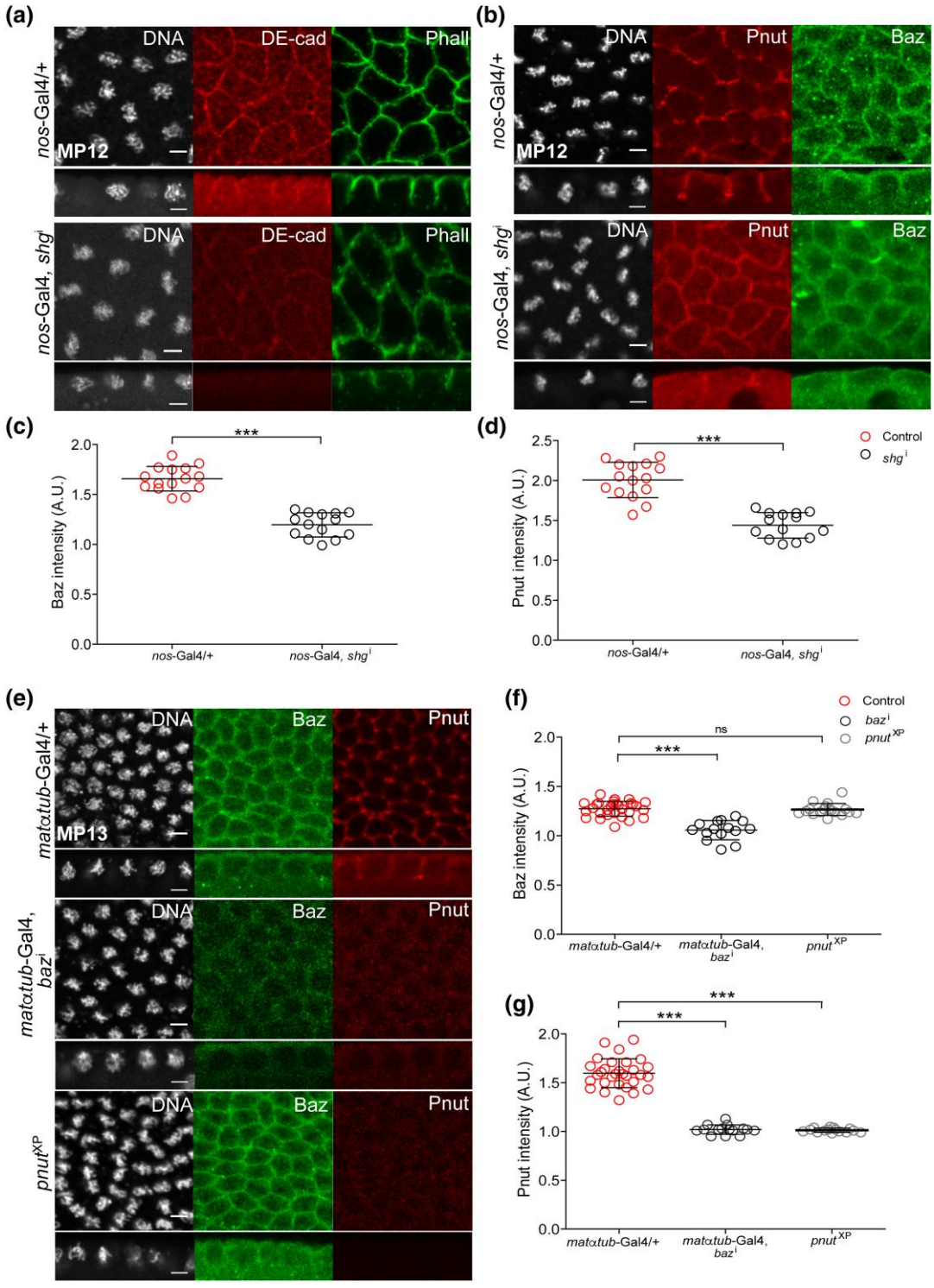

Fig. 3. DE-cad, Baz, and Pnut knockdown embryos show differential loss of polarity proteins at the MP furrow. a–d) DE-cad loss results in the lowering of DE-cad, Baz, and Pnut from the membrane. DE-cad is lowered in *shg*^{i} embryos. *nos*-Gal4/+ ($n = 10$) and *nos*-Gal4; *shg*^{i} (*shg*^{i}) (86% show loss of DE-cad, $n = 21$) embryos are co-stained with DE-cad and phalloidin in MP12 (a); Baz and Pnut in MP12 (b). Quantification of Baz and Pnut levels on the membrane in *shg*^{i} embryos using membrane to cytosol ratios from embryos in MP12 and MP13. Note the enrichment of Pnut at the vertices (white arrows). Baz (c) ($n = 5$ cells per embryo, 4 embryos) and Pnut (d) ($n = 4$–5 cells per embryo, 3 embryos) are both lowered in *shg*^{i} embryos (94% show loss of Baz and Pnut, $n = 16$). Scale bar: 5 µm. e–g) Baz loss results in a decrease of Pnut on the membrane. *matαtub*-Gal4/+ ($n = 20$), *matαtub*-Gal4; *baz*^{i} (*baz*^{i}), and *pnut*^{XP} (germline clone embryos, see Materials and methods) embryos co-stained with Baz and Pnut in MP13. *baz*^{i} shows a decrease in Baz and Pnut (100% loss of Baz and Pnut, $n = 20$) and *pnut*^{XP} shows the loss of Pnut (100% show loss of Pnut, $n = 17$) while Baz (100% embryos show no defect in Baz, $n = 11$) is unaffected (e). Graphs showing the quantification of Baz and Pnut intensities on the membrane using membrane to cytosol ratios in *baz*^{i} and *pnut*^{XP} embryos. Baz is lowered in *baz*^{i} ($n = 5$ cells per embryo, 4 embryos) but not in *pnut*^{XP} embryos ($n = 4$–5 cells per embryo, 4 embryos) (f). Pnut is lowered in both *baz*^{i} ($n = 4$–5 cells per embryo, 4 embryos) and *pnut*^{XP} embryos ($n = 5$ cells per embryo, 3 embryos) (g). Data is represented as mean ± SD, $^{*}P < 0.05$, $^{**}P < 0.01$, and $^{***}P < 0.001$, 2-tailed, unpaired Student's *t* test. Each point in the graph represents the membrane to cytosol ratio of the respective protein in syncytial cells across various embryos. Scale bar: 5 µm.

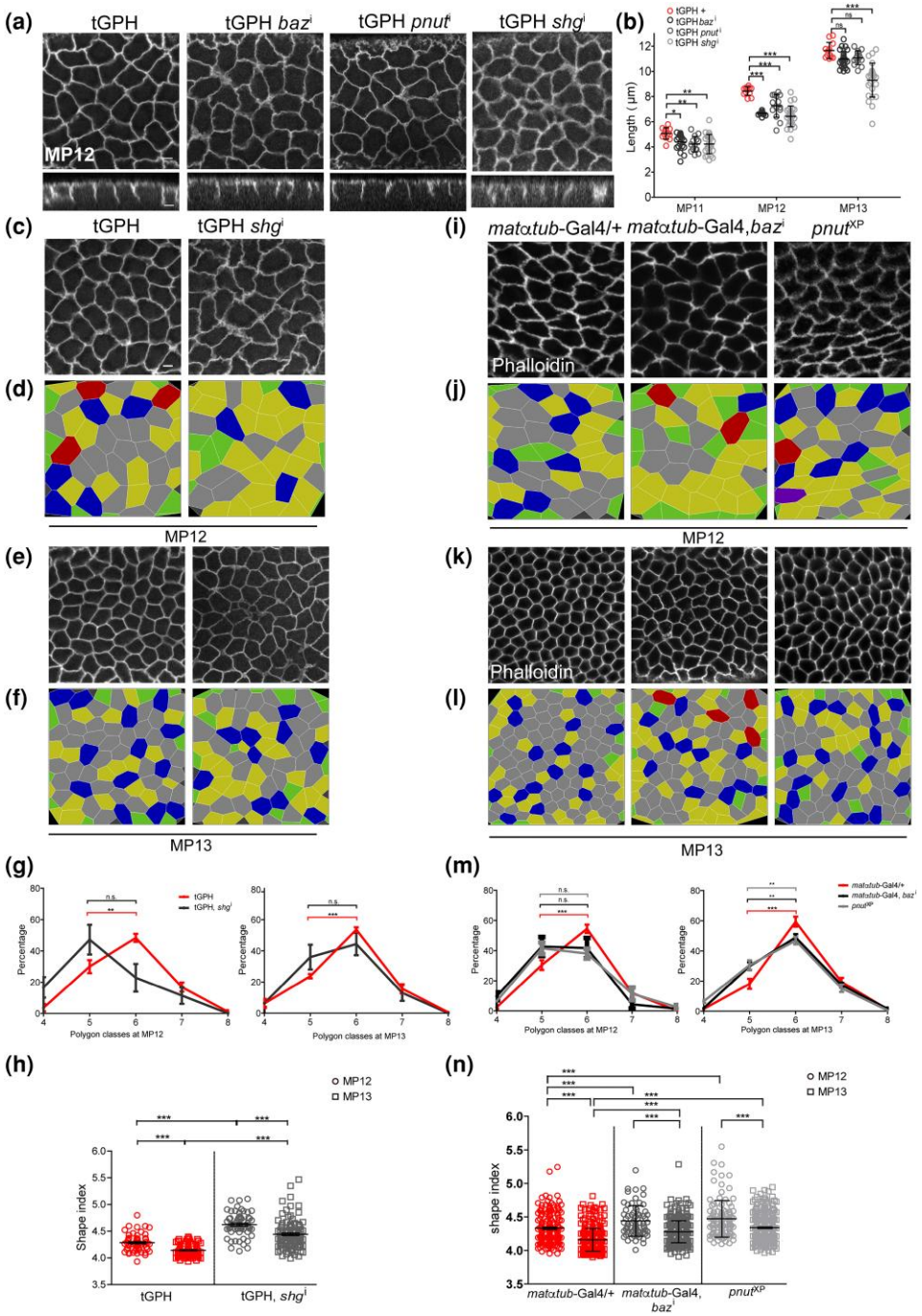

Fig. 4. DE-cad depletion shows a loss of hexagon dominance whereas. Baz and Pnut depletions show a delay in the onset of hexagon dominance. a and b) *baz*, *pnut*, *and shg* knockdown embryos show decreased furrow length. *atub84B*-tGPH (referred to as tGPH) grazing sections in MP12 for control, *matαtub*-Gal4; UAS-*baz*^{i} (*baz*^{i}), *matαtub*-Gal4, UAS-*pnut*^{i} (*pnut*^{i}), and *nos*-Gal4, *shg*^{i} (*shg*^{i}) at NC12 (a). Quantification of MP furrow lengths in tGPH/+, *baz*^{i}, *pnut*^{i}, and *shg*^{i} in NC11–13 ($n = 12$, 4 furrows each; 3 embryos) (c). Data is represented as mean ± SD, $^{*}P < 0.05$, $^{**}P < 0.01$, and $^{***}P < 0.001$, 2 tailed, unpaired Student's *t*-test. Scale bar: 5 µm. c–g) *shg*^{i} embryos show loss of hexagon dominance. tGPH/+ and tGPH; *matαtub*-Gal4, UAS-*shg*^{i} (*shg*^{i}) embryos in MP12–13 (c and e) along with the respective color-coded polygon renderings (d and f). Graph showing polygonal distribution in *shg*^{i} in MP12–13 (g) (n = approximately 120 syncytial cells, 20–30 cells/embryo; 4 embryos). Hexagon dominance is not seen in NC13. Pentagons and hexagons are compared in each cycle using the unpaired, 2 tailed, Student's *t*-test. Data is represented as mean ± SEM, $^{*}P < 0.05$, $^{**}P < 0.01$, and $^{***}P < 0.001$. Graph showing average shape index of all the cells in the field in control and *shg*^{i} embryos in MP12–13 (g) (n = approximately 120 syncytial cells, 20–30 cells/embryo; 4 embryos). The control tGPH cell shape index is repeated from Fig. 1e. Data is represented as mean ± SEM, $^{*}P < 0.05$, $^{**}P < 0.01$, and $^{***}P < 0.001$, 2-tailed, unpaired Student's *t*-test. The NC13 polygon distribution for the control is repeated from Fig. 1d. Scale bar: 5 µm. i–n) *baz*^{i} and *pnut*^{XP} embryos show a delay in the onset of hexagon dominance. Control (*matαtub*-Gal4/+), *matαtub*-Gal4, UAS-*baz*^{i} (*baz*^{i}) and *pnut*^{XP} (germ line clone) embryos stained with phalloidin in MP12–13 (i and k) along with the respective color-coded polygon renderings (j and l). Graph showing polygonal distribution in *baz*^{i} and *pnut*^{XP} in NC12–13 (m) (n = 60–80 syncytial cells, 20–30 cells/embryo; 4–5 embryos). Hexagon dominance in *baz*^{i} and *pnut*^{XP} recovers in NC13. Pentagons and hexagons are compared in each cycle using the 2 tailed, unpaired, Student's *t*-test. Data is represented as mean ± SEM, $^{*}P < 0.05$, $^{**}P < 0.01$, and $^{***}P < 0.001$. Graph showing average shape index of all the cells in the field in Control (+/+), *baz*^{i} and *pnut*^{XP} embryos in MP12–13 (n) (n = approximately 60–80 syncytial cells, 20–30 cells/embryo; 4–5 embryos) Data is represented as mean ± SEM, $^{*}P < 0.05$, $^{**}P < 0.01$, and $^{***}P < 0.001$, 2-tailed, unpaired Student's *t*-test. Scale bar: 5 µm.

We analyzed the polygonal distribution in DE-cad, Baz, and Pnut knockdown embryos in MP12 and MP13 by live imaging mutant embryos expressing tGPH, or with phalloidin staining. To assess the effect of DE-cad loss on polygonal distribution, we quantified the polygon types from the MP of *shg*^{i} live movies obtained with tGPH in the background. *shg*^{i} embryos showed pentagon dominance at MP12. The percentage of pentagons was significantly higher than hexagons in MP12 in *shg*^{i}, unlike control embryos which display hexagon dominance (Fig. 4c–e). *shg*^{i} expressing embryos showed a significant increase in pentagons in MP13 and there was no significant difference between pentagons and hexagons in MP13 as compared to hexagon dominance seen in control embryos (Fig. 4f–h). *shg*^{i} expressing embryos showed ruffled membranes as opposed to the taut and sharp membranes in the controls. The tGPH fluorescence at the furrow membrane was spread over a larger area as compared to control embryos (Supplementary Fig. 4a and b, Supplementary Video 4). Since control embryos showed hexagon dominance at MP and not at 6.5 μm in NC12 (Supplementary Fig. 1), the loss of hexagon dominance in *shg*^{i} expressing embryos is likely to be due to loss of adhesion thereby leading to decreased furrow stability and length in MP12 and MP13. The cell shape index also increased in *shg*^{i} expressing embryos (4.62 in MP12, 4.44 in MP13) as compared to controls (4.28 in MP12 and 4.14 in MP13) in MP12 and MP13 thereby indicating a shift to a more unstable or fluid network (Fig. 4h).

baz^{i} expressing embryos and *pnut*^{XP} germline clone embryos (Fig. 4i–o) stained with fluorescently coupled phalloidin showed a significant increase in the frequency of pentagons and loss of hexagon dominance in MP12 as compared to controls (Fig. 4i, j and m). However, the hexagon dominance was similar to controls in MP13 (Fig. 4k–m). The cell shape index was increased in Baz-depleted embryos as compared to controls (4.44 in MP12 and 4.28 in MP13 as compared to controls 4.33 in MP12 and 4.16 in MP13) (Fig. 4n). The cell shape index was increased in Pnut-depleted embryos as compared to controls (4.47 in MP12 and 4.34 in MP13) (Fig. 4n). Overexpression of the Baz oligomerization domain (BazΔ969-1464-GFP) that lowered Baz and depleted Pnut from the membrane also showed loss of hexagon dominance in MP12 and not in MP13 (Supplementary Fig. 5a–d). However, the cells were better organized as compared to *baz*^{i} and the cell shape index was almost similar to controls in these embryos suggesting that the expression of the oligomerization domain caused a less severe defect as compared to *baz*^{i} (Supplementary Fig. 5d). These data together showed that this decreased furrow length in MP did not support the organization of the PM in a hexagon dominated polygon array and in *baz*^{i} and *pnut*^{i} expressing embryos similar to controls at 6.5 μm (Supplementary Fig. 1). This is further corroborated by the observation that hexagon dominated polygon organization recovered in MP13 of *baz*^{i} and *pnut*^{i} expressing embryos, which also showed longer furrow lengths similar to control MP13. However, the cell shape index remained higher and the network remained more unstable in *baz*^{i} and *pnut*^{i} expressing embryos as compared to controls (Fig. 4k–n).

Therefore, our data shows that the decrease in furrow length seen upon loss of DE-cad, Baz, and Pnut is likely to cause a decrease in its stability as suggested by the increase in cell shape index, and loss of hexagon dominance in syncytial *Drosophila* embryos.

Recovery of hexagon dominance in Bazooka and Peanut mutant embryos occurs during syncytial cycle 13 with furrow extension

Hexagon dominance was seen in the syncytial *Drosophila* embryo on an increase in furrow length at MP in NC12 as well as at shorter furrow lengths of 6.5 μm in the prophase of NC13 (Supplementary Fig. 1b–d). Therefore, we analyzed whether hexagon dominance could also occur at shorter furrow lengths of 6.5 μm in NC13 in Baz and Pnut knockdown embryos. Since the predominant cell shapes in the syncytial embryos were hexagons and pentagons, we plotted the distribution of polygons and the ratio of pentagons to hexagons in controls, Baz, and Pnut depleted embryos, with respect to furrow length, from live movies of embryos expressing tGPH. For control embryos, we found that hexagon dominance was present when the polygonal array was established in NC13 at 6.5 μm in prophase and remained until MP (MP13). However, Baz and Pnut depleted embryos showed pentagon dominance at the furrow length of 6.5 μm in NC13, and hexagon dominance at the maximum furrow length in MP of NC13 (MP13) (Fig. 5a–e). The ratio of pentagons to hexagons increased in Baz and Pnut depleted embryos at 6.5 μm in NC13 and was significantly higher than controls (Fig. 5f) whereas at MP13, the ratio of pentagons to hexagons was not significantly different from controls (Fig. 5f). The cell shape index remained slightly higher than controls in both NC12 and NC13 at 6.5 μm and at MP (Fig. 5g). In summary, hexagon dominance occurred in NC13 in both Baz and Pnut knockdown embryos at longer furrow lengths in MP. It is possible that increased recruitment of polarity and adhesion complexes occurred at increased furrow length and this allowed the furrow to stabilize and get organized as a hexagon-dominant polygon array.

Bazooka and Peanut depleted embryos show an increase in DE-cadherin at the furrow

Furrow formation was affected in embryos depleted of DE-cad possibly due to lack of adhesion and stabilization of furrows. Unlike Baz- and Pnut-depleted embryos that show a delay in the onset of hexagon dominance, we found that loss of DE-cad led to the loss of hexagon dominance in both MP12 and MP13. We tested if DE-cad levels changed in Baz- and Pnut-depleted embryos. We hence imaged DE-cad distribution in live and fixed Baz- and Pnut-depleted embryos. DE-cad levels were estimated in Baz- and Pnut-depleted embryos by immunostaining for DE-cad using an antibody (Fig. 6) and expressing *ubi*-DE-cad-GFP in these embryos (Supplementary Video 5–7). Immunostaining with a DE-cad antibody showed that DE-cad levels increased on the furrow in MP12 and MP13 in Baz and Pnut depleted embryos as compared to controls (Fig. 6a–c). Baz and Pnut depleted embryos expressing DE-cad-GFP did not show a significant change in DE-cad-GFP fluorescence as compared to controls in MP12 (Supplementary Video 5–7). However, 50% of these embryos showed an increase in DE-cad-GFP fluorescence as compared to controls (Fig. 6d and f). DE-cad-GFP levels were significantly increased in MP13 in Baz and Pnut depleted embryos as to controls (Fig. 6e and f). In summary, we observe that DE-cad depletion leads to loss of hexagon dominance (Fig. 3) whereas Baz- and Pnut-depleted embryos showed hexagon dominance in MP13 at higher levels of DE-cad as compared to controls (Figs. 4 and 7). It is interesting to note that increased DE-cad in MP12 did not support hexagon dominance in the absence of Baz and Pnut.

Baz- and Pnut-depleted embryos show an increased accumulation of Dynamin and Rab5 at the furrow membrane

Polarity proteins are known to regulate endocytosis at the PM (Shivas et al. 2010). The levels of DE-cad at the PM will change based on the rates of endocytosis. DE-cad endocytosis increases in *Drosophila* tracheal tissues during active remodeling

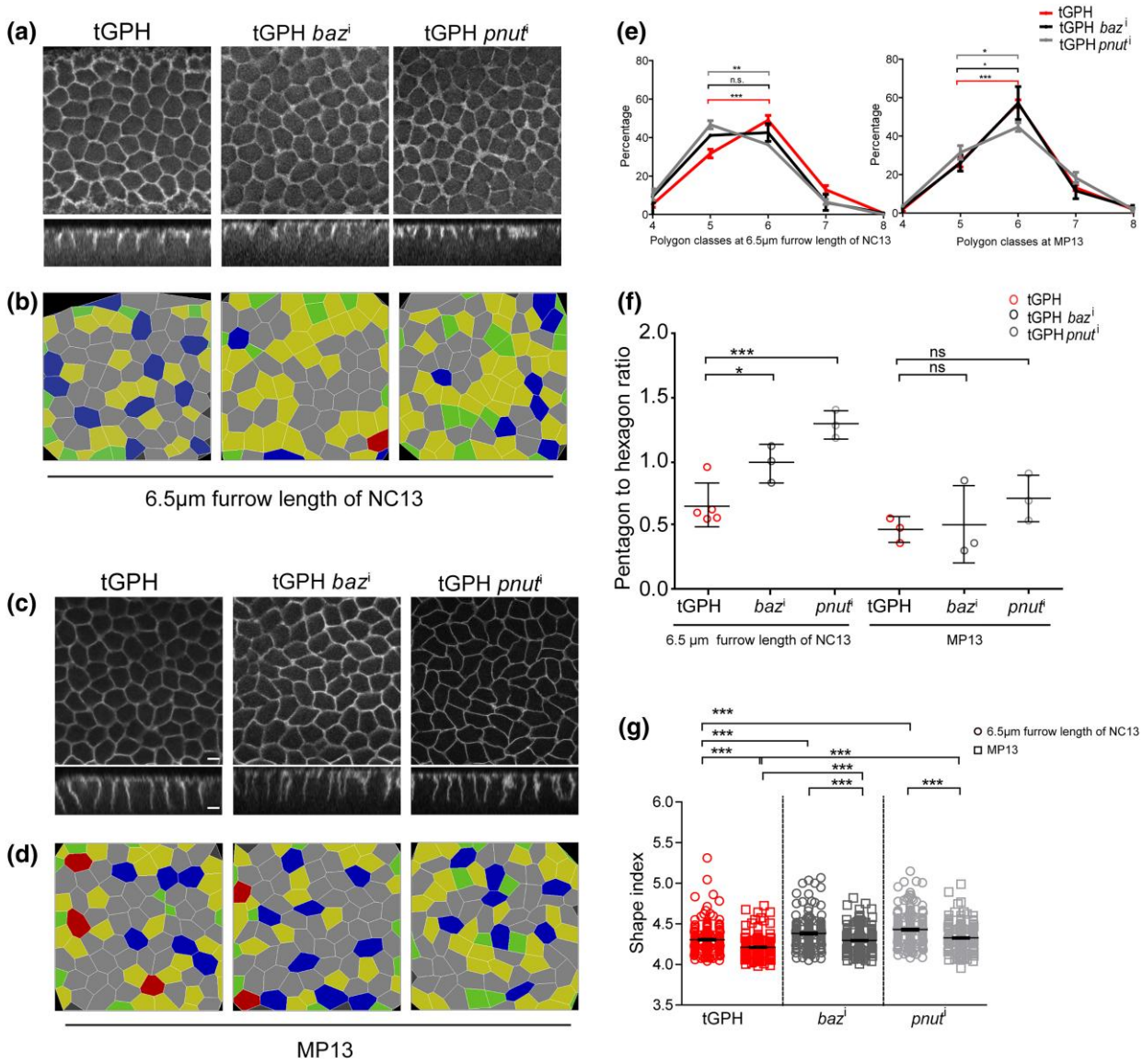

Fig. 5. Appearance of hexagon dominance in Baz and Pnut knockdowns occurs in MP of NC13. a and b) *matatub*-Gal4; *baz*^{i} (*baz*^{i}) and *matatub*-Gal4; *pnut*^{i} (*pnut*^{i}) embryos show loss of hexagon dominance at a shorter furrow length at NC13 when wildtype is already hexagon dominant. Grazing and sagittal sections of *atub84B*-tGPH (referred to as tGPH) expressing control, *baz*^{i} and *pnut*^{i} embryos at NC13 at a short furrow length of 6.5 µm (a) along with the respective color-coded polygon renderings (b). c and d) *baz*^{i} and *pnut*^{i} embryos show recovery of hexagon dominance at the maximum furrow length at MP13. Grazing and sagittal sections of tGPH expressing control, *baz*^{i} and *pnut*^{i} embryos at MP13 at maximum furrow length in MP (c) along with the respective color-coded polygon renderings (d). e–g) Baz and Pnut knockdowns show a length-dependent recovery of hexagon dominance at NC13. Graph showing the polygon distribution of control, *baz*^{i} and *pnut*^{i} embryos at NC13 at a short furrow length of 6.5 µm and at MP (e). Graph showing the pentagon to hexagon ratio of control, *baz*^{i} and *pnut*^{i} embryos at NC13 at a short furrow length of 6.5 µm and at MP (f). Data is represented as mean ± SEM, $^{*}P < 0.05$, $^{**}P < 0.01$, and $^{***}P < 0.001$, 2-tailed, unpaired Student's *t* test. Graph showing average shape index of all the cells in the field in control, *baz*^{i} and *pnut*^{i} embryos at NC13 at a short furrow length of 6.5 µm and at MP (g). Data is represented as mean ± SD, $^{*}P < 0.05$, $^{**}P < 0.01$, and $^{***}P < 0.001$, 2-tailed, unpaired Student's *t*-test. Scale bar = 5 µm.

(Shindo et al. 2008). DE-cad is present at higher levels at the PM in notum epithelial cells when endocytosis decreases in Par6 and aPKC mutants (Georgiou et al. 2008). Dynamin-mediated endocytosis is important for furrow extension in the syncytial blastoderm embryo (Rikhy et al. 2015). Increased accumulation of Dynamin at the furrow in temperature-sensitive mutants of Dynamin, *shibire*, shows decreased endocytosis and accumulation of DE-cad at the furrow (Rikhy et al. 2015). Since DE-cad increased in levels at the furrow in Baz- and Pnut-depleted embryos in MP12 and MP13, we assayed for distribution of Dynamin and early endosome protein Rab5 at the furrow in Baz- and Pnut-depleted embryos. We immunostained Baz and Pnut depleted embryos with Dynamin (Rikhy et al. 2015) and Rab5 (Tanaka et al. 2021) antibodies along with phalloidin and quantified the extent of change of fluorescence at the furrow as a ratio to the adjacent cytoplasm in MP12 and MP13. Dynamin is localized weakly at the furrow marked with phalloidin in control embryos in MP12 and MP13 (Fig. 7a and b). We found that there was an increase in Dynamin fluorescence at the furrow in the form of distinct punctae and in the cytoplasm in both Baz and Pnut depleted embryos (Fig. 7a and b). We specifically quantified the increase in Dynamin fluorescence at the furrow marked by phalloidin as a ratio to the cytoplasm and found that there is a significant increase at the furrow in MP12 and MP13 in Baz- and Pnut-depleted embryos (Fig. 7c).

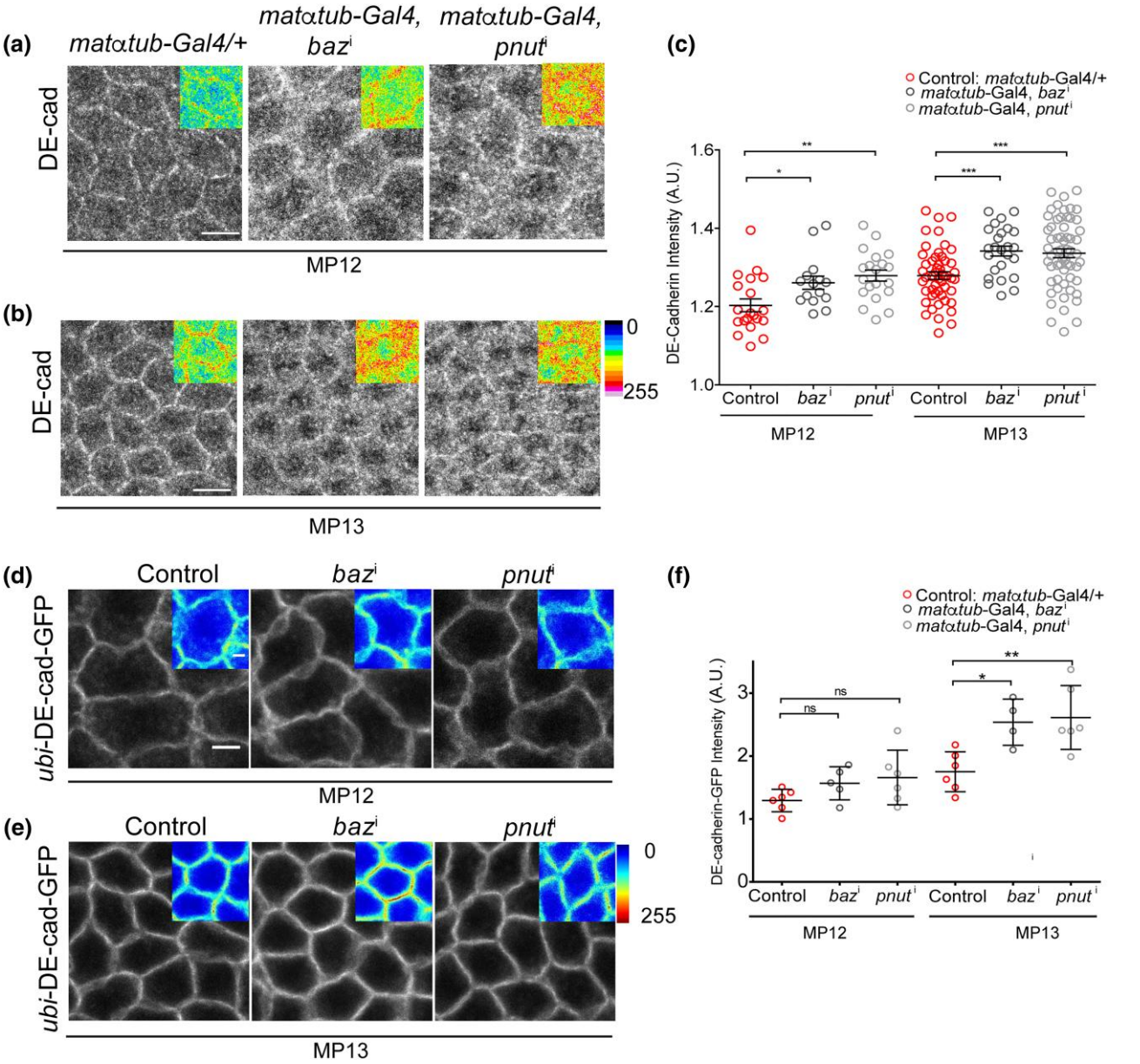

Fig. 6. DE-cad levels increase in Baz and Pnut knockdown embryos. a–c) Grazing sections of control, *matαtub*-Gal4; *baz*^{i} (*baz*^{i}) and *matαtub*-Gal4; *pnut*^{i} (*pnut*^{i}) stained with DE-cad in MP12–13 (a and b). Insets show zoomed in images. The 16 color rainbow scale from the imageJ is used to show fluorescent intensities. Graph showing quantification of the intensity of DE-cad on the membrane using membrane to cytosol ratios in *baz*^{i} (n = 15–25, 4–10 cells per embryo from MP12–13, 3–5 embryos) and *pnut*^{i} embryos (n = 20–60, 5–10 cells per embryo from MP12–13, 4–5 embryos) (c). DE-cad is increased in both *baz*^{i} and *pnut*^{i} embryos with higher significance value in MP13 than MP12. For MP12, DE-Cad accumulations are observed at approximately 2–2.4 microns of furrow length in both *baz*^{i} and *pnut*^{i} embryos. For MP13, DE-Cad accumulations are observed at around 2.4–4 microns of furrow length in both *baz*^{i} and *pnut*^{i} embryos. Data is represented as mean ± SD, *P < 0.05, **P < 0.01, and ***P < 0.001, 2-tailed, unpaired Student's *t*-test. Scale Bar = 10 µm. d–f) Grazing sections of *ubi*-DE-cad-GFP/+, *ubi*-DE-cad-GFP; *matαtub*-Gal4, UAS-*baz*^{i} (*baz*^{i}), and *ubi*-DE-cad-GFP; *matαtub*-Gal4, UAS-*pnut*^{i} (*pnut*^{i}) embryos in MP12–13 (d and e). Insets show zoomed in images. The 16 color rainbow scale from the imageJ is used to show fluorescent intensities. Graph showing quantification of normalized intensity of DE-cad on the membrane using membrane to cytosol ratios in *baz*^{i} and *pnut*^{i} embryos (n = 12–15, MP12–13, 5 cells per embryo, 5 embryos). DE-cad is increased in both *baz*^{i} and *pnut*^{i} embryos in MP13 (f). Data is represented as mean ± SD, *P < 0.05, **P < 0.01, and ***P < 0.001, 2-tailed, unpaired Student's *t*-test. Scale bar = 5 µm.

Rab5 fluorescence was observed in punctae and weakly at the furrow which is marked by phalloidin in control embryos in MP12 and MP13 (Fig. 7d and e). We found that there was an increased accumulation of Rab5 at the furrow in Baz- and Pnut-depleted embryos (Fig. 7d and e). We quantified the Rab5 fluorescence at the furrow in MP12 and MP13 embryos and found that there was a significant increase in accumulation at the furrow (Fig. 7f). This accumulation of Dynamin and Rab5 at the furrow implicates a decrease in endocytosis at the furrow PM in Baz and Pnut depleted embryos and this is likely to be the cause of the accumulation of DE-cad in NC12 and NC13. Future analysis of endocytic mutants will confirm whether loss of endocytosis, in general, leads to loss of furrow stability and hexagon-dominated polygon organization in the syncytial blastoderm *Drosophila* embryo.

In summary, we show that successive division cycles in the syncytial *Drosophila* blastoderm embryo show hexagon dominated PM organization, and a decrease in cell shape index accompanied by an increase in the concentration of polarity proteins at the

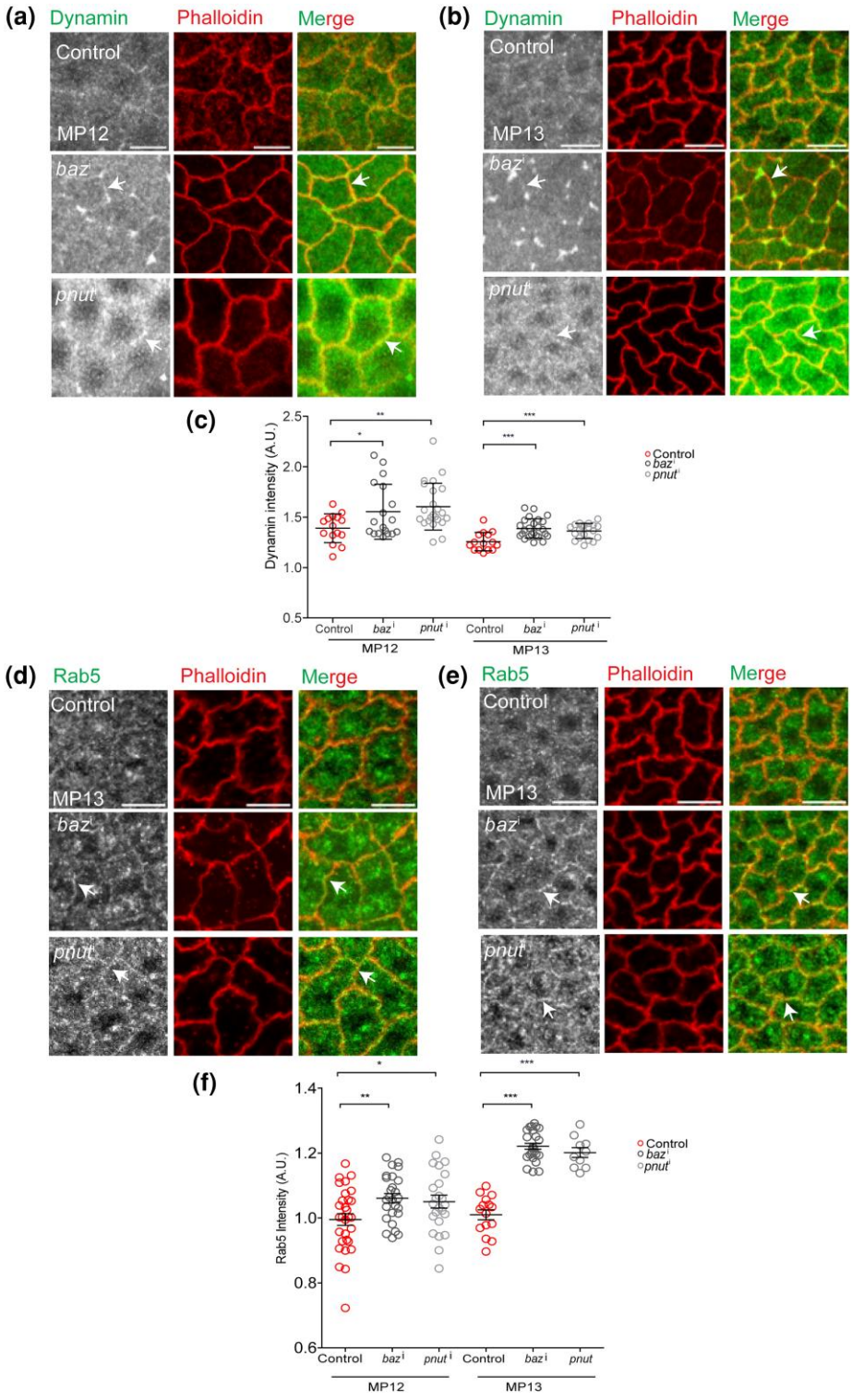

Fig. 7. Dynamin and Rab5 levels increase in Baz and Pnut knockdown embryos. a–c) Grazing sections of control (*matatub*-Gal4/+), *matatub*-Gal4, UAS-*baz*^{i} (*baz*^{i}) and *matatub*-Gal4, UAS-*pnut*^{i} (*pnut*^{i}) stained with Dynamin and Phalloidin in MP12 and MP13 (a and b). Graph showing quantification of fluorescence intensity of Dynamin on the membrane using membrane to cytosol ratios in *baz*^{i} ($n = 15–40$, 5 cells per embryo from MP12–13, 3–8 embryos) and *pnut*^{i} embryos ($n = 30–39$, 4–5 cells per embryo MP12–13, 6–8 embryos) (c). Dynamin is increased in both *baz*^{i} and *pnut*^{i} embryos with higher significance value in MP13 than MP12. For MP12, the image shown for Dynamin accumulations is at approximately 1.8–2.4 microns of furrow length in both *baz*^{i} and *pnut*^{i} embryos. For MP13, the image shown for Dynamin accumulation is at around 2.4–4 microns of furrow length in both *baz*^{i} and *pnut*^{i} embryos. Data is represented as mean ± SD, $^{*}P < 0.05$, $^{**}P < 0.01$, and $^{***}P < 0.001$, 2-tailed, unpaired Student's *t* test. Scale Bar = 10 µm. d–f) Grazing sections of control (+/+), *baz*^{i} and *pnut*^{i} stained with Rab5 in MP of MP12–13 (d and e). Graph showing quantification of intensity of Rab5 on the membrane using membrane to cytosol ratios in *baz*^{i} ($n = 25–26$, 4–5 cells per embryo from NC12–13, 5 embryos) and *pnut*^{i} embryos ($n = 10–25$, 5 cells per embryo from MP12–13, 2–5 embryos) (f). Rab5 is increased in both *baz*^{i} and *pnut*^{i} embryos in MP12 and MP13. For MP12, the image shown for Rab5 accumulation is at approximately 1.8–2.4 microns of furrow length in both *baz*^{i} and *pnut*^{i} embryos. For MP13, the image shown for Rab5 accumulations is at around 2.4–4 microns of furrow length in both *baz*^{i} and *pnut*^{i} embryos. Data is represented as mean ± SD, $^{*}P < 0.05$, $^{**}P < 0.01$, and $^{***}P < 0.001$, 2-tailed, unpaired Student's *t*-test. Scale Bar = 10 µm.

furrow. DE-cad regulates the formation of furrow, cell stability, and hexagon dominance. Baz and Pnut depleted embryos show hexagon dominance coincident with an increase in levels of DE-cad as compared to controls. It is likely that decreased cell shape index and delayed onset of hexagon-dominated polygon organization in Baz and Pnut depleted embryos occurs only when higher levels of DE-cad are obtained in MP13. These observations highlight an inter-regulation of polarity, adhesion, and endocytosis proteins in order to achieve appropriate stabilization of the furrow membrane to achieve a stable hexagon-dominated polygonal array in the syncytial *Drosophila* blastoderm embryo.

Discussion

In this study, we show that the formation of hexagon dominated PM organization in a relatively stable epithelial-like array occurs in the presence of a combination of adhesion and polarity proteins in the syncytial *Drosophila* blastoderm embryo from the MP stage of NC12. Pentagons and hexagons are equally likely in NC11 when edges first form and hexagons are present at a frequency of almost double the number of pentagons from the MP of NC12 up to NC13. Since the syncytial cycles do not have a complete basal domain, the lateral membrane, i.e. the pseudocleavage furrow, is sufficient to regulate the stability of the epithelial-like array showing hexagon dominance. There is a decrease in cell shape index across the syncytial cycle showing that increased crowding correlates with a more stable polygonal array. We have characterized the role of Baz, Pnut, and DE-cad proteins in the regulation of the lateral furrow length and polygon array distribution in the syncytial embryo. This analysis reveals furrow and polygon distribution phenotypes in 2 categories: (1) DE-cad depleted embryos have short furrows, loss of hexagon dominance, and an increase in cell shape index; (2) Baz- and Pnut-depleted embryos have slightly short furrows, delay in hexagon dominance and an increase in cell shape index. Even though the cell shape index is more than controls in DE-cad, Baz, and Pnut depleted embryos, there is a decrease from MP12 to MP13 showing that cell proliferation and associated changes in the PM give rise to a more stable network. Hexagon dominance appears in Baz and Pnut mutant embryos in NC13 with an increase in furrow lengths. This is coincident with an increase in DE-cad levels and accumulation of endocytic machinery at the furrow PM. These studies, therefore, reveal the requirement of stability of the furrow PM, by the combination of polarity and adhesion proteins, and further implicate endocytosis rates in the regulation of de novo hexagon dominant epithelial-like PM in the syncytial *Drosophila* embryo (Fig. 8). DE-cad function is more significant for furrow extension as compared to Baz and Pnut. Baz and Pnut are important for the stabilization of the furrow membrane to give rise to hexagonal dominant furrow membrane organization. Vertices mature and stabilize in NC12 with the accumulation of Baz at edges and Pnut at vertices. Baz presence on the furrow membrane is important for Pnut distribution.

DE-cad loss significantly decreased but did not completely abolish lateral furrows. If this is the major protein responsible for the stabilization of adhesion of furrow membranes of adjacent syncytial cells, we should have obtained a phenotype of complete loss of furrow but we only saw a reduction in furrow length. We argue that this could be due to the inability to deplete DE-cad completely with the RNAi strategy. Also, it could be due to the presence of other proteins that are responsible for keeping the furrow membrane adhered to each other. Other transmembrane proteins such as Crumbs, Neuroglian, and Neurexin are not present in syncytial embryos (Harris and Peifer 2004; Laprise et al. 2009). Future analysis of other cadherin-like adhesion molecules such as Echinoid may be useful in this direction (Wei et al. 2005).

We find that DE-cad levels regulate the stabilization of the furrow and the occurrence of hexagon dominance in the syncytial blastoderm embryo. DE-cad increases during the syncytial division cycles from MP11 to MP13 along with Baz and Pnut. An increase in DE-cad can also occur due to the loss of endocytosis and recycling in the *Drosophila* wing disc epithelium and blastoderm embryo (Classen et al. 2005; Rikhy et al. 2015; Iyer et al. 2019). We observed that Baz and Pnut depletion on the syncytial furrow led to an increase in DE-cad and accumulation of endocytic proteins at the furrow. This shows that Baz and Pnut depleted embryos show hexagon dominance at higher levels of DE-cad than controls. Since DE-cad depletion shows loss of hexagon dominance, this compensatory increase in DE-cad is likely to be responsible for the rescueof hexagon dominance in MP13 in

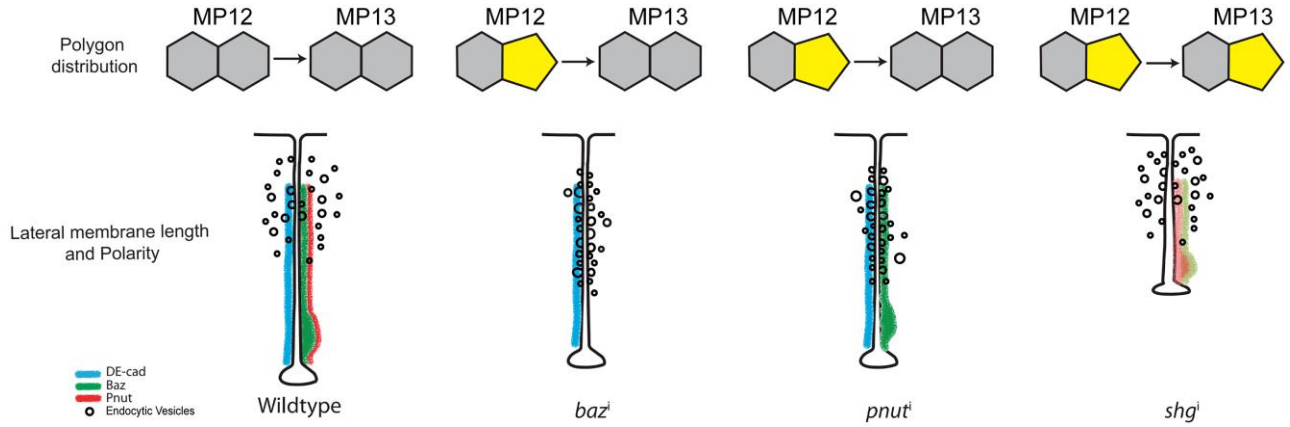

Fig. 8. Summary schematic showing the distribution of DE-cad, Baz and Pnut on the lateral furrow and polygon distribution in the *Drosophila* syncytial blastoderm embryo in NC13. Control embryos show hexagon dominance in MP12–13 with a significant amount of DE-cad, Baz, and Pnut on the lateral furrow. DE-cad undergoes endocytosis at the furrow membrane. Loss of Baz or Pnut results in a shorter furrow and delay in the onset of hexagon dominance while loss of DE-cad results in a shorter furrow along with a loss of hexagon dominance. Note the difference in the protein complex composition in the various mutants along with the possible accumulation of endocytic vesicles on the cell membrane. *baz*^{i} shows the loss of Baz and Pnut, while *pnut*^{i} shows loss of Pnut only. DE-cad is increased in *baz*^{i} and *pnut*^{i} in MP13 along with increased accumulation of endocytic machinery, which correlates with the recovery of hexagon dominance. *shg*^{i}, on the other hand, shows a decrease or mislocalization of DE-cad, Baz, and Pnut.

Baz- and Pnut-depleted embryos. Further elucidation of defects in proteins regulating membrane trafficking will also reveal the mechanisms by which endocytosis decreases in Baz and Pnut depleted embryos.

Baz and DE-cad play significant roles in being the primary molecules initiating the polarity program in different tissues. Baz initiates adherens junction polarity in *Drosophila* cellularization and gastrulation (Müller and Wieschaus 1996; Harris and Peifer 2004; Pilot et al. 2006) but is dispensable in follicle epithelial cells (Shahab et al. 2015). During mesoderm invagination, apical movement of DE-cad precedes the relocation of Baz, and thus, the asymmetry in DE-cad distribution here does not depend on Baz (Weng and Wieschaus 2017). This is similar to mammalian cells where E-cad is recruited to contact points before Baz (Coopman and Djiane 2016). This suggests that depending on the tissue type or developmental stage, the relative importance of Baz and E-cad in initiating polarity may change. We show that DE-cad is important for the distribution of both Baz and Pnut to the furrow. In the absence of identification of other adhesion proteins in the syncytial blastoderm embryo, we conclude that DE-cad assumes a significant role in furrow formation and stabilization in the *Drosophila* syncytial blastoderm embryo.

Asynchronous cell division in *Drosophila* wing disc epithelia is one of the mechanisms that give rise to a hexagon dominant and energy-minimized network (Gibson et al. 2006). It is interesting to note that synchronous divisions in the syncytial *Drosophila* blastoderm embryo also result in hexagon dominance in NC12. These observations are consistent with the presence of nuclei in a hexagon dominated polygonal organization in the syncytial *Drosophila* embryo (Kanesaki et al. 2011; Kaiser et al. 2018). Cytoskeletal dynamics coupled with polarity protein distribution favor the organization of this network.

A decreased number of edges in the polygonal array is a favorable state for cell neighbor exchanges and gives rise to a soft network (Farhadifar et al. 2007). The increase in pentagons in Baz and Pnut depleted embryos indicates a similar transition to a soft network possibly due to decreased stabilization of the furrow even in the presence of DE-cad and furrow length. The contacts in the Baz and Pnut mutant embryos are likely to facilitate neighbor exchanges. An increase in DE-cad on the furrow in MP13 in Baz and Pnut depleted embryos may allow for conversion back to hexagon-dominated state by formation and stabilization of one additional edge and vertex. Future analysis of change in furrow tension in various genetic backgrounds, along with mathematical modeling, will reveal the mechanisms that drive shape morphogenesis in *Drosophila* syncytial blastoderm embryos.

Data availability

The data underlying this article are available in the article and in its online Supplementary material.

Supplemental material available at GENETICS online.

Acknowledgments

We thank the R.R. lab members for their comments and discussion on the data in the manuscript. We thank the *Drosophila* and Microscopy facilities at IISER, Pune, India for help with stocks and microscopy for the experiments. We thank Benoit Aigouy for sharing the Packing analyzer software. We thank Andreas Wodarz (University of Goettingen, Germany) for the Bazooka antibody and Bazooka domain truncation stocks. We thank Manos Mavrakis (Institute Fresnel, Marseilles, France) for *peanut* mutant stocks and Sep1 and 2 antibodies. Stocks obtained from the Bloomington *Drosophila* Stock Center (NIH P40OD018537) were used in this study. R.R. thanks the Wellcome Trust DBT India Alliance Senior Fellowship IA/S/22/1/506232 for support to the lab.

Funding

R.R. thanks the Department of Biotechnology, Ministry of Science and Technology, India for funding BT/PR17317/BRB/10/1521/2016 to this project.

Conflicts of interest

The author(s) declare no conflict of interest.

Literature cited

Aegerter-Wilmsen T, Smith AC, Christen AJ, Aegerter CM, Hafen E, Basler K. 2010. Exploring the effects of mechanical feedback on epithelial topology. Development. 137(3):499–506. doi:10.1242/dev.041731.

Benton R, St Johnston D. 2003. Drosophila PAR-1 and 14-3-3 inhibit Bazooka/PAR-3 to establish complementary cortical domains in polarized cells. Cell. 115(6):691–704. doi:10.1016/S0092-8674(03)00938-3.

Bi D, Lopez JH, Schwarz JM, Manning ML. 2015. A density-independent rigidity transition in biological tissues. Nat Phys. 11(12):1074–1079. doi:10.1038/nphys3471.

Bilder D, Li M, Perrimon N. 2000. Cooperative regulation of cell polarity and growth by Drosophila tumor suppressors. Science. 289(5476):113–116. doi:10.1126/science.289.5476.113.

Britton JS, Lockwood WK, Li L, Cohen SM, Edgar BA. 2002. Drosophila's insulin/PI3-kinase pathway coordinates cellular metabolism with nutritional conditions. Dev Cell. 2(2):239–249. doi:10.1016/S1534-5807(02)00117-X.

Classen A-K, Anderson KI, Marois E, Eaton S. 2005. Hexagonal packing of Drosophila wing epithelial cells by the planar cell polarity pathway. Dev Cell. 9(6):805–817. doi:10.1016/j.devcel.2005.10.016.

Coopman P, Djiane A. 2016. Adherens Junction and E-cadherin complex regulation by epithelial polarity. Cell Mol Life Sci. 73(18):3535–3553. doi:10.1007/s00018-016-2260-8.

Dey B, Rikhy R. 2020. DE-cadherin and Myosin II balance regulates furrow length for onset of polygon shape in syncytial Drosophila embryos. J Cell Sci. 133(10):jcs240168. doi:10.1242/jcs.240168.

Farhadifar R, Röper J-C, Aigouy B, Eaton S, Jülicher F. 2007. The influence of cell mechanics, cell-cell interactions, and proliferation on epithelial packing. Curr Biol. 17(24):2095–2104. doi:10.1016/j.cub.2007.11.049.

Foe VE, Alberts BM. 1983. Studies of nuclear and cytoplasmic behaviour during the five mitotic cycles that precede gastrulation in Drosophila embryogenesis. J Cell Sci. 61(1):31–70. doi:10.1242/jcs.61.1.31.

Foe VE, Field CM, Odell GM. 2000. Microtubules and mitotic cycle phase modulate spatiotemporal distributions of F-actin and myosin II in Drosophila syncytial blastoderm embryos. Development. 127(9):1767–1787. doi:10.1242/dev.127.9.1767.

Georgiou M, Marinari E, Burden J, Baum B. 2008. Cdc42, Par6, and aPKC regulate Arp2/3-mediated endocytosis to control local adherens junction stability. Curr Biol. 18(21):1631–1638. doi:10.1016/j.cub.2008.09.029.

Gibson MC, Patel AB, Nagpal R, Perrimon N. 2006. The emergence of geometric order in proliferating metazoan epithelia. Nature. 442(7106):1038–1041. doi:10.1038/nature05014.

Gramates LS, Agapite J, Attrill H, Calvi BR, Crosby MA, dos Santos G, Goodman JL, Goutte-Gattat D, Jenkins VK, Kaufman T, *et al.* 2022. Flybase: a guided tour of highlighted features. Genetics. 220(4): iyac035. doi:10.1093/genetics/iyac035.

Guillot C, Lecuit T. 2013. Mechanics of epithelial tissue homeostasis and morphogenesis. Science. 340(6137):1185–1189. doi:10.1126/science.1235249.

Harris TJC, Peifer M. 2004. Adherens junction-dependent and -independent steps in the establishment of epithelial cell polarity in Drosophila. J Cell Biol. 167(1):135–147. doi:10.1083/jcb.200406024.

Hayashi T, Carthew RW. 2004. Surface mechanics mediate pattern formation in the developing retina. Nature. 431(7009):647–652. doi:10.1038/nature02952.

Holly RM, Mavor LM, Zuo Z, Blankenship JT. 2015. A rapid, membrane-dependent pathway directs furrow formation through RalA in the early Drosophila embryo. Development. 142(13):2316–2328. doi:10.1242/dev.120998.

Huang J, Zhou W, Dong W, Watson AM, Hong Y. 2009. From the Cover: directed, efficient, and versatile modifications of the Drosophila genome by genomic engineering. Proc Natl Acad Sci U S A. 106(20):8284–8289. doi:10.1073/pnas.0900641106.

Ikenouchi J, Furuse M, Furuse K, Sasaki H, Tsukita S, Tsukita S. 2005. Tricellulin constitutes a novel barrier at tricellular contacts of epithelial cells. J Cell Biol. 171(6):939–945. doi:10.1083/jcb.200510043.

Iyer KV, Piscitello-Gómez R, Paijmans J, Jülicher F, Eaton S. 2019. Epithelial viscoelasticity is regulated by mechanosensitive E-cadherin turnover. Curr Biol. 29(4):578–591.e5. doi:10.1016/j.cub.2019.01.021.

Kaiser F, Lv Z, Marques Rodrigues D, Rosenbaum J, Aspelmeier T, Großhans J, Alim K. 2018. Mechanical model of nuclei ordering in Drosophila embryos reveals dilution of stochastic forces. Biophys J. 114(7):1730–1740. doi:10.1016/j.bpj.2018.02.018.

Kalaji R, Wheeler AP, Erasmus JC, Lee SY, Endres RG, Cramer LP, Braga VM. 2012. ROCK1 And ROCK2 regulate epithelial polarisation and geometric cell shape. Biol Cell. 104(8):435–451. doi:10.1111/boc.201100093.

Kanesaki T, Edwards CM, Schwarz US, Grosshans J. 2011. Dynamic ordering of nuclei in syncytial embryos: a quantitative analysis of the role of cytoskeletal networks. Integr Biol (Camb). 3(11): 1112–1119. doi:10.1039/c1ib00059d.

Krahn MP, Bückers J, Kastrup L, Wodarz A. 2010. Formation of a Bazooka-Stardust complex is essential for plasma membrane polarity in epithelia. J Cell Biol. 190(5):751–760. doi:10.1083/jcb.201006029.

Laprise P, Lau KM, Harris KP, Silva-Gagliardi NF, Paul SM, Beronja S, Beitel GJ, McGlade CJ, Tepass U. 2009. Yurt, Coracle, Neurexin IV and the Na+, K+-ATPase form a novel group of epithelial polarity proteins. Nature. 459(7250):1141–1145. doi:10.1038/nature08067.

Laprise P, Tepass U. 2011. Novel insights into epithelial polarity proteins in Drosophila. Trends Cell Biol. 21(7):401–408. doi:10.1016/j.tcb.2011.03.005.

Letizia A, Ricardo S, Moussian B, Martín N, Llimargas M. 2013. A functional role of the extracellular domain of Crumbs in cell architecture and apicobasal polarity. J Cell Sci. 126(Pt 10):2157–2163. doi:10.1242/jcs.122382.

Lv Z, Rosenbaum J, Mohr S, Zhang X, Kong D, Preiß H, Kruss S, Alim K, Aspelmeier T, Großhans J. 2020. The emergent yo-yo movement of nuclei driven by cytoskeletal remodeling in pseudo-synchronous mitotic cycles. Curr Biol. 30(13):2564–2573.e5. doi:10.1016/j.cub.2020.04.078.

Mavrakis M, Rikhy R, Lilly M, Lippincott-Schwartz J. 2008. Fluorescence imaging techniques for studying Drosophila embryo development. Curr Protoc Cell Biol. Chapter 4:Unit 4.18. doi:10.1002/0471143030.cb0418s39.

Mavrakis M, Rikhy R, Lippincott-Schwartz J. 2009. Plasma membrane polarity and compartmentalization are established before cellularization in the fly embryo. Dev Cell. 16(1):93–104. doi:10.1016/j.devcel.2008.11.003.

Miller KG, Karr TL, Kellogg DR, Mohr IJ, Walter M, Alberts BM. 1985. Studies on the cytoplasmic organization of early Drosophila embryos. Cold Spring Harb Symp Quant Biol. 50:79–90. doi:10.1101/SQB.1985.050.01.012.

Müller HA, Wieschaus E. 1996. Armadillo, bazooka, and stardust are critical for early stages in formation of the zonula adherens and maintenance of the polarized blastoderm epithelium in Drosophila. J Cell Biol. 134(1):149–163. doi:10.1083/jcb.134.1.149.

Nance J. 2014. Getting to know your neighbor: cell polarization in early embryos. J Cell Biol. 206(7):823–832. doi:10.1083/jcb.201407064.

Neufeld TP, Rubin GM. 1994. The Drosophila Peanut gene is required for cytokinesis and encodes a protein similar to yeast putative bud neck filament proteins. Cell. 77(3):371–379. doi:10.1016/0092-8674(94)90152-X.

Park JA, Kim JH, Bi D, Mitchel JA, Qazvini NT, Tantisira K, Park CY, McGill M, Kim S-H, Gweon B, *et al.* 2015. Unjamming and cell shape in the asthmatic airway epithelium. Nat Mater. 14(10): 1040–1048. doi:10.1038/nmat4357.

Pesacreta TC, Byers TJ, Dubreuil R, Kiehart DP, Branton D. 1989. Drosophila Spectrin: the membrane skeleton during embryogenesis. J Cell Biol. 108(5):1697–1709. doi:10.1083/jcb.108.5.1697.

Pilot F, Philippe J-M, Lemmers C, Lecuit T. 2006. Spatial control of actin organization at adherens junctions by a synaptotagmin-like protein Btsz. Nature. 442(7102):580–584. doi:10.1038/nature04935.

Rikhy R, Mavrakis M, Lippincott-Schwartz J. 2015. Dynamin regulates metaphase furrow formation and plasma membrane compartmentalization in the syncytial Drosophila embryo. Biol Open. 4(3):301–311. doi:10.1242/bio.20149936.

Sánchez-Gutiérrez D, Sáez A, Pascual A, Escudero LM. 2013. Topological progression in proliferating epithelia is driven by a unique variation in polygon distribution. PLoS One. 8(11):e79227. doi:10.1371/journal.pone.0079227.

Schmidt A, Grosshans J. 2018. Dynamics of cortical domains in early Drosophila development. J Cell Sci. 131(7):jcs212795. doi:10.1242/jcs.212795.

Schmidt A, Lv Z, Großhans J. 2018. ELMO and Sponge specify subapical restriction of Canoe and formation of the subapical domain in early Drosophila embryos. Development. 145(2):dev157909. doi:10.1242/dev.157909.

Schneider CA, Rasband WS, Eliceiri KW. 2012. NIH Image to ImageJ: 25 years of image analysis. Nat Methods. 9(7):671–675. doi:10.1038/nmeth.2089.

Schulte J, Tepass U, Auld VJ. 2003. Gliotactin, a novel marker of tricellular junctions, is necessary for septate junction development in Drosophila. J Cell Biol. 161(5):991–1000. doi:10.1083/jcb.200303192.

Shahab J, Tiwari MD, Honemann-Capito M, Krahn MP, Wodarz A. 2015. Bazooka/PAR3 is dispensable for polarity in Drosophila follicular epithelial cells. Biol Open. 4(4):528–541. doi:10.1242/bio.201410934.

Sherlekar A, Mundhe G, Richa P, Dey B, Sharma S, Rikhy R. 2020. F-BAR domain protein Syndapin regulates actomyosin dynamics during apical cap remodeling in syncytial Drosophila embryos. J Cell Sci. 133(10):jcs235846. doi:10.1242/jcs.235846.

Sherlekar A, Rikhy R. 2016. Syndapin promotes pseudocleavage furrow formation by actin organization in the syncytial Drosophila embryo. Mol Biol Cell. 27(13):2064–2079. doi:10.1091/mbc.E15-09-0656.

Shindo M, Wada H, Kaido M, Tateno M, Aigaki T, Tsuda L, Hayashi S. 2008. Dual function of Src in the maintenance of adherens junctions during tracheal epithelial morphogenesis. Development. 135(7):1355–1364. doi:10.1242/dev.015982.

Shivas JM, Morrison HA, Bilder D, Skop AR. 2010. Polarity and endocytosis: reciprocal regulation. Trends Cell Biol. 20(8):445–452. doi:10.1016/j.tcb.2010.04.003.

Silverman-Gavrila RV, Hales KG, Wilde A. 2008. Anillin-mediated targeting of Peanut to pseudocleavage furrows is regulated by the GTPase Ran. Mol Biol Cell. 19(9):3735–3744. doi:10.1091/mbc.e08-01-0049.

Silverman-Gavrila RV, Silverman-Gavrila LB. 2008. Septins: new microtubule interacting partners. ScientificWorldJournal. 8:611–620. doi:10.1100/tsw.2008.87.

Stevenson V, Hudson A, Cooley L, Theurkauf WE. 2002. Arp2/3-dependent pseudocleavage [correction of psuedocleavage] furrow assembly in syncytial Drosophila embryos. Curr Biol. 12(9):705–711. doi:10.1016/S0960-9822(02)00807-2.

Sugimura K, Ishihara S. 2013. The mechanical anisotropy in a tissue promotes ordering in hexagonal cell packing. Development. 140(19):4091–4101. doi:10.1242/dev.094060.

Tanaka T, Tani N, Nakamura A. 2021. Receptor-mediated yolk uptake is required for oskar mRNA localization and cortical anchorage of germ plasm components in the Drosophila oocyte. PLoS Biol. 19(4):e3001183. doi:10.1371/journal.pbio.3001183.

Thomas CM, Williams JA. 1999. Dynamic rearrangement of the spectrin membrane skeleton during the generation of epithelial polarity in Drosophila. J Cell Sci. 112(Pt 17):2843–2852. doi:10.1242/jcs.112.17.2843.

Vishwakarma M, Thurakkal B, Spatz JP, Das T. 2020. Dynamic heterogeneity influences the leader–follower dynamics during epithelial wound closure. Philos Trans R Soc Lond B Biol Sci. 375(1807):20190391. doi:10.1098/rstb.2019.0391.

Wang X, Merkel M, Sutter LB, Erdemci-Tandogan G, Manning ML, Kasza KE. 2020. Anisotropy links cell shapes to tissue flow during convergent extension. Proc Natl Acad Sci U S A. 117(24):13541–13551. doi:10.1073/pnas.1916418117.

Wei S-Y, Escudero LM, Yu F, Chang L-H, Chen L-Y, Ho Y-H, Lin C-M, Chou C-S, Chia W, Modolell J, *et al.* 2005. Echinoid is a component of adherens junctions that cooperates with DE-cadherin to mediate cell adhesion. Dev Cell. 8(4):493–504. doi:10.1016/j.devcel.2005.03.015.

Weng M, Wieschaus E. 2017. Polarity protein Par3/Bazooka follows myosin-dependent junction repositioning. Dev Biol. 422(2):125–134. doi:10.1016/j.ydbio.2017.01.001.

Wodarz A, Ramrath A, Kuchinke U, Knust E. 1999. Bazooka provides an apical cue for Inscuteable localization in Drosophila neuroblasts. Nature. 402(6761):544–547. doi:10.1038/990128.

Xie Y, Blankenship JT. 2018. Differentially-dimensioned furrow formation by zygotic gene expression and the MBT. PLoS Genet. 14(1):e1007174. doi:10.1371/journal.pgen.1007174.

Zallen JA, Cohen Y, Hudson AM, Cooley L, Wieschaus E, Schejter ED. 2002. SCAR Is a primary regulator of Arp2/3-dependent morphological events in Drosophila. J Cell Biol. 156(4):689–701. doi:10.1083/jcb.200109057.

Editor: D. Andrew